

Restricted Complexity Control Design for Wave Energy Converters

Xiaoxing Fu

Department of Engineering
University of Leicester
Leicester, LE1 7RH, UK

This dissertation is submitted for the degree of
Doctor of Philosophy

November 2017

Abstract

This thesis introduces various control system designs for wave energy converters. It describes optimal conditions for maximizing the energy absorbed from wave energy converters. Feedback realisation of complex-conjugate control and velocity-tracking control are used to create these conditions. Also, passive loading control and latching control, which correspond to non-optimal conditions, are both discussed here. Several different ways of overcoming the non-causal problem of optimal conditions are also discussed. Firstly, prediction of wave elevation or excitation force can be used to solve the non-causal problem. Several predictive approaches' performances are compared. A new approach, called multi-steps predictive identification, has been shown that have better performance than other approaches. Secondly, the prediction error method, which is used to find a constant approximation of a model's performance can be also used to overcome the non-causal problem. The most important aim of this project is to maximize absorbed energy. The design of a Power Takeoff (PTO) device of a wave energy conversion system here involved direct optimization of the parameters of a mechanical network using the Nelder–Mead method can be linked to power absorption performance. Approximate transfer functions are realized with different admittances are here compared. Real ocean data sets were tested in terms of admittances. Their advantages and disadvantages of each method are presented in this thesis.

Acknowledgements

I would like to thank my supervisor Dr. Andrea Lecchini-Visintini. His valuable guidance has motivated me to explore various control and optimization problems. His timely advice on research topics selections is highly appreciated. Further, he has helped me in various aspects of theoretical and experimental topics related to this thesis. I would also like to thank Prof. Da-Wei Gu for his several suggestions during my PhD course. I am thankful to Prof. Matthew Turner for his advice in the APG transfer.

I would like to thank my lab members Bharani, Angeliki, Peter, Indira , Paresh, Tomas, Emre, and Hasan. They gave several inputs, both academic and non-academic, during the course of my PhD.

I would also like to thank Prof. John Ringwood and Dr. Francesco Fusco. I got fundament wave knowledge and data from their books and published papers. I am thankful to RS Aqua Ltd for real wave data supplying.

Finally, I would like to thank my parents for their support and funding for course.

Contents

List of Figures	vii
1 Introduction	1
1.1 Background to wave energy resources	1
1.1.1 Principles and Classification of Wave Energy Converters (WECs)	2
1.1.2 Power and Energy Flow Transmission	5
1.2 Motivation and Previous Work	7
1.3 Thesis Layout	8
1.4 Contributions	10
1.5 Publication	11
2 Waves and oscillating system description	12
2.1 Introduction	12
2.2 Ocean wave description	12
2.2.1 Spectrum analysis	15
2.2.2 Simulation of the Pierson-Moskowitz Spectrum and Irregular Waves	17
2.3 Oscillating buoy and its model	22
2.3.1 WEC dynamic model in the time domain	22
2.3.2 Frequency domain dynamic model	25
2.3.3 Power transmission in the frequency domain	28
2.4 Chapter summary	29
3 Control of wave energy converter	31
3.1 Chapter overview	31
3.2 Optimal conditions for maximising absorption energy	31
3.2.1 Optimal condition expressed in complex amplitude with a simplified model	32

3.2.2	Optimal conditions in the complex amplitude and frequency domain using the full model	33
3.3	Causality and non-causality of optimal conditions	37
3.4	Different control methods	39
3.4.1	Implementations under two different sets of optimal conditions . . .	39
3.4.2	Implementations without optimal conditions	46
3.5	Chapter summary	49
4	Prediction of wave elevation	51
4.1	Chapter overview	51
4.2	Wave description and the control force	52
4.2.1	Wave description	52
4.3	Least-squares system identification and prediction	55
4.4	Long-range predictive identification and prediction	58
4.5	Multi-step predictive identification and prediction	61
4.6	Comparison of different predictive approaches	64
4.6.1	Model Order Selection	74
4.7	Chapter summary	80
5	Model approximation	82
5.1	Chapter overview	82
5.2	Impedance Approximation	83
5.2.1	Approximation of intrinsic impedance	85
5.2.2	Approximation of control impedance	88
5.2.3	Approximation of optimal non-causal impedance	89
5.3	Causal approximation and model order reduction	92
5.4	Hydrodynamic Parameters	97
5.5	Causal approximations tested with two control methods	100
5.5.1	Test with velocity-tracking control	100
5.5.2	Test with complex conjugate control	101
5.6	Chapter summary	103
6	Control approaches and mechanical implementations	105
6.1	Chapter overview	105
6.2	Comparison of absorbed energy using different control methods	106
6.2.1	Passive loading control	108

6.2.2	Velocity-tracking control	111
6.2.3	Approximate complex conjugate control	113
6.3	Maximizing absorbed wave energy from a wave energy converter	114
6.4	Mechanical network realisation for WEC	120
6.4.1	Background and introduction to mechanical network realisation . .	120
6.4.2	Mechanical network realisation for WEC systems and simulation results	124
6.5	Chapter summary	137
7	Test with real ocean data	139
7.1	Chapter overview	139
7.2	Description of real ocean data and wave spectrum	139
7.3	Real waves tested with prediction methods	146
7.3.1	Berth	146
7.3.2	Galway Bay	151
7.3.3	Pico	157
7.4	Restricted complexity control tested with real wave data	162
7.4.1	Berth	162
7.4.2	Galway Bay	165
7.4.3	Pico	168
7.5	Chapter summary	172
8	Conclusion and further work	174
8.1	Conclusion	174
8.2	Further work	177
	Bibliography	178
	Appendix A Test with real ocean data	185
	Appendix B BerthB2012-05-16T12h00Z-spectrum	192
	Appendix C BerthB2012-05-16T12h00Z	195

List of Figures

1.1	Global distribution of wave power in kW/m[51]	2
1.2	The basic concept of the oscillating water column [95]	3
1.3	Structure of an overtopping device [95]	3
1.4	Structures of the three different types of heaving buoy [95]	4
1.5	Power transmission from waves to WEC	5
1.6	Energy flow from waves to a PTO	6
2.1	Simulation of sea surface elevation	18
2.2	PM spectrum simulation plot	18
2.3	PM spectra with different H_s values	19
2.4	Sea elevation with H_s equals to $6m$	19
2.5	Sea elevation with H_s equals to $9m$	20
2.6	Sea elevation with H_s equals to $12m$	20
2.7	PM spectrum with different T_z values	21
2.8	Sea elevation variation with T_z equals to $6s$	21
2.9	Sea elevation variation with T_z equals to $8s$	21
2.10	Sea elevation variation with T_z equals to $10s$	22
2.11	Oscillating body and PTO system for a WEC	23
3.1	Relationship between useful power and excitation power[23]	35
3.2	Block diagram for a velocity-tracking construction	40
3.3	Block diagram for feedback implementation of complex-conjugate control.	43
3.4	Block diagram for the feedforward control	45
3.5	Block diagram for passive loading control	47
3.6	Block diagram for latching control	49
4.1	Wave spectra calculated using PM spectrum with $\omega_p = 0.3rad/s$	53
4.2	Wave spectra calculated by PM spectrum with $T_z = 10s$	53

4.3	Wave spectra calculated using PM spectrum with $\omega_p = 0.6rad/s$ and $1rad/s$	54
4.4	Wave spectra calculated by PM spectrum with $T_z = 6s$ and $3s$	54
4.5	PM spectrum with $H_{1/3} = 6m$ and $T_z = 10s$	65
4.6	The prediction accuracy with $H_{1/3} = 6m$ and $T_z = 10s$	65
4.7	Wave elevation estimation with the LS method	66
4.8	Wave elevation estimation with the LRPI method	66
4.9	Wave elevation estimation with the MSPI method	66
4.10	The prediction accuracy including an ideal band-pass filter over the range 0.3rad/s to 1.2rad/s	67
4.11	Wave elevation estimation using the LS method	68
4.12	Wave elevation estimation using the LRPI method	68
4.13	Wave elevation estimation using the MSPI method	68
4.14	The prediction accuracy with an ideal low-pass filter	69
4.15	Wave elevation estimation using the LS method	70
4.16	Wave elevation estimation using the LRPI method	70
4.17	Wave elevation estimation using the MSPI method	70
4.18	Wave spectra calculated from PM spectra with $T_z = 6s$ and $3s$	71
4.19	Prediction with a 6s zero-crossing period	71
4.20	Prediction with a 3s zero-crossing period	72
4.21	Wave spectra calculated with PM spectra with $\omega_p = 0.6rad/s$ and $1rad/s$	73
4.22	Prediction with a 0.6rad/s peak frequency	73
4.23	Prediction with a 1rad/s peak frequency	74
4.24	AIC and BIC with one step and five steps ahead prediction	75
4.25	AIC and BIC with 10 steps and 20 steps ahead prediction	75
4.26	AIC and BIC with 40 steps ahead prediction	76
4.27	AIC and BIC with one step and five steps ahead prediction	76
4.28	AIC and BIC with 10 steps and 20 steps ahead prediction	77
4.29	AIC and BIC with 40 steps ahead prediction	77
4.30	Prediction accuracy of prediction approaches with model order 10	78
4.31	Prediction accuracy of prediction approaches with a model order of 20	78
4.32	Prediction accuracy of prediction approaches with a model order of 30	79
5.1	Fourth-order approximation of intrinsic impedance	85
5.2	Sixth-order approximation of intrinsic impedance	86
5.3	Seventh-order approximation of intrinsic impedance	86

5.4	Eighth-order approximation of intrinsic impedance	87
5.5	The comparison of $\widehat{Z}_i(-s)$	89
5.6	Magnitude comparison of fourth-order approximated transfer function and estimation dataset	91
5.7	Comparison of the phase of the fourth-order approximated transfer function and estimation dataset	91
5.8	Comparison of the bode diagram with the sixth- and second-order transfer functions, as calculated with PEM	93
5.9	Bode diagram of the sixth- and second-order approximation, as calculated without PEM	94
5.10	Bode diagram of the sixth-order and two different second-order approximations	95
5.11	Phase comparison of fourth-order approximation and two constant approximations	97
5.12	Magnitude curve fits using different order polynomials	99
5.13	Phase curve fits with different order polynomials	99
5.14	Block diagram of the velocity-tracking construction	100
5.15	The energy absorbed by the velocity-tracking construction	100
5.16	The energy absorbed by the velocity-tracking construction	101
5.17	Block diagram of the feedback control	102
5.18	The energy absorbed by the feedback construction	102
5.19	The energy absorbed by the feedback construction	103
6.1	Comparison of magnitudes of the eighth-order approximation and the optimal approximation	109
6.2	Phase comparison for the eighth-order approximation and the optimal approximation	109
6.3	The optimal resistance $R_{opt}(\omega)$ against frequency	110
6.4	The construction of the passive loading control	110
6.5	The energy absorbed using the passive loading control against time	111
6.6	The construction of the velocity-tracking control using a PID controller	112
6.7	The energy absorbed by the velocity-tracking construction using a PID controller	112
6.8	The energy absorbed by velocity-tracking using an IMC controller	113
6.9	The construction of the feedback control	114
6.10	The energy absorbed by the feedback control	114

6.11 Bode plot of load impedance	115
6.12 Comparison between the different order approximated transfer functions using the Nelder-Mead method	117
6.13 Comparison of first-order transfer functions using the Nelder-Mead method	118
6.14 Comparison of second-order transfer functions using the Nelder-Mead method	119
6.15 Comparison of the third-order transfer functions using the Nelder-Mead method	120
6.16 WEC power take-off devices: S1 basic ideal, S2 parallel idea with mass term, S3 serial idea with mass term	122
6.17 Configurations S4 and S5	123
6.18 Configurations S6 and S7	123
6.19 PTO device includes mass term	125
6.20 System with admittance6.48	126
6.21 System with admittance6.49	126
6.22 System with admittance6.55	128
6.23 Block diagram of proposed spring-damper system	129
6.24 Block diagram of proposed complex conjugate control	129
6.25 Block diagram of proposed control with admittance6.48	130
6.26 Block diagram of proposed control with admittance6.49	130
6.27 The absorbed energy extracted by the feedback control with the spring- damper system	131
6.28 The absorbed energy extracted by the complex conjugate control with the mass-spring-damper system	131
6.29 The absorbed energy extracted by the feedback control with admittance6.48	132
6.30 The absorbed energy extracted by the feedback control with admittance6.49	132
6.31 The useful energy extracted by the feedback control with the spring-damper system	133
6.32 The useful energy extracted by the complex conjugate control with the mass-spring-damper system	133
6.33 The useful energy extracted by the complex conjugate control with admit- tance6.48	134
6.34 The useful energy extracted by the complex conjugate control with admit- tance6.49	134
6.35 The reactive energy extracted by the feedback control with the SD system .	135
6.36 The reactive energy extracted by the feedback control with the mass-spring- damper system	135

6.37	The reactive energy extracted by the feedback control with admittance6.48 .	136
6.38	The reactive energy extracted by the feedback control with admittance6.49 .	136
7.1	Wave spectra measured from 12 : 00 to 13 : 30	140
7.2	Wave elevations measured from 12 : 00 to 13 : 30	142
7.3	Wave spectra measured from 00 : 00 to 01 : 30	142
7.4	Wave elevations measured between 00 : 00 and 01 : 30	144
7.5	Wave spectrum measured between 00 : 19 and 01 : 49	144
7.6	Wave elevation measured from 00 : 19 to 01 : 49	146
7.7	Comparison of prediction accuracies from 12 : 00 to 12 : 30	147
7.8	Real wave elevation and estimation using the LS method (12 : 00)	147
7.9	Real wave elevation and estimation using the LRPI method (12 : 00)	148
7.10	Real wave elevation and estimation using the MSPI method (12 : 00)	148
7.11	Real wave elevation and estimation using the LS method (12 : 30)	148
7.12	Real wave elevation and estimation using the LRPI method (12 : 30)	149
7.13	Real wave elevation and estimation using the MSPI method (12 : 30)	149
7.14	Comparison of prediction accuracies from 12 : 00 to 12 : 30 using a model order of 24	149
7.15	Real wave elevation and estimation using the LS method (12 : 00)	150
7.16	Real wave elevation and estimation using the LRPI method (12 : 00)	150
7.17	Real wave elevation and estimation using the MSPI method (12 : 00)	150
7.18	Real wave elevation and estimation using the LS method (12 : 30)	151
7.19	Real wave elevation and estimation using the LRPI method (12 : 30)	151
7.20	Real wave elevation and estimation using the MSPI method (12 : 30)	151
7.21	Comparison of prediction accuracies between 00 : 00 and 00 : 30	152
7.22	Real wave elevation and estimation using the LS method (00 : 00)	152
7.23	Real wave elevation and estimation using the LRPI method (00 : 00)	152
7.24	Real wave elevation and estimation using the MSPI method (00 : 00)	153
7.25	Real wave elevation and estimation using the LS method (00 : 30)	153
7.26	Real wave elevation and estimation using the LRPI method (00 : 30)	153
7.27	Real wave elevation and estimation using the MSPI method (00 : 30)	154
7.28	Comparison of prediction accuracies between 00 : 00 and 00 : 30	154
7.29	Real wave elevation and estimation using the LS method (00 : 00)	155
7.30	Real wave elevation and estimation using the LRPI method (00 : 00)	155
7.31	Real wave elevation and estimation using the MSPI method (00 : 00)	155

7.32 Real wave elevation and estimation using the LS method (00 : 30)	156
7.33 Real wave elevation and estimation using the LRPI method (00 : 30)	156
7.34 Real wave elevation and estimation using the MSPI method (00 : 30)	156
7.35 Comparison of prediction accuracies between 00 : 19 and 01 : 19	157
7.36 Real wave and estimated wave elevations using the LS method (00 : 19) . .	157
7.37 Real wave and estimated wave elevations using the LRPI method (00 : 19) .	158
7.38 Real wave and estimated wave elevations using the MSPI method (00 : 19) .	158
7.39 Real wave and estimated wave elevations using the LS method (00 : 49) . .	158
7.40 Real wave and estimated wave elevations using the LRPI method (00 : 49) .	159
7.41 Real wave and estimated wave elevations using the MSPI method (00 : 49) .	159
7.42 Comparison of prediction accuracies between 00 : 19 and 01 : 19	159
7.43 Real wave and estimated wave elevations using the LS method (00 : 19) . .	160
7.44 Real wave and estimated wave elevations using the LRPI method (00 : 19) .	160
7.45 Real wave and estimated wave elevations using the MSPI method (00 : 19) .	160
7.46 Real wave and estimated wave elevations using the LS method (00 : 49) . .	161
7.47 Real wave and estimated wave elevations using the LRPI method (00 : 49) .	161
7.48 Real wave and estimated wave elevations using the MSPI method (00 : 49) .	161
7.49 Absorbed energies extracted from the feedback control model using three admittances	162
7.50 Useful energies extracted from the feedback control model using three ad- mittances	163
7.51 Reactive energies extracted by the feedback control model using three admit- tances	163
7.52 Absorbed energies extracted by the feedback control using three different kinds of admittance	164
7.53 Useful energies extracted by the feedback control using three different kinds of admittance	164
7.54 Reactive energies extracted by the feedback control using three different kinds of admittance	165
7.55 Absorbed energies extracted by the feedback control using three different admittances	165
7.56 Useful energies extracted by the feedback control using three different ad- mittances	166
7.57 Reactive energies extracted by the feedback control using three different admittances	166

7.58	Absorbed energies extracted by the feedback control using three different admittances	167
7.59	Useful energies extracted by the feedback control using three different admittances	167
7.60	Reactive energies extracted by the feedback control using three different admittances	168
7.61	Absorbed energies extracted by the feedback control using three different admittances	168
7.62	Useful energies extracted by the feedback control using three different admittances	169
7.63	Reactive energies extracted by the feedback control using three different admittances	169
7.64	Absorbed energies extracted by the feedback control using three different admittances	170
7.65	Useful energies extracted by the feedback control using three different admittances	170
7.66	Reactive energies extracted by the feedback control using three different admittances	171

Chapter 1

Introduction

1.1 Background to wave energy resources

As the world's demand for primary energy sources continues to rise, associated prices are also increasing sharply. In addition, safety and environmental protection requirements have correspondingly become more stringent. As a result, resources such as oil, natural gas and coal will be increasingly replaced by renewable energy sources, e.g., wind, solar, and wave energy; wave energy in particular may have the potential to satisfy the majority of future energy demands.

Wave energy has several advantages over other renewable energy sources. The potential usable wave power worldwide has been estimated to be greater than $2TW$ [17, 94]. Comparing solar and wind energies with wave energy, it is clear that the latter is much more spatially concentrated than the former. With solar energy ideally being converted to wind energy, power flow intensity can be up to $0.5kW/m^2$ perpendicular to the direction of the wind (solar radiation creates temperature differences in the atmosphere, creating air pressure differences; essentially, wind is the result of air pressure differences). In comparison, when wind energy is converted to wave energy, power flow intensity can be up to $2 - 3kW/m^2$ perpendicular to the direction of wave propagation; in other words, the power intensity of the latter is considerably greater [24]. A key example is wind and wave energy development in Ireland. About $6.4 \times 10^{-3}TWh$ has been generated of a total practical annual capacity from wind energy of $6.7TWh$ [20, 53]; on the other hand, the total annual resources that can be practically obtained from wave energy is $14TWh$, but to date none of this has been used to generate power[20]; this reflects the most common situation worldwide. Indeed, whilst wind and solar energy conversion devices have been extensively developed, due to its high cost and control complexities, wave energy technology has not been widely implemented.

1.1 Background to wave energy resources

However, its high energy potential means that wave energy is, nevertheless, still competitive. Figure 1.1 presents the available wave power levels worldwide.

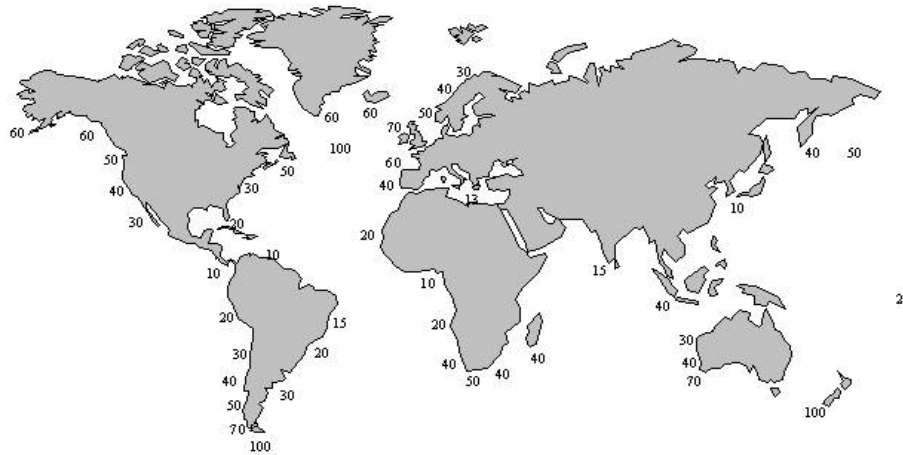


Figure 1.1 Global distribution of wave power in kW/m[51]

Wave energy conversion produces low amounts of carbon over its life-cycle[73], and also can reduce CO_2 emissions to levels that will satisfy the Kyoto Protocol[24]. The other advantage of wave energy is that the supply of energy available from this source is far more consistent, and can thus be predicted more easily than for other forms of renewable energy[24]. It lasts throughout the year, and is not easily affected by other elements. Any country which has significant lengths of coastline may use this technology, which has considerable future potential. Wave energy is essentially undeveloped at present, and its huge potential for the future is one of the motivations for this report.

1.1.1 Principles and Classification of Wave Energy Converters (WECs)

WECs do not have a long history. In fact, the first recorded WEC was built by P. Wright in 1898 [79], but it was not until the 1970s that their development become widespread when the oil crisis motivated increased WEC development. Many concepts for wave energy converters have been designed and tested [16], and WECs can accordingly be classified in many different ways, such as via their operating position, operating principles, and means of reaction [French].

One widely used concept is that of the WEC based on the oscillating water column (OWC). The basic concept of the OWC is presented in the following figure1.2. It can be seen from figure1.2 that an OWC is usually positioned on the shoreline [101]. As the incident waves oscillate inside the chamber the air inside is accordingly compressed and

1.1 Background to wave energy resources

uncompressed, causing it to flow. This air flow is used to provide a unidirectional rotational motion of the turbine [79, 83], which allows for the generation of electricity. More details can be found in [40, 79, 83].

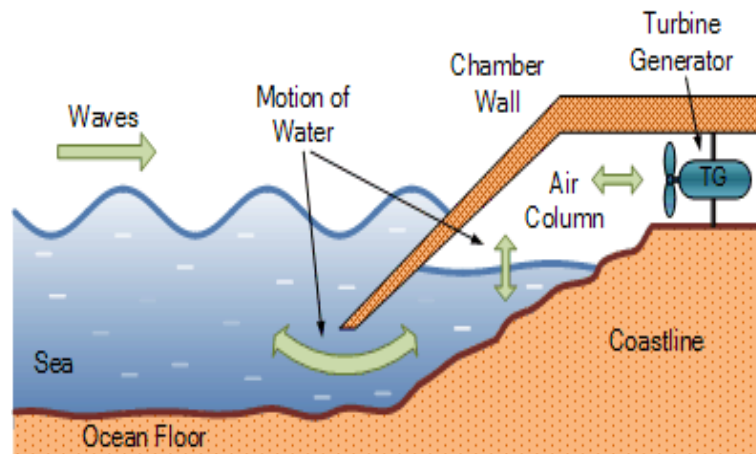


Figure 1.2 The basic concept of the oscillating water column [95]

The other popular device is based on the overtopping principle. The basic principle behind an overtopping device is the conversion of wave and tidal kinetic energy to potential energy. This potential energy can then be converted into electricity by a turbine. A simple representation of the overtopping device is given in figure 1.3 below:

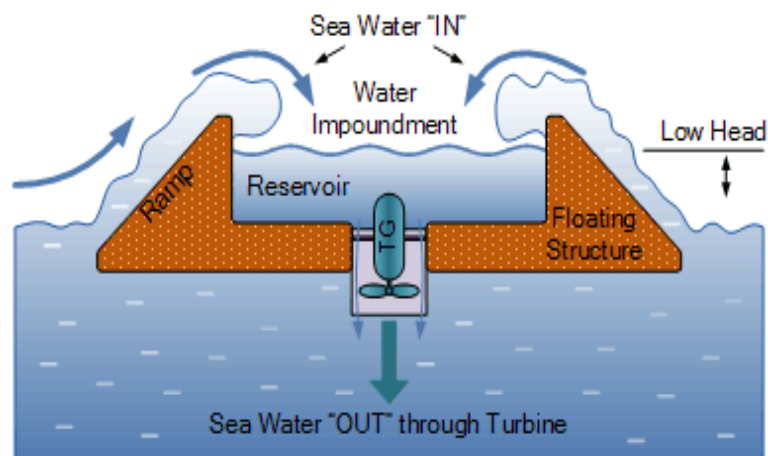


Figure 1.3 Structure of an overtopping device [95]

As can be seen from figure 1.3, waves overtop both sides of the ramp, allowing water to be stored in the reservoir. The turbine will operate when the reservoir releases water. The potential energy of the water pushes the turbine, after which the former returns to the sea.

1.1 Background to wave energy resources

The advantage of overtopping devices is their insensitivity to tidal height [79, 89]. They can also protect the harbour in which they are installed with their ramp [79].

However, the most common type of WEC is the heaving buoy. There are three such types of devices: one is called the Archimedes Wave Swing (self-reacting device) [18]; the second is the Bottom-referenced Heaving Buoy; and the third is the Linear Heaving Buoy. These devices are illustrated in the following figure 1.4:

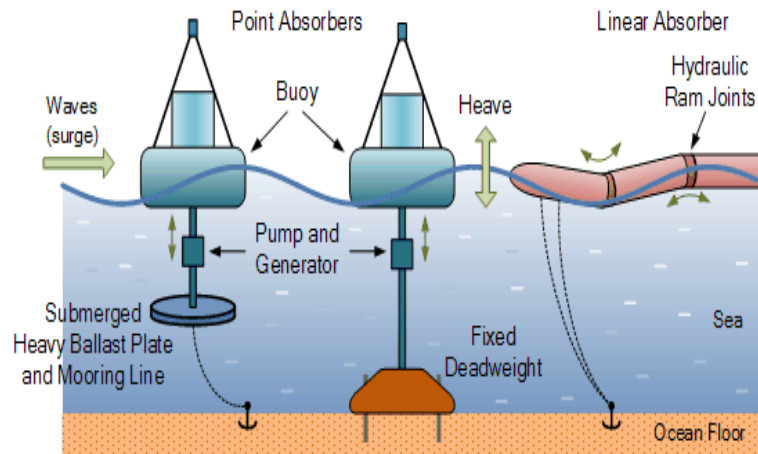


Figure 1.4 Structures of the three different types of heaving buoy [95]

It can be seen that the self-reacting device consists of distinct sections, namely the mooring on the sea bed and the floating section on the surface. The latter can undergo two motions: pitching and heaving. The advantage of this type of device is that it can operate offshore in the deep sea [95].

The central device in figure 1.4 is the bottom-referenced heaving buoy. The difference between this and the self-reacting device is that the heaving buoy connects directly to the seabed. As perfect heaving motion is difficult to obtain in the real world, the device is constrained to a vertical motion for convenience [79], and is usually only operated in shallow water. This thesis will focus on the bottom-referenced heaving buoy.

The linear heaving buoy has been described by Yemm [102]. It is called the Pelamis, and is constructed from several structures. It usually floats on the sea surface and undergoes two types of motion, similar to the self-reacting device. Waves act on the Pelamis, driving the connection arm between each of the structures in order to capture energy. The advantage of the Pelamis is that several separate floating buoys can be connected together with one mooring line. It is also suitable for deep-sea usage [95].

1.1.2 Power and Energy Flow Transmission

As the bottom-referenced heaving buoy is the subject of this thesis, an understanding of power flow transmission between incident waves and the heaving buoy is important and worth pursuing. This transmission can be classified as intercepted power, absorbed power, useful power, and reaction power.

The intercepted power can be seen as the incident wave power that is intercepted by the buoy. The generation process of intercepted power can be described as follows. First, incident waves hit the buoy. The incident power (excitation power) so produced can be categorised as intercepted power, Froude-Krylov power, and diffraction power. All the incident power returns back to the waves if there is no PTO (power take-off) device connected. Froude-Krylov power and diffraction power are associated with the non-causality of excitation force, and will be discussed in detail in chapter 2. Note that the radiation power equals the intercepted power if there is no PTO device. It is generated when the buoy pushes water out of the way [47].

The absorbed power can be seen as a part of intercepted power. Given that radiation power is equal to the intercepted power if there is no PTO connected, some of the radiation power is converted to absorbed power via the PTO; however, not all of the absorbed power can be used. The absorbed power can itself be classified as either useful power or reaction power, as some power will be lost in the active elements of the PTO. For example, one might consider a PTO constructed of a simple mass-spring-damper system. The mass and spring of the PTO can be seen as active parts, and do not themselves absorb power from waves. All useful power is absorbed by the PTO damper, which can be seen as the passive part of the construction.

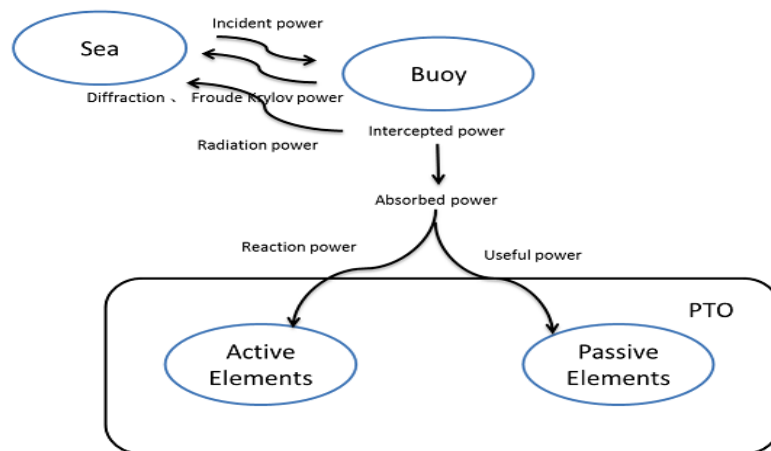


Figure 1.5 Power transmission from waves to WEC

1.1 Background to wave energy resources

The relationship between intercepted power, absorbed power, useful power, and reaction power is shown in the figure 1.5.

However, maximising useful energy is the object of this project. Energy is the amount of work performed by a force, and is equal to the integral of power over time. Hence, the energy relationship between the waves and WEC can be represented as per figure 1.6. Note that maximising useful energy is the key point, and so only the relationship between absorbed energy, reaction energy, and useful energy will be analysed.

The absorbed energy is the sum of the reaction energy and the useful energy. The energy flow from the sea to the active elements is defined as E_{S2A} , whilst that from the sea to the passive elements is defined as E_{S2P} . Conversely, the energy flow from the active elements to sea is defined as E_{A2S} , and that from the active elements to the passive elements is E_{A2P} . A "–" sign indicates that energy is "absorbed", whilst a "+" sign indicates energy "delivery". The relationships between the above can be expressed as per the following equations:

$$E_{Abs} = |E_{A2S}| - |E_{S2A}| - |E_{S2P}| \quad (1.1)$$

$$E_{Rec} = |E_{A2S}| + |E_{A2P}| - |E_{S2A}| \quad (1.2)$$

$$E_{Use} = -|E_{A2P}| - |E_{S2P}| \quad (1.3)$$

$$E_{Abs} = E_{Rec} + E_{Use} \quad (1.4)$$

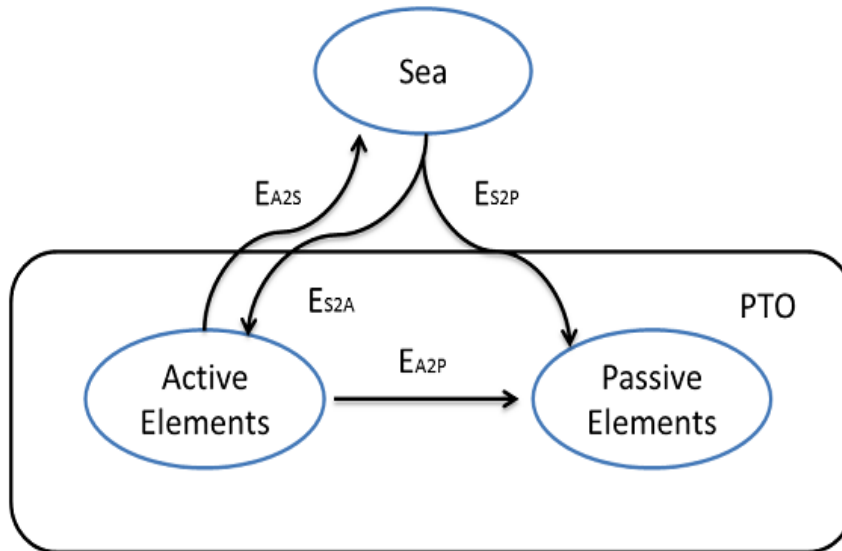


Figure 1.6 Energy flow from waves to a PTO

1.2 Motivation and Previous Work

WECs rely on efficiency control, or would otherwise become essentially passive devices, and unsuitable for use under a variety of sea conditions. Control can be classified across different stages according to power flow.

There are several important elements that could effect the economy of a system used for wave energy conversion. The size of the WEC should be minimised, which can reduce the buoy's cost and the complexity of its structure. The dip surfaces of WEC systems should be smooth to reduce viscous losses. WECs should be able to undergo various types of motion in order to follow wave direction. Various other control designs can be used to protect WECs, which can help avoid damage due to severe weather. [10, 23, 26, 29]. All of the above controls can be classified as physical controls, that is, they are only associated with the physical elements of the WEC.

All of these factors are aimed at maximising the absorbed power. Many research projects have been conducted in the attempt to discover the means by which wave energy absorption can be maximised, with a particular focus on WECs consisting of oscillating systems [21, 23, 26]. Various optimal conditions have been introduced, all of which express the relationship between the velocity of buoy oscillation and the force produced by the wave within the frequency domain. One of the strategies for control is that of complex-conjugate control [23], [38], [42], which optimises conditions for absorbing energy by making the optimal load impedance equal to the complex conjugate of the intrinsic impedance. An alternative control strategy, known as phase control, requires the oscillation velocity to be in phase with the excitation force [23], [38]. Phase control is also called latching control. As the name implies, latching control consists of a locking and releasing motion of the energy conversion device that is directly related to the peak and trough of the wave. This aims to synchronise the wave force in phase with the velocity of the device [2, 58, 59]. Recently, another control method has been developed, which is called model predictive control (MPC), which has been used to solve the constrained optimisation problem. The velocity and force of WECs can be directly involved with control design [45]. All of these control designs can be classified as PTO controls.

However, in irregular waves, the optimal control problem becomes non-causal because the excitation force is not directly generated by the wave [22]. This means the calculation of the excitation force requires information regarding the future elevation of the waves. Several early results in wave energy research have demonstrated the importance of wave prediction.

Accurate wave prediction was introduced in [58] to aid control in order to gain considerable improvements at lower wave spectral frequencies. The controller can adjust the accumulator's internal pressure, causing the valve to open and close more accurately when using wave prediction. As mentioned earlier, the flow velocity was more stable and faster. Korde argued that the energy conversion device could extract more useful power with lower-frequency waves; as a result, smaller devices may be considered for use in low sea states (that is, where the sea looks calm and smooth). This means precision wave prediction could be extremely helpful in reducing the energy conversion device's size while still extracting more power.

In 2010, short-term wave prediction [36] was described in the literature. One approach to wave elevation prediction is via a time series that is only dependent on past history. Autoregressive models could offer accurate predictions for low-frequency sea waves up to two wave periods in the future. In [37], the authors not only focus on short-term wave prediction but also on that of wave excitation force.

On the other hand, several different causal approximations have been reported [38, 74], where the power absorption performance of the WEC is only slightly reduced compared to non-causal conditions.

The last control classification is that of useful power delivery. Wave power is converted to useful power via WECs. Then, useful power has to be converted to electricity and be delivered to the power grid, for which voltage control, power storage, and frequency have to be considered. More details can be found in reference [56].

A new method has been applied in this thesis to optimise the restricted complexity PTO mechanism for wave energy conversion. Mechanical network realisation with Brune Synthesis has been considered, whereas most researchers focus on mathematical notions to represent the PTO mechanism regarding wave energy conversion. The concept of mechanical network realisation with Brune Synthesis is used to make the mathematical notions of PTO a reality through physical constructions. The design of a restricted complexity PTO via direct optimisation of the parameters of a mechanical network will be presented.

1.3 Thesis Layout

This thesis includes the following sections: chapter 2 describes the physical model and different types of waves. A degree of background into harmonic waves and real ocean waves will be given. As a wave spectrum can be used analyse the main characteristics of waves, several spectra are presented in this chapter. The advantages and disadvantages of these

spectra are discussed. A literature review of mechanical oscillation is given in chapter 2. The oscillating buoy and associated models considered in this thesis are then presented. The time domain and frequency domain of a dynamic wave energy conversion model will be given for the purpose of analysis.

Control design criteria are introduced in chapter 3, and the concept of the optimal control condition is discussed; the causality and non-causality of optimal conditions has also been analysed. Implementations of different control designs are also described in chapter 3.

As mentioned above, the excitation force is non-causal and requires information on future wave elevation; hence, the means by which to predict wave elevation is described in chapter 4. Three system identifications, namely least squares, long-range predictive, and multi step predictive, are introduced. Simulated wave elevations, as generated with different wave characteristics, have been tested with these three identifications. Comparisons of different predictive approaches will be presented in this chapter.

The model approximation and various numerical simulation results are introduced in chapter 5. The complex conjugate of intrinsic impedance is required for the control design, and hence, the prediction error method will be utilised to obtain the complex conjugate of intrinsic impedance calculations. However, model approximation is another solution to overcoming the non-causal problem. A second-order system approximation will be calculated using the prediction error method and partial fraction decomposition. Hydrodynamic parameters will also be collected in this chapter, where different order polynomials will be used to fit the hydrodynamic data, and will be used to control system disturbance excitation force calculations. Finally, system approximation results will be inserted into the control systems based on two optimal control conditions.

Chapter 6 focuses on the results of the simulations and mechanical network realisation. Numerical optimisation to design a restricted complexity PTO mechanism for wave energy conversion will be presented in this chapter. The Nelder–Mead method (Matlab command '*fminsearch*') will be used for numerical optimisation. Control designs introduced in chapter 3 will be tested with simulation data. The design of the PTO based on the numerical optimisation of the parameters of a mechanical network will be presented. Two control structures for a PTO realised via Brune Synthesis were obtained, and will be compared with a simple mass-spring-damper system.

In chapter 7, real wave data collected in three locations will be analysed. Wave spectra from different locations will be compared, and the wave elevations at these locations will be presented. As mentioned in chapter 4, three system identifications will be compared and tested with simulation data, and the real wave data will also be tested. Finally, real wave data

will be entered into the control designs introduced in chapter 6; these will be compared in order to examine the influence of different wave spectra and elevations.

Chapter 8 gives the conclusions to the work carried out in this thesis and, additionally, a number of future recommendations. Any weaknesses in the experiments and associated possible solutions will be described in chapter 8.

1.4 Contributions

Contributions associated with this thesis are as follows:

1. Multi step predictive identification advantages have been verified:

Least squares and long-range predictive identifications have been widely used. However, least squares identification predicts K steps ahead values based on only one step ahead estimators, which is poor for several steps ahead prediction. Long-range predictive identification can be used to predict several steps ahead based on the investigation of the whole prediction horizon [84]. However, disturbances or errors may accumulate from previous recursive calculations. Multi step predictive identification can provide a cost function for each prediction step. There are no disturbances or errors that may accumulate in these calculations. Prediction results calculated by multi step predictive identification has obvious advantages.

2. The prediction error method has been used for model approximation and reduction:

The prediction error method has been used for model approximation. The method does not consider the model mismatch or the likelihood of the corresponding statistical model, such as the least squares or maximum likelihood method. It is used for estimating the parameters of a dynamic model based on recorded observations [61]. Model approximation is used to overcome the non-causality problem.

In the other hand, the system model order, as reduced by the prediction error method, can fit an optimal model with 97.94% accuracy. It shows better performance than partial fraction decomposition, which is described in references [75] and [38]. Partial fraction decomposition, which reduces system model order by ignoring components of the numerator and denominator, does not have a particularly significant effect on the system. In contrast, prediction error method reduces system model order by considering the accuracy of the predictions based on given observations. Reduction models have been inserted in complex conjugate and velocity-tracking control loops.

3. Brune synthesis and the Nelder–Mead method have been used for numerical optimisation to design a restricted complexity power take-off mechanism:

The Nelder–Mead method has been used to optimise impedance. The advantage of the Nelder–Mead method is that it can be used to find a local minimum of a function without requiring any derivative information [63, 85].

Brune Synthesis has been used to obtain restricted complexity control for WECs with different structures. One solution to constructing physical reality corresponds to systems of differential equations. Two control impedances, as calculated by Brune Synthesis, have been compared with a simple mass-spring-damper system. They can absorb a little more absorbed energy than the mass-spring-damper system using simulation data; however, they show significant improvement using real ocean wave data that contains a low wave spectrum.

1.5 Publication

- Fu, Xiaoxing and Lecchini-Visintini, Andrea, Optimisation of restricted complexity control for wave energy conversion. In *Control (CONTROL), 2016 UKACC 11th International Conference on*, pages 1–5. IEEE.

Chapter 2

Waves and oscillating system description

2.1 Introduction

Wave energy is available to any country with a coastline. Ocean wave investigation and analysis are extremely important for extracting wave energy data. Harmonic waves and irregular waves will be described in section 2.2, where their characteristics will be analysed and the connection between them examined. The simulation of irregular waves, as based on the Pierson-Moskowitz spectrum, will be described. A wave energy conversion (WEC) system consisting of a single oscillating buoy is used to extract wave energy data from ocean waves. In section 2.3, an analysis of an oscillating buoy in irregular waves will be discussed, and the different forces that act on the buoy will be described; the power generated by these forces will also be described in this section.

2.2 Ocean wave description

In this section, two types of waves and their characteristics in relation to wave energy, and thus the focus of this study, will be presented. Simulations of ocean waves, as based on the Pierson-Moskowitz spectrum, will also be given in this section.

Firstly, the frequency domain and time domain of a signal have to be distinguished and analysed. For any signal presented in the time domain, there is an equivalent frequency domain expression. A Fourier transform can be used to decompose a time domain signal into the frequency domain, whilst its inverse can be used to reconstruct the original time domain signal.

Harmonic Waves

The harmonic wave is a simple starting point in the simulation studies of ocean waves. As mentioned in chapter 1, a bottom-referenced heaving buoy will be used in this thesis. Only a unidirectional wave propagating at one frequency will be measured by such a buoy. Harmonic waves can be seen as continuous, sinusoidal signals. The wave elevation $\eta(t)$ in the time-domain can be obtained as follows:

$$\eta(t) = A \sin(\omega t + \phi) \quad (2.1)$$

where A is the wave amplitude, ϕ is the phase, and ω is the frequency [31].

Real Ocean Waves

Harmonic waves were introduced in the previous section. However, the waves observed in the ocean are, clearly, far more random than this simplistic model suggests. As wave period and wave height change continuously, real ocean waves are considered to be a stochastic processes. Assuming real waves, or so-called irregular waves, can be seen as superpositions of regular waves of different frequencies, then irregular waves can be calculated by recalling eq(2.1), as below:

$$\eta(t) = \int_0^{\infty} A \sin(\omega t + \alpha) d\omega \quad (2.2)$$

where α is the phase angle and A is the wave amplitude. The distribution of irregular wave elevations is assumed to be Gaussian around the zero mean [70].

However, wave elevation is usually measured as discrete data. Discrete measurements with digital processing can be used more easily and more intuitively than analogue processing. The discrete time domain of wave elevation can be presented as follows:

$$\eta(t) = \sum_{i=1}^{N-1} A(i) \sin(\omega(i)t + \phi(i)) \quad (2.3)$$

where N is number of measurements. Further details and applications of the discrete time domain of wave elevation will be presented in section 2.2.4.

So, proceeding with the assumption that irregular waves can be seen as a superposition of regular waves of different frequencies, it can be further understood that wave spectral density is important in distinguishing a wave's characteristics [67]. The wave spectral density

function is represented by the symbol $S(\omega)$. Wave spectral density is the energy per unit area of a wave's surface for each of the wave components of the whole wave system [67].

The wave power spectral density is defined as follows [70]:

$$S(\omega) = \lim_{T \rightarrow \infty} \frac{1}{2\pi T} |\Xi_T(\omega)|^2 \quad (2.4)$$

where T is the wave period and is equal to $\frac{2\pi}{\omega}$. The $\Xi_T(\omega)$ is the Fourier transform of wave elevation:

$$\Xi_T(\omega) = \int_{-T}^T \eta(t) e^{-j\omega t} dt \quad (2.5)$$

Sea State Parameters

Apart from the wave spectrum, various other parameters are useful in defining a wave's characteristics. The spectral moments are the key points used to calculate wave spectrum characteristics, which include average wave height, average period, and so on. The spectral moments method obtains values according to a Fourier spectrum[99]. The n^{th} spectral moment is[67]:

$$m_n = \int_0^{\infty} \omega^n S(\omega) d\omega \quad (2.6)$$

And the $zero^{th}$ moment can be given as:

$$m_0 = \int_0^{\infty} S(\omega) d\omega \quad (2.7)$$

As shown in the above equation, the $zero^{th}$ moment is the variance of the wave spectrum[99].

A significant wave height is an important parameter by which one can characterise a sea wave. It is defined as the mean wave height of the top one-third highest waves[23]. It can also be defined as four times the square root of the $zero^{th}$ moment, which can be expressed as:

$$H_s = 4\sqrt{m_0} \quad (2.8)$$

Following this, the other important parameter is the zero crossing period, which can be calculated as follows:

$$T_z = 2\pi\sqrt{\frac{m_0}{m_2}} \quad (2.9)$$

Eq(2.9) is also used to represent the mean period of all waves in the entire record.

Furthermore, the energy period is important for power calculations, and is given by:

$$T_e = 2\pi\frac{m_{-1}}{m_0} \quad (2.10)$$

In equation 2.10, the wave is assumed to be a regular wave that has the same significant height and same power density in any one period.

2.2.1 Spectrum analysis

As mentioned above, irregular waves are the superposition of a number of harmonic waves whose amplitudes can be derived from the wave energy spectrum, which can be used to analyse the main characteristics of waves. It constitutes several of the parameters introduced in the previous section, such as the significant wave height, the zero crossing period, the peak period or the energy period, and so on.

There are four main types of wave spectrum. One is called the Pierson-Moskowitz (PM) spectrum. It is used to describe the relationship between wave energy distribution and frequency. It assumes that if the wind blows for a long time over a large area, then wave motion will achieve equilibrium with the wind. For further information, key publications in the literature describing PM spectra are available [76, 77, 90]. However, the PM spectrum only works for fully developed seas (a fully developed sea occurs when the energy input from the wind balances the energy output by waves breaking [88]). The JONSWAP spectrum is another type of spectrum that can be used with fetch limitations (the location of waves may have particular physical characteristics that do not allow the waves to fully develop [92]), such as low frequency and narrow-band swells. More details on JONSWAP spectra can be found in [13, 46, 46]. There are two other spectra can be seen as specific cases of a PM spectrum. One is the Bretschneider spectrum, which can be considered as a two-parameter PM spectrum [5–7]. The other one is the Ochi-Hubble spectrum [71, 72]. It can also be seen as a specific case of a three-parameter PM spectrum. Both types can be used with irregular waves with certain fetch limitations. Spectral expressions are given in table 2.1:

Table 2.1 Spectrum Analysis

Wave spectrum	Spectrum expression	Alternative definition	Explanation
Original PM spectrum	$S(\omega) = \frac{\alpha g^2}{\omega^5} \exp \left[-\beta \left(\frac{g}{\omega U_{19.5}} \right)^4 \right]$	$\alpha = 0.0081$ $\beta = 0.74$	
PM spectrum defined by peak freq ω_p	$S(\omega) = \frac{\alpha g^2}{\omega^5} \exp \left[-\beta \left(\frac{\omega_p}{\omega} \right)^4 \right]$	$\omega_p = \frac{4\beta^{\frac{1}{4}} g}{5 U_{19.4}}$ $\alpha = \frac{5\pi^4 H_s^2}{g^2 T_p^4}$	where the ω is the wave frequency and g is gravity, U is defined as wind speed, and ω_p is the peak frequency of the wave
PM spectrum defined by H_s and peak wave period T_p	$S(\omega) = 5\pi^4 \frac{H_s^2}{T_p^4} \cdot \frac{1}{\omega^5} \exp \left[-\left(\frac{20\pi^4}{T_p^4} \right) \cdot \frac{1}{\omega^4} \right]$	$\beta = \frac{20\pi^4 U_{19.4}}{T_p^4 g^4}$	
PM spectrum defined by H_s and T_z	$S(\omega) = 4\pi^3 \frac{H_s^2}{T_z^4} \cdot \frac{1}{\omega^5} \exp \left[-\left(\frac{16\pi^3}{T_z^4} \right) \cdot \frac{1}{\omega^4} \right]$	$\alpha = \frac{4\pi^3 H_s^2}{g^2 T_z^4}$ $\beta = \frac{16\pi^3 U_{19.4}}{T_z^4 g^4}$	
JONSWAP spectrum	$S(\omega) = \frac{\alpha g^2}{\omega^5} \exp \left[-\beta \frac{\omega_p^4}{\omega^4} \right] \gamma^\alpha$	$\alpha = \exp \left[-\frac{(\omega - \omega_p)^2}{2\omega_p^2} \sigma^2 \right]$ $\beta = \frac{5}{4}$ $\begin{cases} \sigma_a & \text{if } \omega \leq \omega_p \\ \sigma_b & \text{if } \omega \geq \omega_p \end{cases}$	α is a constant value, σ_a and σ_b represent the left- and right-sided widths of the spectral peak, and γ is the ratio of the maximal spectral energy to the PM spectrum's spectral energy.
The Bretschneider spectrum	$S(\omega) = \frac{1.25\omega_p^4}{4\omega^5} H_s^2 \exp \left[-\beta \frac{\omega_p^4}{\omega^4} \right]$	$\beta = 1.25$	
Ochi-Hubble spectrum	$S(\omega) = \frac{1}{4} \frac{(\frac{4\lambda+1}{4} \omega_p^4)^\lambda}{\Gamma(\lambda)} \frac{H_s^2}{\omega^{4\lambda+1}} \exp \left[-\left(\frac{\omega_p}{4} \right) \left(\frac{\omega - \omega_p}{\omega} \right)^\lambda \right]$		where the $\Gamma(\lambda)$ is the Gamma function, and λ is the steepness of the spectral peak.

2.2.2 Simulation of the Pierson-Moskowitz Spectrum and Irregular Waves

Some real sea wave records are given in reference [67], which were collected from the west coast of Ireland. The sampling frequency is given as $f_s = 1.28Hz$. In addition, the PM spectrum function related to significant wave height H_s and zero crossing period T_z can be given as:

$$S(\omega) = \frac{0.11H_s^2T_z}{2\pi} \left(\frac{\omega T_z}{2\pi}\right)^{-5} \exp[-0.44\left(\frac{\omega T_z}{2\pi}\right)^{-4}] \quad (2.11)$$

Nolan [69] suggested that the spectrum be divided into 512 equally spaced frequency components, where the starting frequency is $0.3rad/s$, and the interval, $d\omega$, is equal to $0.00625rad/s$, so the maximum frequency is $3.5rad/s$. The choice of $d\omega$ was discussed in [67]. The increase in $d\omega$ may cause the mean frequency, the standard deviation of the peak frequency, and the mean magnitude of the peak frequency to change significantly. The divide interval $d\omega = 0.00625rad/s$ has been verified as being appropriate for dividing wave spectra to simulated wave records[67].

A time series for the wave elevation can be simulated with the spectrum eq(2.11). Hence, the time domain wave elevation can be expressed with the discrete function eq(2.3). The time series-based sea wave elevation, $\eta(t)$, can be simulated via the spectrum's frequencies as follows:

$$\eta(t) = \sum_{i=1}^{512} A(i) \sin(\omega(i)t + \phi(i)) \quad (2.12)$$

with

$$A(i) = \sqrt{2S(\omega(i))d(\omega)} \quad (2.13)$$

where $\phi(i)$ are the random phase angles which are distributed between 0 and 2π . A is wave amplitude, and changes with frequency, ω .

The reason the Pierson-Moskowitz spectrum has been chosen here is that this is the simplest method by which one can calculate the wave spectrum, and because it can deal with two-wave conditions: unidirectional seas and fully developed (input wind energy in equilibrium with output wave energy) seas. The direction of the waves is not important in this instance, as the WEC system which is utilised in this study moves in the vertical direction only [67].

2.2 Ocean wave description

The significant wave height H_s is set to be 6 meters, and the zero crossing period T_z is set to be 6 seconds in this thesis, which are close to the wave conditions found for the Irish coast [66]. Simulation results can be achieved using these parameters:

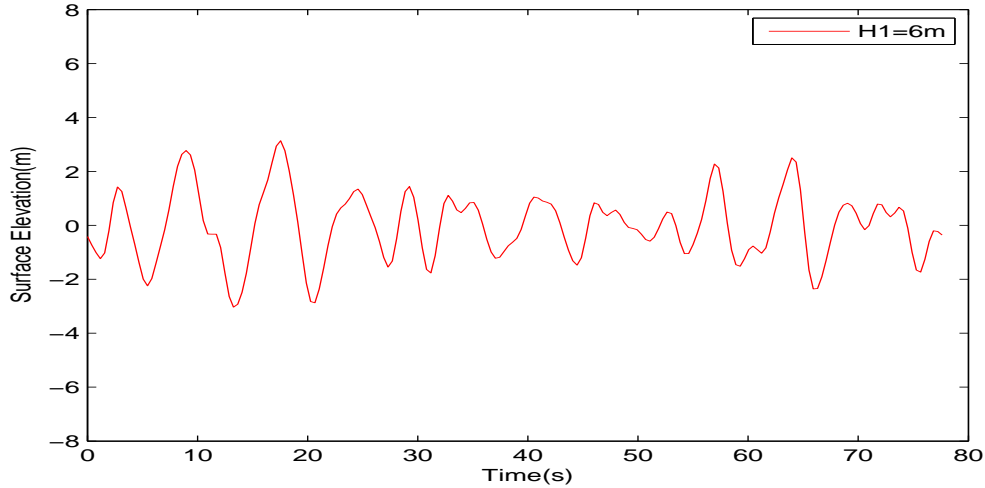


Figure 2.1 Simulation of sea surface elevation

The total duration time of the above figure is 0 to $1/f_s \times 200 = 78s$. The PM spectrum plotted from the equation defined by $H_s = 6m$ and $T_z = 6s$ is presented as follows:

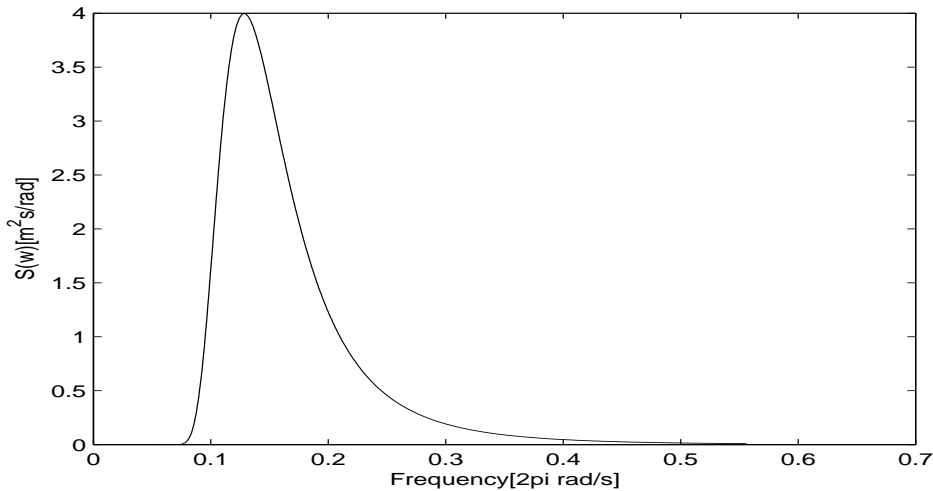


Figure 2.2 PM spectrum simulation plot

The changing values of the significant wave height and zero crossing period will affect the spectrum and wave elevation. A comparison, using different $H_{1/3}$ and T_z , is given in

2.2 Ocean wave description

the figure2.3 and 2.7. A comparison of the different values of H_s and how they affect the spectrum is shown below as follows ($H1 = 6m, H2 = 9m, H3 = 12m$):

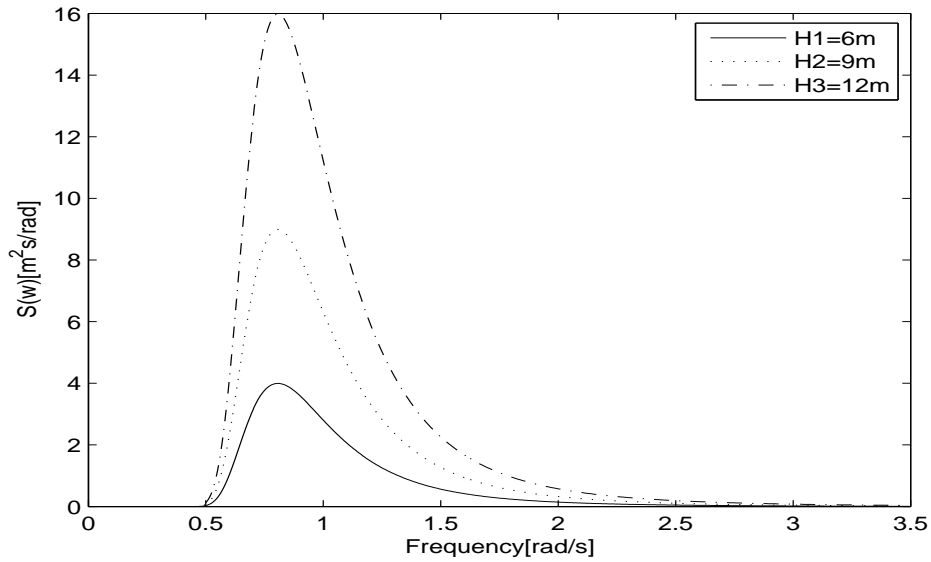


Figure 2.3 PM spectra with different H_s values

As can be seen in figure 2.3, as the significant wave height H_s increased, the spectral density value also increased; however, the peak frequencies are not affected and so H_s is directly proportional to the power spectrum S_ω .

Sea wave elevations with different significant wave heights H_s are illustrated in figure2.4, 2.5, and 2.6:

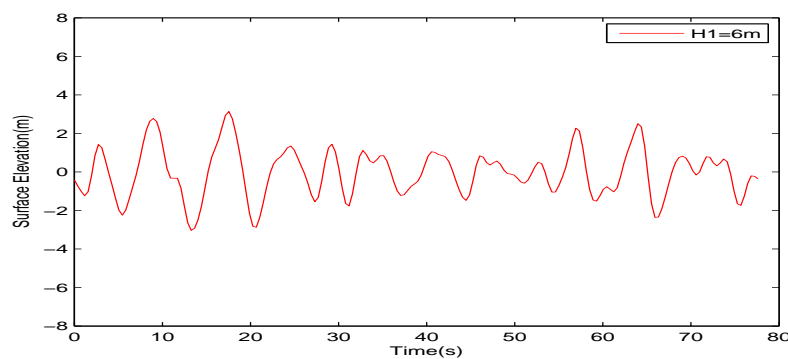


Figure 2.4 Sea elevation with H_s equals to 6m

According to figure2.4, 2.5, and 2.6, the overall sea elevation increases slightly as the H_s value increases. Wave elevations shown in figure2.4, 2.5, and 2.6 correspond to those in eq(2.11) and eq(2.12). Wave elevation is proportional to significant wave height.

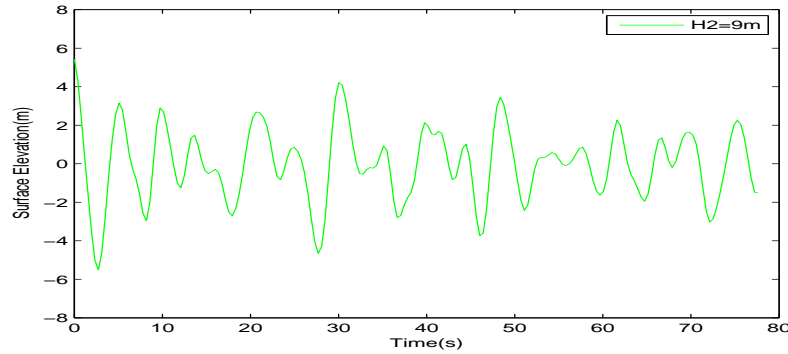


Figure 2.5 Sea elevation with H_s equals to 9m

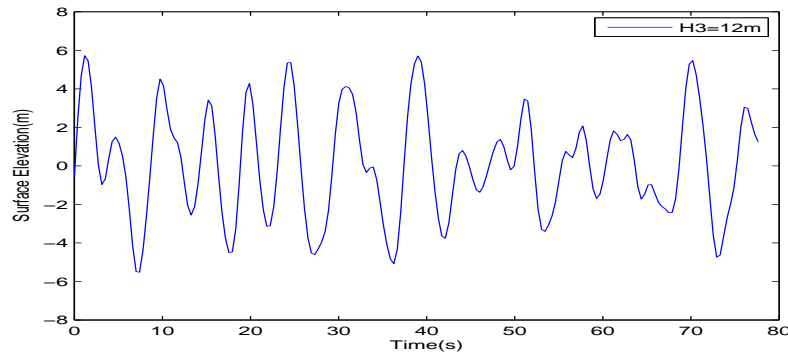


Figure 2.6 Sea elevation with H_s equals to 12m

Further to this, the influence of the remaining important parameter, the zero crossing period, can be investigated through figure 2.7. Figure 2.7 presents spectra that are affected by different zero crossing periods T_z , where $T_1 = 6s$, $T_2 = 8s$ and $T_3 = 10s$. As the zero crossing period T_z increases, the spectral density value also increases. The relationship between the zero crossing period T_z and the power spectrum S_ω is more complex than that for significant wave height.

On the other hand, as zero crossing period T_z increases, the peak frequency decreases. The peak frequency can be defined as the inverse of the frequency corresponding to the maximum value in the power spectrum $S(\omega)_{max}$, which is obtained as per the following:

$$S(\omega = \frac{2\pi}{T_p}) = S(\omega)_{max} \quad (2.14)$$

Wave elevations are affected by different zero crossing periods T_z as illustrated in the figure 2.8, 2.9, and 2.10.

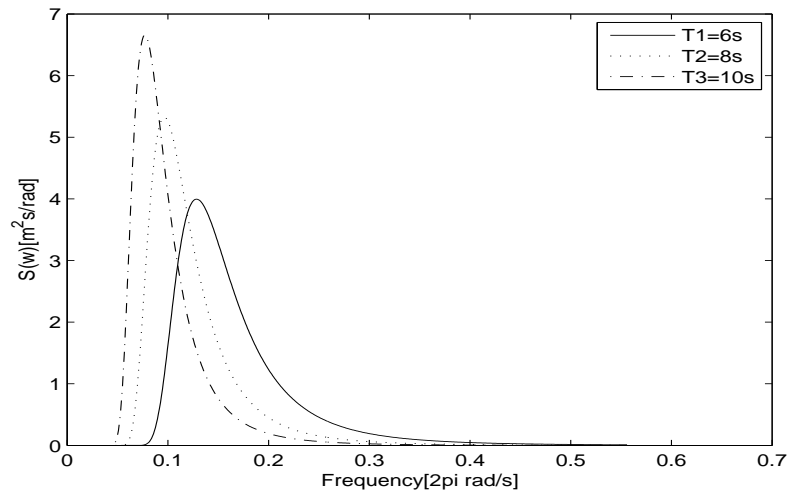


Figure 2.7 PM spectrum with different T_z values

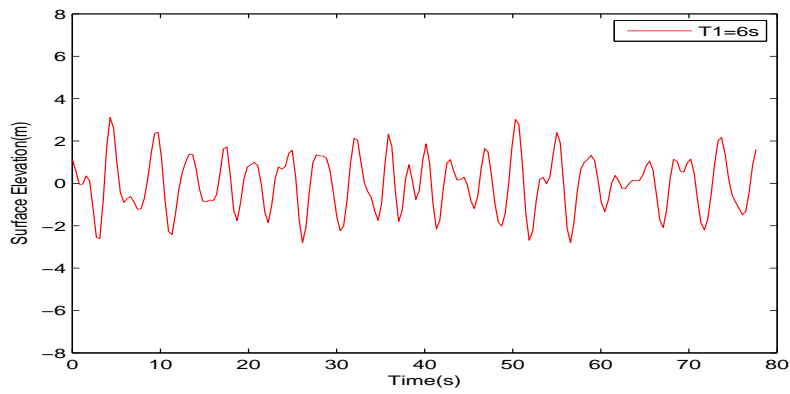


Figure 2.8 Sea elevation variation with T_z equals to 6s

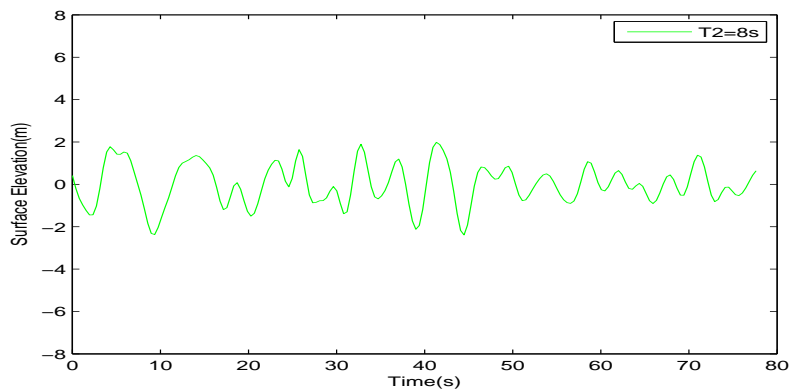


Figure 2.9 Sea elevation variation with T_z equals to 8s

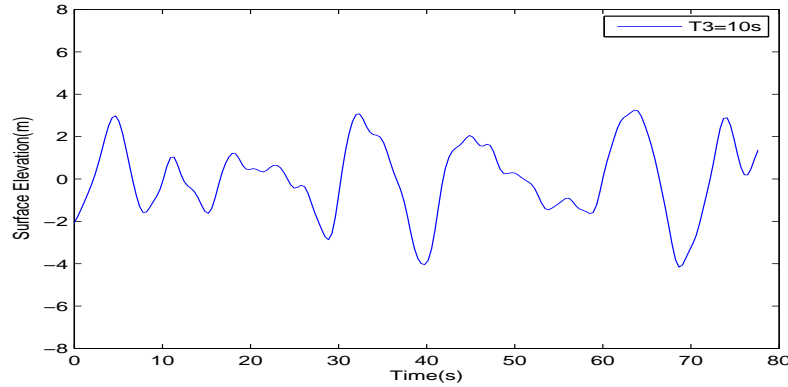


Figure 2.10 Sea elevation variation with T_z equals to 10s

Each wave component's period becomes slightly longer as the zero crossing period T_z increases.

2.3 Oscillating buoy and its model

The following section presents the relationship between the wave force and wave energy converter, which has been constructed using data from an oscillating buoy. The way in which each force acts on the WEC is described in detail. Furthermore, the dynamic equation of the WEC is expressed in both the time and frequency domains. In addition, the power delivered by each force is also given.

2.3.1 WEC dynamic model in the time domain

The linear model consists of an oscillating body and PTO system that is used to analyse the motion of the WEC. The construction of the system can be illustrated as figure 2.11. The dynamic equation for the system shown in figure 2.11 can be expressed as:

$$f_{ex} = ma + f_r + f_s + f_v + f_{pto} \quad (2.15)$$

where f_{ex} is the excitation force, f_r the radiation force, f_s the net buoyancy force, f_v the viscous force, and f_{pto} is the control force.

The excitation force, f_{ex} , is caused by the dynamic pressure resulting from the incident wave [42]. In other words, the excitation force is not generated directly by the incident wave. The excitation force includes the Froude-Krylov force and the diffraction force; the

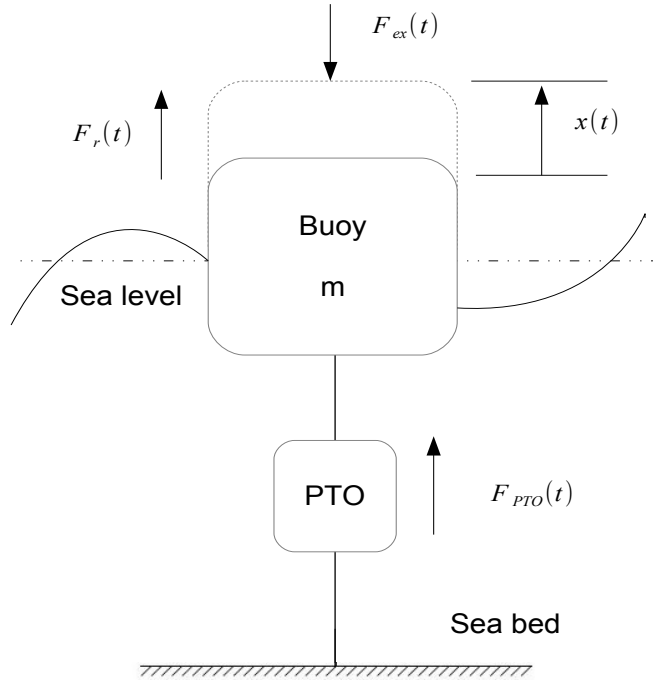


Figure 2.11 Oscillating body and PTO system for a WEC

Froude-Krylov force is caused by the oscillating body immersed in the pressure field of the undisturbed waves [27], whilst the diffraction force is generated by the scattering of diffracted waves by the oscillating body [62].

The excitation force can be modelled in the time domain as follows [22]:

$$\begin{aligned}
 F_{ex}(t) &= \int_{-\infty}^{\infty} h_{ex}(\tau)\eta(t-\tau)d\tau \\
 &= \int_{-\infty}^t h_{ex}(\tau)\eta(t-\tau)d\tau + \int_t^{\infty} h_{ex}(\tau)\eta(t-\tau)d\tau
 \end{aligned} \tag{2.16}$$

Due to the non-causality of the system, $t \geq 0$, the result of $F_{ex}(t)$, is equal to $\int_{-\infty}^t h_{ex}(\tau)\eta(t-\tau)d\tau + \int_t^{\infty} h_{ex}(\tau)\eta(t-\tau)d\tau$, otherwise, the value of $F_{ex}(t)$ is equal to $\int_{-\infty}^t h_{ex}(\tau)\eta(t-\tau)d\tau$. For this reason, $F_{ex}(t)$ depends on future values of wave elevation $\eta(t)$, where $h_{ex}(t)$ is the excitation coefficient and $\eta(t)$ is the wave elevation.

The second force is expressed as the radiation force. It is created by the relative oscillating wave of the buoy, the concept of which was introduced in chapter 1. The time domain

2.3 Oscillating buoy and its model

expression for the radiation force is given in [23, p. 138-141], and can be given as:

$$F_r(t) = - \int_{-\infty}^t h_r(\tau)v(t - \tau)d\tau - M_a(\infty)a(t) \quad (2.17)$$

Falnes states that the above linear system is causal [22]. This is because the input, $v(t)$ (velocity of the oscillating body), is the actual cause of the radiation force. $h_r(\tau)$ is the radiation impulse response function [24]. $M_a(\infty)$ is the added mass, which is the weight of the buoy's surface water when the buoy is deformed. Water on the buoy's surface is lifted from troughs to crests [23, p. 50]. Thus the added mass will change with time.

The net buoyancy force is presented as $F_s(t)$, which is defined as the restoring force; this changes with the oscillating body's motion [65] at different sea levels. As a result, the net buoyancy force can be seen as the difference between the gravitational and total buoyancy forces [44]. It can also be considered as a spring force in the mass-spring-damper system, as shown in figure2.11. The net buoyancy force is given as:

$$F_s(t) = -K_s x(t) \quad (2.18)$$

where K_s is the constant of buoyancy. This can also be seen as the stiffness coefficient, which depends on density, ρ , gravity, g , and water plane area, S_w . The equation above can also be written as:

$$K_s = \rho g S_w \quad (2.19)$$

However, eq(2.19) is an approximation, whereby the buoy's water plane area is assumed to be constant [23]. The net buoyancy force can be seen as the spring effect of the spring-damper-mass system.

The force, $F_v(t)$, from damping losses excluding radiation and PTO damping, is assumed to be linear. The force lost in the time domain is:

$$F_v(t) = -K_v \dot{x}(t) \quad (2.20)$$

where K_v is the viscous coefficient. Actually, the losses are not just from fluid losses, but also from mechanical losses. Viscous losses are proportional to velocity, whereas mechanical losses result from friction within the PTO system or buoy. Nevertheless, $F_v(t)$ is, for convenience, referred to as viscous force.

In the mass-spring-damper system, the viscous force and the radiation force can be assumed to generate a damping effect when acting together.

The dynamic equation for the WEC system in the time domain can be expressed as follows, which combines eq(2.16), (2.17), (2.18), and eq(2.20):

$$m\ddot{x} + M_a(\infty)\ddot{x} + \int_0^{\infty} h_r(\tau)v(t-\tau)d\tau + K_v\dot{x}(t) + K_sx(t) = \int_{-\infty}^{\infty} h_{ex}(\tau)\eta(t-\tau)d\tau + F_{pto}(t) \quad (2.21)$$

2.3.2 Frequency domain dynamic model

A Fourier transform can be used to transform the time domain equation (2.21) into the frequency domain. The frequency domain is simpler to deal with than the time domain function, and each term can be analysed in detail; in particular, the characteristics of the radiation force can be analysed. The frequency domain can be obtained by performing each term of eq(2.21) with the Fourier transform:

$$\begin{aligned} (j\omega)^2 mX(j\omega) + j\omega H_r(j\omega)X(j\omega) + (j\omega)^2 M_a(\infty)X(j\omega) + j\omega K_v X(j\omega) + K_s X(j\omega) \\ = F_{ex}(j\omega) + F_{pto}(j\omega) \end{aligned} \quad (2.22)$$

where $F_{ex}(j\omega)$ is equal to:

$$F_{ex}(j\omega) = H_{ex}(j\omega)\Xi(j\omega) \quad (2.23)$$

$H_{ex}(j\omega)$ and $\Xi(j\omega)$ are the Fourier transforms of the excitation coefficient, $h_{ex}(t)$, and wave elevation, $\eta(t)$, respectively.

$X(\omega)$ represents the Fourier transform of the displacement $x(t)$.

In fact, the radiation force should be written as follows:

$$F_r(j\omega) = j\omega Z_r(j\omega)X(j\omega) \quad (2.24)$$

However, the inverse Fourier transform of the radiation impedance, $Z_r(j\omega)$, cannot be obtained because it is not equal to zero when the frequency tends to infinity. The radiation impedance is usually decomposed into real and imaginary parts:

$$Z_r(t) = B(j\omega) + j\omega M_a(j\omega) \quad (2.25)$$

2.3 Oscillating buoy and its model

where the real part, $B(j\omega)$, is called the radiation resistance and the imaginary part, $M_a(j\omega)$, is called the added mass. $M_a(\infty)$ is the added mass at infinite frequency. Note that $M_a(j\omega)$ does not tend to 0 in the limit $\omega \rightarrow \infty$ [23, p. 140]. This singularity has to be removed by separating $M_a(j\omega)$ from the radiation impedance, so the related radiation impedance can be expressed as:

$$H_r(j\omega) = B(j\omega) + j\omega[M_a(j\omega) - M_a(\infty)] \quad (2.26)$$

$B(j\omega)$ tends to zero as $j\omega$ tends to infinity. The impedance, $H_r(j\omega)$, will tend to zero as the frequency approaches infinity. The singularity, $M_a(\infty)$, can then be removed. Finally, the radiation force in the frequency domain can be found using eq(2.25) and eq(2.26):

$$F_r(j\omega) = -Z_r(j\omega)V(j\omega) = -j\omega H_r(j\omega)X(j\omega) - (j\omega)^2 M_a(\infty)X(j\omega) \quad (2.27)$$

The second term of the radiation force is proportional to acceleration. Korde notes that an immersed body produces both radiated and evanescent waves [48] as a response to the real and imaginary parts of the radiation force.

The natural frequency is changed due to the fact that there is an added mass. m_∞ is the inverse Fourier transform of $M_a(\infty)$. The velocity reaches a maximum when the frequency equals the natural frequency [65]. Under the condition, the values of $M_a(j\omega)$ and $B(j\omega)$ are quite small, when compared to the mass of the buoy and the net buoyancy force. The natural frequency can be expressed as follows [65]:

$$\omega_0 \approx \sqrt{\frac{K_s}{m + m_\infty}} \quad (2.28)$$

The related radiation impedance, $H_r(j\omega)$, can be separated as per eq(2.27). Hence, eq(2.22) can be expanded as:

$$\begin{aligned} -\omega^2(m + M_a(j\omega))X(j\omega) + j\omega B(j\omega)X(j\omega) + j\omega K_v X(j\omega) + K_s X(j\omega) \\ = F_{ex}(j\omega) + F_{pto}(j\omega) \end{aligned} \quad (2.29)$$

The relationship between the displacement and sum of the excitation and the PTO forces can be expressed as follows:

$$\frac{X(j\omega)}{F_{ex}(j\omega) + F_{pto}(j\omega)} = \frac{1}{j\omega[B(j\omega) + K_v] - \omega^2[m + M_a(j\omega)] - K_s} \quad (2.30)$$

2.3 Oscillating buoy and its model

The velocity $V(j\omega)$ is the merely the differential of $X(j\omega)$ with respect to time, so:

$$V(j\omega) = j\omega X(j\omega) \quad (2.31)$$

Hence, the velocity response of the sum of the excitation force and the PTO force can be expressed as per eq(2.30):

$$\frac{V(j\omega)}{F_{ex}(j\omega) + F_{pto}(j\omega)} = \frac{j\omega X(j\omega)}{F_{ex}(j\omega) + F_{pto}(j\omega)} = \frac{1}{B(j\omega) + K_v + j\omega[m + M_a(j\omega) - \frac{K_s}{\omega^2}]} \quad (2.32)$$

Finally, the intrinsic impedance can expressed as:

$$Z_i(j\omega) = B(j\omega) + K_v + j\omega[m + M_a(j\omega) - \frac{K_s}{\omega^2}] \quad (2.33)$$

The PTO force is used to make the oscillating body of the WEC more efficient, and can be expressed as a function of impedance and velocity:

$$F_{pto}(j\omega) = -Z_{pto}(j\omega)V(j\omega) \quad (2.34)$$

where $Z_{pto}(j\omega)$ is the PTO impedance or load impedance. The generalised PTO complex impedance function can be expressed as follows:

$$Z_{pto}(j\omega) = R_{pto}(j\omega) + jX_{pto}(j\omega) \quad (2.35)$$

where $R_{pto}(j\omega)$ is the load resistance, and $X_{pto}(j\omega)$ is the load reactance [23].

The load reactance, $X_{pto}(j\omega)$, can be decomposed into different parts which correspond to the linear model order. If the PTO force is used in a linear model with a constant numerator, then:

$$X_{pto}(j\omega) = \frac{k_{pto}(j\omega)}{j\omega} \quad (2.36)$$

Hence, the PTO force in the frequency with a first-order numerator is:

$$F_{pto}(j\omega) = -R_{pto}(j\omega)V(j\omega) - \frac{k_{pto}(j\omega)}{j\omega}V(j\omega) \quad (2.37)$$

2.3 Oscillating buoy and its model

In the case of a second-order numerator, $X_{pto}(j\omega)$ can be written as:

$$X_{pto}(j\omega) = j\omega b(j\omega) + \frac{k_{pto}(j\omega)}{j\omega} \quad (2.38)$$

The PTO force in a model with a second-order numerator can then be expressed as:

$$F_{pto}(j\omega) = -j\omega b(j\omega) - R_{pto}(j\omega)V(j\omega) - \frac{k_{pto}(j\omega)}{j\omega}V(j\omega) \quad (2.39)$$

The PTO force is usually set by convention to act in the opposite direction to the excitation force. Hence, the value of $R(j\omega)$ can affect the absorbed power. The absorbed power is negative when the value of $R(j\omega)$ is greater than zero. In contrast, the absorbed power is positive, which means all absorbed power has been lost.

There is another impedance called the net impedance, which is the combination of the intrinsic impedance and the PTO impedance. The excitation is:

$$F_{ex}(j\omega) = Z_i(j\omega)V(j\omega) + Z_{pto}(j\omega)V(j\omega) \quad (2.40)$$

therefore, the relationship between the velocity and the excitation force can be shown to be:

$$\frac{F_{ex}(j\omega)}{V(j\omega)} = Z_i(j\omega) + Z_{pto}(j\omega) = Z_{net}(j\omega) \quad (2.41)$$

The excitation force is the only external input to the WEC system, and the velocity is the only output from the system.

2.3.3 Power transmission in the frequency domain

The equation giving the balance of forces in the frequency domain is given in eq(2.29). The average power of the WEC system, which is delivered by the excitation force, can be calculated using the following equation:

$$P_{ex}(j\omega) = \frac{1}{4}(F_{ex}(j\omega)V(j\omega)^* + F_{ex}(j\omega)^*V(j\omega)) = \frac{1}{2}Re\{F_{ex}(j\omega)V(j\omega)^*\} \quad (2.42)$$

By recalling eq(2.40), the excitation force can be expressed as:

$$\begin{aligned}
 P_{ex}(j\omega) &= \frac{1}{2} \text{Re}\{Z_{net}(j\omega)\} |V(j\omega)|^2 \\
 &= \frac{B(j\omega) + K_v + R_{pto}(j\omega)}{|B(j\omega) + K_v + j\omega[m + M_a(j\omega) - \frac{K_s}{\omega^2}] + Z_{pto}(j\omega)|^2} |F_{ex}(j\omega)|^2
 \end{aligned} \tag{2.43}$$

where the excitation force, $F_{ex}(j\omega)$, is given as $H_{ex}(j\omega)\Xi(j\omega)$.

The average radiation power can be expressed as:

$$P_r(j\omega) = \frac{1}{2} \text{Re}\{(F_r(j\omega)V(j\omega))^*\} = \frac{1}{2} \frac{B(j\omega)}{|Z_i(j\omega) + Z_{pto}(j\omega)|^2} \tag{2.44}$$

The average viscous power can be shown to be:

$$P_v(j\omega) = \frac{1}{2} \text{Re}\{(F_v(j\omega)V(j\omega))^*\} = \frac{1}{2} \frac{K_v}{|Z_i(j\omega) + Z_{pto}(j\omega)|^2} \tag{2.45}$$

Finally, the average PTO power can be expressed as:

$$P_{pto}(j\omega) = \frac{1}{2} \text{Re}\{(F_{pto}(j\omega)V(j\omega))^*\} = \frac{1}{2} \frac{R_{pto}(j\omega)}{|Z_i(j\omega) + Z_{pto}(j\omega)|^2} \tag{2.46}$$

The average PTO power can also be expressed as:

$$P_{pto}(j\omega) = P_{ex}(j\omega) - P_r(j\omega) - P_v(j\omega) \tag{2.47}$$

Note that there is no average net buoyancy force power because $\text{Re}\{j\omega \cdot \frac{K_s}{\omega^2}\} = 0$. More details concerning the average PTO power are introduced in the next section, where it will be explained how this can be maximised.

2.4 Chapter summary

Harmonic waves were introduced in section 2.2.1. Real ocean waves have been assumed to be the superpositions of harmonic waves at different frequencies. The power spectrum is the key to analysing wave power, and hence different wave power spectra have been analysed and simulated.

In section 2.4, the actions of irregular waves on the WEC system have been presented. Each force that acts on the oscillating buoy has been analysed. Dynamic equations for the

2.4 Chapter summary

WEC system have been expressed in the time and the frequency domains. Finally, the power transmission of the WEC system was presented in the frequency domain.

However, power transmission requires prior knowledge to control the WEC system effectively. The means by which the absorbed power can be maximised will be given in chapter 3.

Chapter 3

Control of wave energy converter

3.1 Chapter overview

Power transmission was described in the last chapter. Here we consider the absorbed power, which is dependent on frequency. The relationship between velocity and force has presented in section 2.3.2. The main objective of this chapter, however, is to gain an understanding of the optimal conditions that enable the maximum absorption of energy. However, optimal frequency domain conditions have a number of limitations when they are used for real-time control. Firstly, frequency domain optimal conditions do not consider physical constraints. Secondly, the non-causality of control can not be considered in the optimal frequency domain conditions, and hence the time domain function will be used for non-causal analysis. This chapter will focus on the non-causality of control. Optimal conditions, based on the frequency domain in order to maximise the absorption of energy, will be introduced in section 3.2, whilst the causality and non-causality of optimal conditions will be analysed in section 3.3. Several control methods for the bottom-referenced heaving buoy will be presented in section 3.4.

3.2 Optimal conditions for maximising absorption energy

Falnes presents a one-degree oscillating system as having the optimal phase conditions when at resonance with a wave [23], or in other words when the frequency of the waves is the same as the natural frequency of oscillation of the buoy. Additionally, optimal phase conditions can be obtained when the excitation force is in phase with the buoy oscillation velocity. This process will be discussed below.

3.2.1 Optimal condition expressed in complex amplitude with a simplified model

Assume the excitation force's oscillation is harmonic, and can thus be represented in the time domain as:

$$F_{ex}(t) = Re\{\hat{F}_{ex}e^{j\omega t}\} = F_{ex} \cos(\omega t + \varphi) \quad (3.1)$$

where φ is the angle between the excitation force in the complex amplitude, \hat{F}_{ex} , and its real part in the complex plane. The excitation force can be rewritten as:

$$\hat{F}_{ex} = F_{ex}e^{j\varphi} \quad (3.2)$$

where we assume the viscous force is not considered, and the radiation force is considered to be linear for convenience. The PTO force is given as:

$$\hat{F}_{pto} = F_{pto}e^{j\varphi} \quad (3.3)$$

The dynamic equation for an oscillating system can be described as:

$$\hat{F}_{pto} + \hat{F}_{ex} = j\omega m \hat{v} + B \hat{v} + (K_s/j\omega) \hat{v} \quad (3.4)$$

The impedance complex function of the PTO force is given in eq(2.32). Hence, the above equation can be written in response to the velocity and the excitation force:

$$\begin{aligned} \hat{v} &= \frac{\hat{F}_{ex}}{j\omega m + B + \frac{K_s}{j\omega} + Z_{pto}} \\ &= \frac{\hat{F}_{ex}}{(B + R_{pto}) + j(\omega m + X_{pto} - K_s/\omega)} \end{aligned} \quad (3.5)$$

The power absorbed from the PTO device can be written as:

$$P_{pto} = \frac{1}{2} R_{pto} |\hat{v}|^2 = \frac{(R_{pto}/2) |\hat{F}_{ex}|^2}{(B + R_{pto})^2 + (\omega m + X_{pto} - K_s/\omega)^2} \quad (3.6)$$

The maximum value of P_{pto} can be calculated by taking the derivative of R_{pto} . The maximum is obtained when $\frac{\partial P_{pto}}{\partial R_{pto}}$ is equal to zero, such that the optimal value of R_{pto} can be

3.2 Optimal conditions for maximising absorption energy

found as:

$$R_{pto} = \{B^2 + (\omega m + X_r - K_s/\omega)^2\}^{\frac{1}{2}} \quad (3.7)$$

In addition, the second term of the denominator of absorbed power, P_{pto} , is always greater than or equal to zero. In order to obtain the maximum value for absorbed power, the denominator should be kept as small as possible. Hence, $\omega m + X_{pto} - K_s/\omega$ is set equal to zero, and the optimal value of R_{pto} can be obtained from eq(3.7):

$$R_{pto,opt} = B \quad (3.8)$$

Finally, the maximum value of absorbed power can be determined by simplifying eq(3.6):

$$P_{pto,max} = \frac{|\hat{F}_{ex}|^2}{8R_{pto}} \quad (3.9)$$

The relationship between the velocity and the excitation force becomes [23]:

$$\hat{v} = \frac{|\hat{F}_{ex}|}{2R_{pto}} \quad (3.10)$$

It can be shown from eq(3.10) that one of the optimal conditions for maximising the absorbed power is when the excitation force is in phase with the buoy's oscillation velocity.

3.2.2 Optimal conditions in the complex amplitude and frequency domain using the full model

As mentioned, the effects of viscous force were ignored in the previous section. Nevertheless, the power absorbed can usually be decomposed into two parts in the oscillating system. One is useful power, P_u , whilst the other is the viscous power, or lost power, P_v .

Assuming a useful resistance, R_u , is given, the useful force, F_u , can be expressed as:

$$F_u = -R_u V \quad (3.11)$$

Also, the average excitation power can be calculated using eq(3.1):

$$P_{ex} = \frac{1}{2} Re\{\hat{F}_{ex}\hat{v}^*\} = \frac{1}{2} F_{ex} V \cos \varphi \quad (3.12)$$

3.2 Optimal conditions for maximising absorption energy

where V is the amplitude and φ is the phase difference between the velocity \hat{v} and \hat{F}_{ex} .

The average radiation power is:

$$P_r = \frac{1}{2} Re\{\hat{F}_r \hat{v}^*\} = \frac{1}{2} B V^2 \quad (3.13)$$

The average viscous power can be given as:

$$P_v = \frac{1}{2} Re\{K_v \hat{v} \hat{v}^*\} = \frac{1}{2} K_v V^2 \quad (3.14)$$

Hence, the useful power can be expressed as:

$$P_u = \frac{1}{2} R_u V^2 \quad (3.15)$$

It also can be expressed in terms of the average power as:

$$\begin{aligned} P_u &= P_{ex} - P_r - P_v \\ &= \frac{1}{2} F_{ex} V \cos \varphi - \frac{1}{2} B V^2 - \frac{1}{2} K_v V^2 \end{aligned} \quad (3.16)$$

It is clear that the excitation power maximum, $P_{ex,max}$, can be obtained when $\varphi = 0$, which means the excitation force is in phase with the velocity. Finally, the control force has to be designed in order to achieve the desired velocity value:

$$\frac{\partial P_u}{\partial V} = \frac{\partial}{\partial V} \left[\frac{1}{2} F_{ex} V \cos \varphi - \frac{1}{2} (B + K_v) V^2 \right] = 0 \quad (3.17)$$

Assuming φ is equal to 0, the magnitude of the velocity can be calculated as:

$$V = \frac{F_{ex}}{2(B + K_v)} \cos \varphi = \frac{F_{ex}}{2(B + K_v)} \quad (3.18)$$

Figure 3.1 shows the average excitation power in proportion to the velocity. The total power lost (the sum of the radiation power and the viscous power) is proportional to the square of the velocity; the useful power also has a similar relationship with velocity, in that it will increase as the velocity increases and then decrease because the total power lost increases. This relationship can be described as figure 3.1 [23]:

3.2 Optimal conditions for maximising absorption energy

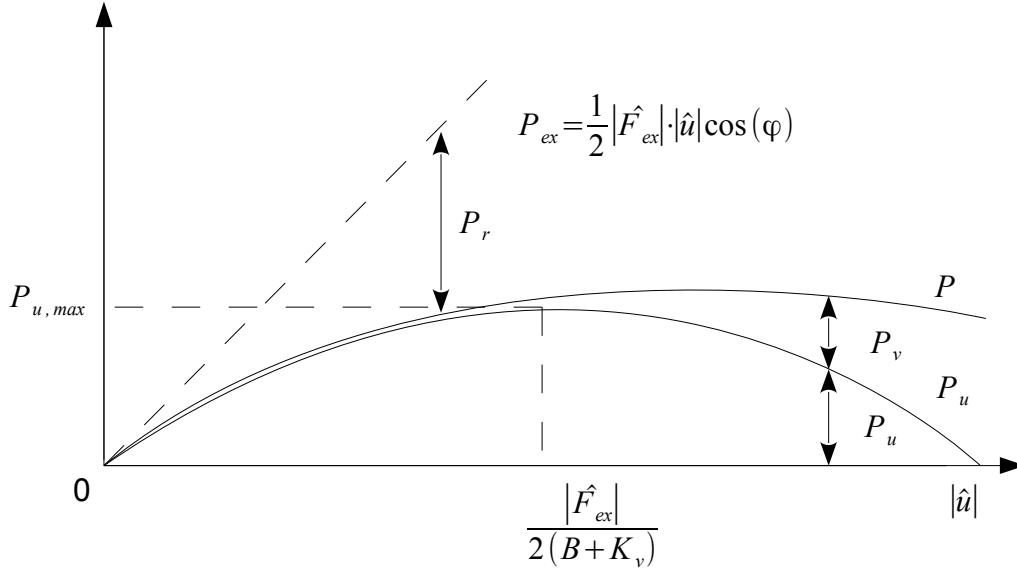


Figure 3.1 Relationship between useful power and excitation power[23]

Finally, the maximum average useful power can be obtained as:

$$P_{u,max} = \frac{F_{ex}^2}{8(B + K_v)} \quad (3.19)$$

Note that $R_{u,opt} = B + K_v$ can be obtained from eq(3.6), (3.7) and (3.8). The optimal condition is defined by the velocity and the excitation force, as discussed above. The other condition, as defined by F_u , will be discussed later. Newton's second law has been applied in eq(2.32) and (2.33), so the oscillating system can be described by:

$$\hat{F}_{ex} + \hat{F}_u = Z_i \hat{v} \quad (3.20)$$

where Z_i is used to express the complex function ω . It can also be written as $Z_i = Z_i(j\omega) = R_i(j\omega) + jX_i(j\omega)$.

To this point, optimal conditions for maximising wave energy have been discussed in terms of complex amplitudes, which is because a harmonic force is only considered in one frequency. However, more general expressions of optimal conditions will have to be capable of dealing with more than one frequency. Hence, in the following section, the optimal conditions will be expressed in the frequency domain.

3.2 Optimal conditions for maximising absorption energy

The useful force can be expressed as:

$$F_u(j\omega) = -Z_u(j\omega)V(j\omega) \quad (3.21)$$

By recalling eq(3.15), the frequency domain for the useful power can be presented as:

$$\begin{aligned} P_u(j\omega) &= -\frac{1}{2}Re\{\hat{F}_u\hat{v}^*\} \\ &= \frac{1}{2}Re\{Z_u(j\omega)\}|V(j\omega)|^2 \end{aligned} \quad (3.22)$$

The above equation can be written by inserting eq(3.20) into eq(3.21) as follows:

$$\begin{aligned} P_u(j\omega) &= \frac{1}{2}Re\{Z_u(j\omega)\} \frac{|F_{ex}(j\omega)|}{|Z_i(j\omega) + Z_u(j\omega)|^2} \\ &= \frac{1}{2} \frac{R_u(j\omega)}{|Z_i(j\omega) + Z_u(j\omega)|^2} |F_{ex}(j\omega)|^2 \\ &= \frac{1}{2} \frac{R_u(j\omega)}{[R_i(j\omega) + R_u(j\omega)]^2 + [X_i(j\omega) + X_u(j\omega)]^2} |F_{ex}(j\omega)|^2 \end{aligned} \quad (3.23)$$

The denominator of eq3.23 takes its the optimal value when $R_u(j\omega)$ is equal to $R_i(j\omega)$, and when the imaginary part $X_u(j\omega)$ is equal to $-X_i(j\omega)$. The calculation process is the identical to that for eq(3.6), eq(3.7) and eq(3.8). Hence, the optimal condition for maximising the useful power can be found when the load impedance is equal to the complex conjugate of the intrinsic impedance:

$$Z_{u,opt}(j\omega) = Z_i^*(j\omega) \quad (3.24)$$

This is called the complex conjugate control.

The average useful power in the frequency domain can be expressed as eq3.25 by recalling complex amplitudes, as given in eq(3.19):

$$P_{u,max}(j\omega) = \frac{|F_{ex}(j\omega)|^2}{8R_u(j\omega)} \quad (3.25)$$

where $R_u(j\omega) = B(j\omega) + K_v(j\omega)$. With complex conjugate control, as given by eq(3.24), the other optimal condition can be obtained as follows:

$$V_{opt}(j\omega) = \frac{F_{ex}(j\omega)}{2R_u(j\omega)} \quad (3.26)$$

This is used to express the relationship between velocity and excitation force, and is hence called the phase control.

3.3 Causality and non-causality of optimal conditions

The optimal conditions for maximising the amount of power absorbed were given in the previous section. However, only complex amplitudes and the frequency domain for the optimal conditions have been discussed to this point as they are not particularly useful for causality and non-causality analysis. Indeed, to conduct such an analysis, the time domain function has to be considered in order to analyse the causality and non-causality of the control.

One of the optimal conditions has been given eq3.26. Supposing there is no loss in the viscous force, F_v , then eq(3.26) can be written as:

$$V(j\omega) = \frac{F_{ex}(j\omega)}{2B(j\omega)} \quad (3.27)$$

Falnes introduced this as the phase control that can be used to find the optimal velocity [23], as the velocity should have the same phase as the excitation force under this condition. The frequency domain of the above condition should be transferred to the time domain because of the causality analysis, where the time domain of the phase control can be given as follows:

$$v(t) = \int_{-\infty}^t h_v(\tau) f_{ex}(t - \tau) d\tau \quad (3.28)$$

where $h_v(t)$ is the reverse Fourier transform of the real function:

$$h_v(t) = \mathcal{F}^{-1} \left\{ \frac{1}{2B(j\omega)} \right\} \quad (3.29)$$

where $2B(j\omega)$ is the radiation resistance, and is a real, even function that is non-causal due to the properties of the Fourier transform, $h_v(t) = h_v(-t)$ as this gives negative values for the time.

The other optimal condition is given by eq(3.24), which is called the reactive (complex conjugate) control. It is given as follows:

$$F_{pto}(j\omega) = -Z_i^*(j\omega)V(j\omega) \quad (3.30)$$

3.3 Causality and non-causality of optimal conditions

It can be seen that finding the optimal PTO impedance is the object of the condition.

The time domain of the reactive control is:

$$f_{pto}(t) = - \int_{-\infty}^t h_f(\tau)v(t - \tau)d\tau \quad (3.31)$$

and is non-causal, which can be proved through a similar process to that of the phase control.

$h_f(t)$ is equal to:

$$h_f(t) = \mathcal{F}^{-1}\{Z_i^*(j\omega)\} \quad (3.32)$$

and:

$$Z_i^*(j\omega) = Z_i(-j\omega) \quad (3.33)$$

Hence:

$$h_f(t) = \mathcal{F}^{-1}\{Z_i(-j\omega)\} = z_i(-t) \quad (3.34)$$

$z_i(t)$ is causal because radiation is a causal process. Hence, $h_f(t)$ can be shown to be anti-causal (it becomes zero when t is greater than 0).

Causal reactive control

In the case of causal control, the PTO impedance should represent the only frequency. All PTO coefficients are constant. This is different from the non-causal control that responds to all frequencies, as causal control means no future information regarding the velocity or excitation force is required.

The frequency, as mentioned previously, is chosen when under optimal conditions. The frequency is usually chosen from the peak of the power spectrum [9], as indicated by ω_p . The reason for choosing this frequency is that the maximum power is contained in waves of this frequency.

Assuming a mass-spring-damper system is used in the PTO device, the control force is given as per eq(3.30). The complex conjugate of the intrinsic impedance can be decomposed into mass, spring, and damper terms, and the PTO impedance can now be said to depend on constant coefficients; the description now becomes one of a second-order system. The choice of these coefficients is important because they can effect the control force.

The control force can be written as:

$$F_{pto}(j\omega_p) = -(m + M_{a,p})\dot{V}(j\omega_p) + B_p V(j\omega_p) - k_{s,p} V(j\omega_p/j\omega) \quad (3.35)$$

where the added mass, $M_{a,p}$, is independent of the peak frequency. B_p still used to represent the radiation resistance, but this value does not change with frequency. The last term of the equation can be seen as the spring effect.

Non-causal reactive control

In non-causal control, the PTO impedance should respond to every frequency of a polychromatic excitation force:

$$F_{pto}(j\omega) = -[m + M_a(\omega)]\dot{V}(j\omega) + B(j\omega)V(j\omega) + \frac{k_s(j\omega)}{\omega}V(j\omega) \quad (3.36)$$

The singularity $M_a(\infty)$ has to be removed by separating $M_a(\omega)$ from the radiation impedance, as per eq(2.26). Hence, eq(3.36) can be rewritten as:

$$F_{pto}(j\omega) = -[m + M_a(\infty)]\dot{V}(j\omega) + H_r^*(j\omega)V(j\omega) - \frac{k_s(j\omega)}{j\omega}V(j\omega) \quad (3.37)$$

3.4 Different control methods

Optimal conditions were discussed in chapter 3.2. These can be utilised in real-time control, though the method by which this may be achieved has different approaches. The causal and non-causal control will also be discussed in terms of their implementation in real-time control. Several control solutions that use impedance matching will be compared. These adjust the PTO impedance by tuning the value of the damper, mass or spring to achieve optimal conditions. In addition, purely passive control and latching control will be introduced that relate to the phase control.

3.4.1 Implementations under two different sets of optimal conditions

The optimal conditions described in chapter 3.2 were expressed in the frequency domain. In the natural world, sea waves are irregular and can be constructed from the superposition of many regular waves, as described in chapter 2.1. This means that real waves contain many ideal waves at different frequencies. These have been proved to be non-causal, which means

further information regarding the velocity of the oscillating system or the excitation force is required. However, these cannot be directly implemented in practice.

The non-causality problem has to be overcome somehow. One way by which to tackle this problem is through the appreciation that the future value of the velocity or excitation force of a wave can be predicted. The second option is that regular waves can be used instead of irregular waves, for which there is no need for any attempt at prediction. The last solution is to approximate the non-causal transfer function by a presumed causal equivalent. Three control structures will be given in the following section to demonstrate how they cope with the non-causal problem.

Velocity-tracking construction

Falnes introduced two possible approaches to overcoming the non-causality of the control [23]. The first of these is called the velocity-tracking construction for the phase control, the block diagram for which can be given as follows:

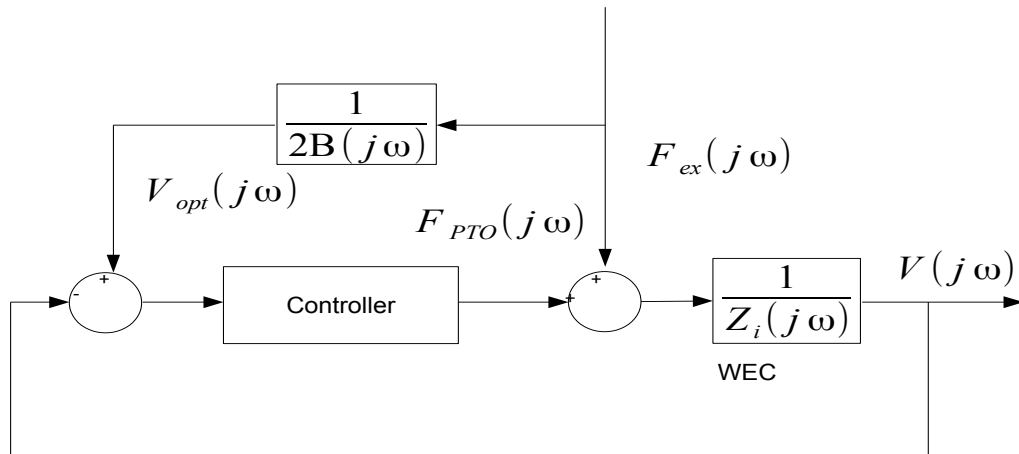


Figure 3.2 Block diagram for a velocity-tracking construction

As illustrated in figure 3.2, where the excitation force is determined through a transfer function $\frac{1}{2B(j\omega)}$, the optimal velocity can be obtained; it can be seen as a reference signal. The controller shown in the block diagram is used to determine the difference between the feedback signal, $V(t)$, and the reference signal, $V_{opt}(t)$. This corresponds to the phase control:

$$V_{opt}(j\omega) = \frac{F_{ex}(j\omega)}{2B(j\omega)} \quad (3.38)$$

3.4 Different control methods

The non-causal problem can be overcome by approximating the transfer function, $\frac{1}{2B(j\omega)}$, to a constant value. The non-causality of $B(j\omega)$ has already been demonstrated. The other option is to predict the future value of the excitation force.

There are various possibilities for the type of controller that can be used in figure 3.2. One simple example is the P controller, the PI controller or the PID controller.

The time domain for eq 3.52 can be given as follows:

$$v(t) = \int_{-\infty}^{\infty} h_v(\tau) f_{ex}(t - \tau) d\tau \quad (3.39)$$

where the $h_v(t)$ is equal to $\mathcal{F}^{-1}\{\frac{1}{2B(j\omega)}\}$. This has been discussed for eq(3.28) and eq(3.29). $f_{ex}(t)$ is determined as the product of the wave elevation and the excitation coefficient.

In [97], a second-order model of the oscillating system has been identified in the time domain:

$$f_{ex}(t) + f_{pto}(t) = M\dot{v}(t) + H_r v(t) + K_s \int_0^t v(\tau) d\tau \quad (3.40)$$

This is the complete dynamic equation that was introduced in chapter 3.3. The non-causal term $B(j\omega)$ has been simplified through its simple representation as the constant B . In the result, the velocity of the oscillating system and the excitation force have a proportional relationship, which can be given as follows:

$$v(t) = \frac{f_{ex}(t)}{2B} \quad (3.41)$$

The reference velocity can be directly implemented with the excitation force. The non-causal problem $B(j\omega)$ has been overcome with constant B .

There are various options available for use as the system controller in this case. A simple proportional controller can be used to impose the reference velocity. The control force then becomes:

$$f_{pto}(t) = Bv(t) \quad (3.42)$$

A proportional integral control can also be used to track the difference between the desired velocity and the real velocity. The control force is then given as follows:

$$f_{pto}(t) = Bv(t) - M(t)\dot{v}(t) \quad (3.43)$$

The complex-conjugate control can be translated to a PID controller, which has been introduced in the causality of the optimal condition. The control force can then be expressed as:

$$f_{pto}(t) = -M\dot{v}(t) + Bv(t) - k_{pto}(t) \int_0^t v(\tau)d\tau \quad (3.44)$$

where the $k_{pto} = k_s$.

Fusco also presented the internal model control that can be used in the controller [39]. He introduced the oscillating system, which is nonlinear due to the hydro-viscous force when the system is immersed in the ocean, where the velocity of the oscillating system will vary depending on the wave elevation.

The velocity-tracking control has been proven to absorb much more power than the uncontrolled model [57]; however, it requires the design of a low-level control. Several such designs have been introduced in the literature [34, 96, 98], some of which have been proven to have suitable performances [44]. The solution to overcoming the non-causal issue has also been given in reference [23, 74]. The authors of this work noted that a causal approximation based on one frequency has to be varied depending on different sea states.

Feedback realisation for complex conjugate control

The other optimal condition for maximising the absorbed power is called the reactive control or complex conjugate control. It is given as follows:

$$F_{pto}(j\omega) = -Z_i^*(j\omega)V(j\omega) \quad (3.45)$$

It also contains the non-causal problem, but again this issue can be overcome through one of various solutions that can be implemented in real time. The feedback realisation for the control is used to solve the problem.

The construction of the feedback control can be demonstrated through the figure3.3. The block $Z_i^*(j\omega)$ in the figure3.3 is the complex-conjugate of the intrinsic impedance $Z_i(j\omega)$. It supplies the feedback from the velocity of the oscillating system. The inverse Fourier transform of $Z_i^*(j\omega)$ is equal to $z_i(-t)$, as shown in eq(3.33). The time domain of the complex-conjugate control can be expressed as:

$$f_{pto}(t) = - \int_{-\infty}^t h_f(\tau)v(t-\tau)d\tau \quad (3.46)$$

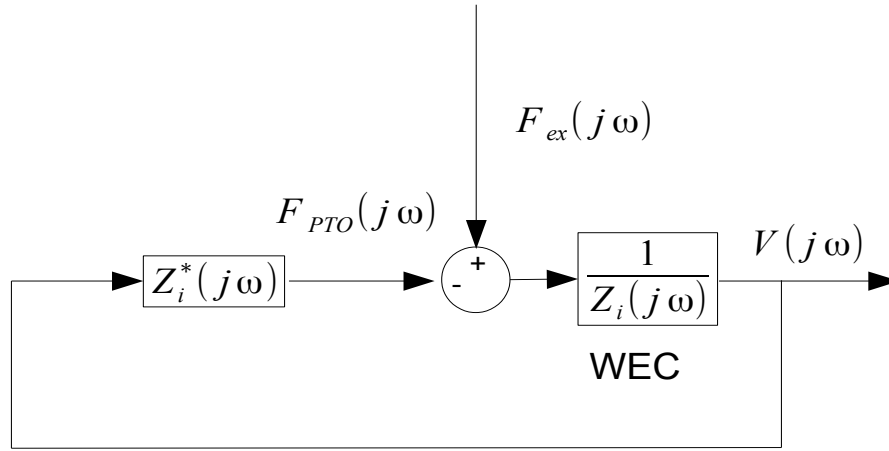


Figure 3.3 Block diagram for feedback implementation of complex-conjugate control.

where the $h_f(t)$ is anti-causal. This means that the control force, $f_{pto}(t)$, depends on some future value of the velocity. This cannot be implemented in real time in practice, and hence different causal approximations for the complex-conjugated control have been used to overcome the non-causal problem.

One approach to overcoming the non-causal issue has been through the attempt to predict the future value of the velocity. This approach was introduced by Korde [57] and Fusco [33], where the control force is given as the convolution of the reaction force and the future value of the velocity, and can be expressed as follows [39]:

$$f_{pto}(t) = - \int_t^{-\infty} z_i(-\tau)v(t - \tau)d\tau \quad (3.47)$$

This has been further decomposed as follows:

$$f_{pto}(t) = -(m + m_\infty)\dot{v}(t) + \int_0^\infty h_r(\tau)v(t + \tau)d\tau + K_v v(t) - K_s \int_{-\infty}^t v(\tau)d\tau \quad (3.48)$$

where the second term in eq(3.48) has been demonstrated to be anti-causal, due to the fact that future information for the velocity is required.

The mass term, the viscous term and the spring term combined together become a PID force:

$$f_{PID}(t) = -(m + m_\infty)\dot{v}(t) - K_v v(t) + K_s \int_{-\infty}^t v(\tau)d\tau \quad (3.49)$$

However, this force can not be implemented in real-time control because the order of the numerator is higher than the denominator of the transfer function of the derivative term, or the so-called added mass term. One way to solve the problem is to multiply a high-frequency pole by the denominator of the transfer function.

The remainder of eq(3.48) depends on the future value of the velocity. However, the radiation force term includes the radiation resistance term and the added mass term. The radiation resistance term is given as:

$$\int_{-T}^T \mathcal{F}^{-1}\{B(\omega)\}(\tau)v(t-\tau)d\tau \quad (3.50)$$

where T is the time in seconds into the future. The resistance term can be seen as the damper that requires passive loading.

The added mass term can be combined with the spring and the mass terms of the PID force that produce the reactive force. The reactive force is generated by the spring effect and the mass, and has been described in chapter 2. This will generate the reactive power flow which will be discussed in chapter 6.

The other approach to overcoming the non-causal issue can be obtained by reviewing the velocity-tracking control, where the oscillating system can be approximated via a second-order model. This method can be also used in the feedback control. The associated second-order dynamic system is described by eq3.35. The control force generated by the feedback control is given as follows:

$$F_{pto}(j\omega) = M_{pto}V(j\omega) \cdot j\omega + R_{pto}V(j\omega) + \frac{K_{pto}V(j\omega)}{j\omega} \quad (3.51)$$

where M_{pto} is equal to the negative value of $m + m_\infty$, and K_{pto} should be equal to the negative value of K_s . The optimal value of R_{pto} is equal to the radiation resistance B introduced in section 3.2.1. The non-causal part of the radiation resistance, B , has been described by a second-order approximation. Hence, the control force is also causal, and can thus be used in real time in practice.

Korde presented the PID control force by a high-frequency pole in a method that can achieve significant improvements [57]. It is worth pursuing the PID control in this case by comparing with the system without a controller. Korde also used a recursive autoregressive predictor to determine future values for the velocity of an oscillating system in a method that can overcome the non-causal problem arising from the inverse Fourier transform of $Z_i^*(j\omega)$. Nevertheless, the performance with the AR predictor does not confer

any additional advantages. Korde did point out that the longer prediction horizon may improve the performance of the system, however, and this will be discussed in the prediction chapter. However, the causal approximation has also been discussed in eq3.51; the variety of frequencies in a real wave do not need to be considered and, further, there is no need to consider the design of a lower-level controller such as a velocity-checking control. Feedback realisation for complex conjugate control will be used in the following chapters of thesis.

Feedforward implementation of optimal conditions

Another control construction is the implementation of optimal conditions that allow for the maximisation of absorbed power, as described in reference [64]. This is called the feedforward implementation of control, and is based on the integration of the phase control and the reactive control. The frequency domain for the control can be described as follows:

$$F_{pto}(j\omega) = -\frac{Z_i^*(j\omega)}{2B(j\omega)}F_{ex}(j\omega) \quad (3.52)$$

where it can be seen that the numerator on the right-hand side of the equation is based on the complex conjugate control. The velocity can be calculated from the phase control.

The block diagram for the feedforward implementation is as follows:

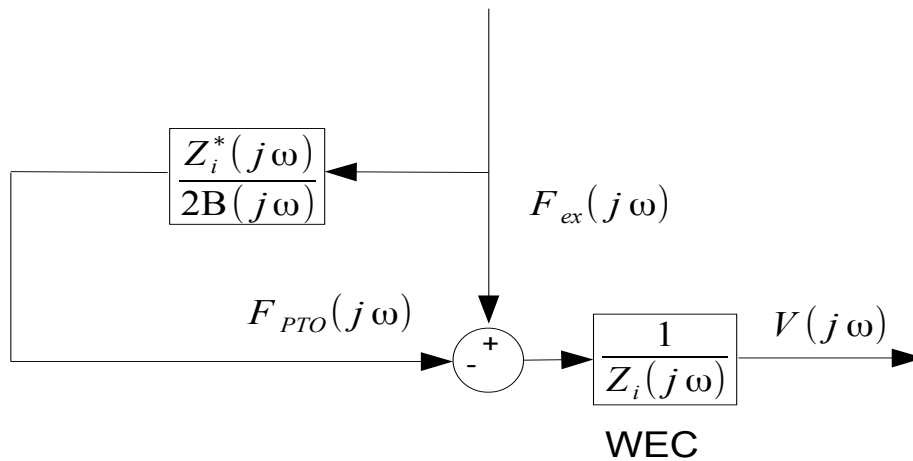


Figure 3.4 Block diagram for the feedforward control

The time domain for the control force is:

$$f_{pto}(t) = -\int_{-\infty}^{\infty} h(\tau)f_{ex}(t-\tau)d\tau \quad (3.53)$$

which assumes the future wave elevation is known by noting $\eta_{-L}(t)$, which is the value of the wave elevation measured L metres away from the system. The excitation force at time $t + LT$ can be expressed as:

$$f_{ex}(t + LT) = \int_{-\infty}^{\infty} h_L(\tau) \eta_{-L}(t + LT - \tau) d\tau \quad (3.54)$$

where the causal approximation can be implemented by setting a larger L . The $|h_L(t)|$ approximates to zero with $t < LT$ under the above conditions [64]. Now, the excitation force has the causal approximation:

$$f_{ex}(t + LT) = \int_{LT}^{\infty} h_L(\tau) \eta_{-L}(t + LT - \tau) d\tau \quad (3.55)$$

Feedforward control is similar to feedback reactive control. Naito and Nakamura proved performance results of feedforward control are much better than no control case with simulation data [64]. However, feedforward control may accumulate any errors in the real-time control process.

All of the above control constructions are based on either the the phase control or the reactive control. They all require the PTO device to supply reactive power; in other words, they can be classified as either being reactive controllers or complex-conjugate controllers. The comparison of the power absorbed by each of the different control constructions will be investigated in chapter 5.

The complex-conjugate and phase control is good for any wave. There is no doubt that they can achieve optimum amplitudes by supplying reactive power, though physical constraints are not considered in this thesis, otherwise the size, velocities and forces of the WECs may influence control performance.

3.4.2 Implementations without optimal conditions

In the previous section, control methods under optimal conditions have been introduced. However, it should also be noted that there are a number of other types of controllers that do not generate reactive power in an oscillating system.

Passive loading control

A basic control assumption is that control force is generated by purely passive loading. The frequency domain for the control force can be given as:

$$F_{pto}(j\omega) = -R_{opt}(j\omega)V(j\omega) \quad (3.56)$$

It can be seen here that the control force is proportional to the velocity. The optimal setting for the control resistance was introduced in reference [43], where Hals noted that the optimal control resistance is equal to the absolute value of the intrinsic impedance of the system. The optimal control resistance is thus given by:

$$R_{opt}(j\omega) = \sqrt{R_i(j\omega) + X_i(j\omega)} \quad (3.57)$$

where R_i is the resistance part, and X_i the reactance part, of the intrinsic impedance. The PTO device that contains the damper is purely passive, which means that there is no other component that generates reactive power flow. Passive loading control is the easiest control method by which to achieve this objective; however, it can nevertheless be seen as a starting point and reference for wave energy absorption. The block diagram for passive loading control is shown in the following figure:

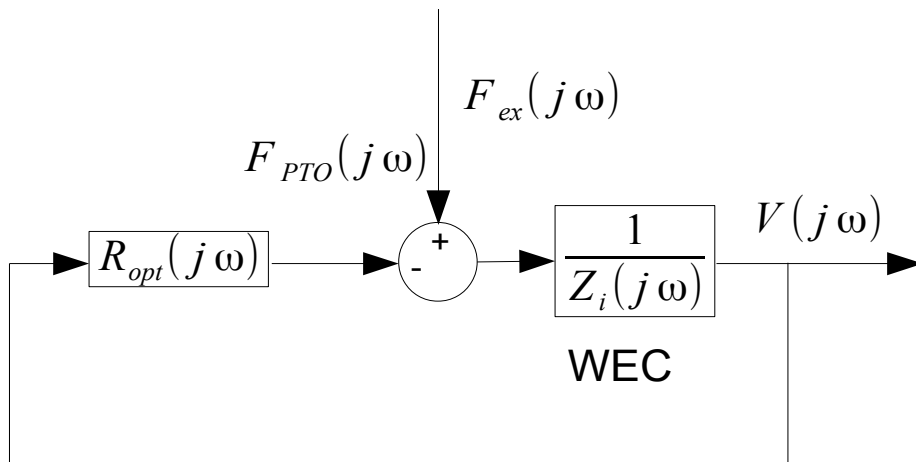


Figure 3.5 Block diagram for passive loading control

Latching control

Latching control is defined as an active method which to achieve the optimal phase between the excitation and the velocity. The optimal phase can be obtained by locking the buoy at zero velocity and releases it at rest of time [25, 54, 68]. It may be considered an alternative means of phase control. In addition, it is an improved solution to the passive loading control.

It can operate in latching and unlatching state with proper timing, with the result that the velocity of the oscillating system will be in phase with the excitation force.

Compared with phase control, latching control locks the damper of the PTO when the velocity equals zero, and releases it at the trough or crest of the wave. As a result, the excitation force remains in phase with the velocity, which corresponds to phase control. It only contains the passive loading during the unlatching stage so that no reactive power will be produced, which is analogous to passive loading control. Whilst it does not produce reactive power, the velocity amplitude will nevertheless remain at zero during the latching stage. The average value of the velocity will be less than the velocity produced under phase control.

The difficulty in implementing the latching control in an effective manner is that it determines the proper timing of the unlatching. The correct time at which to carry out any unlatching can easily be determined when considering only regular waves, as the appropriate instant can be straightforwardly obtained when the next period of the wave elevation is accurately known. Fusco also noted that the timing for the unlatching can be calculated as the half of the wave period, as the velocity increases from zero to a maximum over this time interval.

Another limitation of latching control was raised in [3]. The buoy moves with a freely oscillating motion with a passive damper during the unlatching time interval. As discussed in chapter 2.2.1, if the control damper is quite small, the buoy oscillates at its natural frequency, eventually becoming stable after just a few oscillations. The solution to the problem is to choose a large damper, or force the velocity of the system to be in phase with an excitation force whose frequency is lower than the natural frequency of the system.

The control force for the latching control is given by the following:

$$F_{PTO}(j\omega) = -[R_{pto} + H(j\omega)R_L]V(j\omega) \quad (3.58)$$

$H(j\omega)$ presents two states of control. $H(j\omega) = 0$ indicates the system in its unlatched state, and $H(j\omega) = 1$ indicates the control during the latching time interval. R_L has a very large resistance, which will be added to the control force and will lock the system during latching instants. The block diagram for latching control is shown in figure 3.6.

Latching control is easily implemented, and has no need for any reactive power flow through the machinery; furthermore, it is good for high waves sea state. As mentioned earlier, physical constraint is not considered in this thesis, otherwise latching control could be designed with physical constraints so as to protect the WECs.

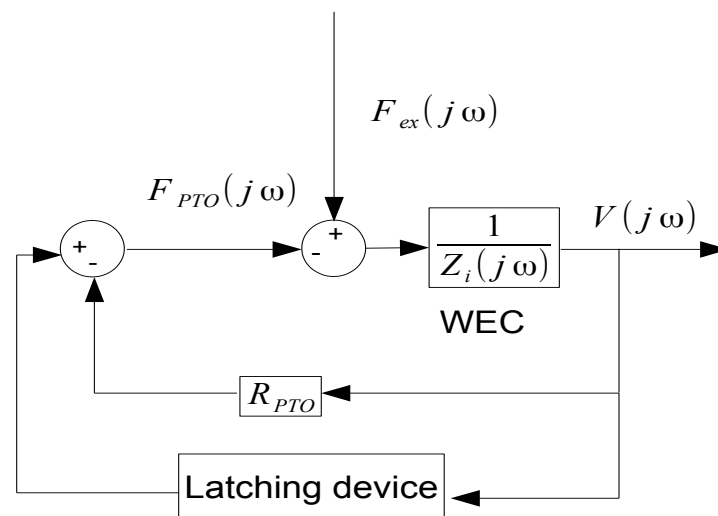


Figure 3.6 Block diagram for latching control

3.5 Chapter summary

This chapter proposes different optimal control conditions for wave energy conversion. The objective of control is to absorb the maximum amount of power from the waves as mechanically possible; however, the efficiency of the WEC also has to be considered.

The analysis and derivation process for optimal control conditions was introduced in section 3.2.1. The dynamics equation described in there is based on a simple mass-damper-spring system. The optimal condition that relates the velocity of the oscillating system to the excitation force is also described in section 3.2.1, where it has been shown that these are in phase when at the optimal resistance. The maximum absorption of power can be obtained under this condition.

In section 3.2.2, a full model for the WEC system has been given. The optimal relationship between the velocity and the excitation force has been found to be when the two are in phase, which is identical to the findings in section 3.2.1. This optimal condition is called the phase control, or amplitude control. Additionally, another optimal condition has been determined to occur when the maximum useful power has been obtained. The optimal control impedance is equal to the complex conjugate of the intrinsic impedance. This is called the complex conjugate control, or reactive control.

However, optimal control conditions cannot be implemented directly in real time as they are non-causal. The difference between causal and non-causal has been discussed in section 3.3, where the reasons for the non-causality of the oscillating system have been presented.

Possible solutions to approximating a non-causal situation with a causal one have also been described.

Real-time implementations of the optimal conditions have been introduced in section 3.4.1 that obtain the maximum absorbed power for different constructions. Solutions for overcoming non-causality problem of the velocity-tracking construction, the feedback construction, and the feedforward construction are very similar. They deal with the issue of non-causality by estimating either the future value of the velocity or the excitation force. Also, the system can be approximated with a second-order transfer function to overcome non-causality. The feedback construction will be used in the following chapters due to its construction is simple. However, the velocity-tracking construction may be good for system with significant non-linearities. The lower level controller of the velocity-tracking construction can be designed to be robust to model uncertainties [39]. The velocity-tracking construction could one of the future researches.

In contrast, there are some other non-optimal controls have been presented in section 3.4.2. One such control is called passive loading control, and contains only a linear damper in the PTO device. The optimal value of the damper is equal to the absolute value of the intrinsic impedance. However, for various reasons there is little point in investigating this mechanism in detail, and is only used here as a point of comparison with the other controllers.

The last control described in this chapter was that of latching control. The latching control pursues the optimal phase between the velocity and the excitation force. This last control and phase control have this characteristic in common. Several limitations were discussed in previous section and not give in detail.

Chapter 4

Prediction of wave elevation

4.1 Chapter overview

As the requirements for overcoming non-causality were discussed in the previous chapter, the present chapter will consider possible solutions to solving this problem. As discussed previously, system approximations and predictions of the velocity of a wave energy conversion system or the excitation force can be used in this manner; however, prediction methods will be the subject of this chapter. The velocity of the oscillating system is the differential of the wave elevation. The prediction should be based on the wave elevation, which can be investigated using a time series.

The predictive approaches used to predict future wave elevations based on present and past values will be presented in this chapter. It is assumed that all values of wave elevation are collected at the same position, though this assumption is only for convenience. There are some other approaches that can measure the wave elevation more precisely; for example, Belmont and Tedd showed how one or more observers can be fixed around the WEC system at a given distance (or distances), and the WEC obtains the real future values from these observers [4, 93]. On the other hand, these methods require external measurement devices which may result in significant additional cost. In addition, the dynamic model becomes numerically complex, as discussed in reference [35].

Three different prediction approaches will be analysed and investigated in this chapter. A brief review of the Pierson-Moskowitz (PM) spectral method will be given in section 4.2.1, which has been used to estimate wave elevation in the past. The least-squares prediction method, which is based on the one step ahead model, will be introduced in section 4.3. The long-range predictive identification method, which is based on the autoregressive model, will be described in section 4.4. The last method that will be considered is multi-step predictive

identification, which will be described in section 4.5. A comparison of these three methods will be given in section 4.6, and a summary of the chapter will be given in section 4.7.

4.2 Wave description and the control force

Waves were simulated using the Pierson-Moskowitz Spectrum, which was described in section 2.1.6. It can be assumed that the waves are collected at the same location. Different values for the sampling frequency and significant wave heights will be examined. Prior to this, however, a brief introduction to the control force will be given because the non-causal kernel forms part of the control force.

4.2.1 Wave description

The objective of the proposed solutions is that of predicting wave elevation. Information about the waves is contained in the wave spectrum. This is used to express how energy is distributed across different frequency components of the wave. It is important to distinguish the characteristics of the wave that may be useful in judging sea states or locations. However, the PM spectrum, which was introduced in section 2.1.5, will be used in this section.

The PM spectrum is constructed using several parameters that can be extracted from information from the waves. One of these parameters is the significant wave height H_s , which was defined in section 2.1.4, and is the average value of the one-third highest waves. It can be also calculated using the *zeroth* moment, that is, the variance of the wave spectrum. The zero-crossing period, T_z , is another important parameter. As defined in section 2.1.4, this only relates to the *0th* and *2nd* spectral moments. It is not linearly proportional to the peak frequency. The peak frequency is also used to describe the PM spectrum with another expression related to the equation shown in table 2.1; it is expressed in terms of the majority of the wave's energy being concentrated around this frequency. A change in peak frequency affects the maximum spectrum value with the same significant wave height, H_z . Fusco also briefly described a high energy wave's peak frequency ω_p as being located at a low frequency and the spectrum of the wave having a narrower spread [33]. The simulation is based on the simulated wave data. However, the fact of the wave energy being concentrated around the low frequencies can also be demonstrated by the PM spectrum simulation. If the significant wave height takes the same value, an increase of peak frequency will result in a flatter spectrum being obtained. As mentioned earlier, the high energy peak frequency ω_p is located at a low frequency. Hence, the low frequency will be the key object of interest.

4.2 Wave description and the control force

Two PM spectrum expressions, each based on different parameters, will be presented in the following section. It should be assumed that the significant wave height, H_z , is fixed at 6 meters herein.

One PM spectrum expression which is based on the PM spectrum equation defined by the peak frequency ω_p in table2.1 gives spectra as follows:

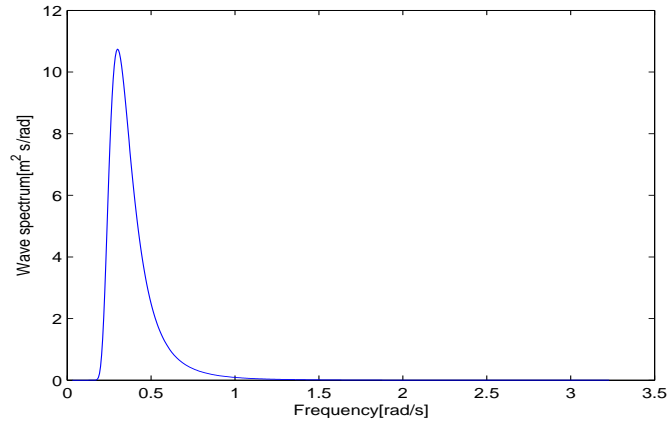


Figure 4.1 Wave spectra calculated using PM spectrum with $\omega_p = 0.3 \text{ rad/s}$

where the peak frequency is calculated as:

$$\omega_p = 2\pi/T_p \quad (4.1)$$

The other PM spectrum expression based on the PM spectrum equation can be defined by H_s and T_z in table2.1 and gives spectra as follows:

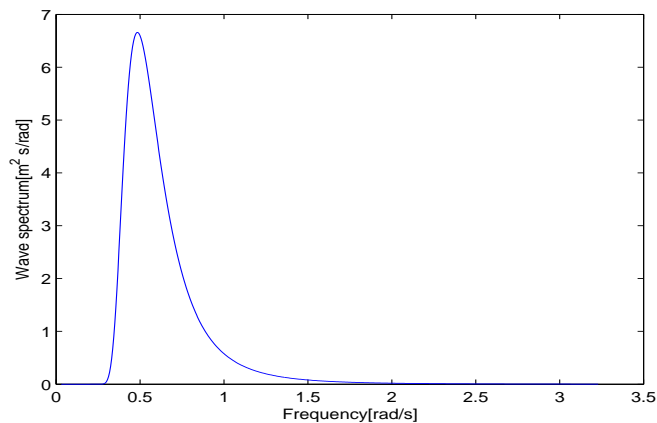


Figure 4.2 Wave spectra calculated by PM spectrum with $T_z = 10 \text{ s}$

4.2 Wave description and the control force

Two more spectra, calculated using different parameter values obtained from each of the two PM expressions, are compared in the figure below:

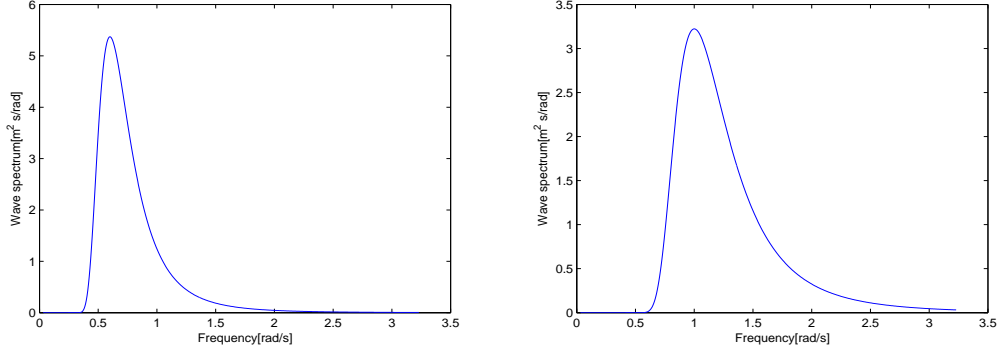


Figure 4.3 Wave spectra calculated using PM spectrum with $\omega_p = 0.6 \text{ rad/s}$ and 1 rad/s

PM spectra with different zero-crossing periods are illustrated in the figure below:

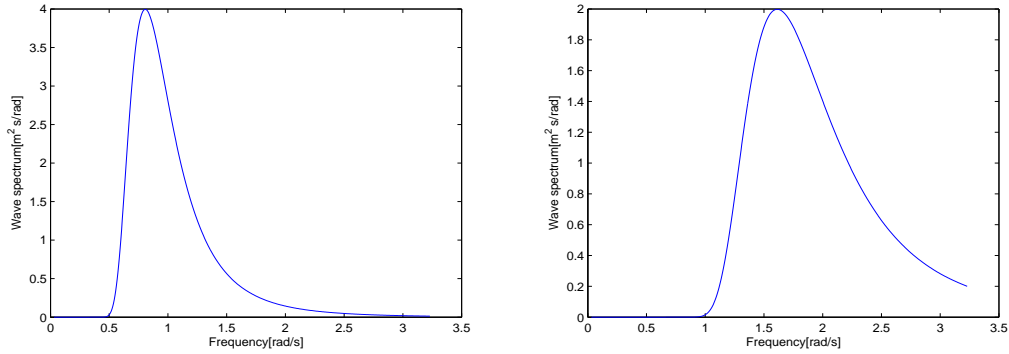


Figure 4.4 Wave spectra calculated by PM spectrum with $T_z = 6 \text{ s}$ and 3 s

As shown in fig4.3, the spectral density decreased as the peak frequency ω_p increased. In contrast, the spectral density increased as the zero-crossing period T_z increased, as presented in fig4.4. Also, the peak frequency decreased as the zero-crossing period T_z increased. It will be of interest to investigate the relationship between the zero-crossing period T_z and the peak frequency ω_p . This relationship between peak frequency ω_p and zero-crossing period T_z can be obtained using PM spectrum defined by ω_p and PM spectrum defined by T_z which shown in table2.1:

$$\omega_p = \left(\frac{8}{5T_z^4} \right)^{\frac{1}{4}} \quad (4.2)$$

4.3 Least-squares system identification and prediction

The effects of the zero-crossing period T_z and the peak frequency ω_p on predictions will be given later in this section.

4.3 Least-squares system identification and prediction

The time domain for the wave elevation was discussed in section 2.2.4. The real wave elevation has been simulated as a superposition of regular waves with different frequencies. The wave elevation equation was given in eq(2.12):

$$\eta(t) = \sum_{i=1}^n A(i) \sin(\omega(i)t + \phi(i)) \quad (4.3)$$

where A is the wave amplitude and n is the number of frequency components. The different frequencies can be obtained by dividing the range of frequencies by a constant interval. Hence, each wave represents a unique frequency with random noise, ϕ .

The autoregressive model has been used because it can deal with time series. The AR model is used to determine the next output value given previous output values [60]. The linear difference equation for wave elevation can be expressed as:

$$\begin{aligned} \eta(t) &= a_1\eta(t-1) + a_2\eta(t-2) + \dots + a_n\eta(t-n) + \phi(t) \\ &= \sum_{i=1}^n (a_i\eta(t-i)) + \phi(t) \end{aligned} \quad (4.4)$$

where ϕ is a random process with zero mean, and a_i are the autoregressive coefficients [19].

This can also be written as:

$$\eta(t) = Y(t)\theta + \phi(t) \quad (4.5)$$

where:

$$\theta = [a_1 \quad a_2 \quad \dots \quad a_n]^T \quad (4.6)$$

$$Y(t) = [\eta(t-1) \quad \eta(t-2) \quad \dots \quad \eta(t-n)] \quad (4.7)$$

$Y(t)$ can be regarded as the signal output vector, n is the model order and θ represents the vectors of the AR coefficients.

4.3 Least-squares system identification and prediction

It is assumed an estimated autoregressive model can be based on past data of the same order as eq(4.4):

$$\eta(t) = \hat{a}_1\eta(t-1) + \hat{a}_2\eta(t-2) + \dots + \hat{a}_n\eta(t-n) + \hat{\phi}(t) \quad (4.8)$$

where \hat{a}_i are the estimated autoregressive coefficients, and $\hat{\phi}(t)$ are the innovations. The estimated value of $\eta(t)$ is given by its past processes:

$$\hat{\eta}(t) = \sum_{i=1}^n (\hat{a}_i\eta(t-i)) \quad (4.9)$$

Hence, the residual [19] between eq(4.8) and eq(4.9) may be obtained:

$$\eta(t) - \hat{\eta}(t) = \hat{\phi}(t) \quad (4.10)$$

Supposing a given model in which the values of the coefficients in vector θ are unknown, there are several methods that can be used to find estimated values for the coefficients with measured outputs, which include the Yule-Walker, Burg and least-squares methods [19]. Details of the least-squares estimation method will be presented in the following section.

The cost function of the LS coefficient estimation can be calculated using the residual, which has been previously obtained:

$$J(\theta) = \sum_{t=1}^N (\eta(t) - \hat{\eta}(t|t-K))^2 \quad (4.11)$$

where N is the number of observed output data and K is the number of predictive steps used for model identification; K is set to be equal to one, which gives a one step ahead LS estimation. $\hat{\eta}(t|t-1)$ is the one step ahead predicted output, as based on past measurements:

$$\begin{aligned} \hat{\eta}(t|t-1) &= [\eta(t-1) \quad \eta(t-2) \quad \dots \quad \eta(t-n)] \cdot \hat{\theta} \\ &= Y(t)\hat{\theta} \end{aligned} \quad (4.12)$$

The coefficient vector, $\hat{\theta}$, can be estimated via the LS method. Initially, a matrix called the autoregressive design matrix is constructed using past measurement vectors at different times, and is given by eq4.13:

$$\Theta = \begin{bmatrix} \eta(t) & \cdots & \eta(t-n+1) \\ \eta(t+1) & \cdots & \eta(t-n) \\ \vdots & \ddots & \vdots \\ \eta(t+N-1) & \cdots & \eta(t+N-n) \end{bmatrix} \quad (4.13)$$

then, the estimated coefficient vector, $\hat{\theta}$, can be expressed as follows:

$$\hat{\theta} = [\Theta^T \Theta]^{-1} \Theta^T \eta \quad (4.14)$$

here, η represents the measured outputs vector, and N is the number of outputs:

$$\eta = [\eta(t+1), \quad \eta(t+2), \quad \dots, \quad \eta(t+N)]^T \quad (4.15)$$

The coefficient vector, $\hat{\theta}$, which is calculated from eq(4.14), can minimise the difference between the observed data, $\eta(t)$, and the estimated data, $\hat{\eta}(t|t-1)$. The optimal value of the coefficient vector, $\hat{\theta}$, for one step ahead prediction can thus be obtained.

Note that $\eta(t)$ is linear and a Gaussian process, and hence is time reversible. An estimated autoregressive model for future wave elevation can be obtained as follows:

$$\hat{\eta}(t+K|t) = \sum_{i=1}^n \hat{a}_i \hat{\eta}(t+K-i|t) \quad (4.16)$$

where K is used to represent the prediction steps. $\hat{\eta}(t+K|t)$ represents the estimate at a time $t+K$, given observations up to time t .

The one step ahead predictor can be calculated in a straightforward manner by shifting eq(4.12) by one step, with the estimated coefficient vector obtained from eq(4.14):

$$\hat{\eta}(t+1|t) = [\eta(t) \quad \eta(t-1) \quad \dots \quad \eta(t-n+1)] \cdot \hat{\theta} \quad (4.17)$$

The two- and three-step predictors are is obtained as:

$$\hat{\eta}(t+2|t) = [\hat{\eta}(t+1|t) \quad \eta(t) \quad \dots \quad \eta(t-n+2)] \cdot \hat{\theta} \quad (4.18)$$

$$\hat{\eta}(t+3|t) = [\hat{\eta}(t+2|t) \quad \hat{\eta}(t+1|t) \quad \dots \quad \eta(t-n+3)] \cdot \hat{\theta} \quad (4.19)$$

4.4 Long-range predictive identification and prediction

The four-step predictor is obtained as:

$$\hat{\eta}(t+4|t) = [\hat{\eta}(t+3|t) \quad \hat{\eta}(t+2|t) \quad \dots \quad \eta(t-n+4)] \cdot \hat{\theta} \quad (4.20)$$

Finally, the K -step predictor can be calculated in a similar manner:

$$\hat{\eta}(t+K|t) = [\hat{\eta}(t+K-1|t) \quad \hat{\eta}(t+K-2|t) \quad \dots \quad \hat{\eta}(t+K-n|t)] \cdot \hat{\theta} \quad (4.21)$$

Note that the algorithm introduced here is based on an off-line estimation; in other words, it requires a set of data from the past. The larger the dataset that can be provided, the more accurate the estimation that can be obtained. However, it would require a certain amount of time for the model to read this past dataset, and it could not be adapted during the control run.

4.4 Long-range predictive identification and prediction

The previous section introduces the means by which the K -steps ahead predictor can be implemented based on the standard one step ahead estimator. However, the wave elevation requires long-range prediction, which means several steps ahead are required. On the other hand, the one step ahead prediction given by the least-squares algorithm cannot predict several steps ahead simultaneously. It is obvious that the LS algorithm may not be an appropriate approach to predicting wave elevation.

An alternative approach by Shook [84], which has been mentioned previously, is called the long-range predictive identification. As the name implies, it is used to deal with the K steps ahead predictor and investigates the entire prediction horizon. The cost function of the long-range predictive estimated coefficient is:

$$J(\theta) = \sum_{t=1}^N \sum_{K=1}^{N2} (\eta(t) - \hat{\eta}(t|t-K))^2 \quad (4.22)$$

where the K range is $[1, 2, \dots, N2]$ and represents the entire prediction horizon, and N is the number of measurement samples. The primary calculation is based on the least-squares method.

Clarke [14, 15] and Rossiter [80] summarised a recursive formula for the above equation:

$$\hat{a}_j^{[K+1]} = (\hat{a}_{j+1}^{[K]} - \hat{a}_1^{[K]} \hat{a}_j^{[1]}) \quad (4.23)$$

4.4 Long-range predictive identification and prediction

where j ranges from 1 to the order of the model, n . Note that the square bracket is used to denote the prediction steps of the predictive model. The K steps ahead predictive equations can be represented as follows:

$$\hat{\eta}(t|t-K) = \hat{a}_1^{[K]} \eta(t-1) + \hat{a}_2^{[K]} \eta(t-2) + \dots + \hat{a}_n^{[K]} \eta(t-n) \quad (4.24)$$

The initial values of \hat{a} are calculated based on eq(4.15) and eq(4.17). This formula only calculates the coefficient vector recursively instead of using the $Y(t)$ signal output matrix to reduce the complexity of the predictor.

Each step for the estimated model equation can be considered by recalling eq(4.24):

$$\begin{aligned} \hat{\eta}(t|t-1) &= [\eta(t-1) \quad \eta(t-2) \quad \dots \quad \eta(t-n)] \cdot \hat{\theta} \\ &= \hat{a}_1^{[1]} \eta(t-1) + \hat{a}_2^{[1]} \eta(t-2) + \dots + \hat{a}_n^{[1]} \eta(t-n) \end{aligned} \quad (4.25)$$

$$\begin{aligned} \hat{\eta}(t|t-2) &= [\hat{\eta}(t-1|t-2) \quad \eta(t-2) \quad \dots \quad \eta(t-n)] \cdot \hat{\theta}2 \\ &= \hat{a}_1^{[2]} \eta(t-1) + \hat{a}_2^{[2]} \eta(t-2) + \dots + \hat{a}_n^{[2]} \eta(t-n) \end{aligned} \quad (4.26)$$

⋮

$$\begin{aligned} \hat{\eta}(t|t-N2) &= [\hat{\eta}(t-N2+1|t-N2) \quad \hat{\eta}(t-N2|t-N2-1) \quad \dots \quad \eta(t-n)] \cdot \hat{\theta}2 \\ &= \hat{a}_1^{[N2]} \eta(t-1) + \hat{a}_2^{[N2]} \eta(t-2) + \dots + \hat{a}_n^{[N2]} \eta(t-n) \end{aligned} \quad (4.27)$$

The first estimated coefficient vector, $\hat{\theta}$, can be calculated using the least-squares method [84]. Note that $\hat{\theta}$ in eq(4.25) is equal to $\hat{\theta}$ in eq(4.12); however, $\hat{\theta}2$ in eq(4.26) and eq(4.27) are not the same as $\hat{\theta}$ in eq(4.25) in the long-range predictive model. The new $\hat{\theta}2$ is calculated by the cost function, eq(4.22).

A more general estimated model can be used to express eq(4.25) to eq(4.27) as follows:

$$\hat{H} = A \cdot H_{past} \quad (4.28)$$

where,

$$\hat{H} = \begin{bmatrix} \hat{\eta}(t|t-1) \\ \hat{\eta}(t|t-2) \\ \vdots \\ \hat{\eta}(t|t-N2) \end{bmatrix}, H_{past} = \begin{bmatrix} \eta(t-1) \\ \eta(t-2) \\ \vdots \\ \eta(t-n) \end{bmatrix}, A = \begin{bmatrix} \hat{a}_1^{[1]} & \dots & \hat{a}_n^{[1]} \\ \hat{a}_1^{[2]} & \dots & \hat{a}_n^{[2]} \\ \vdots & \vdots & \vdots \\ \hat{a}_1^{[N2]} & \dots & \hat{a}_n^{[N2]} \end{bmatrix} \quad (4.29)$$

4.4 Long-range predictive identification and prediction

It can be seen from eq(4.29) that estimated coefficients can be calculated with the recursive formula, eq(4.23). Then, they are multiplied by the same past-values array $[\eta(t-1)\eta(t-2)\cdots\eta(t-n)]$ to obtain the estimate, $\hat{\eta}(t)$.

The prediction process for LRPI is similar to that for the LS method. The AR model is time-reversible, as discussed earlier. The one step ahead predictive equation can be calculated by shifting eq(4.25) one step ahead:

$$\begin{aligned}\hat{\eta}(t+1|t) &= [\eta(t) \quad \eta(t-1) \quad \dots \quad \eta(t-n+1)] \cdot \hat{\theta}_2 \\ &= \hat{a}_1^{[1]}\eta(t) + \hat{a}_2^{[1]}\eta(t-1) + \dots + \hat{a}_n^{[1]}\eta(t-n+1)\end{aligned}\quad (4.30)$$

The two step ahead predictor can be obtained using the same process:

$$\begin{aligned}\hat{\eta}(t+2|t) &= [\hat{\eta}(t+1|t) \quad \eta(t) \quad \dots \quad \eta(t-n+2)] \cdot \hat{\theta}_2 \\ &= \hat{a}_1^{[2]}\eta(t) + \hat{a}_2^{[2]}\eta(t-1) + \dots + \hat{a}_n^{[2]}\eta(t-n+1)\end{aligned}\quad (4.31)$$

Finally, the N_2 steps predictor is equal to:

$$\begin{aligned}\hat{\eta}(t+N_2|t) &= [\hat{\eta}(t+N_2-1|t+N_2-2) \quad \hat{\eta}(t+N_2-2|t+N_2-3) \quad \dots \quad \eta(t-n+3)] \cdot \hat{\theta}_2 \\ &= \hat{a}_1^{[N_2]}\eta(t) + \hat{a}_2^{[N_2]}\eta(t-1) + \dots + \hat{a}_n^{[N_2]}\eta(t-n+1)\end{aligned}\quad (4.32)$$

where the superscript on the coefficient is used to represent which step ahead prediction it is relevant to.

A generalised predictive model can be used to express eq(4.30) to eq(4.32):

$$H_{predict} = A \cdot H \quad (4.33)$$

where,

$$H_{predict} = \begin{bmatrix} \hat{\eta}(t+1|t) \\ \hat{\eta}(t+2|t) \\ \vdots \\ \hat{\eta}(t+N_2|t) \end{bmatrix}, H = \begin{bmatrix} \eta(t) \\ \eta(t-1) \\ \vdots \\ \eta(t-n+1) \end{bmatrix}, A = \begin{bmatrix} \hat{a}_1^{[1]} & \dots & \hat{a}_n^{[1]} \\ \hat{a}_1^{[2]} & \dots & \hat{a}_n^{[2]} \\ \vdots & \vdots & \vdots \\ \hat{a}_1^{[N_2]} & \dots & \hat{a}_n^{[N_2]} \end{bmatrix} \quad (4.34)$$

4.5 Multi-step predictive identification and prediction

The LRPI method contains recursive calculations within the prediction process. The disadvantage of recursive calculations is that any disturbances or errors will accumulate during the process. The prediction model calculations that are based on this method may not be sufficiently accurate for long-term predictions. Haber [41] and Rossiter [81] both discuss another method of estimation for long-range prediction models which is called the Multi Steps Ahead Predictive Identification method.

The main idea behind the MSPI method is very similar to that of LRPI. Their identification process investigates not just one step, but the entire prediction horizon. The main difference with MSPI is that each step in the prediction horizon has an individual model [41]. As a result, the cost function can be written individually for the individual prediction steps, as compared to LRPI:

$$J(\theta_1) = \sum_{t=1}^N (\eta(t) - \hat{\eta}(t|t-1))^2 \quad (4.35)$$

$$J(\theta_2) = \sum_{t=1}^N (\eta(t) - \hat{\eta}(t|t-2))^2 \quad (4.36)$$

⋮

$$J(\theta_{N2}) = \sum_{t=1}^N (\eta(t) - \hat{\eta}(t|t-N2))^2 \quad (4.37)$$

Each cost function can be calculated by referring to the standard one step least-squares estimate, eq(4.12). The current output signal, $\hat{\eta}(t|t-K)$, (where $K \in (1, 2, \dots, N2)$) can be estimated from the estimated coefficient vectors, $\hat{\theta}_1, \hat{\theta}_2, \dots, \hat{\theta}_{N2}$, as:

$$\begin{aligned} \hat{\eta}(t|t-1) &= [\eta(t-1) \quad \eta(t-2) \quad \dots \quad \eta(t-n)] \cdot \hat{\theta}_1 \\ &= \hat{a}_1^{(1)} \eta(t-1) + \hat{a}_2^{(1)} \eta(t-2) + \dots + \hat{a}_n^{(1)} \eta(t-n) \end{aligned} \quad (4.38)$$

$$\begin{aligned} \hat{\eta}(t|t-2) &= [\eta(t-2) \quad \eta(t-3) \quad \dots \quad \eta(t-n-1)] \cdot \hat{\theta}_2 \\ &= \hat{a}_1^{(2)} \eta(t-2) + \hat{a}_2^{(2)} \eta(t-3) + \dots + \hat{a}_n^{(2)} \eta(t-n-1) \end{aligned} \quad (4.39)$$

⋮

$$\begin{aligned} \hat{\eta}(t|t-N2) &= [\eta(t-N2) \quad \eta(t-N2-1) \quad \dots \quad \eta(t-N2-n+1)] \cdot \hat{\theta}_{N2} \\ &= \hat{a}_1^{(N2)} \eta(t-N2) + \hat{a}_2^{(N2)} \eta(t-N2-1) + \dots + \hat{a}_n^{(N2)} \eta(t-N2-n+1) \end{aligned} \quad (4.40)$$

4.5 Multi-step predictive identification and prediction

Solutions for estimated coefficients in eq(4.38), eq(4.39), and eq(4.40) may be expressed as follows:

$$\underbrace{\begin{bmatrix} \eta(t) \\ \eta(t-1) \\ \vdots \\ \eta(t-N) \end{bmatrix}}_{\Theta_1} = \underbrace{\begin{bmatrix} \eta(t-1) & \eta(t-2) & \cdots & \eta(t-n) \\ \eta(t-2) & \eta(t-3) & \cdots & \eta(t-n-1) \\ \vdots & \vdots & \vdots & \vdots \\ \eta(t-N-1) & \eta(t-N-2) & \cdots & \eta(t-N-n) \end{bmatrix}}_{\Theta_1} = \begin{bmatrix} \hat{a}_1^{(1)} \\ \hat{a}_2^{(1)} \\ \vdots \\ \hat{a}_n^{(1)} \end{bmatrix} \quad (4.41)$$

$$\underbrace{\begin{bmatrix} \eta(t) \\ \eta(t-1) \\ \vdots \\ \eta(t-N) \end{bmatrix}}_Y = \underbrace{\begin{bmatrix} \eta(t-2) & \eta(t-3) & \cdots & \eta(t-n-1) \\ \eta(t-3) & \eta(t-4) & \cdots & \eta(t-n-2) \\ \vdots & \vdots & \vdots & \vdots \\ \eta(t-N-2) & \eta(t-N-3) & \cdots & \eta(t-N-n-1) \end{bmatrix}}_{\Theta_2} = \begin{bmatrix} \hat{a}_1^{(2)} \\ \hat{a}_2^{(2)} \\ \vdots \\ \hat{a}_n^{(2)} \end{bmatrix} \quad (4.42)$$

and:

$$\underbrace{\begin{bmatrix} \eta(t) \\ \eta(t-1) \\ \vdots \\ \eta(t-N) \end{bmatrix}}_Y = \underbrace{\begin{bmatrix} \eta(t-N2) & \eta(t-N2-1) & \cdots & \eta(t-N2-n+1) \\ \eta(t-N2-1) & \eta(t-N2-2) & \cdots & \eta(t-N2-n) \\ \vdots & \vdots & \vdots & \vdots \\ \eta(t-N2-N) & \eta(t-N2-N-1) & \cdots & \eta(t-N2-N-n+1) \end{bmatrix}}_{\Theta_{N2}} = \begin{bmatrix} \hat{a}_1^{(N2)} \\ \hat{a}_2^{(N2)} \\ \vdots \\ \hat{a}_n^{(N2)} \end{bmatrix} \quad (4.43)$$

where:

$$\hat{\theta}_1 = \begin{bmatrix} \hat{a}_1^{(1)} \\ \hat{a}_2^{(1)} \\ \vdots \\ \hat{a}_n^{(1)} \end{bmatrix}, \hat{\theta}_2 = \begin{bmatrix} \hat{a}_1^{(2)} \\ \hat{a}_2^{(2)} \\ \vdots \\ \hat{a}_n^{(2)} \end{bmatrix}, \text{ and } \hat{\theta}_{N2} = \begin{bmatrix} \hat{a}_1^{(N2)} \\ \hat{a}_2^{(N2)} \\ \vdots \\ \hat{a}_n^{(N2)} \end{bmatrix} \quad (4.44)$$

Note that the bracket in $\hat{a}_n^{(K)}$ is also used to denote the predictive steps of the prediction model. **The main difference between MSPI and LRPI can be described as follows: in MSPI, there is no relationship between each $\hat{a}_n^{(K)}$. They do not follow the recursive formula, eq(4.23). In contrast, each $\hat{a}_j^{[K]}$ of LRPI follows the recursive relationship eq(4.23).**

4.5 Multi-step predictive identification and prediction

Hence, the bracket is used instead of the square bracket for clarity. Calculations of $\hat{\theta}_1$, $\hat{\theta}_2$, and $\hat{\theta}_{N2}$ are based on the least-squares method, eq(4.14):

$$\hat{\theta}_1 = [\Theta_1^T \Theta_1]^{-1} \Theta_1^T Y \quad (4.45)$$

$$\hat{\theta}_2 = [\Theta_2^T \Theta_2]^{-1} \Theta_2^T Y \quad (4.46)$$

$$\hat{\theta}_{N2} = [\Theta_{N2}^T \Theta_{N2}]^{-1} \Theta_{N2}^T Y \quad (4.47)$$

It can be seen that no recursive calculation has been used in multi steps predictive identification. Estimated coefficients are calculated directly with the least-squares method.

The past and present data have been evaluated via the previous equation. The K steps ahead predictor can be obtained, as based on the current data and past data. The one step ahead predictor can be obtained by shifting eq(4.38) one step ahead:

$$\begin{aligned} \hat{\eta}(t+1|t) &= [\eta(t) \quad \eta(t-1) \quad \dots \quad \eta(t-n)] \cdot \hat{\theta}_1 \\ &= \hat{a}_1^{(1)} \eta(t) + \hat{a}_2^{(1)} \eta(t-1) + \dots + \hat{a}_n^{(1)} \eta(t-n) \end{aligned} \quad (4.48)$$

The two steps ahead predictor can be obtained by shifting eq(4.39) two steps ahead:

$$\begin{aligned} \hat{\eta}(t+2|t) &= [\eta(t) \quad \eta(t-1) \quad \dots \quad \eta(t-n)] \cdot \hat{\theta}_2 \\ &= \hat{a}_1^{(2)} \eta(t) + \hat{a}_2^{(2)} \eta(t-1) + \dots + \hat{a}_n^{(2)} \eta(t-n) \end{aligned} \quad (4.49)$$

Finally, the K steps ahead predictor can be obtained when $K = N2$:

$$\begin{aligned} \hat{\eta}(t+N2|t) &= [\eta(t) \quad \eta(t-1) \quad \dots \quad \eta(t-n)] \cdot \hat{\theta}_{N2} \\ &= \hat{a}_1^{(N2)} \eta(t) + \hat{a}_2^{(N2)} \eta(t-1) + \dots + \hat{a}_n^{(N2)} \eta(t-n) \end{aligned} \quad (4.50)$$

All of these predictors can be estimated at the same time due to the measured output signals $[\eta(t) \quad \eta(t-1) \quad \dots \quad \eta(t-n+1)]$ being the same. This is different from the LRPI method, as this observes the entire prediction horizon. The MSPI method is expected to provide better results than LRPI. Each step predictor is calculated with the least-squares method rather than the K steps recursive calculation in LRPI.

The major drawback of the MSPI method is that it is much more computationally expensive than the LRPI method. Parameters or called coefficients increase as the prediction horizon increases. Several models have to be calculated simultaneously; however, each

model calculated with the least-squares method can be expected to give higher accuracy results when compared to the recursive least-squares method.

4.6 Comparison of different predictive approaches

The predictive approaches that have been introduced previously can be tested with simulated wave datasets. A different setting for the peak frequency and the significant wave height can simulate different sea states through the PM spectrum. Wave spectra with different peak frequencies have been described in section 4.2.1.

In the beginning, a standard has to be set by which to judge the performance of the predictive approaches. A method called Efron's Pseudo-R-squared has been used to measure the predictions' accuracies. Lave and Efron proposed different datasets that can be measured in standard regression and analysis of variance. The equation is presented as follows [12, 49]:

$$R(K) = 100 \cdot \left(1 - \frac{\sum_{t=1}^N (y(t+K) - \hat{y}(t+K|t))^2}{\sum_{t=1}^N (y(t+K) - \bar{y}(t+K))^2} \right) \quad (4.51)$$

where N is the number of observations, $y(t+K)$ is the measured wave elevation and $\hat{y}(t+K|t)$ is the estimated wave elevation, which is computed via different predictive approaches. The bar above y indicates the mean wave elevation. The equation measures the difference between measured data and estimated data, which is expressed as a percentage. 100% of $R(K)$ means that the K steps ahead estimated wave elevation corresponds perfectly to the measured wave elevation.

A low-pass filter is used in an attempt to focus on the high-energy region of the wave spectrum[33]. Hence, the application of a low-pass filter to the wave signal should be considered.

Case 1

We assume the significant wave height to be 6 meters and that the zero-crossing period is 10 seconds. ω ranges from 0.03 to 3.23 *rad/sec*. The PM spectrum is presented in fig4.5, and a comparison of the prediction accuracy of the LS, LRPI and MSPI methods is given in the figure4.6.

Where the prediction steps have been set to 15 and the sample frequency to 2.5641. As the figure4.6 shows, the three prediction methods have similar performances over the first few steps. The differences become apparent after 6 steps. With six steps ahead prediction

4.6 Comparison of different predictive approaches

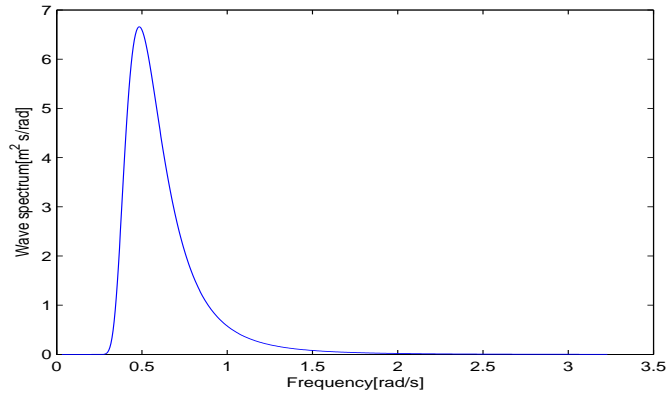


Figure 4.5 PM spectrum with $H_{1/3} = 6m$ and $T_z = 10s$

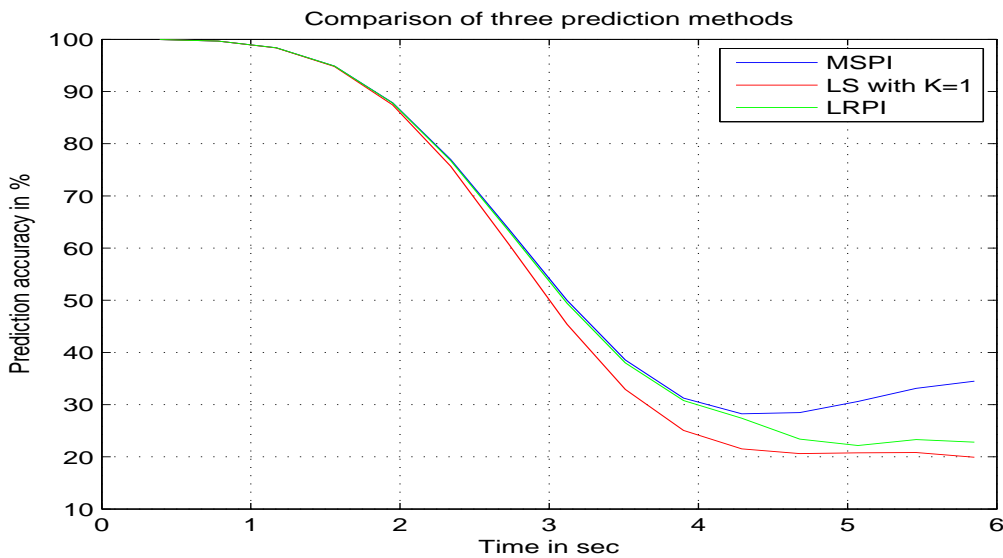


Figure 4.6 The prediction accuracy with $H_{1/3} = 6m$ and $T_z = 10s$

($\approx 1.95sec$), three of the prediction methods can obtain more than 85% prediction accuracy. In the last, the estimated wave elevation calculated by the MSPI method obtained only 34% prediction accuracy with 15 steps ahead prediction ($\approx 5.85sec$). The LRPI method can obtain about 23% prediction accuracy which with 15 steps ahead prediction ($\approx 5.85sec$), whilst the LS method can obtain about 20% prediction accuracy which with 15 steps ahead prediction ($\approx 5.85sec$). Hence, the MSPI method has the best performance of the three methods. LRPI performs better than the LS method, the latter being based on the one step ahead estimation. As shown in fig4.6, a longer prediction horizon and the differences in the predicted accuracies between the three prediction methods will be presented. Any disturbance

4.6 Comparison of different predictive approaches

or error will accumulate in the recursive calculations (LS and LRPI) for the longer prediction horizon. These performance results meet the expectations discussed in previous sections.

A comparison of measured and estimated wave elevations is also given in the figure 4.7, 4.8, and 4.9:

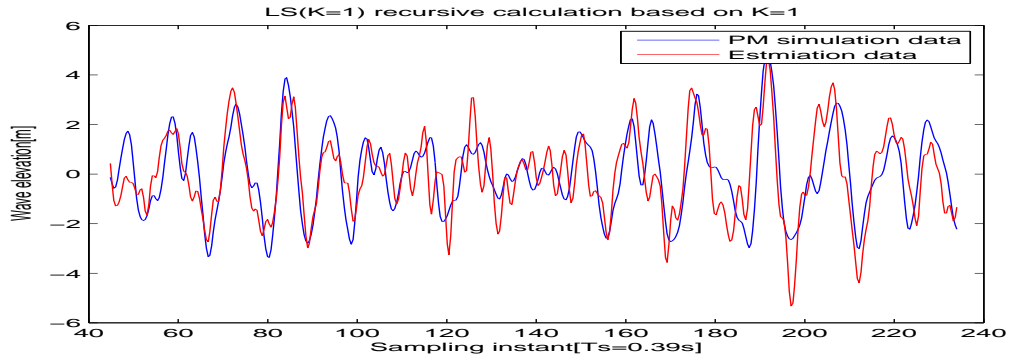


Figure 4.7 Wave elevation estimation with the LS method

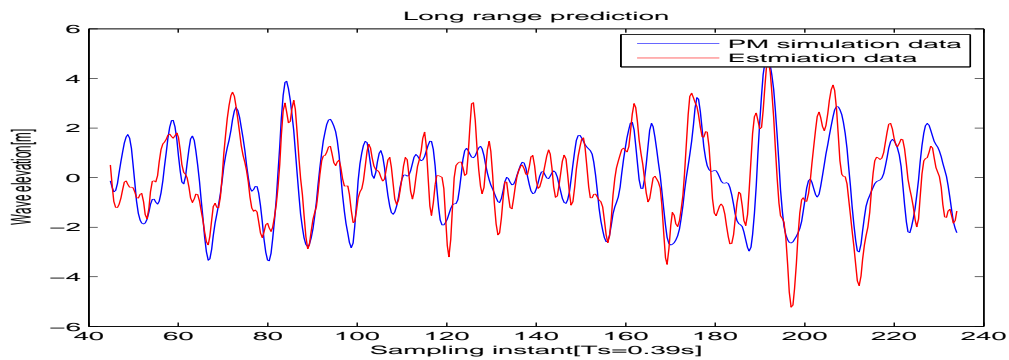


Figure 4.8 Wave elevation estimation with the LRPI method

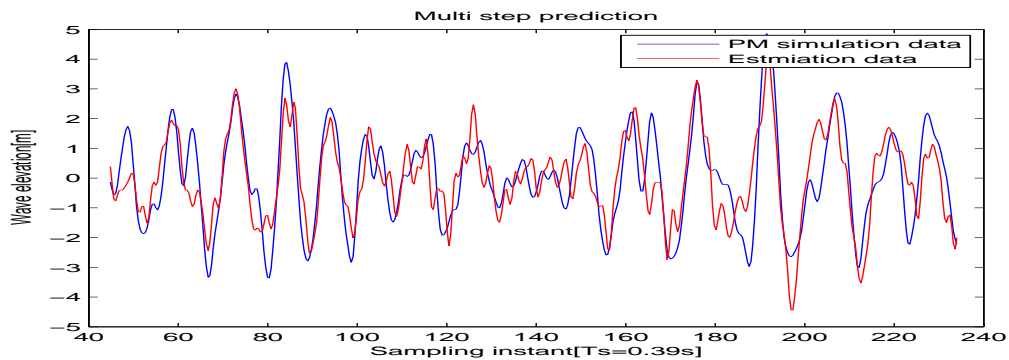


Figure 4.9 Wave elevation estimation with the MSPI method

4.6 Comparison of different predictive approaches

Case 2

As can be seen from fig4.6, the most energy is stored in the spectrum over the range $0.3rad/s$ to $1.2rad/s$. It is interesting to investigate the performance of predictive approaches under these conditions. The significant wave height and the zero-crossing period are kept the same as before. Assuming an ideal band-pass filter is applied to the wave signal, a lower cut-off frequency of $0.3rad/s$ and a higher cut-off frequency of $1.2rad/s$ will be applied. Hence, a comparison of the predictive accuracy of the three prediction approaches can be given as follows:

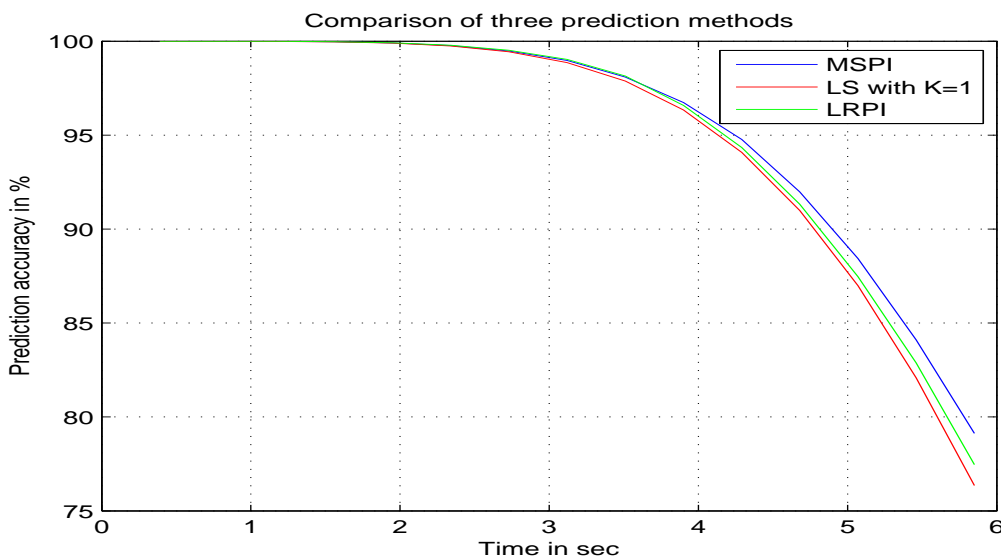


Figure 4.10 The prediction accuracy including an ideal band-pass filter over the range $0.3rad/s$ to $1.2rad/s$

It can be seen from the figure4.10 that the performance of the prediction approaches has greatly improved. All the prediction approaches can obtain 80% accuracy with 13 steps ahead prediction ($\approx 5.07sec$). In comparison, prediction accuracy dies away quickly after five steps ahead prediction ($\approx 1.95sec$) in the instance of 0.03 to 3.23 rad/sec . The LS prediction method can only obtain 20% accuracy with 10 steps ahead prediction ($\approx 3.9sec$) with a spectrum in the 0.03 to 3.23 rad/sec range. The LRPI prediction method's performance was almost identical to that of the LS method, with 10 steps ahead prediction shown in fig4.6. Even the MSPI can only obtains 30% accuracy with 10 steps ahead prediction, as per fig4.6. In fig4.10, the MSPI method can still be seen to have the greatest prediction accuracy compared to the other two methods. The performance of LRPI is slightly better than that of

4.6 Comparison of different predictive approaches

LS. High-frequency wave components have been filtered out in fig4.10. The lesser influence of wave non-linearity results in a better prediction accuracy in fig4.10 [91].

The time domains of the estimated wave elevation and estimated wave elevation with different prediction approaches are given as:

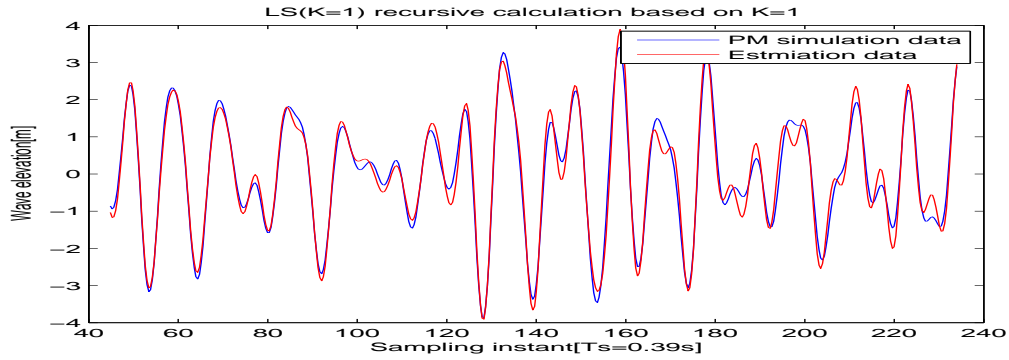


Figure 4.11 Wave elevation estimation using the LS method

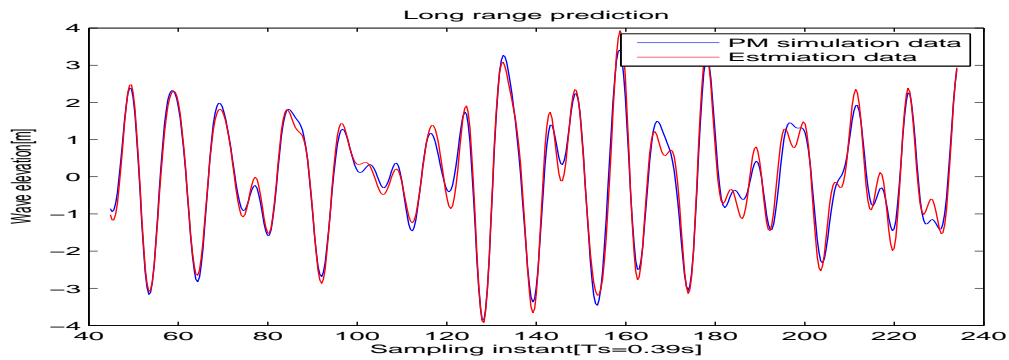


Figure 4.12 Wave elevation estimation using the LRPI method

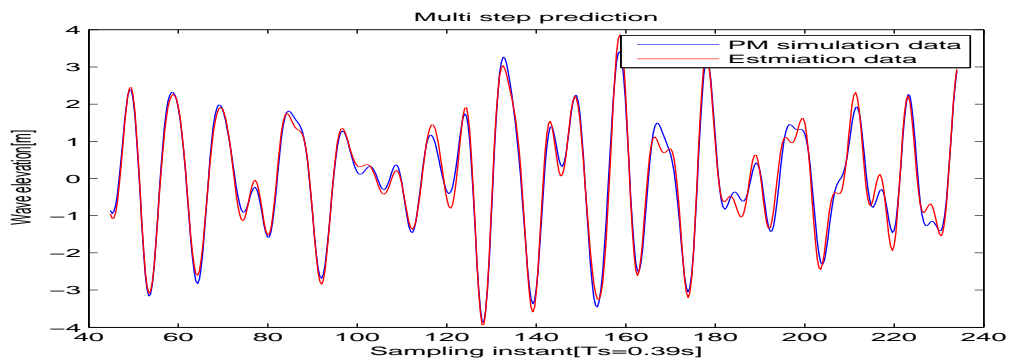


Figure 4.13 Wave elevation estimation using the MSPI method

4.6 Comparison of different predictive approaches

All of the estimated wave elevations almost overlap with the measured wave elevations. Estimated wave elevations fit the measured wave elevations much better than those in figs 4.7, 4.8, and 4.9.

Case 3

Assuming the same PM spectrum has been used, and an ideal low-pass filter with a cut-off frequency equal to the peak frequency of 0.48 rad/s , a comparison of the prediction accuracy for the three prediction approaches can be given as follows:

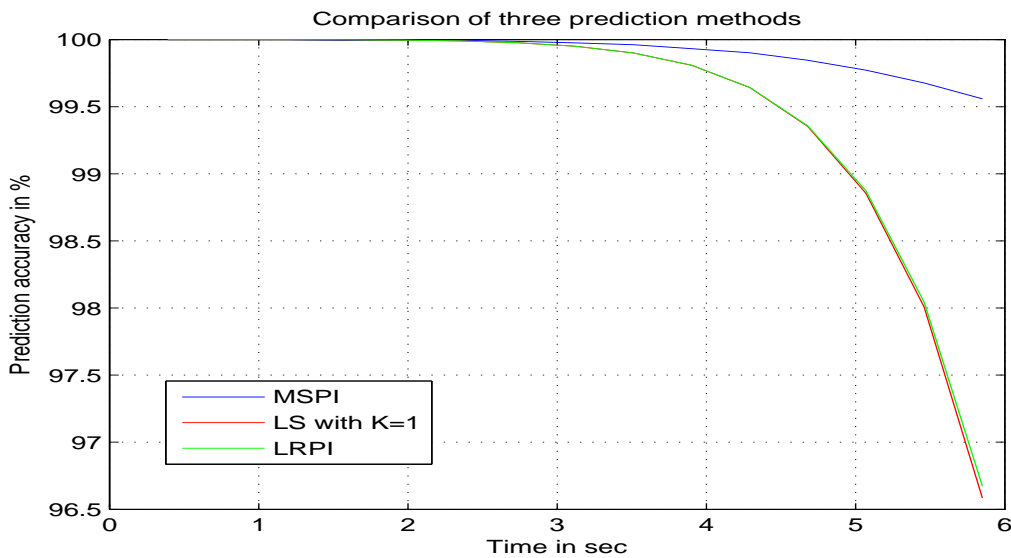


Figure 4.14 The prediction accuracy with an ideal low-pass filter

The MSPI method obtained more than 99.5% prediction accuracy with 13 steps ahead prediction ($\approx 5.07 \text{ sec}$). The prediction accuracies of the LS method and LRPI methods die out very quickly for the 13 steps ahead prediction; also, the LRPI method does not show any particular benefit compared to the LS method. However, they both still obtain 98.9% prediction accuracy for 13 steps ahead prediction, but the prediction accuracy of the MSPI method is, clearly, significantly better than these latter two methods, however. On the other hand, the result shown in fig 4.14 demonstrates that prediction methods that use high-energy waves show better performance.

As expected, the estimated wave elevations should be very close to the measured wave elevations with the low-pass filter in place:

4.6 Comparison of different predictive approaches

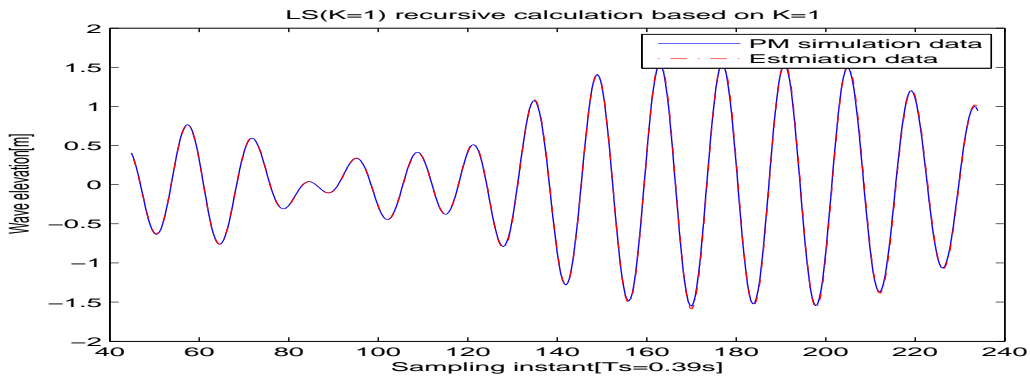


Figure 4.15 Wave elevation estimation using the LS method

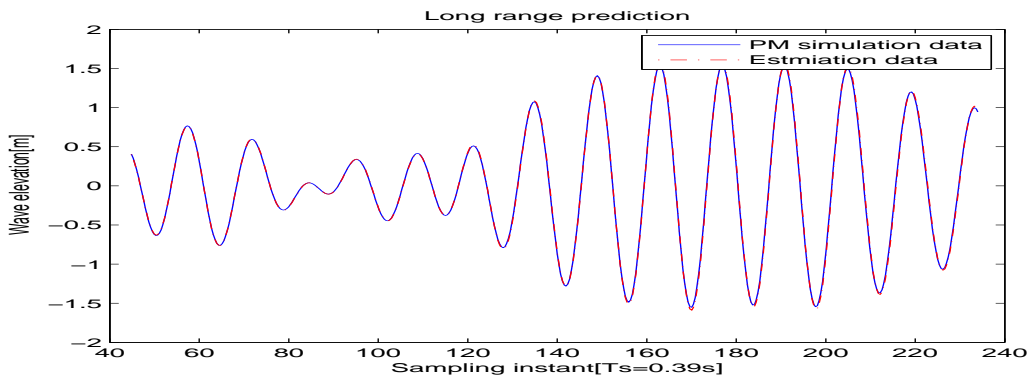


Figure 4.16 Wave elevation estimation using the LRPI method

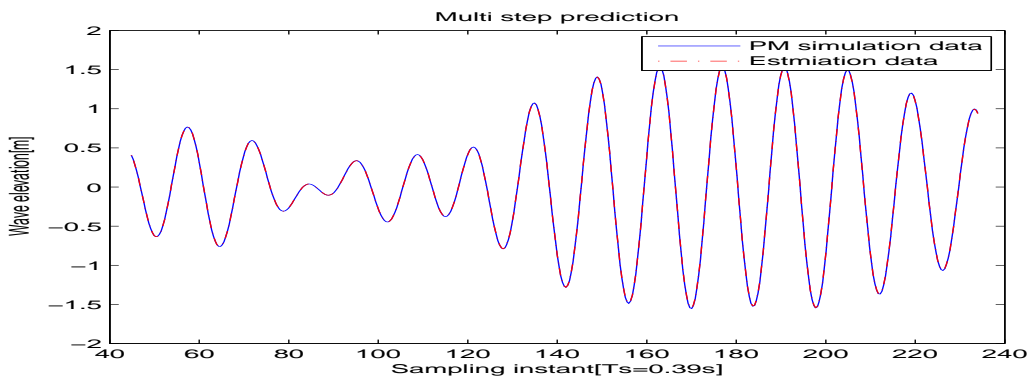


Figure 4.17 Wave elevation estimation using the MSPI method

Case 4.1 and 4.2

Reviewing section 4.2.1, different values of the zero-crossing period and the peak frequency can effect the PM spectrum. As a result, the prediction accuracy should change as well.

4.6 Comparison of different predictive approaches

Wave spectra calculated from PM spectra with zero-crossing periods equal to 6s and 3s should be compared:

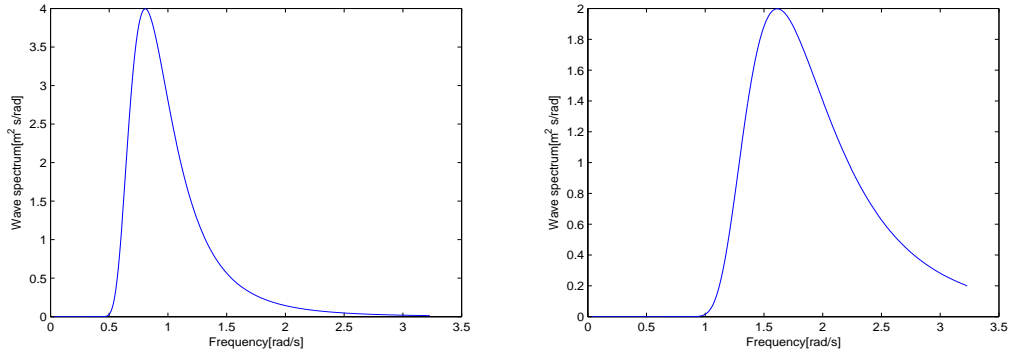


Figure 4.18 Wave spectra calculated from PM spectra with $T_z = 6s$ and $3s$

It can be seen from fig.4.18 that the peak frequency of the PM spectrum with $T_z = 6s$ is lower than the that with $T_z = 3s$. Also, the spectral distribution of the wave spectrum with $T_z = 6s$ is much narrower than the spectrum with $T_z = 3s$. As mentioned earlier, the majority of the wave energy is concentrated over the low-frequency wave components. Prediction methods show better performance with high energy waves, as demonstrated earlier.

The prediction accuracies of the three prediction methods with 6s and 3s zero-crossing periods are compared below:

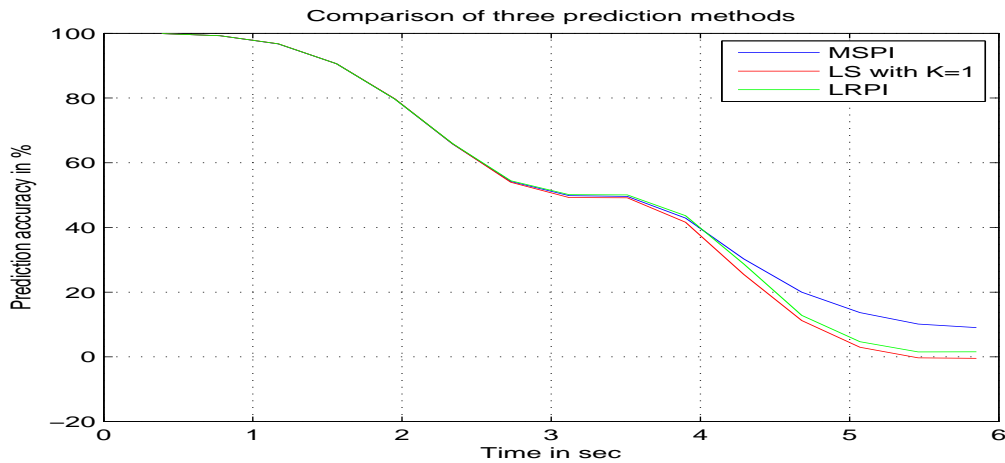


Figure 4.19 Prediction with a 6s zero-crossing period

If the zero-crossing period decreases to 3s, then the prediction accuracies of three prediction approaches can be given as figure4.20:

4.6 Comparison of different predictive approaches

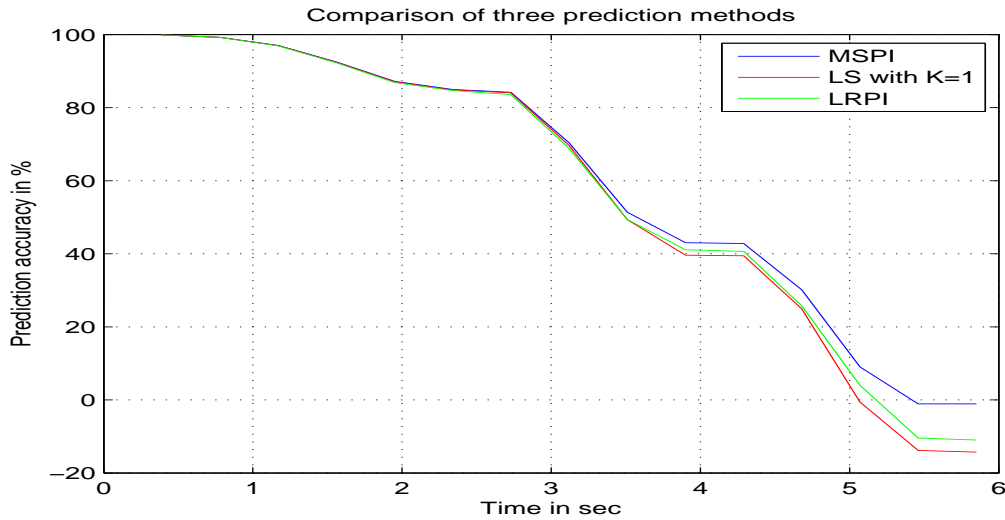


Figure 4.20 Prediction with a 3s zero-crossing period

The prediction accuracy was found to decrease as the value of the zero-crossing period decreased. The MSPI method was found to obtain 10% accuracy with 13 steps ahead prediction and the 6s zero-crossing period wave spectrum. In contrast, the MSPI method obtained 0% accuracy with 13 steps ahead prediction and the 3s zero-crossing period wave spectrum. The other two prediction methods show worse prediction accuracies than the MSPI method. This is a consequence of the results obtained in section 4.2.1. The peak frequency was found to increase when the value of the zero-crossing period decreased, as shown in fig4.18. Hence, the wave spectrum with the higher frequency cannot produce the same prediction accuracy as the one with the lower frequency.

Case 5.1 and 5.2

In section 4.2.1, PM spectra with different peak frequencies were presented. As mentioned earlier, the prediction accuracy can be affected by a change in peak frequency. A comparison of spectra with different peak frequencies is given in fig4.21.

It can be seen from fig4.21 that the wave spectral distribution with $\omega_p = 0.6rad/s$ is more concentrated at the lower frequencies than the one with $\omega_p = 1rad/s$. Also, the wave spectrum value with $\omega_p = 0.6rad/s$ is larger than that for $\omega_p = 1rad/s$. The prediction methods can be expected to show better prediction accuracy with $\omega_p = 0.6rad/s$.

The prediction accuracies of the three prediction approaches with a $0.6rad/s$ peak frequency are shown in figure4.22.

4.6 Comparison of different predictive approaches

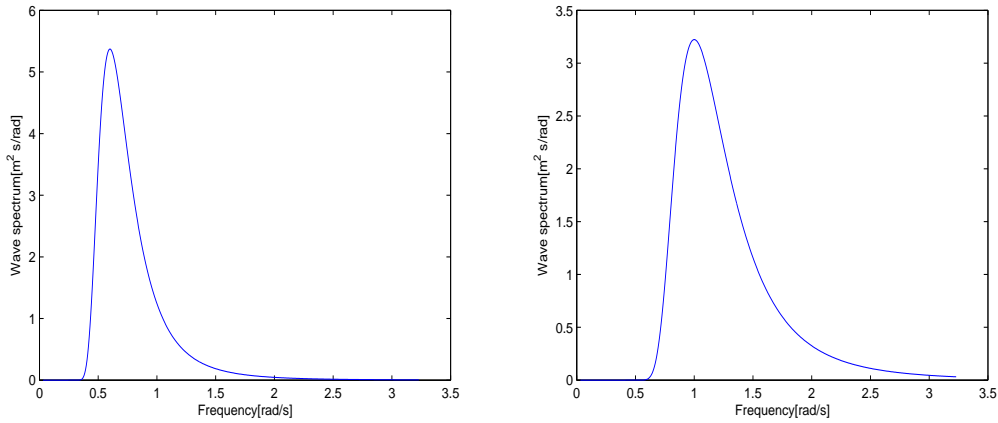


Figure 4.21 Wave spectra calculated with PM spectra with $\omega_p = 0.6 \text{ rad/s}$ and 1 rad/s

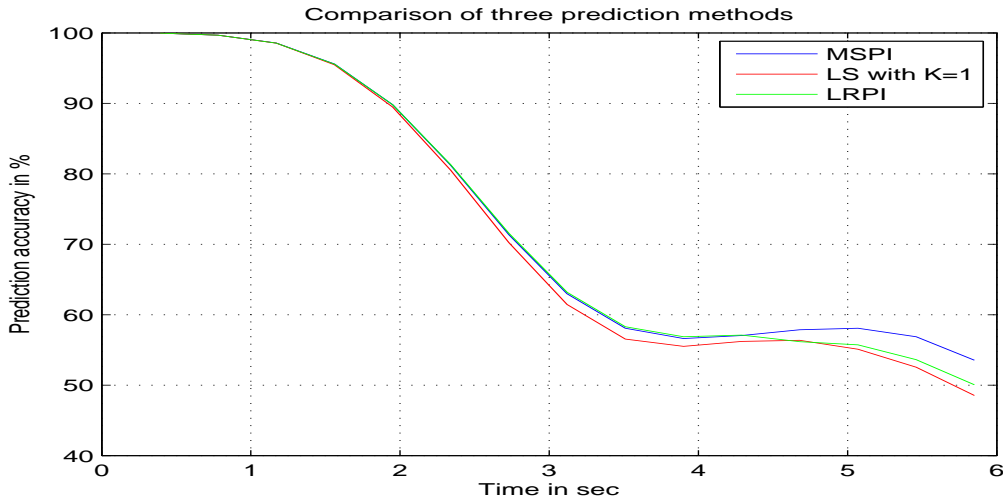


Figure 4.22 Prediction with a 0.6 rad/s peak frequency

Also, the prediction accuracies of the three prediction approaches with the 1 rad/s peak frequency are given in figure 4.23.

Following fig 4.22 and fig 4.23, the prediction accuracy decreased when the peak frequency increased. It can be seen from fig 4.22 and fig 4.23 that the prediction accuracy obtained with the 0.6 rad/s wave spectrum is considerably better than the one at 1 rad/s . All prediction methods can obtain about 50% accuracy with 13 steps ahead prediction. In contrast, they can only obtain about 0% to 10% accuracy with 13 steps ahead prediction. The prediction accuracy again shows that the majority of the energy is stored in the low-frequency region.

4.6 Comparison of different predictive approaches

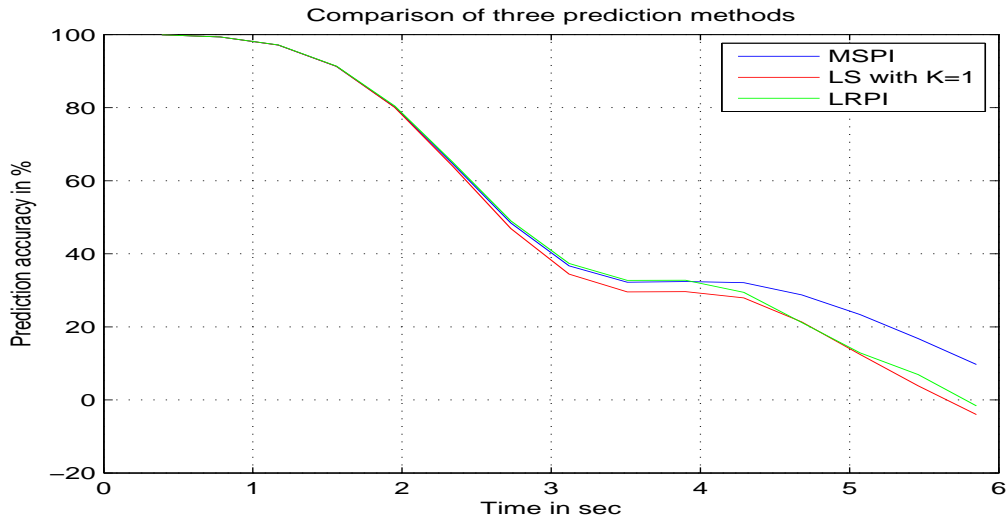


Figure 4.23 Prediction with a 1rad/s peak frequency

4.6.1 Model Order Selection

As mentioned in section 4.3, any present estimated wave elevation depends on past observations and coefficients. The number of coefficients will affect the accuracy of the present estimated wave elevation. The number of coefficients also relates to the model order in the autoregressive model. The choice of model order has to be considered carefully, as too large value for the model order may make the model overly complex, whilst too small value may unnecessarily reduce the accuracy of the estimated model. Usually, maximum likelihood is used to choose the order of a model by statisticians. However, this is only choosing the highest possible order for a model that seems to fit observations well; this may still make the model too complex and unwieldy.

Fusco proposed the Akaike information criterion (AIC) and Bayesian information criterion (BIC) to find the appropriate order for the autoregressive model[36].

The AIC criterion was introduced by Akaike in 1974 [1]:

$$AIC = \log(\|J\|^2) + (n + 1) \frac{2}{N} \quad (4.52)$$

where J is the prediction error between the measured data and the estimated data, n is the model order or the number of coefficients, and N is the number of observations. Akaike suggested maximising the value of the likelihood function for each model, after which the most suitable model order can be chosen with the minimum AIC value [82].

4.6 Comparison of different predictive approaches

The BIC criterion was described by Schwarz in 1978 [82]. BIC is closely related to AIC; the only difference is that it generally penalises free parameters (N) more strongly than AIC. It may be given as follows:

$$BIC = \log(\|J\|)^2 + (n + 1) \frac{\log(N)}{N} \quad (4.53)$$

Assuming the significant wave height and the zero-crossing period are fixed at 6 meters and 6s, the prediction steps K vary from 1,5,10,20,40. The wave signal with an ideal band-pass filter has been discussed previously. The results are given as follows:

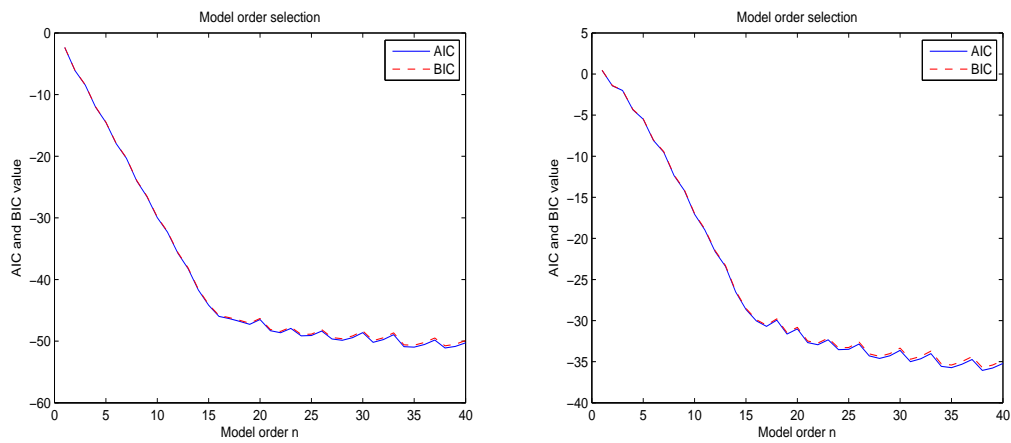


Figure 4.24 AIC and BIC with one step and five steps ahead prediction

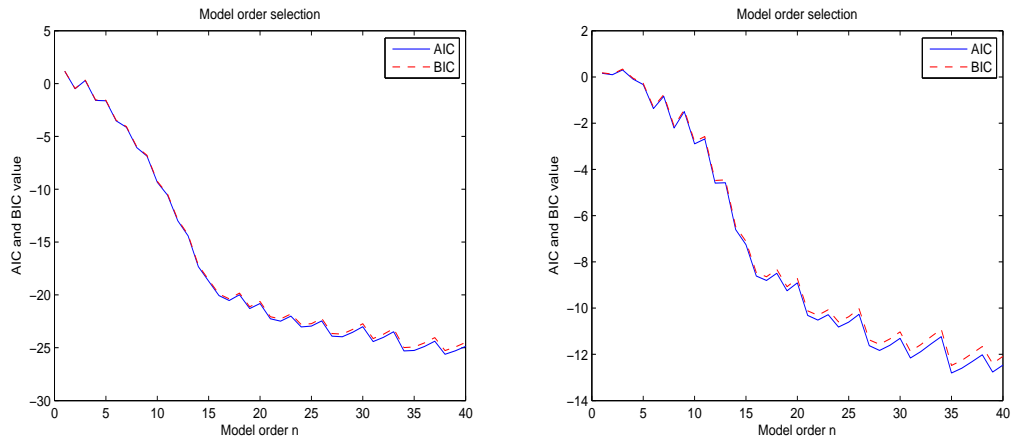


Figure 4.25 AIC and BIC with 10 steps and 20 steps ahead prediction

As figures 4.24, 4.25, and 4.26 show, the performances of AIC and BIC are very similar. Most models return accurate predictions with a large order ranging from 15 to 40. However,

4.6 Comparison of different predictive approaches

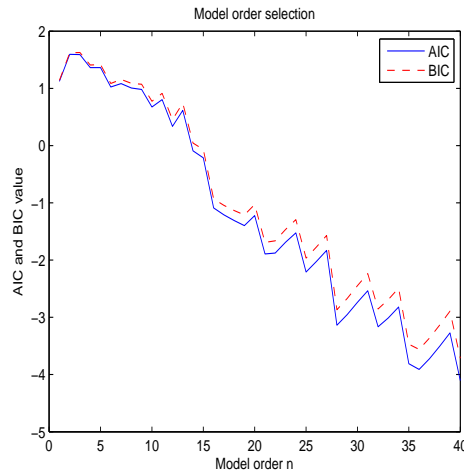


Figure 4.26 AIC and BIC with 40 steps ahead prediction

AIC and BIC cannot obtain accurate predictions when the number of prediction steps is larger than 20.

The choice of range of frequencies will affect the prediction accuracy of the prediction method, as demonstrated previously. If an ideal low-pass filter at $0.48\text{rad}/s$ is applied to the wave signal, the results for AIC and BIC can be obtained as figure 4.27, 4.28 and 4.29:

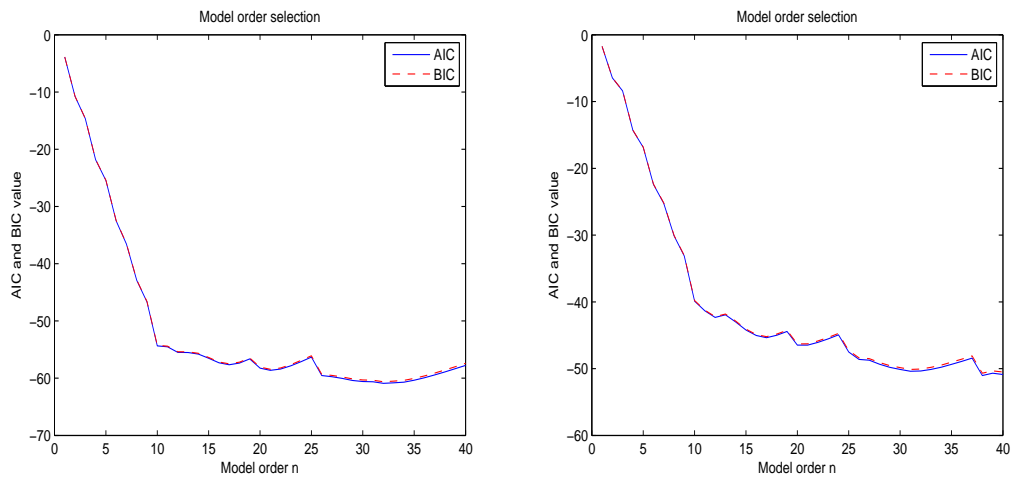


Figure 4.27 AIC and BIC with one step and five steps ahead prediction

It can be seen that the performance of AIC and BIC has been improved greatly. Predictions with one and five steps ahead were found to return good results with model orders larger than 10. Orders larger than 15 are needed in the previous case. The AIC and BIC can still return accurate predictions with K larger than 20 when the model order is larger than 20. They even have acceptable prediction accuracies when the model order is larger than 30 and

4.6 Comparison of different predictive approaches

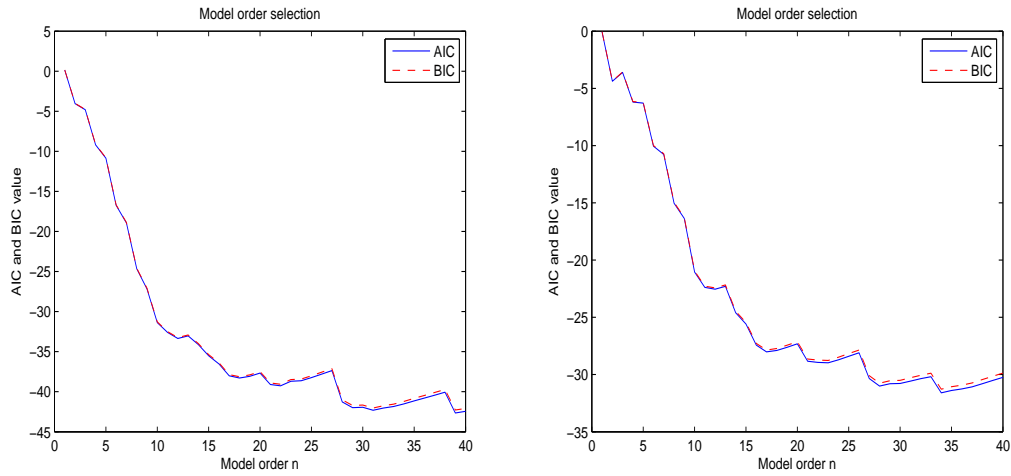


Figure 4.28 AIC and BIC with 10 steps and 20 steps ahead prediction

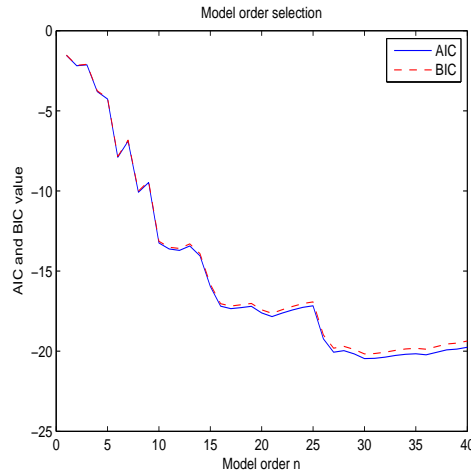


Figure 4.29 AIC and BIC with 40 steps ahead prediction

prediction steps are larger than 40. Model order can be reduced greatly for short-time (one to five steps) predictions. Mid-range time (10 to 20 steps) predictions can be dealt with through reduced-order AR models. Only long-time predictions require high-order AR models.

Hence, eq(4.51) should be recalled to investigate the effects of changing the model order. The model order will be chosen from 10, 20, and 30, and the results for each will be compared.

Case 6

The prediction accuracies of different prediction approaches with model order 10 are shown in figure4.30:

4.6 Comparison of different predictive approaches

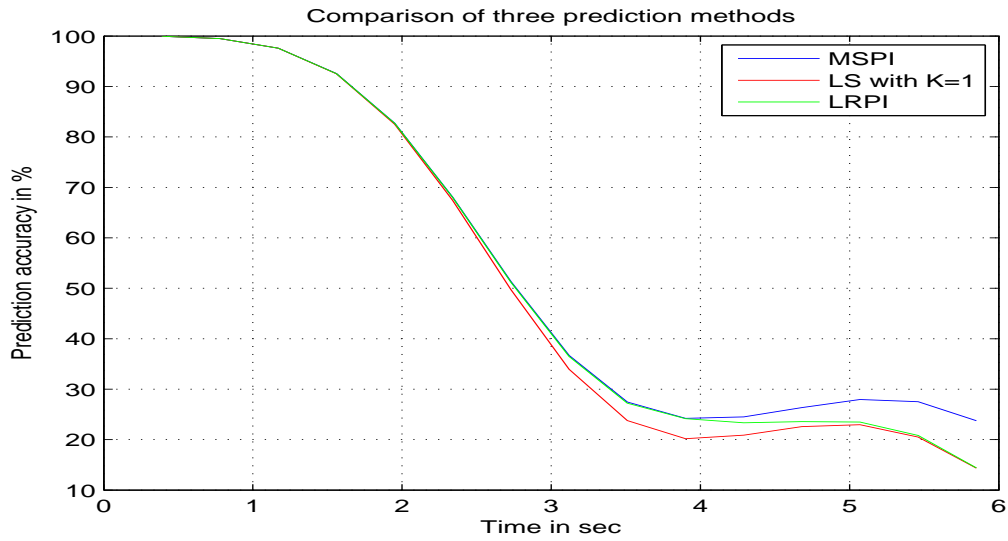


Figure 4.30 Prediction accuracy of prediction approaches with model order 10

Case 7

The prediction accuracy for a model order of 20 is given as figure4.31:

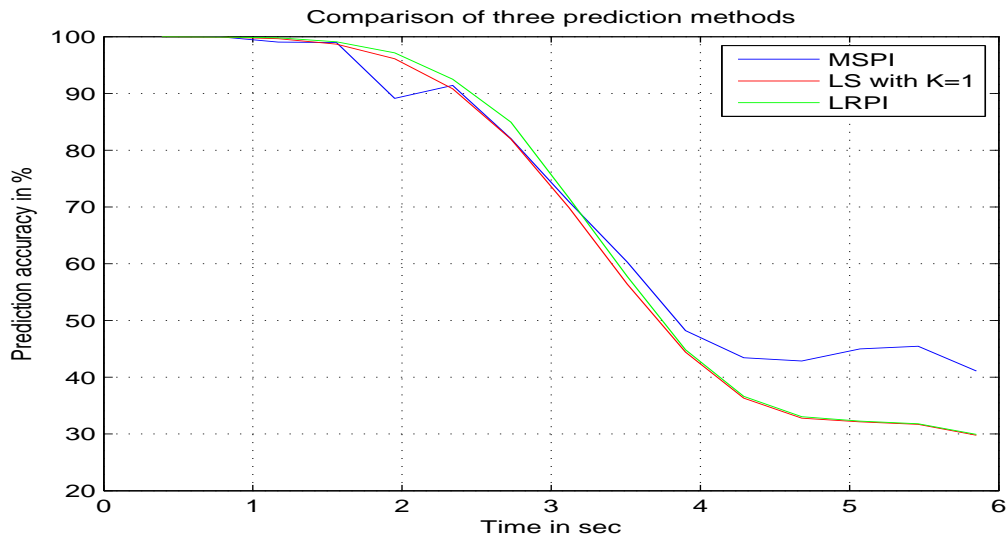


Figure 4.31 Prediction accuracy of prediction approaches with a model order of 20

Case 8

The prediction accuracy for a model order of 30 is given as figure4.32:

4.6 Comparison of different predictive approaches

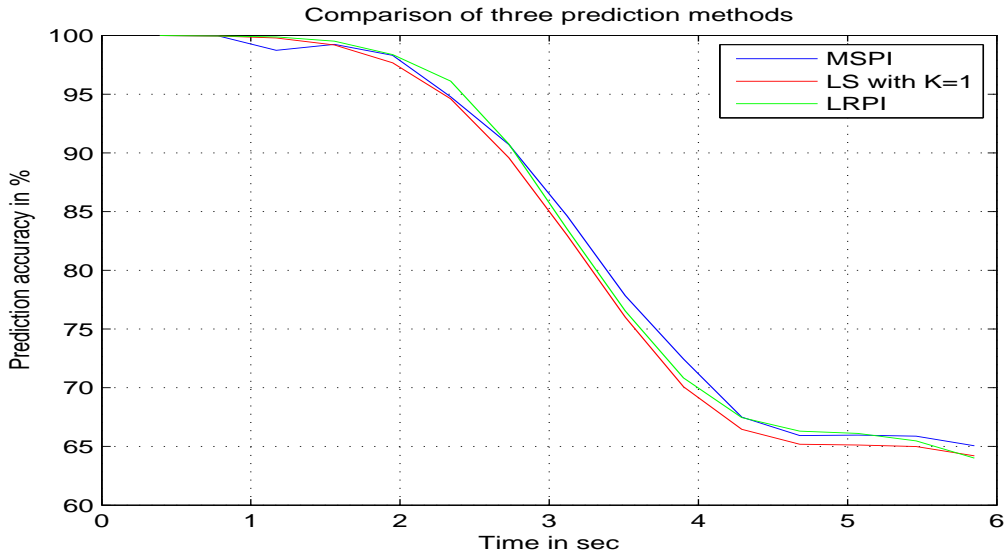


Figure 4.32 Prediction accuracy of prediction approaches with a model order of 30

The prediction accuracy increases as the model order increases. These three methods can obtain an overall 20% prediction accuracy after 5s with a model order of 10. A prediction horizon of 5s is almost equal to 13 prediction steps. The MSPI prediction accuracy increased by more than 20% when the model order was increased from 10 to 20. Also, the LS and the LRPI prediction accuracies increased by 10% in the same situation. The prediction accuracies of the three prediction methods with model orders of 30 were significantly increased compared to the previous cases. The three prediction methods can obtain 65% accuracy with 13 steps ahead prediction. The results of the comparisons presented in fig4.30, fig4.31, and fig4.32 were entirely expected based on the AIC and BIC values. As mentioned earlier, the most suitable model order can be chosen with the minimum AIC value and BIC values. As shown in fig4.27, 4.28, and 4.29, the AIC and BIC values decreased as model order n increased. In conclusion, an increase in model order can improve the performance of all three prediction approaches. However, a suitable model order should be chosen via AIC and BIC values to avoid excessive model complexity.

Table 4.1 Performance Table 1 (measured at 5s)

Pred Acc	Low-pass filter comparison		
	Case 1	Case 2	Case 3
LS	21.5%	87.7%	98.9%
LRPI	23.1%	88.2%	98.9%
MSPI	30%	89.1%	99.8%

Table 4.2 Performance Table 2 (measured at 5sec)

	Different wave spectrum comparison			
Pred Acc	Case 4.1	Case 4.2	Case 5.1	Case 5.2
LS	4.2%	4.2%	55.3%	14.7%
LRPI	6.3%	8.4%	55.8%	14.7%
MSPI	14.7%	12.6%	57.9%	24.2%

Table 4.3 Performance Table 3 (measured at 5sec)

	Different model order comparison		
Pred Acc	Case 6	Case 7	Case 8
LS	22.5%	32.6%	65.1%
LRPI	23.3%	32.7%	66.1%
MSPI	27.5%	44.3%	66.1%

4.7 Chapter summary

The main objective of this chapter was to find an efficient predictive approach. Accurate wave elevation prediction is important for maximising the absorbed wave power, as discussed in chapter 3.

Section 4.2 gives a brief review of wave characteristics. How changes to the significant wave height and the zero-crossing period can affect the PM spectrum was also examined.

The simple least-squares system identification was introduced in section 4.3. The autoregressive model was used to simulate the wave elevation. The calculation process for the LS method was presented, and a recursive least-squares method has been described that reduces the complexity of the model.

Long-range predictive identification was proposed in section 4.4 due to various limitations in the simple least-squares method. Prediction usually requires more than one step ahead. Long-range predictive identification can be used to find the best estimated coefficient vector in order to observe the entire prediction horizon.

Another prediction approach was introduced in section 4.5 called multi-step predictive Identification. It also observes the entire prediction horizon in a similar manner to the LRPI method. The difference is that the MSPI method calculates the estimated coefficient vector for each prediction step; it also calculates each estimated coefficient vector simultaneously, which can increase efficiency.

The comparison of these prediction approaches was given in section 4.6. Performance tables for these prediction approaches are reported in table4.1, 4.2, and 4.3.

It has been shown that the MSPI method can obtain the best performance in terms of wave elevation prediction. The LRPI method obtained a prediction performance that was somewhat worse than that of MSPI. As expected, the simple LS method gave the worst results. The prediction performances have been judged on the basis of the associated prediction accuracies. The prediction accuracy was also tested using different wave conditions, which were based on the PM spectrum. The majority of the wave energy is located in the low frequency range of the spectrum, and so the prediction accuracy can be improved using a low frequency range. In addition, the model order is another efficient way by which to improve the prediction accuracy of the prediction approach; however, a larger model order value may make the prediction model too complex. The choice of model order can be considered through the AIC and BIC criteria.

System approximation is another way to overcome non-causality. The next chapter will give details regarding system approximation. Real-time control will be based on a system approximation that will be given in chapter 6.

Chapter 5

Model approximation

5.1 Chapter overview

The system time domain equation was given in eq(2.21). It includes an integro-differential term that is difficult to analysis. Hence, Prony's approximation method was introduced in reference [38]. This method is used to approximate the whole system as per eq(2.21), which allows for an analysis.

The design of controllers in chapter 2 relies on the approximation transfer function obtained from reference [38]. The controller chosen for this thesis uses a complex conjugate control, which is closely connected to the approximation transfer function. The method to find the approximation of the intrinsic impedance is of vital importance, and hence two different methods to address this issue will be presented in section 5.2.1. One is referred to as the prediction error method; the other is the direct inverse of the approximation transfer function, which was obtained from reference [38]. Comparisons of these methods will also be made.

The other motivation for the model approximation is to overcome the non-causality problem. As mentioned in chapter 3, there are two possible solutions for overcoming non-causality. One is the prediction of the velocity of a wave energy conversion system or the excitation force that can be used to overcome the problem, as described in the previous chapter. The other is a system approximation.

A second-order system approximation is given in section 5.3. This second system approximation can reduce the complexity of the system whilst maintaining most of its performance. The prediction error method will again be used, and the results compared with the partial fraction decomposition obtained from references [38] and [75].

The hydrodynamic parameter collection will then be introduced in section 5.4. The key point here is to calculate the disturbance of the control system. The excitation force will be set as such a disturbance. Polynomials are used to represent the hydrodynamic data supplied by reference [38]. The hydrodynamic data itself will be collected by a software suite called the Tracer. Matlab figure tools can easily fit these data with different order polynomials.

Finally, two optimal conditions for maximising the absorbed energy will be tested in section 5.5. Constant approximations will be used in velocity-tracking control and complex-conjugate control.

5.2 Impedance Approximation

The time domain equation of the model was given in chapter 2 as follows:

$$m\ddot{x} + M_a(\infty)\ddot{x} + \int_0^\infty h_r(\tau)v(t-\tau)d\tau + K_v\dot{x}(t) + K_sx(t) = \int_{-\infty}^\infty h_{ex}(\tau)\eta(t-\tau)d\tau + F_{pto}(t) \quad (5.1)$$

Then, taking the Laplace transform, the above equation can be rewritten as:

$$s[m + M_a(\infty)]V(s) + H_r(s)V(s) + \frac{K_s}{s}V(s) + K_vV(s) = F_{ex}(s) + F_u(s) \quad (5.2)$$

where $s = j\omega$. The particular emphasis here is on the relationship between the velocity and the force. Hence, eq(5.2) is rewritten as follows:

$$\frac{V(s)}{F_{ex}(s) + F_u(s)} = \frac{1}{s[m + M_a(\infty)] + H_r(s) + \frac{K_s}{s} + K_v} \quad (5.3)$$

The intrinsic mechanical impedance of the floating system is obtained as the denominator, which comes from the previous equation, eq(5.3) [32]:

$$Z_i(s) = s[m + M_a(\infty)] + H_r(s) + \frac{K_s}{s} + K_v \quad (5.4)$$

Then, the velocity response equation can be simplified to:

$$\frac{V(s)}{F_{ex}(s) + F_u(s)} = \frac{1}{Z_i(s)} \quad (5.5)$$

The example WEC system with specific parameters can be found in reference [38]. The radiation impedance, $H_r(j\omega)$, can only be simulated numerically for certain frequencies with

the WAMIT hydrodynamic software. A sixth-order approximation of the system is also given in reference [38]. It can be seen as the plant of the control system:

$$\frac{1}{\widehat{Z}_i(s)} = \frac{1.8 \times 10^{-6}s^5 + 4.86 \times 10^{-6}s^4 + 7.128 \times 10^{-6}s^3 + 4.716 \times 10^{-6}s^2 + 1.296 \times 10^{-6}s}{s^6 + 2.7s^5 + 5.44s^4 + 6.748s^3 + 6.408s^2 + 3.784s + 0.96} \quad (5.6)$$

Two optimal control conditions were presented in section 3.2.2. One is the velocity-tracking control; the other is a complex conjugate control, and both can be related to intrinsic impedance. Hence, there are three impedance approximations that will be pursued.

Intrinsic impedance

The inverse of the intrinsic impedance is given by eq(5.6). Firstly, the approximation of the intrinsic impedance, $\widehat{Z}_i(s)$, should be calculated; this will be presented in section 5.2.1.

Control impedance

One of optimal control conditions is that of complex conjugate control, which was introduced in section 3.2. The expression for this is given by:

$$F_u(j\omega) = -\widehat{Z}_{u,opt}(j\omega)V(j\omega) = -\widehat{Z}_i^*(j\omega)V(j\omega) \quad (5.7)$$

Hence, the Laplace transform of eq(5.7) is:

$$F_u(s) = -\widehat{Z}_{u,opt}(s)V(s) = -\widehat{Z}_i(-s)V(s) \quad (5.8)$$

The approximation for the control impedance will be presented in section 5.2.2.

Optimal non-causal impedance

The other optimal control condition is called velocity-tracking control. It is used to express the optimal relationship between the velocity and the excitation force:

$$\widehat{Z}_{r,opt}(j\omega) = \frac{F_{ex}(j\omega)}{V(j\omega)} = \frac{1}{2(B(j\omega) + K_v)} = \frac{1}{\widehat{Z}_i(j\omega) + \widehat{Z}_i(-j\omega)} \quad (5.9)$$

The Laplace transform of optimal non-causal impedance is:

$$\widehat{Z}_{r,opt}(s) = \frac{1}{\widehat{Z}_i(s) + \widehat{Z}_i(-s)} \tag{5.10}$$

More details of the optimal non-causal impedance approximation will be given in section 5.2.3.

5.2.1 Approximation of intrinsic impedance

The prediction error method is one solution by which to determine a finite-order approximation of the intrinsic impedance, $Z_i(s)$. The Matlab command `tfest` can be used to estimate the model using the prediction error method.

The cost function of the optimal $Z_i(j\omega)$ and different order approximation, $\widehat{Z}_i(j\omega)$, can be written as:

$$J(\widehat{Z}_i) = \int_{-\infty}^{\infty} \|(Z_i(j\omega) - \widehat{Z}_i(j\omega))\|^2 \tag{5.11}$$

The higher the order of $\widehat{Z}_i(j\omega)$, the greater the accuracy of the transfer function that will be obtained. Transfer functions with different orders will be tested; their comparison is given as follows, which uses different approximation orders, with $n = [4, 6, 7, 8]$:

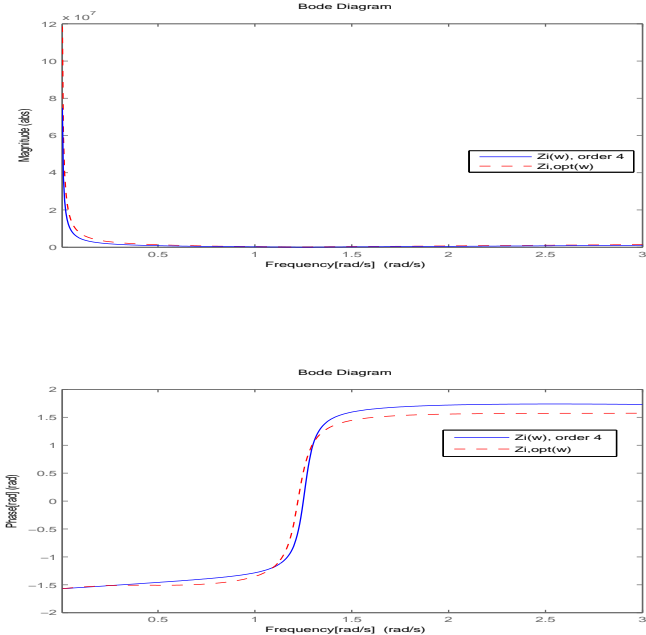


Figure 5.1 Fourth-order approximation of intrinsic impedance

5.2 Impedance Approximation

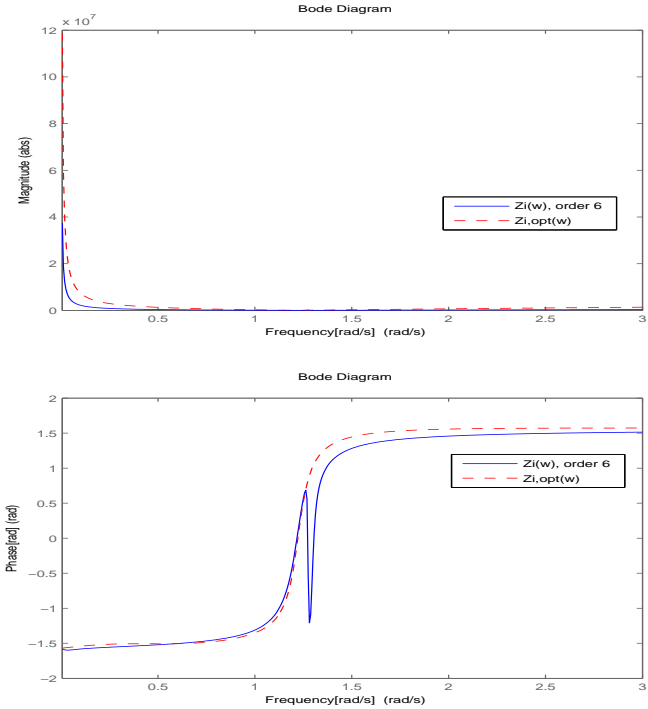


Figure 5.2 Sixth-order approximation of intrinsic impedance

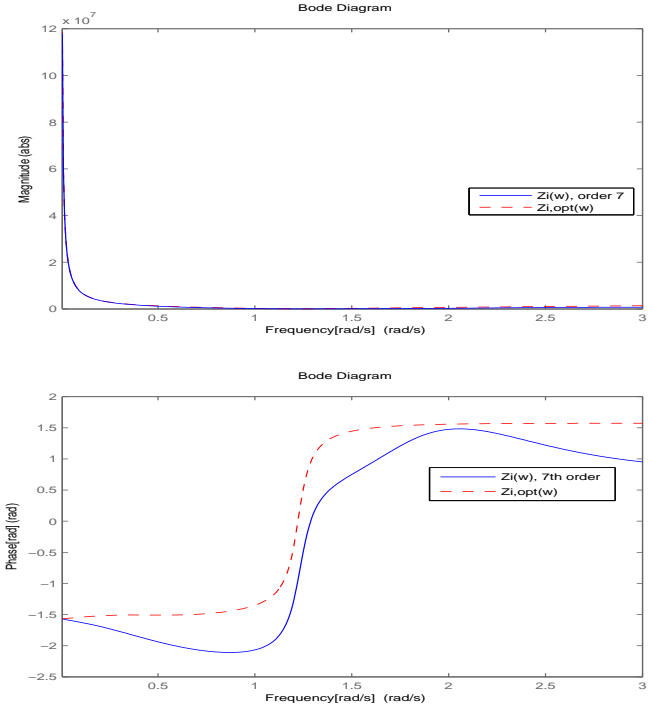


Figure 5.3 Seventh-order approximation of intrinsic impedance

5.2 Impedance Approximation

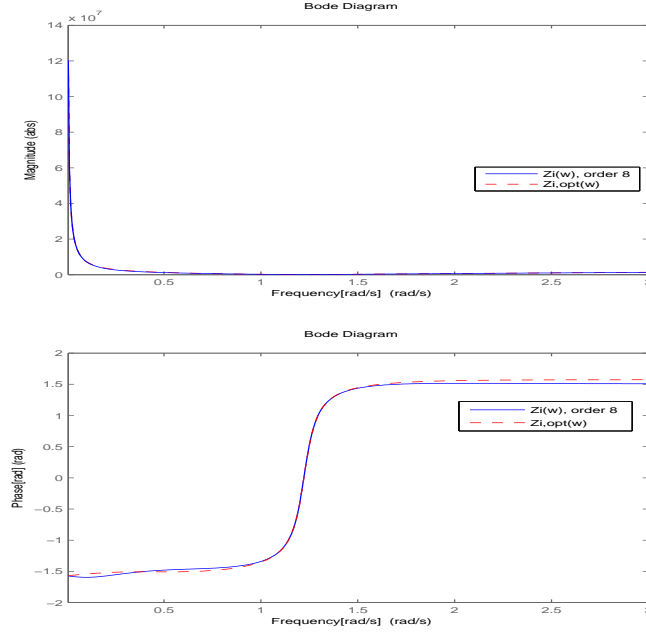


Figure 5.4 Eighth-order approximation of intrinsic impedance

The accuracy of the system is determined via Efron's pseudo R-squared method, given in section 4.6, as follows:

$$R(j\omega) = 100 \cdot \left(1 - \frac{\sum_{s=1}^N (Z_i(j\omega) - \widehat{Z}_i(j\omega))}{\sum_{s=1}^N (Z_i(j\omega) - \overline{\widehat{Z}_i(j\omega)})} \right) \quad (5.12)$$

where the bar of $\widehat{Z}_i(j\omega)$ is the mean value of $\widehat{Z}_i(j\omega)$. The accuracy of the estimate for the intrinsic impedance of order 4 that can be achieved is 62.74%. The intrinsic impedance transfer function of order 6 would be expected to show better performance; however, the accuracy of this latter intrinsic impedance was found to be only 30.66%. The order 7 estimated intrinsic impedance has also been tested, giving an accuracy of 93.19%. Finally, the accuracy of the estimated intrinsic impedance of order 8 was found as 97.63%. It can be seen that the intrinsic impedance of higher order n can achieve greater accuracy, with the exception of the intrinsic impedance of order 6. The reason for this anomaly might be due to the search curves having many local minima [61].

The approximate transfer function of $Z_i(s)$ is:

$$\widehat{Z}_i(s) = \frac{1 \times 10^9 (1.126s^7 + 3.947s^6 + 8.332s^5 + 12.77s^4 + 12.98s^3 + 10.31s^2 + 4.467s + 0.628)}{s^8 + 13.35s^7 + 2286s^6 + 7394s^5 + 1.282 \times 10^4 s^4 + 1.268 \times 10^4 s^3 + 6279s^2 + 837s + 0.0218} \quad (5.13)$$

5.2.2 Approximation of control impedance

The optimal condition for the complex conjugate control can be satisfied with the following transfer function:

$$F_u(s) = -\widehat{Z}_i(-s)V(s) \quad (5.14)$$

The approximated intrinsic impedance, $\widehat{Z}_i(s)$, was determined via eq(5.13). Hence, the approximated complex conjugate of the intrinsic impedance, $\widehat{Z}_i(-s)$, can be processed.

The approximated complex conjugate of intrinsic impedance, $\widehat{Z}_i(-s)$, can be obtained via eq5.13 as follows:

$$\widehat{Z}_i(-s) = \frac{1 \times 10^9(-1.126s^7 + 3.947s^6 - 8.332s^5 + 12.77s^4 - 12.98s^3 + 10.31s^2 - 4.467s + 0.628)}{s^8 - 13.35s^7 + 2286s^6 - 7394s^5 + 1.282 \times 10^4s^4 - 1.268 \times 10^4s^3 + 6279s^2 - 837s + 0.0218} \quad (5.15)$$

The non-causality of the control impedance, $\widehat{Z}_i(s)$, has thus been overcome. It should be compared with the fifth-order non-causal approximated complex conjugate of the intrinsic impedance:

$$\widehat{Z}_i(-s) = \frac{s^6 - 2.7s^5 + 5.44s^4 - 6.748s^3 + 6.408s^2 - 3.784s + 0.96}{-1.8 \times 10^{-6}s^5 + 4.86 \times 10^{-6}s^4 - 7.128 \times 10^{-6}s^3 + 4.716 \times 10^{-6}s^2 - 1.296 \times 10^{-6}s} \quad (5.16)$$

This is calculated directly by inverting eq(5.6) as follows:

$$\widehat{Z}_i(s) = \frac{s^6 + 2.7s^5 + 5.44s^4 + 6.748s^3 + 6.408s^2 + 3.784s + 0.96}{1.8 \times 10^{-6}s^5 + 4.86 \times 10^{-6}s^4 + 7.128 \times 10^{-6}s^3 + 4.716 \times 10^{-6}s^2 + 1.296 \times 10^{-6}s} \quad (5.17)$$

Note that the fifth-order non-causal approximated function cannot be used directly in phase control; however, it is given in figure5.5 for comparative purposes.

A comparison of two different approximated complex conjugate of intrinsic impedances is given as fig5.5. It can be seen from fig5.5 that the two approximated complex conjugate of intrinsic impedances are very close.

The complex conjugate condition is given as:

$$Z_{u,opt}(s) = \widehat{Z}_i(-s) \quad (5.18)$$

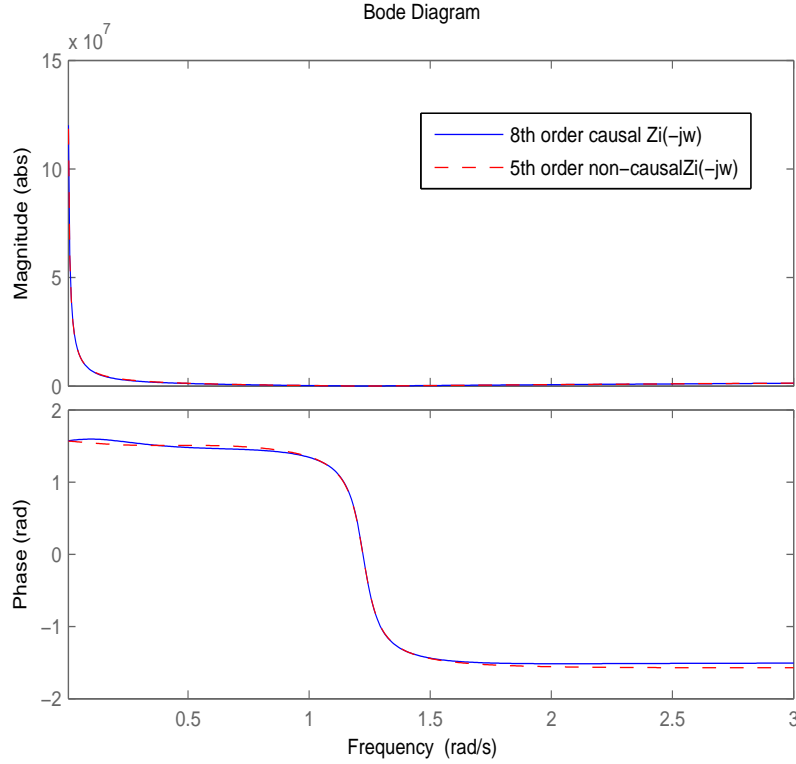


Figure 5.5 The comparison of $\widehat{Z}_i(-s)$

Calculated results from this subsection will be used in the simulation presented in section 5.5.2. The order of eq(5.15) will be reduced in section 5.3 with the causal approximation.

5.2.3 Approximation of optimal non-causal impedance

As discussed in sections 3.3 and 3.4, the non-causality of the $B(j\omega)$ has been demonstrated. The frequency domain of the optimal phase control can be written as follows, using eq(3.26):

$$V(j\omega) = \frac{F_{ex}(j\omega)}{2(B(j\omega) + K_v)} \quad (5.19)$$

The intrinsic impedance was given in eq(5.4), as follows:

$$Z_i(j\omega) = j\omega[m + M_a(\infty)] + H_r(j\omega) + \frac{K_S}{j\omega} + K_v \quad (5.20)$$

The radiation impedance without a singularity, $j\omega M_a(\infty)$, was described in section 2.3 as follows:

$$H_r(j\omega) = B(j\omega) + j\omega[M_a(j\omega) - M_a(\infty)] \quad (5.21)$$

Hence, eq(5.19) can be rewritten as follows:

$$V(j\omega) = \frac{F_{ex}(j\omega)}{Z_i(j\omega) + Z_i^*(j\omega)} \quad (5.22)$$

Now, the excitation force and velocity are only related to the intrinsic impedance and its complex conjugate.

Assuming an optimal relationship between the velocity and the excitation force is called the optimal non-causal impedance, $Z_{r,opt}$. The reason that can be seen from eq(5.22), the mass term, is that the net-buoyancy coefficients have been negated by the characteristics of the complex conjugate; in other words, only the radiation impedance affects the relationship between the velocity and the excitation force.

The approximation of the optimal radiation impedance will be useful for further comparison with the constant approximation, which will be introduced in the next section. This is the fundamental principle that explains why a second-order approximation function can be used to overcome the non-causality problem, and further why the optimal radiation impedance is key to velocity-tracking control. The simulation results for the velocity-tracking control will be given in section 5.5.1. The optimal non-causal impedance is given by:

$$Z_{r,opt}(j\omega) = \frac{1}{2(B(j\omega) + K_v)} \quad (5.23)$$

The Laplace transform of eq(5.23) is:

$$Z_{r,opt}(s) = \frac{1}{2(B(s) + K_v)} = \frac{1}{Z_i(s) + Z_i(-s)} \quad (5.24)$$

Hence, the transfer function of $Z_{r,opt}(s)$ can be calculated with the approximation transfer function, eq(5.15), as follows:

$$\hat{Z}_{r,opt}(s) = \frac{1 \times 10^{-12}(3.24s^{10} + 2.041s^8 + 9.634s^6 + 8.078 \times 10^{-16}s^5 - 3.765s^4 + 1.68s^2)}{4.752 \times 10^{-7}s^8 + 3.224 \times 10^{-6}s^6 + 1.664 \times 10^{-6}s^4 + 7.534 \times 10^{-7}s^2} \quad (5.25)$$

It can be shown from eq(5.25) that the order of the numerator is larger than that of the denominator, which means that this cannot be implemented as a real-time control. The

5.2 Impedance Approximation

prediction error method with approximation has to be used to solve this problem. A fourth-order approximated transfer function can be obtained as follows:

$$\hat{Z}_{r,opt}(s) = \frac{-3.31 \times 10^{-15}s^3 - 4 \times 10^{-4}s^2 - 9.744 \times 10^{-15}s - 4.851 \times 10^{-5}}{s^4 + 3.869 \times 10^{-11}s^3 + 21.21s^2 + 2.425 \times 10^{-10}s + 93.62} \quad (5.26)$$

The fourth-order approximate transfer function can achieve 99.64% accuracy compared to eq(5.25).

The comparison of the approximation transfer function and the estimation dataset is given as follows:

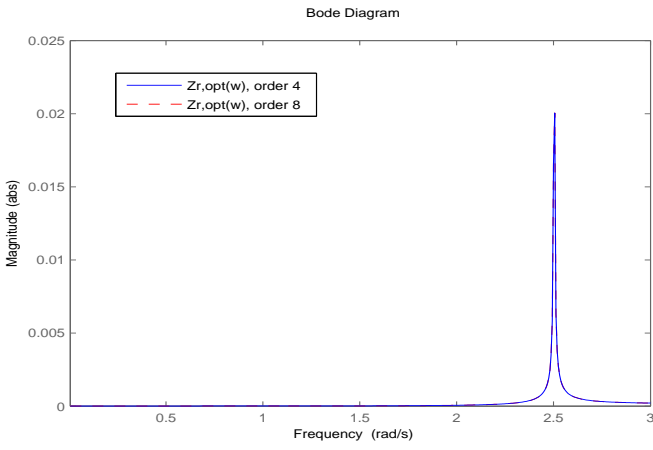


Figure 5.6 Magnitude comparison of fourth-order approximated transfer function and estimation dataset

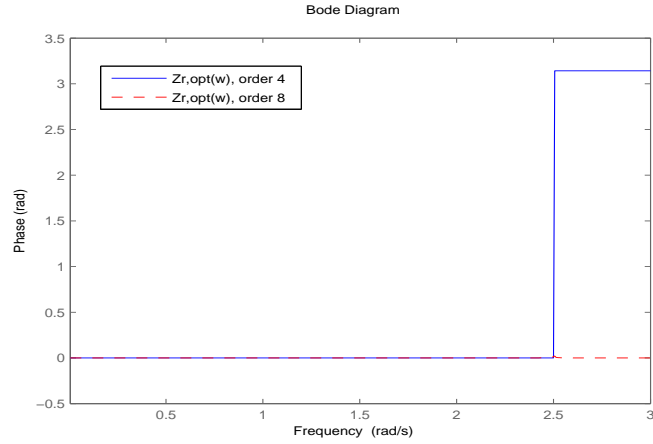


Figure 5.7 Comparison of the phase of the fourth-order approximated transfer function and estimation dataset

It can be seen from figure 5.6 that the magnitudes of the approximated transfer functions completely coincide with each other. The phase of the estimation dataset is shown in figure 5.7. The figure 5.7 shows the phase is 0 over most of the frequencies that are neglected.

5.3 Causal approximation and model order reduction

The authors of references [75] and [38] noted some of the components of the intrinsic impedance may not have a significant affect on the WEC system. Hence, the second-order approximated mode mentioned in chapter 3; this can be used to overcome the non-causality of the system. Detail regarding the second-order approximation will be given in the following section. The application will be verified with two different control constructions.

In the first, the optimal relationship between the velocity and the excitation force was presented in the previous section with the **optimal non-causal impedance**, $Z_{r,opt}$, which was given in eq 5.26. The estimated frequency domain of the optimal non-causal impedance, $\hat{Z}_{r,opt}(j\omega)$, was given in fig 5.6 and fig 5.7. The value of $\hat{Z}_{r,opt}(j\omega)$ is very small, and is essentially constant between $0rad/s$ to $2rad/s$. It was also shown in chapter 4 that most of the wave's energy is stored in the low-frequency sea state. A constant approximation of $\hat{Z}_{r,opt}(j\omega)$ crosses most values of $\hat{Z}_{r,opt}(j\omega)$ in the low frequency range, and so is worth pursuing later [38].

Note that the PEM was used to estimate the control impedance in the previous subsection. The dynamic function of the WEC system was given in eq 5.2. The relationship between the velocity and the sum of the excitation and the control force is given in eq (5.6) as a sixth-order approximation. The PEM can also be used to approximate and reduce the order of the inverse of the estimated intrinsic impedance. The second-order approximated transfer function can be calculated with an order of $n = 2$; for the WEC system, this is as follows:

$$\frac{1}{\hat{Z}_{i,2nd}(s)} = \frac{1.934 \times 10^{-6}s + 1.024 \times 10^{-7}}{s^2 + 0.9774s + 1.499} \quad (5.27)$$

The prediction accuracy was determined by eq (5.12) as 97.94%. The comparison of the bode diagram of the sixth-order transfer function and that of the second-order transfer function is given in figure 5.8.

The other method used to estimate the second-order transfer function, which can be found in references [75] and [38], is shown in here for comparison. The initial sixth-order WEC model remains the same as eq (5.6); however, it has to be written in a partial fraction

5.3 Causal approximation and model order reduction

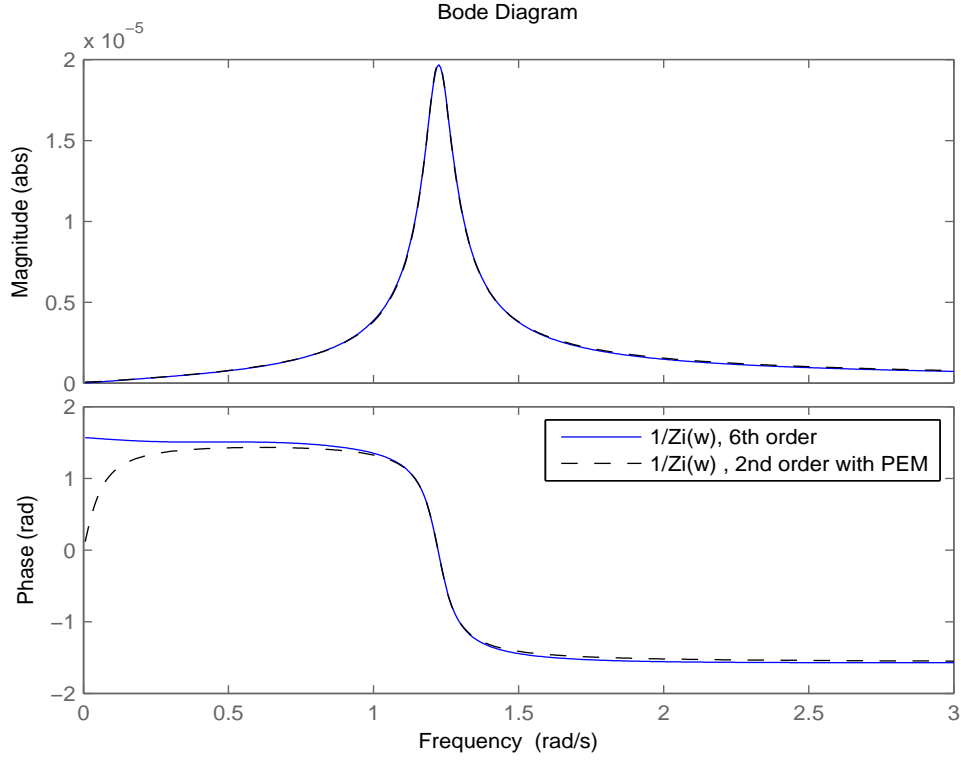


Figure 5.8 Comparison of the bode diagram with the sixth- and second-order transfer functions, as calculated with PEM

decomposition, as below:

$$\hat{Z}_i(s) = \sum_{k=1}^n \frac{R_k}{s - P_k} \quad (5.28)$$

where R_k are the residuals and P_k are the poles of the inverse intrinsic impedance [38, 75]. The particular case of eq(5.6) with partial fraction decomposition can be written as follows [38]:

$$\frac{1}{\hat{Z}_i(s)} = \frac{1.8 \times 10^{-6} s(s^2 + 1.1s + 0.4)(s^2 + 1.6s + 1.8)}{(s^2 + 1.2s + 0.4)(s^2 + 1.4s + 1.6)(s^2 + 0.1s + 1.5)} \quad (5.29)$$

The poles are calculated from the denominator, $s^2 + 0.1s + 1.5$, which is much smaller than for the other four. The other two components of the denominator do not have a particularly significant effect on the WEC system and can thus be ignored [75], [38]; then, only the second-order denominator will have been kept. The numerator only keeps the first-order

5.3 Causal approximation and model order reduction

term required to make the estimated transfer function reasonable. Hence, eq(5.29) has been reduced in order, giving the following:

$$\frac{1}{\widehat{Z}_{i,2nd}(s)} = \frac{1.8 \times 10^{-6}s}{s^2 + 0.1s + 1.5} \quad (5.30)$$

The comparison of the bode diagrams of the sixth-order and second-order transfer functions is given in figure5.9.

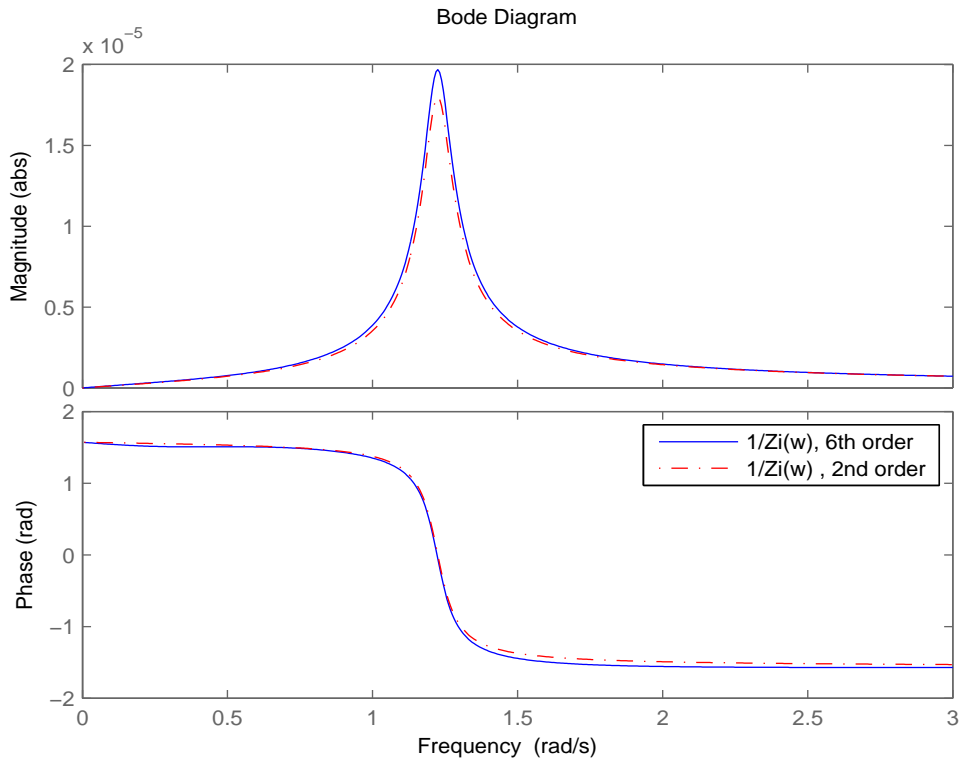


Figure 5.9 Bode diagram of the sixth- and second-order approximation, as calculated without PEM

The comparison of the sixth-order transfer function and two different second-order estimated transfer functions is given in fig5.10.

It can be seen from fig5.10 that the second-order estimated transfer function calculated with PEM is very similar to the sixth-order transfer function. From a practical perspective, the magnitude of the second-order estimated transfer function (PEM) has the better performance of the two.

5.3 Causal approximation and model order reduction

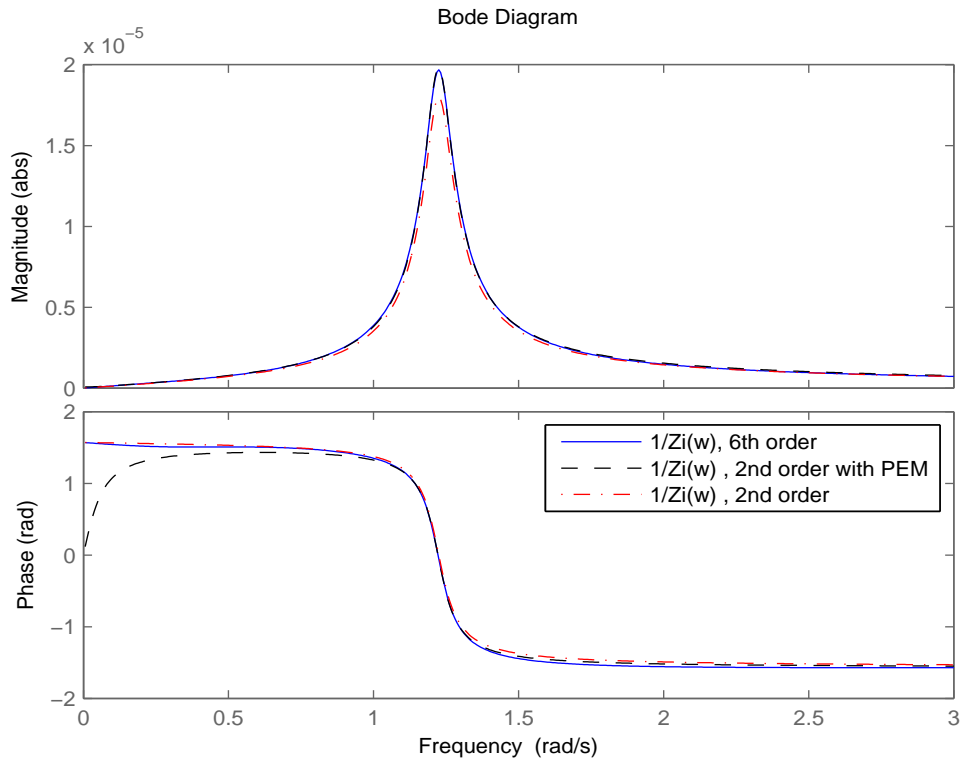


Figure 5.10 Bode diagram of the sixth-order and two different second-order approximations

A second-order model of the oscillating system was introduced in section 3.4. It is similar to a mass-spring-damper system with mass \hat{M} , damping \hat{B} and stiffness \hat{K} . The time domain of the second-order model can be expressed as follows, with the excitation force and the control force:

$$f_{ex}(t) + f_{pto}(t) = \hat{M}\dot{v}(t) + \hat{B}v(t) + \hat{K} \int_{-\infty}^t v(\tau) d\tau \quad (5.31)$$

The Laplace transform of the intrinsic impedance of the second-order model can be expressed as follows:

$$\frac{1}{\widehat{Z}_{i,2nd}(s)} = \frac{1}{\hat{M}s + \hat{B} + \frac{\hat{K}}{s}} \quad (5.32)$$

The transfer function of the estimated intrinsic impedance is given as:

$$\widehat{Z}_{i,2nd}(s) = \hat{M}s + \hat{B} + \frac{\hat{K}}{s} \quad (5.33)$$

5.3 Causal approximation and model order reduction

The second-order approximated intrinsic impedance, which is calculated using PEM, is given in eq(5.27). The values of mass \hat{M} , damping \hat{B} and stiffness \hat{K} are calculated as follows:

$$\hat{M} = \frac{1}{1.934 \times 10^{-6}} \quad \hat{B} = \frac{0.9774}{1.934 \times 10^{-6}} \quad \hat{K} = \frac{1.499}{1.934 \times 10^{-6}} \quad (5.34)$$

The estimated control impedance transfer function is the complex conjugate of eq(5.33), which is:

$$\hat{Z}_{i,2nd}^*(s) = -\hat{M}s + \hat{B} - \frac{\hat{K}}{s} \quad (5.35)$$

The estimated optimal non-causal impedance transfer function is given as follows, which is :

$$\hat{Z}_{r,opt}(s) = \frac{1}{2\hat{B}(s)} \quad (5.36)$$

However, the non-causal kernel, \hat{B} , becomes a constant value and the viscous coefficient, K_v , has been ignored. The optimal condition is given in eq(5.36), which demonstrates that the excitation force is proportional to the velocity. The value of $\hat{Z}_{r,opt}(s)$ is given as 9.8936^{-6} , as calculated using PEM.

The second-order approximated intrinsic impedance calculated using the method provided by references [75] and [38] is given in eq(5.30). The values of mass $\hat{M}1$, damping $\hat{B}1$ and stiffness $\hat{K}1$ can be calculated as follows:

$$\hat{M}1 = \frac{1}{1.8 \times 10^{-6}} \quad \hat{B}1 = \frac{0.1}{1.8 \times 10^{-6}} \quad \hat{K}1 = \frac{1.5}{1.8 \times 10^{-6}} \quad (5.37)$$

The value of $\hat{Z}1_{r,opt}(s)$ was found to be 9.0006^{-6} .

As mentioned previously, constant approximations of $\hat{Z}_{r,opt}(s)$ cross the most common value of $\hat{Z}_{r,opt}(s)$ in the low frequency range. The constant value $\hat{Z}_{r,opt}(s) = 9.8936^{-6}$ and $\hat{Z}1_{r,opt}(s) = 9.0006^{-6}$ can be compared with the fourth-order approximated optimal non-causal impedance which shown in figure5.11.

It can be seen from fig5.11 that the constant value $\hat{Z}_{r,opt}(s) = 9.8936^{-6}$ is closer to the flat part of the fourth-order approximated optimal non-causal impedance. It should be expected that the constant value $\hat{Z}_{r,opt}(s)$ has better performance than the constant value $\hat{Z}1_{r,opt}(s)$. Simulation results will be discussed in section 5.5.

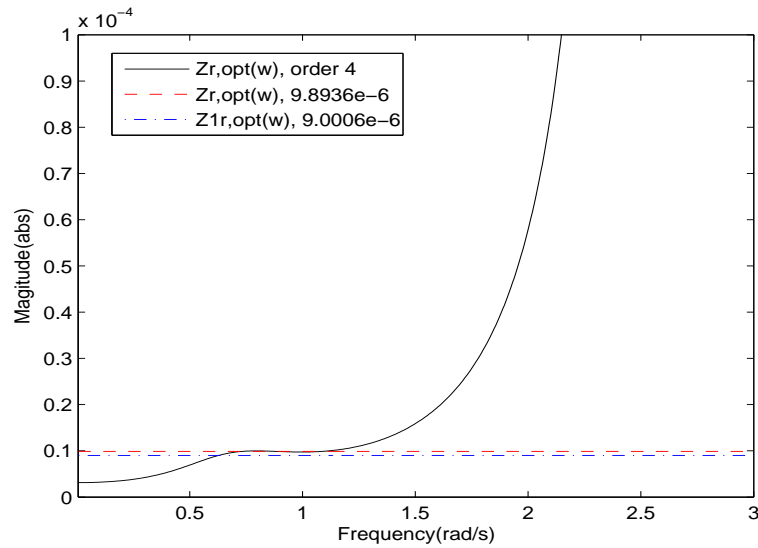


Figure 5.11 Phase comparison of fourth-order approximation and two constant approximations

5.4 Hydrodynamic Parameters

The control plant of control system was given in eq(5.6). Similarly, the controller of the complex conjugate control was also given in eq(5.35). Eq(5.36) can be used as a reference input for the velocity-tracking input. However, disturbances to the two systems have not been previously introduced. The excitation force will be used as the disturbance to the control system, as discussed in the following section.

The hydrodynamic dynamic coefficients used in this thesis are based on those in reference [38]. The important hydrodynamic coefficients, such as the excitation coefficient, H_{ex} , and the radiation coefficient, H_{ex} , are generated through the WAMIT software [50]. WAMIT requires various parameters relating to the floating buoy, such as the radius of the heaving cylinder, the height of the cylinder, and the mass of the buoy. It also requires the value of the distance between the sea bed and the centre of gravity of the buoy. However, no further detail will be given in this thesis.

The oscillation system with WEC, which is described in Fusco's paper, is connected to the sea bed. It moves with wave's heave direction. Also, the external force acts on the buoy in a vertical direction.

The Tracer [55] software is used to capture coefficients from reference [38]. It tracks a graphic and converts it to a set of data. The accuracy of this method depends on the accuracy of the graphic and the number of data used to express the graphic. For example, a set of

coefficients were captured from a diagram in reference [38] using the Tracer. The set of coefficients can be plotted as a digital diagram using Matlab. If the new digital diagram of the set of coefficients and the original diagram in reference [38] were superimposed, this would mean the differences between the captured coefficients from the Tracer and actual coefficients used by reference [38] were very small.

The author of reference [38] gave the bode diagram of the excitation coefficient. The Tracer is used to convert a diagram to two sets of data. One set of data is used to represent the frequency, ω . The other represents the phase or magnitude.

The excitation force was introduced in chapter 2, and is the disturbance to the control system. Also, the time domain of irregular waves was given by eq(2.12). Hence, the time domain of the excitation force is given as follows:

$$F_{ex}(t) = \sum_{i=1}^n A(i) |H_{ex}(\omega(i))| \sin \omega(i)t + \phi(i) + \angle H_{ex}(\omega(i)) \quad (5.38)$$

The frequency response of the excitation coefficient can be calculated (along with its phase and magnitude), and is given as follows:

$$H_{ex}(\omega) = |H_{ex}(\omega)| (\cos \angle H_{ex}(\omega) + j \sin \angle H_{ex}(\omega)) \quad (5.39)$$

The magnitude of the excitation coefficient, $|H_{ex}(\omega)|$, and phase, $\angle H_{ex}(\omega)$, can be calculated separately.

Note that the transfer function for H_{ex} is not required. Hence, the Matlab figure tool, **Basic Fitting**, can be used to obtain a polynomial function.

Different orders of polynomials can be chosen within Matlab to be fit to the collected dataset. The magnitude curve, as fit with different order polynomials, can be illustrated as follows:

It can be seen from figure 5.12 that the seventh-order polynomial provided an excellent fit to the data, and is given as follows:

$$|H_{ex}(\omega)| = -5909.2\omega^7 + 61936\omega^6 - 2.3279 \times 10^5 \omega^5 + 2.9547 \times 10^5 \omega^4 + 2.7453 \times 10^5 \omega^3 - 8.8359 \times 10^5 \omega^2 + 47066\omega + 8.0081 \times 10^5 \quad (5.40)$$

The phase curve fit can be obtained through a similar method with third- and fourth-order polynomials, which are shown as follows:

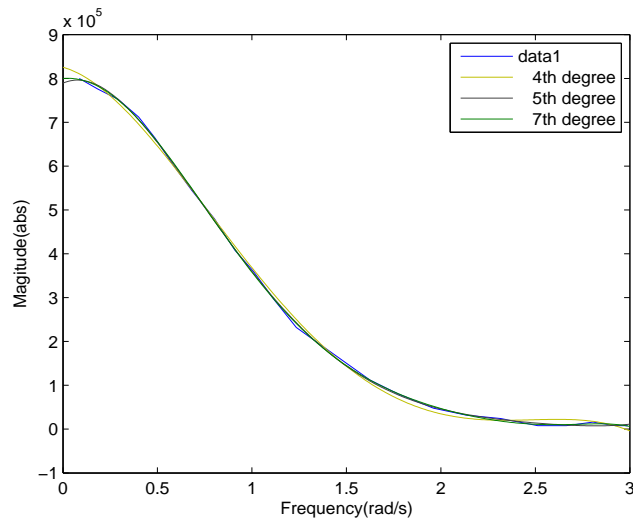


Figure 5.12 Magnitude curve fits using different order polynomials

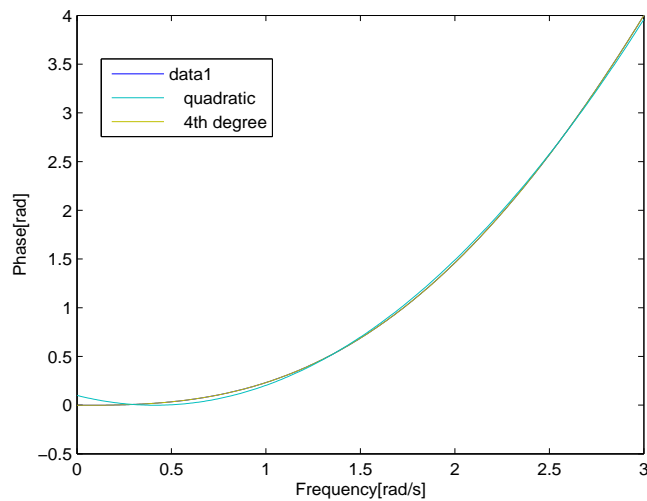


Figure 5.13 Phase curve fits with different order polynomials

The fourth-order polynomial can be seen to provide a good fit to the data. It is given as follows:

$$\angle H_{ex}(\omega) = -0.0253\omega^4 + 0.02046\omega^3 + 0.0621\omega^2 - 0.0085\omega - 0.0014 \quad (5.41)$$

The frequency response of the radiation coefficient can be obtained in a similar manner. Note that the estimated intrinsic impedance given in the previous section can be ignored with this calculation. More details regarding the use of the excitation will be given in chapter 6.

5.5 Causal approximations tested with two control methods

5.5.1 Test with velocity-tracking control

The block diagram for the velocity-tracking construction has been given in section 3.4. The constant approximation is used instead of the non-causal block, $\frac{1}{2B(j\omega)}$, which is shown in fig3.2. A simple PID controller can be used in the controller block. The excitation force can be calculated using eq(5.38). The velocity-tracking control is given as per fig5.14:

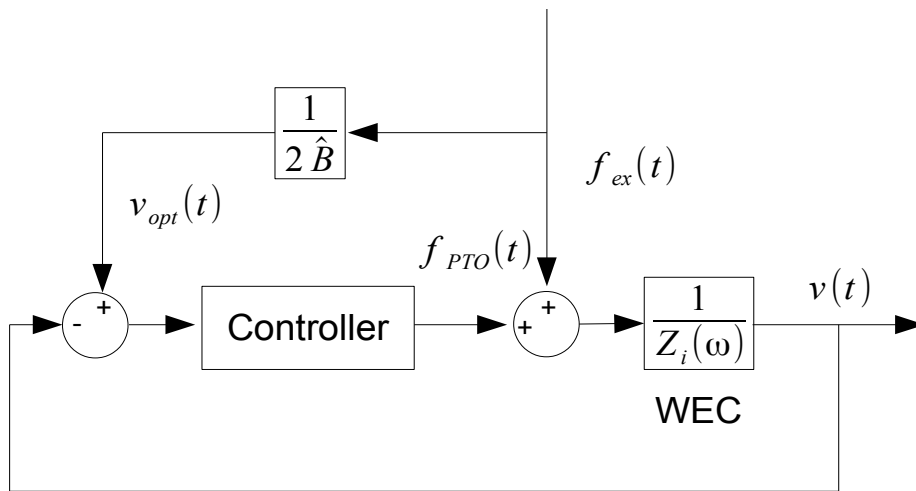


Figure 5.14 Block diagram of the velocity-tracking construction

The absorbed energy with $\widehat{Z}1_{r,opt}(s)$ is given as follows:

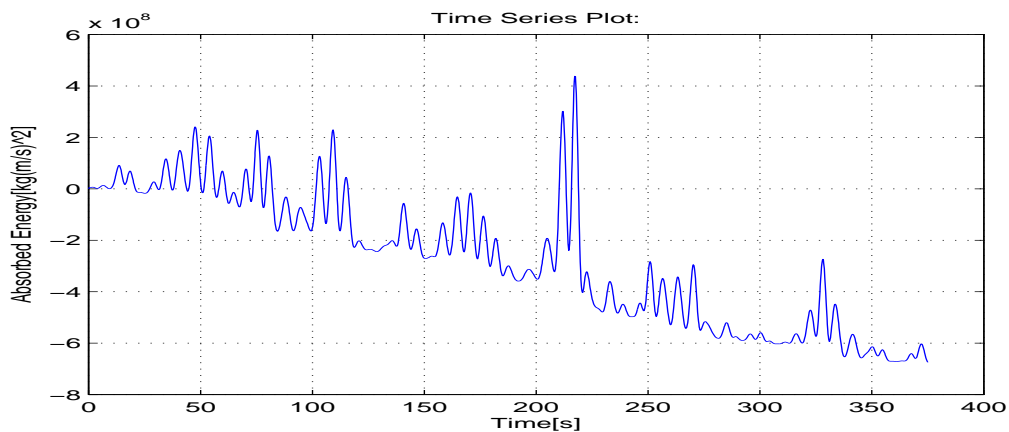


Figure 5.15 The energy absorbed by the velocity-tracking construction

5.5 Causal approximations tested with two control methods

The absorbed energy with $\widehat{Z}_{r,opt}(s)$ is given as follows:

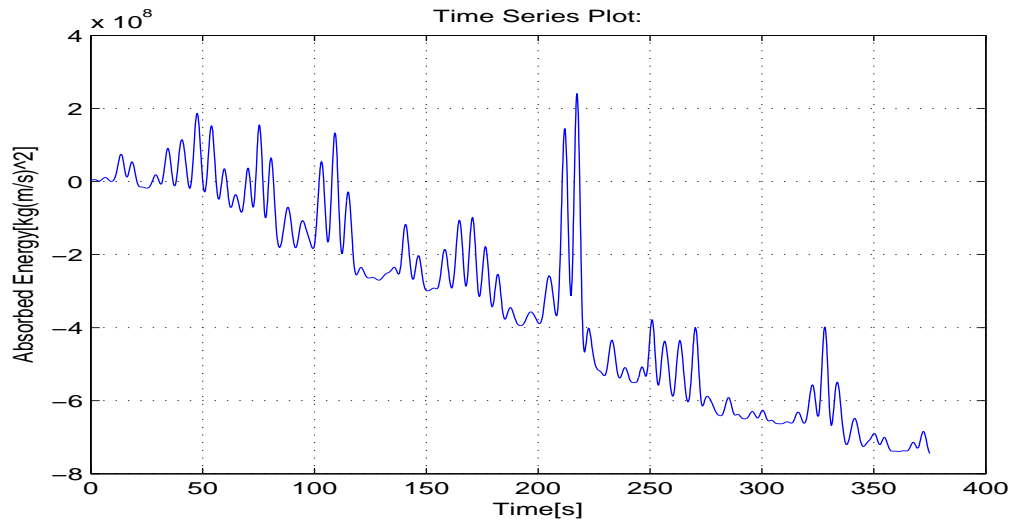


Figure 5.16 The energy absorbed by the velocity-tracking construction

The maximum energy absorbed by $\widehat{Z}_{r,opt}(s)$ is $-7.444 \times 10^8 \text{kg} \cdot (\text{m}/\text{s})^2$. The maximum energy absorbed by $\widehat{Z}_{1r,opt}(s)$ is $-6.745 \times 10^8 \text{kg} \cdot (\text{m}/\text{s})^2$. It can be seen from the absorbed energy with $\widehat{Z}_{r,opt}(s)$ that it gains a little extra performance compared to $\widehat{Z}_{1r,opt}(s)$. Performance results meet general expectations, and it can be seen that the constant approximations can successfully reduce the model order from fourth-order optimal non-causal impedance.

5.5.2 Test with complex conjugate control

The block diagram for the feedback construction was also been given in section 3.4, and is called the complex conjugate control. The constant approximation of mass \widehat{M} , damping \widehat{B} and stiffness \widehat{K} are used instead of the non-causal block, $Z_i^*(j\omega)$, which is shown in fig3.3. Also, the eighth-order approximation control impedance, eq(5.15), has been reduced to second-order. \widehat{M} and \widehat{K} should be negative. The complex conjugate control with constant approximation is given in fig5.17.

The absorbed energy with different sets of constant approximations $\widehat{M}1, \widehat{B}1, \widehat{K}1, \widehat{M}, \widehat{B}, \widehat{K}$ are given in figure5.18 and 5.19.

The energy absorbed with $\widehat{M}, \widehat{B},$ and \widehat{K} also shows better performance than the one calculated by the partial fraction decomposition. The maximum energy absorbed can reach more than $-7.351 \times 10^8 \text{kg} \cdot (\text{m}/\text{s})^2$ which presented in figure5.19. In contrast, the maximum energy absorbed by $\widehat{M}1, \widehat{B}1,$ and $\widehat{K}1$ is $-6.363 \times 10^8 \text{kg} \cdot (\text{m}/\text{s})^2$ which shown in figure5.18.

5.5 Causal approximations tested with two control methods

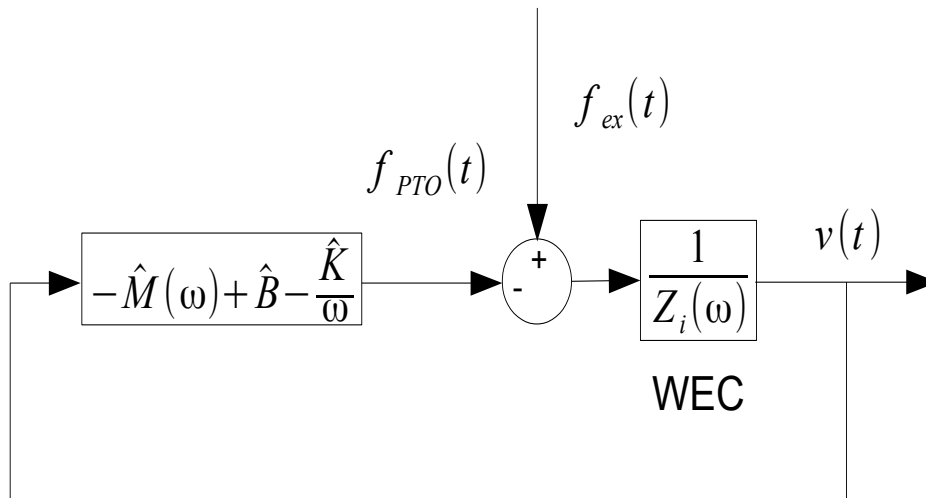


Figure 5.17 Block diagram of the feedback control

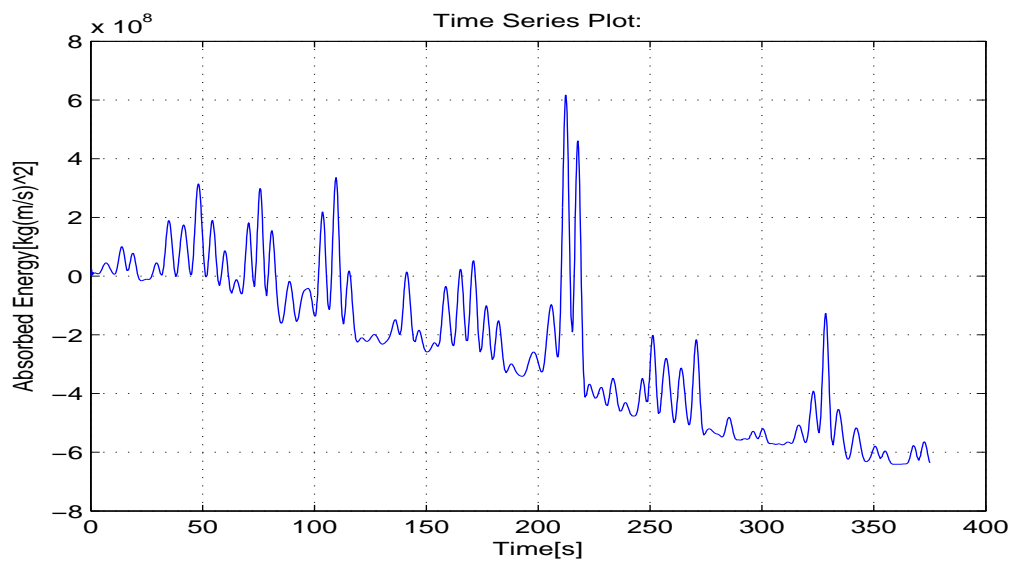


Figure 5.18 The energy absorbed by the feedback construction

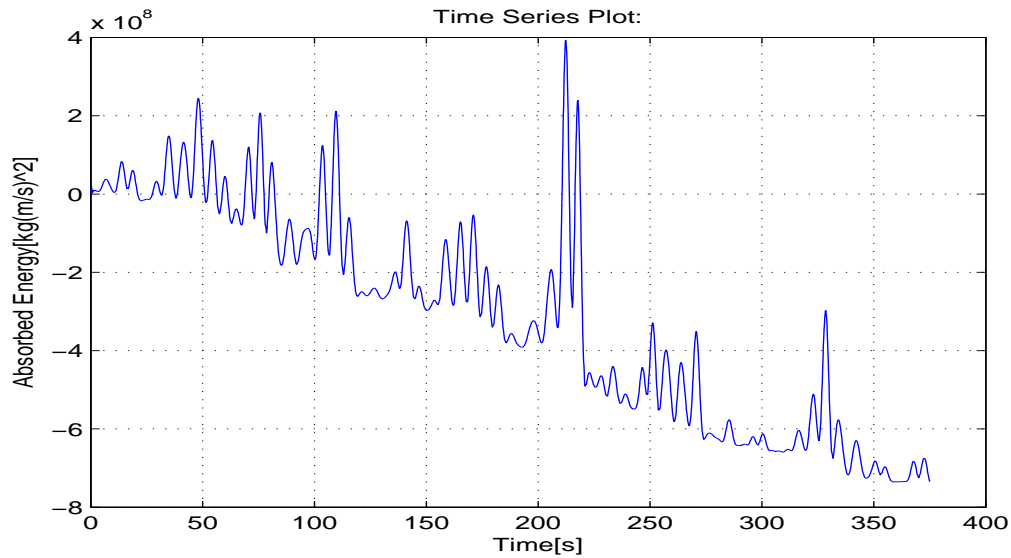


Figure 5.19 The energy absorbed by the feedback construction

5.6 Chapter summary

Several objectives were addressed in this chapter. Firstly, the approximation of the intrinsic impedance was introduced in section 5.2.1. For real-time control, the time domain dynamic equation for the WEC system has to be converted to the Laplace domain. The intrinsic impedance is used to express the relationship between the velocity and the excitation force with the control force. A sixth-order approximation of the inverse of the intrinsic impedance has been given from reference [38]. However, the complex conjugate control requires the complex conjugate of the intrinsic impedance, and so the approximation of the intrinsic impedance has to be calculated. This method is called the prediction error method, which can be used to find an eighth-order approximation for the intrinsic impedance; the eighth-order approximated transfer function can fit estimated data with 97.63% accuracy. In addition, the optimal non-causal impedance has been obtained. This is used to express the relationship between the optimal velocity and the excitation force. A fourth-order approximated transfer function with 99.64% accuracy was finally obtained.

A second-order approximated transfer function for the WEC system is presented in section 5.3. The non-causality of optimal non-causal impedance has been overcome by using a constant value. The different means by which to approximate the second-order transfer function of the WEC system have been compared. One such way, mentioned in reference [75], is to directly remove certain components of the denominator. The poles of

the components of the denominator are very small, and may not have any significant effect on the WEC system. On the other hand, the prediction error method is used to calculate the second-order approximation again. The bode diagram of the second-order approximation with the prediction error method is better than the one that removes the components of the denominator.

The approximation for the excitation coefficient is presented in section 5.4, and is the key element of the excitation force. The Tracer software described in this section was used to capture coefficient data from reference [38].

The energy absorbed from the velocity-tracking and complex-conjugate controls with second-order approximations has also been given. The energy absorbed with the second-order approximation calculated by the prediction error method is higher than that where components of the denominator are removed.

Chapter 6

Control approaches and mechanical implementations

6.1 Chapter overview

As discussed in chapter 3, the optimal control condition for maximising the absorbed power of the WEC system is critical for the obvious reason that it can increase system efficiency.

The different control methods and their implementations are described in section 6.2. Specifically, purely passive resistive control, complex conjugate control, and phase control are compared. The power absorbed from each control method will be compared to allow their different performances to be evaluated. The performance results can help to choose the most appropriate control method for mechanical realisation.

Optimal control impedance is used to extract the maximum absorbed power from the wave through the WEC system. Transfer functions for extracting the maximum absorbed power have already been discussed in section 5.2. The best fit for the transfer function can be found using the Nelder-Mead method, which is described and simulated below.

Following this, in section 6.4, the design of the power take-off (PTO) device for the WEC system will be introduced. The physical mechanical impedance of the PTO approximates the ideal optimal frequency domain expression of the the PTO; this is based on the complex conjugate control, which will be further discussed [30]. Some control constructions with a mass term on the design of a restricted-complexity PTO through the direct optimisation of a suitable design criterion will be presented. The Brune Synthesis is used to realise the admittance of the system.

6.2 Comparison of absorbed energy using different control methods

As mentioned in chapter 3, several control methods can be used in the WEC system to absorb energy. These can be classified in numerous ways, depending on the construction of the control system. In addition, the causal approximated function was introduced in chapter 5. A comparison of the energy absorbed using different control methods is presented in the following section.

The complete dynamics of an oscillating body for wave energy conversion can be expressed as:

$$m\ddot{x}(t) = F_{ex}(t) - F_r(t) - F_s(t) - F_v(t) + F_u(t) \quad (6.1)$$

An oscillating body of mass m for wave energy conversion is constrained to oscillate vertically. Assuming the vertical displacement is $x(t)$, the oscillating body, as acted on by external forces, can be used to construct a dynamic system, as shown in eq(6.1). The entire oscillating body system for wave energy conversion is given in Figure2.11.

The model, as expressed in the time domain, eq(6.1), can be rewritten in the frequency domain as follows:

$$\begin{aligned} j\omega[m + M_a(\infty)]V(j\omega) + H_r(j\omega)V(j\omega) + \frac{K_s}{j\omega}V(j\omega) \\ + K_vV(j\omega) \\ = F_{ex}(j\omega) + F_{PTO}(j\omega) \end{aligned} \quad (6.2)$$

where $V(j\omega)$ is the buoy movement speed. The controllable force from a PTO device is called the control force or PTO force, as shown in fig2.11. The control force, $F_{PTO}(j\omega)$, can also be assumed to be a function of position and its derivatives; this can be shown in the frequency domain as follows:

$$F_{PTO}(j\omega) = -Z_u(j\omega)V(j\omega) \quad (6.3)$$

The velocity response to the excitation force plus the control force can be rewritten using eq(6.2):

$$\frac{V(j\omega)}{F_{ex}(j\omega) + F_{PTO}(j\omega)} = \frac{1}{Z_i(j\omega)} \quad (6.4)$$

6.2 Comparison of absorbed energy using different control methods

where $Z_i(j\omega)$ is the intrinsic mechanical impedance of the floating system.

The power derived from the external force that passes through the floating system has to be considered. As discussed previously, the floating system can simply be considered to be a mass-spring-damper system. The power absorbed in the frequency domain can be expressed as:

$$P_{pto}(j\omega) = \frac{1}{2} \Re\{Z_{pto}(j\omega)\} |\hat{v}|^2 \quad (6.5)$$

The relationship between the excitation force, the control force and the velocity can be expressed in the frequency domain as per eq(3.20). Thus, in this instance the equation 6.5 can be rewritten in the frequency domain as [23, p. 203]:

$$\begin{aligned} P_{pto}(j\omega) &= \frac{1}{2} \Re\{Z_{pto}(j\omega)\} \frac{|F_{ex}(j\omega)|}{|Z_i(j\omega) + Z_{pto}(j\omega)|} \\ &= \frac{1}{2} \frac{R_u(j\omega)}{|Z_i(j\omega) + Z_{pto}(j\omega)|^2} |F_{ex}(j\omega)|^2 \end{aligned} \quad (6.6)$$

Following the equation above, the optimal conditions have already been established, as per section 3.2:

$$Z_{pto}(j\omega) = Z_i^*(j\omega) \equiv Z_{pto,opt}(j\omega) \quad (6.7)$$

The purpose of this project is to maximise wave energy. The total energy is the most important criterion by which to evaluate the effectiveness of a WEC system. The total energy is equal to the integral of the time-averaged power:

$$E = - \int_{-\infty}^{\infty} F_{pto}(t)v(t)dt \quad (6.8)$$

Converting the equation above to the frequency domain using the frequency convolution theorem [23, p. 37] gives the following equation:

$$\begin{aligned} E &= -\frac{1}{2\pi} \int_{-\infty}^{\infty} P_{pto}(\omega)d\omega \\ &= -\frac{1}{2\pi} \int_{-\infty}^{\infty} F_{pto}(\omega)V(-\omega)d\omega \\ &= -\frac{1}{2\pi} \int_{-\infty}^{\infty} F_{pto}(\omega)V^*(\omega)d\omega \\ &= -\frac{1}{2\pi} \int_{-\infty}^{\infty} Z_{pto}(\omega) \cdot V(\omega) \cdot V^*(\omega)d\omega \end{aligned}$$

6.2 Comparison of absorbed energy using different control methods

$$= -\frac{1}{2\pi} \int_{-\infty}^{\infty} Z_{pto}(\omega) V(\omega)^2 d\omega \quad (6.9)$$

The relationship between F_{pto} and F_{ex} is:

$$F_{pto}(j\omega) = \frac{Z_{pto}(j\omega)}{Z_{pto}(j\omega) + Z_i(j\omega)} F_{ex}(j\omega) \quad (6.10)$$

and the velocity is:

$$V(j\omega) = \frac{1}{Z_{pto}(j\omega) + Z_i(j\omega)} F_{ex}(j\omega) \quad (6.11)$$

The spectra expression of F_{pto} can be provided by combining the two equations above, as follows:

$$\begin{aligned} \Phi_{F_{pto}, V}(j\omega) &= \frac{Z_{pto}(j\omega)}{Z_{pto}(j\omega) + Z_i(j\omega)} \cdot \frac{1}{Z_{pto}(j\omega) + Z_i(j\omega)} \\ &\quad \cdot F_{ex}(j\omega) \cdot \overline{F_{ex}(j\omega)} \\ &= \frac{Z_{pto}(j\omega)}{|Z_{pto}(j\omega) + Z_i(j\omega)|^2} \Phi_{F_{ex}}(j\omega) \end{aligned} \quad (6.12)$$

where $\Phi_{F_{ex}}(j\omega) = S(j\omega)|H_{ex}(j\omega)|^2$ is the spectrum of the excitation force and $S(j\omega)$ is the Pierson-Moskowitz spectrum.

Finally, the total energy converted by the WEC can be expressed as follows:

$$E = -\frac{1}{2\pi} \int_{-\infty}^{\infty} \frac{Z_{pto}(j\omega)}{|Z_{pto}(j\omega) + Z_i(j\omega)|^2} \Phi_{F_{ex}}(j\omega) d\omega \quad (6.13)$$

6.2.1 Passive loading control

Passive loading control was introduced in section 3.4, and is the most basic control assumption of the WEC. The optimal load resistance is set to be:

$$R_{opt}(j\omega) = \sqrt{R_i(j\omega) + X_i(j\omega)} \quad (6.14)$$

and

$$Z_i(j\omega) = R_i(j\omega) + jX_i(j\omega) \quad (6.15)$$

6.2 Comparison of absorbed energy using different control methods

The eighth-order approximation of the intrinsic impedance was calculated in section 5.2. The magnitude and phase of the eighth-order approximation are shown in figs 6.1 and 6.2.

The relationship between $R_{opt}(\omega)$ and frequency is given in fig 6.3. $R_{opt}(\omega)$ can be taken to be a constant value for a given, specified frequency of irregular waves. This specified frequency can be set to be the peak frequency of the wave spectrum, as discussed in chapter 2.

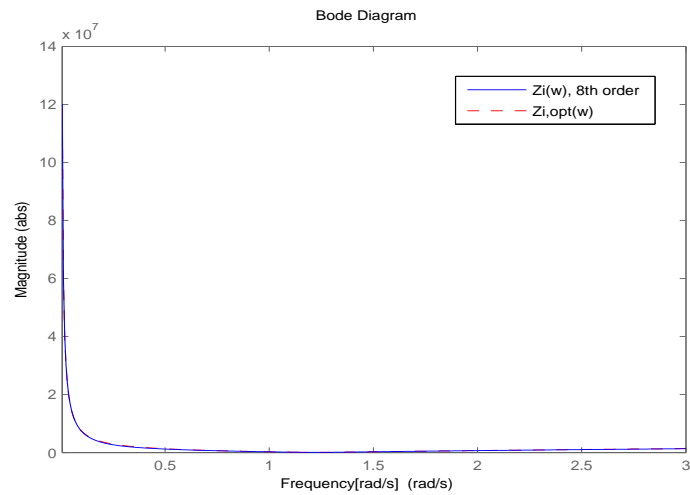


Figure 6.1 Comparison of magnitudes of the eighth-order approximation and the optimal approximation

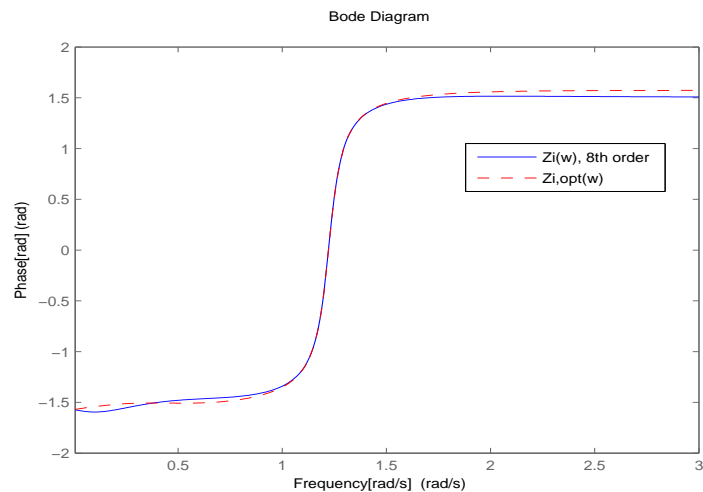


Figure 6.2 Phase comparison for the eighth-order approximation and the optimal approximation

6.2 Comparison of absorbed energy using different control methods

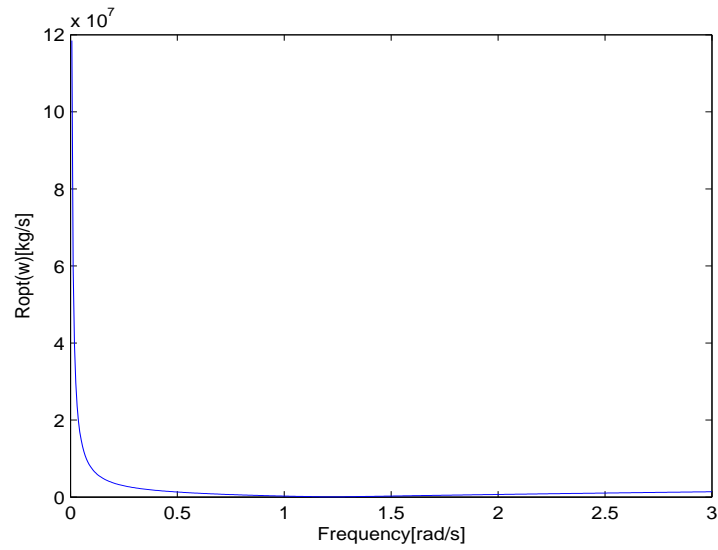


Figure 6.3 The optimal resistance $R_{opt}(\omega)$ against frequency

The construction of the passive loading control is as follows:

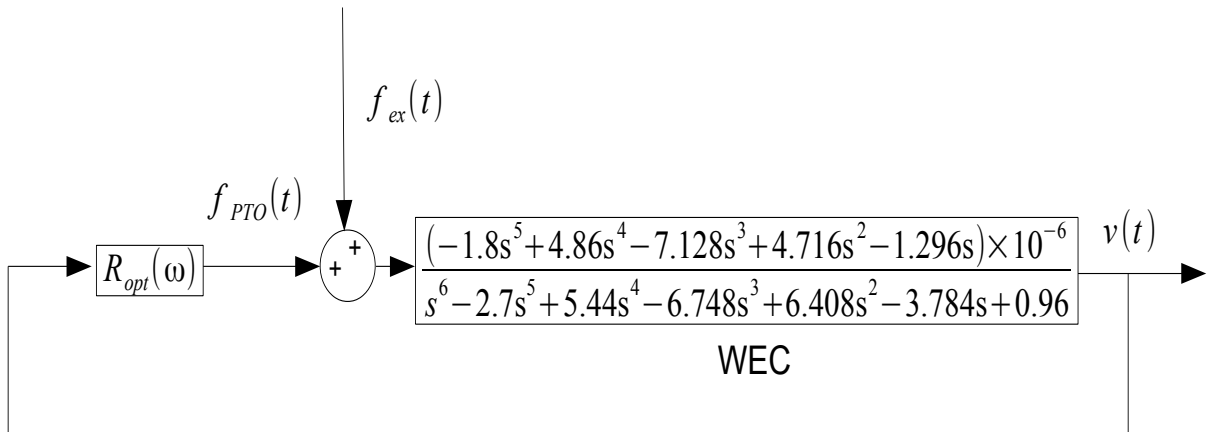


Figure 6.4 The construction of the passive loading control

The energy absorbed using the passive loading control can be determined as follows:

$$\begin{aligned}
 E &= -\frac{1}{2\pi} \int_{-\infty}^{\infty} F_{pto}(\omega) V(-\omega) d\omega \\
 &= -\frac{1}{2\pi} \int_{-\infty}^{\infty} R_{opt}(\omega) |V(\omega)|^2 d\omega
 \end{aligned} \tag{6.16}$$

6.2 Comparison of absorbed energy using different control methods

The relationship between absorbed energy with time is:

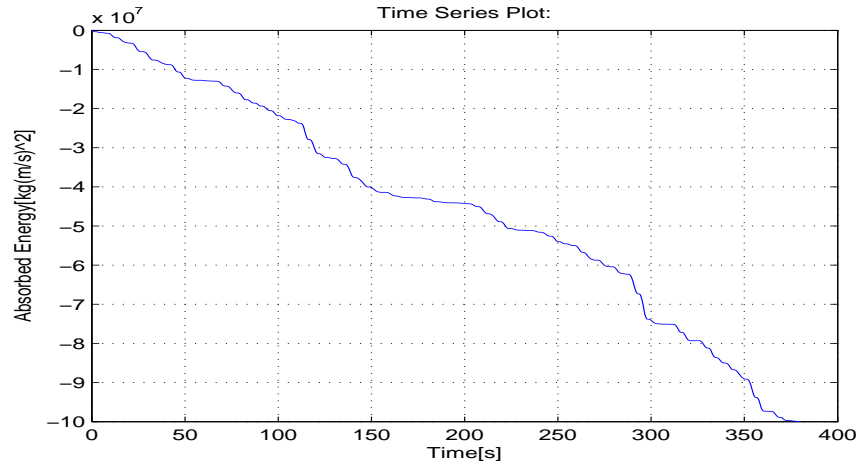


Figure 6.5 The energy absorbed using the passive loading control against time

The absorbed energy achieved by this system is around $-9.998 \times 10^{-7} \text{kg} \cdot (\text{m/s})^2$.

6.2.2 Velocity-tracking control

Velocity-tracking control is used to deliver the optimal velocity. The optimal relationship was given in section 5.2, and is as follows:

$$Z_{r,opt}(j\omega) = \frac{1}{2(B(j\omega) + K_v)} \quad (6.17)$$

The Laplace transform of eq(6.17) is:

$$Z_{r,opt}(s) = \frac{1}{2(B(s) + K_v)} = \frac{1}{Z_i(s) + Z_i(-s)} \quad (6.18)$$

The second-order approximated transfer function for the intrinsic impedance was also given in section 5.3. Hence, the constant approximated value of $Z_{r,opt}(j\omega)$ is 9.8936^{-6} . The controller plant was described by eq(5.6), where the lower level controller could be any given controller. Two different lower level controllers will be compared in the following section.

PID control

A PID controller can be used as a lower level controller to track the optimal velocity. The construction of the velocity-tracking control is as follows:

6.2 Comparison of absorbed energy using different control methods

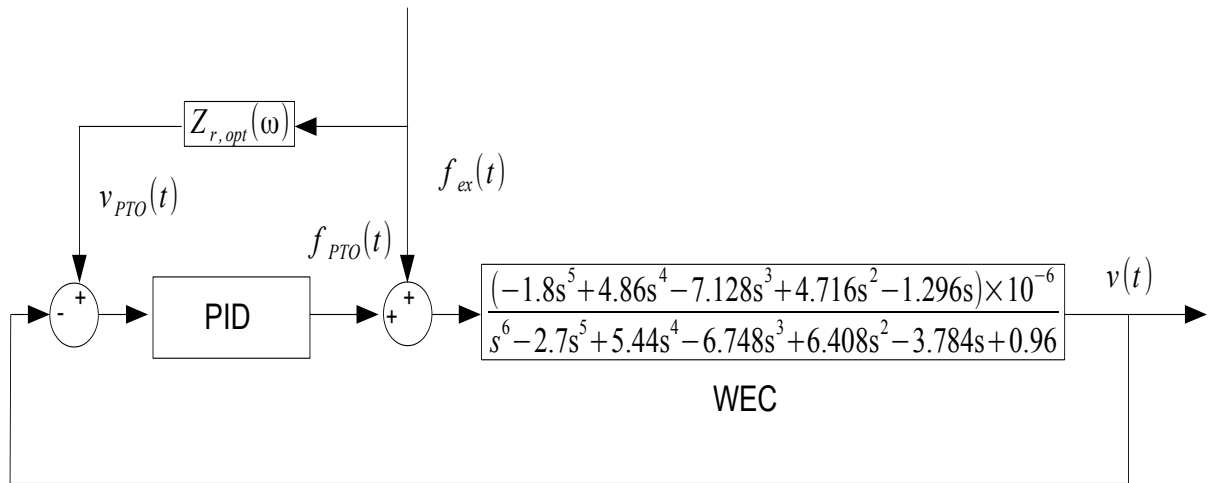


Figure 6.6 The construction of the velocity-tracking control using a PID controller

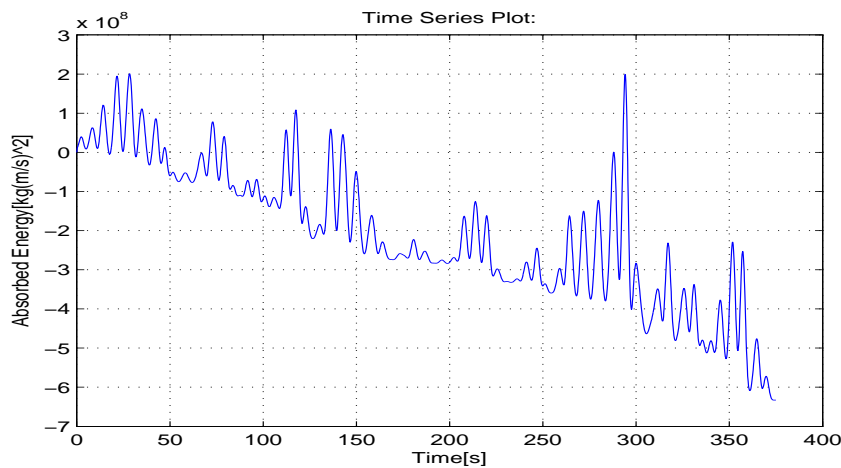


Figure 6.7 The energy absorbed by the velocity-tracking construction using a PID controller

The energy absorbed by the velocity-tracking control using a PID controller is shown in fig6.7. It can be seen that the energy absorbed from the velocity-tracking control is much higher than that for the passive loading control. It can achieve $-6.33 \times 10^8 \text{ kg} \cdot (\text{m/s})^2$.

IMC control

An internal model control (IMC) was introduced in reference [39], which could also be used instead of the previous PID control. The energy absorbed by the IMC controller will be given for comparison. More details about the IMC can be found in reference [39].

6.2 Comparison of absorbed energy using different control methods

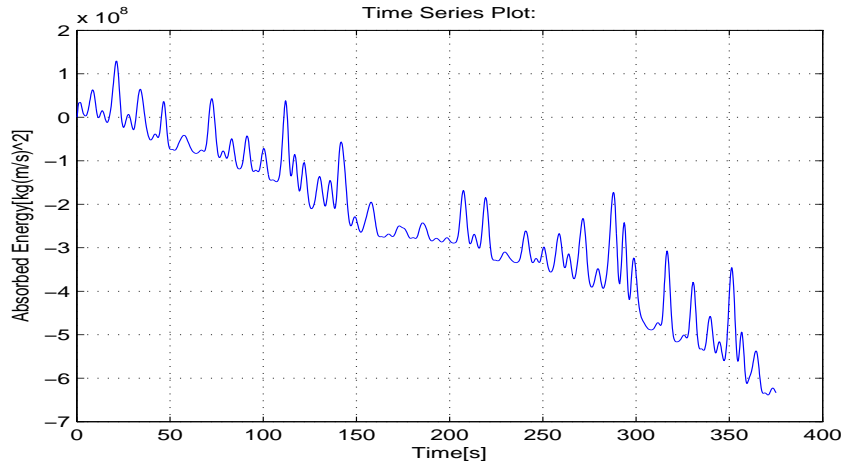


Figure 6.8 The energy absorbed by velocity-tracking using an IMC controller

The energy absorbed by velocity-tracking using an IMC controller is around $-6.386 \times 10^8 \text{ kg} \cdot (\text{m/s})^2$, which is slightly greater than that absorbed by the PID controller, at $-6.33 \times 10^8 \text{ kg} \cdot (\text{m/s})^2$.

6.2.3 Approximate complex conjugate control

Approximate complex conjugate control was described in section 3.4.1. The ideal situation is that the control impedance equals the complex conjugate of the intrinsic impedance. The frequency domain of the control force is given as follows:

$$F_{pto}(j\omega) = -Z_i^*(j\omega)V(j\omega) \quad (6.19)$$

Complex conjugate control can be implemented via eq(6.19); there is no need to calculate the optimal velocity for the system. The construction of complex conjugate control is given in fig6.9.

The energy absorbed by the complex-conjugate control construction is given in fig6.10. The maximum absorbed energy extracted from the feedback control construction is $-6.58 \times 10^8 \text{ kg} \cdot (\text{m/s})^2$. Thus, it can absorb more energy compared to the other control constructions and, certainly, more than the IMC control. Moreover, the complex conjugate control construction is simpler than the others, so complex conjugate control has been chosen for simulation in the following section.

6.3 Maximizing absorbed wave energy from a wave energy converter

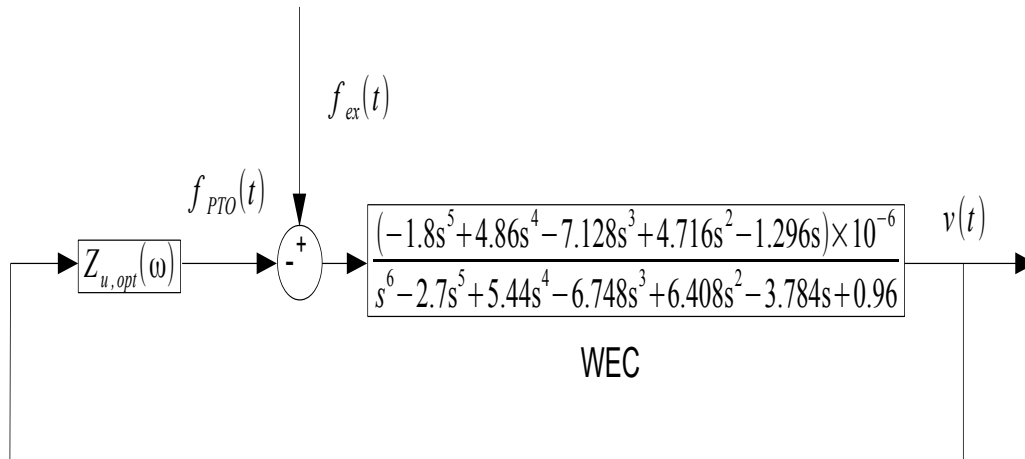


Figure 6.9 The construction of the feedback control

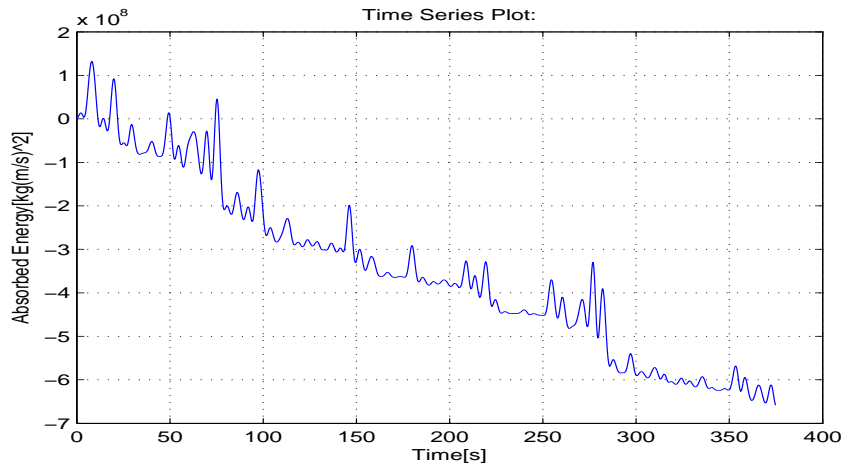


Figure 6.10 The energy absorbed by the feedback control

6.3 Maximizing absorbed wave energy from a wave energy converter

The optimal complex conjugate of the intrinsic impedance was calculated in section 5.2 using eq(5.16) as follows:

$$\begin{aligned}
 Z_{pto}(j\omega) &= Z_i^*(j\omega) \\
 &\cong \frac{s^6 - 2.7s^5 + 5.44s^4 - 6.748s^3 + 6.408s^2 - 3.784s + 0.96}{-1.8 \times 10^{-6}s^5 + 4.86 \times 10^{-6}s^4 - 7.128 \times 10^{-6}s^3 + 4.716 \times 10^{-6}s^2 - 1.296 \times 10^{-6}s} \quad (6.20)
 \end{aligned}$$

6.3 Maximizing absorbed wave energy from a wave energy converter

And the bode plot of $Z_{pto}(j\omega)$ is as follows:

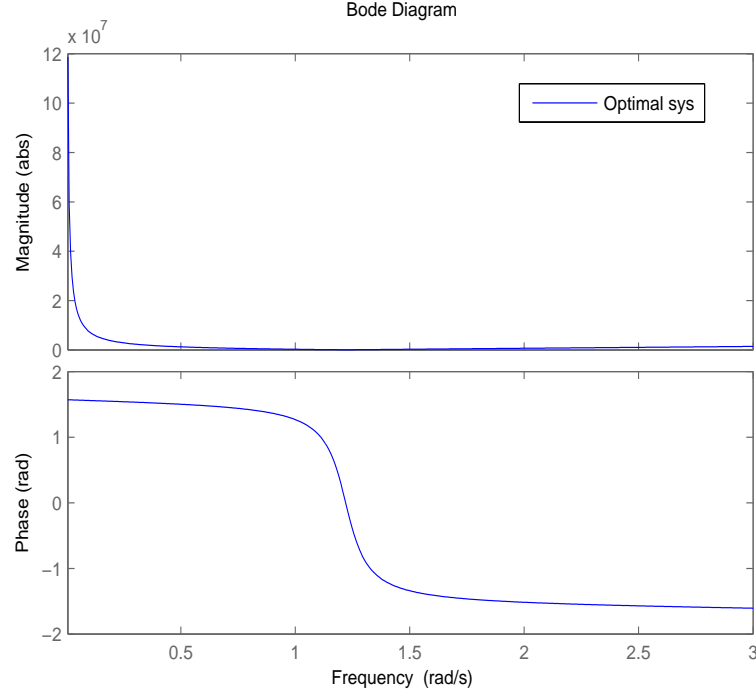


Figure 6.11 Bode plot of load impedance

Eq(6.20) was shown to be non-causal in chapter 3. Hence, it can be approximated via the Nelder–Mead method to gain a causal approximation.

A cost function, $(J(\cdot))$, has been proposed to calculate the difference between the optimal control impedance, $Z_{pto}(s)$, and the approximated control impedance, $G(s)$:

$$J(G(s)) = \int_{-\infty}^{\infty} |Z_{pto}(s) - G(s)|^2 \quad (6.21)$$

where $G(s)$ is the different approximated transfer functions used to determine the control impedance; the Matlab code **fminsearch** can be used to calculate the cost function above.

The Nelder–Mead method

As mentioned earlier, the Matlab function **fminsearch** can be used to calculate the cost function. The Nelder-Mead simplex method is the inside algorithm of the Matlab command **fminsearch**. The theory underlying the Nelder-Mead simplex method will be presented in the following section. However, the calculation of the cost function only relies on the the Matlab command **fminsearch**.

6.3 Maximizing absorbed wave energy from a wave energy converter

The Nelder–Mead method can be used to find the local minima of a function without requiring any derivative information [63, 85].

The Nelder–Mead method is first used to construct an initial simplex. The simplex is N -dimensional and contains $N + 1$ test variables. It compares the value of the objective function with each test variable. It essentially searches for a new test variable to replace one of its earlier test variables, the concept being to replace the worst-performing test variable with a new variable on the midpoint of the line [63] between the best-performing and the second best performing test variables. If the value of the function with the new test variable is smaller than the current best test variable, then another new test variable is found along the extension line between the worst performing variable and the midpoint; the new test variable should move away from the worst variable. By contrast, if the value of the function with the new test variable is larger than the second-worst performing variable, then the search would move towards the worst variable.

The processes above can be classified by the four steps described in reference [78]. The first step is called the reflection, which creates a new variable that is reflected through the centroid of the best, the worst, and the second-worst variables. If the value of the function using this new variable is between the best and the second-worst variable, then the iteration process stops. The second step is called the expansion. It is used to find a new variable when the value of the function is smaller than the function with the best variable. The third step is called the contraction and is the opposite of the expansion step. The last step is called shrinking. The worst and the second-worst variables shrink towards the best variable.

The first-order approximated transfer function for the control impedance can be obtained by recalling the cost function, eq(6.21), as follows:

$$\hat{Z}_{pto,1st}(s) = \frac{4.742 \times 10^4 s - 7.332 \times 10^5}{s} \quad (6.22)$$

The first approximated transfer function with second-order numerators can be calculated using the Nelder–Mead method:

$$\hat{Z}_{pto,2nd}(s) = \frac{-5.264 \times 10^5 s^2 + 4.742 \times 10^4 s - 7.418 \times 10^5}{s} \quad (6.23)$$

The second-order approximated transfer function with third-order numerators can be obtained using the same process:

$$\hat{Z}_{pto,3rd}(s) = \frac{-4.048 \times 10^4 s^3 - 5.248 \times 10^5 s^2 + 0.804 \times 10^4 s - 7.419 \times 10^5}{0.1003s^2 + s} \quad (6.24)$$

6.3 Maximizing absorbed wave energy from a wave energy converter

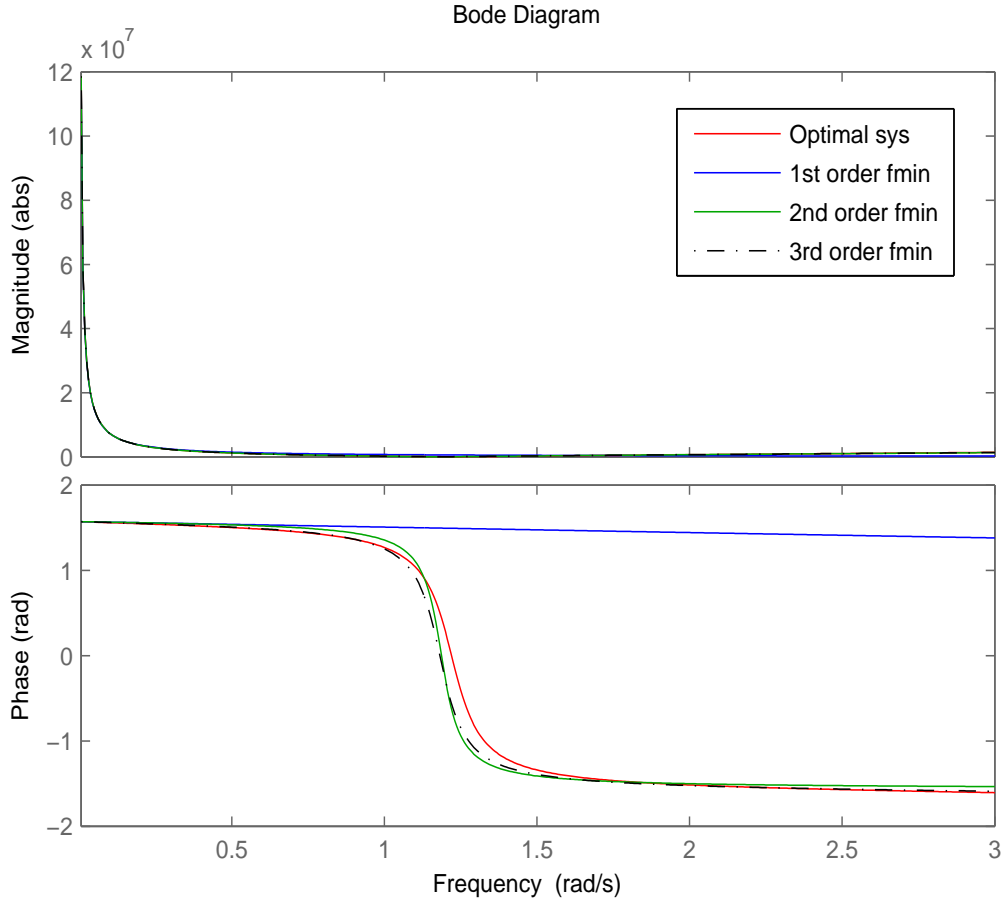


Figure 6.12 Comparison between the different order approximated transfer functions using the Nelder-Mead method

The comparison of the bode diagram of the transfer functions eq(6.22), (6.23), and (6.24) set out above with the optimal control impedance given as eq(6.20) in fig6.12.

However, establishing the approximated transfer functions eq(6.22), (6.23), and (6.24) are not the objective of this project. Rather, it is to maximise the total energy converted by the WEC. In order to do this, the cost function, eq(6.13), should be recalled:

$$J(E) = -\frac{1}{2\pi} \int_{-\infty}^{\infty} \frac{\hat{Z}_{pto}(s)}{|\hat{Z}_{pto}(s) + Z_i(s)|^2} \Phi_{F_{ex}}(s) \quad (6.25)$$

which relates to eq(6.13). The previous different order approximated transfer functions can be assumed to be the initial transfer functions for eq(6.25).

The Nelder-Mead method is again used to improve the accuracy of the first-order approximated transfer function. The comparative result is given in fig6.13.

6.3 Maximizing absorbed wave energy from a wave energy converter

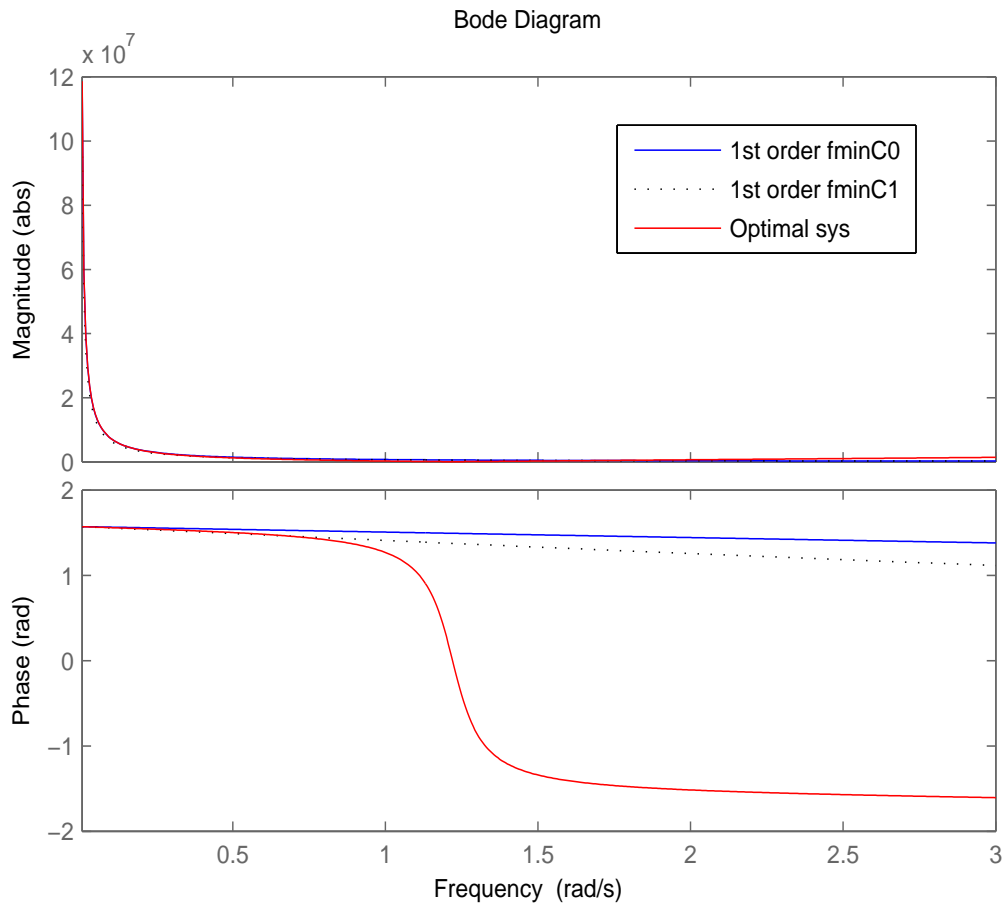


Figure 6.13 Comparison of first-order transfer functions using the Nelder-Mead method

The cost function using the first-order transfer function was found to be $-5.7377e^6$. The new first-order transfer function is given as follows:

$$\tilde{Z}_{pto,1st}(s) = \frac{9.89 \times 10^4 s - 7.436 \times 10^5}{s} \quad (6.26)$$

If eq(6.23) is substituted into eq(6.25), then the new first-order approximated transfer function with second-order numerator can be calculated using the Nelder-Mead method:

$$\tilde{Z}_{pto,2nd}(s) = \frac{-4.076 \times 10^5 s^2 + 8.244 \times 10^4 s - 7.407 \times 10^5}{s} \quad (6.27)$$

The comparison of two first-order approximated transfer functions are given in fig6.14.

6.3 Maximizing absorbed wave energy from a wave energy converter

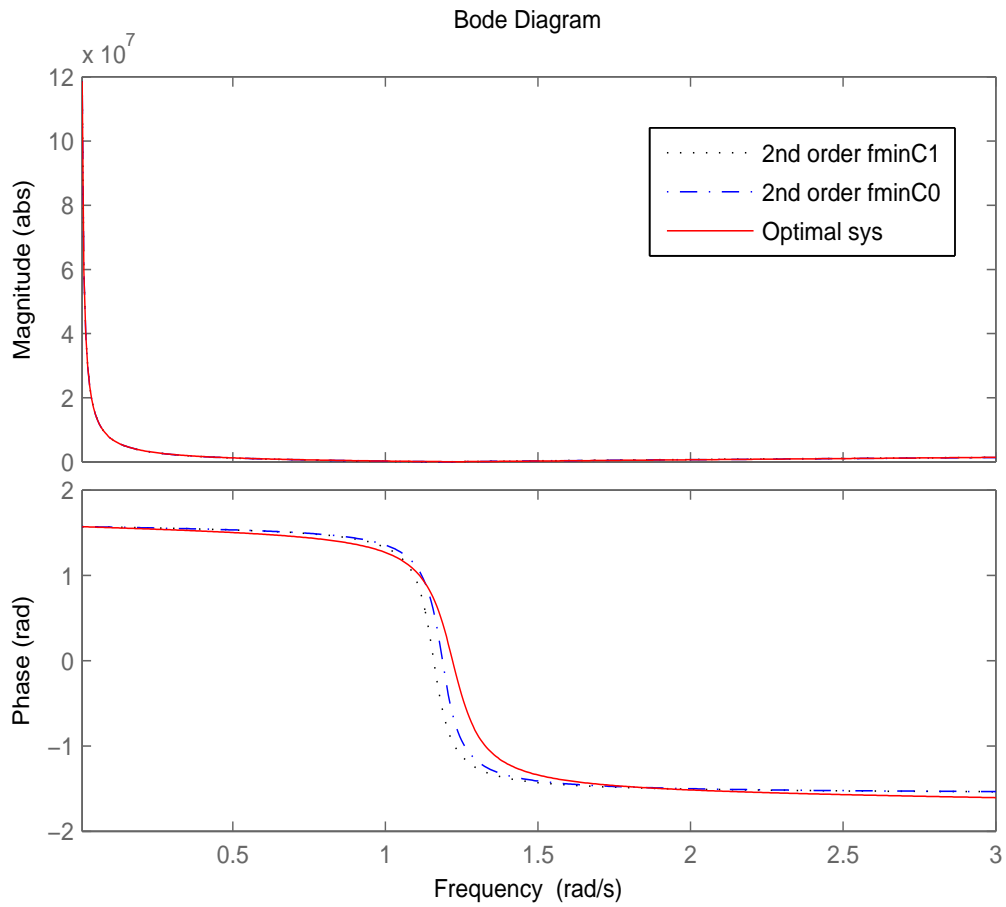


Figure 6.14 Comparison of second-order transfer functions using the Nelder-Mead method

The cost function $J_{2nd}(E)$ for the second-order transfer function is equal to $-7.1532e6$.

The new second-order transfer function with third-order numerator can be directly found using the same method. Hence, the new second-order transfer function can be calculated using eq(6.25) and is obtained as follows:

$$\hat{Z}_{pto}(s)_{3rd} = \frac{-4.374e^4 s^3 - 4.776e^5 s^2 + 8272s - 7.416e^5}{0.1007s^2 + s} \quad (6.28)$$

The result is given in fig6.15. The cost function, $J_{3rd}(E)$, is the smallest of all the cost functions; its value is $-7.1853e6$. It means the cost function $J_{3rd}(E)$ closest to the optimal system.

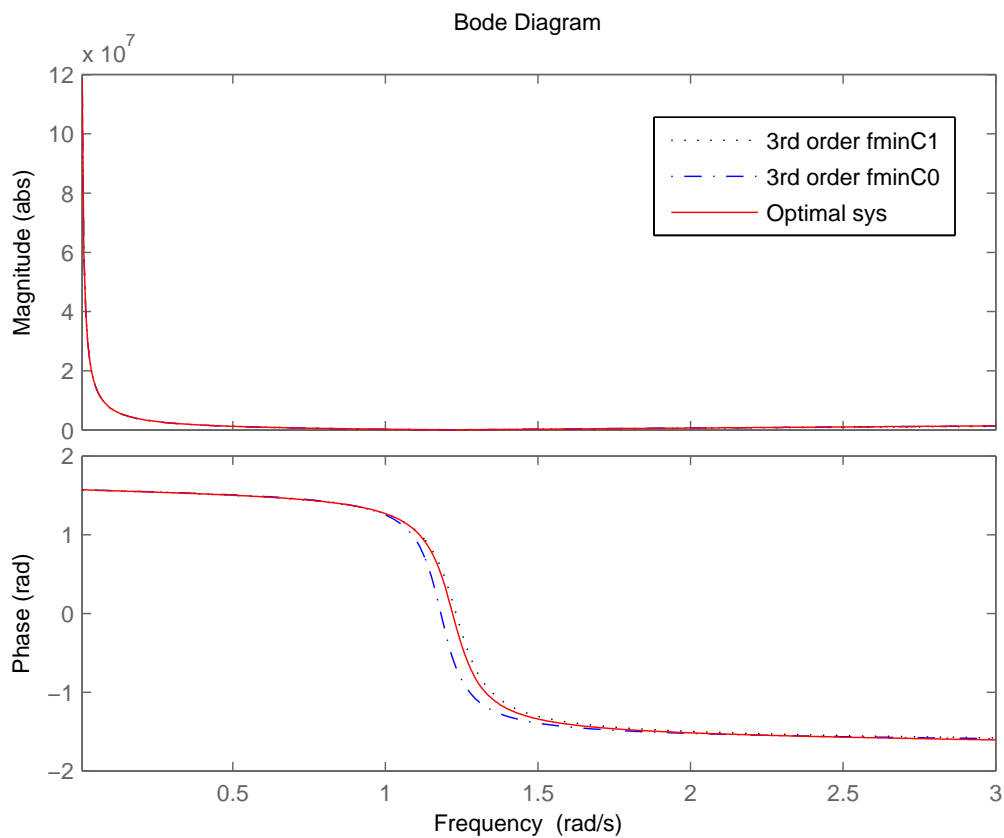


Figure 6.15 Comparison of the third-order transfer functions using the Nelder-Mead method

6.4 Mechanical network realisation for WEC

6.4.1 Background and introduction to mechanical network realisation

Mechanical network realisation will be introduced in this section via a one-degree of freedom floating system for wave energy conversion, which is one type of mechanical one-port network. The inerter was introduced as the mass element with an applied force that is proportional to the relative acceleration across the terminal networks [87, 100]. Mass is an element of an ideal mechanical one-port network [86], assuming that such a network consists of elements such as springs, masses, and dampers. Similarly, the electrical system involves an inductor, resistance, and capacitor. The force-current analogy is used to present the relationship between them, and was introduced in reference [86] as follows:

force \leftrightarrow *current*
velocity \leftrightarrow *voltage*
spring \leftrightarrow *inductor*
damper \leftrightarrow *resistor*
mass \leftrightarrow *capacitor*

The reason for the mass-capacitor analogy is that this follows Newton's Second Law. It defines one terminal as the centre of mass, and the other as a fixed point in the inertial frame. Hence, the mass can be seen as a grounded capacitor.

An RLC circuit can be used to express the relationship presented in section 6.4.1. The equation of the inductor is given as follows:

$$\frac{di}{dt} = \frac{1}{L}(v_2 - v_1) \quad (6.29)$$

where L is the inductance and v_1, v_2 it the voltage across the inductance.

The capacitor is given as:

$$i = C \frac{d(v_2 - v_1)}{dt} \quad (6.30)$$

where C is the capacitance.

The last element of the RLC circuit is the resistor, which is given as follows:

$$i = \frac{1}{R}(v_2 - v_1) \quad (6.31)$$

where R is the resistance.

The corresponding mechanical system is a mass-spring-damper system. It includes a spring, mass, and damper with the following definitions:

$$\frac{dF}{dt} = \frac{1}{k}(v_2 - v_1) \quad (6.32)$$

$$F = m \frac{d(v_2 - v_1)}{dt} \quad (6.33)$$

$$F = c(v_2 - v_1) \quad (6.34)$$

6.4 Mechanical network realisation for WEC

where the F is the force, k is the stiffness, v is the velocity, m is the mass and c is the load resistance.

Hence, it can be seen that the force acting on the mass can be expressed as follows:

$$F = a(\dot{v}_2 - \dot{v}_1) \quad (6.35)$$

where a is called the inertance, in units of kilograms, and \dot{v} is the acceleration. The stored energy in the inerter is also given as follows:

$$E = \frac{1}{2}a(v_2 - v_1)^2 \quad (6.36)$$

As mentioned in reference [86], the inerter can be seen as a kind of mass. However, it has to meet several requirements. Firstly, the inerter device should have a small mass, and this is independent of the required value of the inertance. Secondly, there is no need to connect the mechanical ground. Thirdly, it has a finite linear travel. The last condition is that inerter should satisfy any motion and direction. An inerter could be one solution to the realisation of a mechanical network.

The mass term is used in the WEC power take-off device, which may have two basic connections [100]:

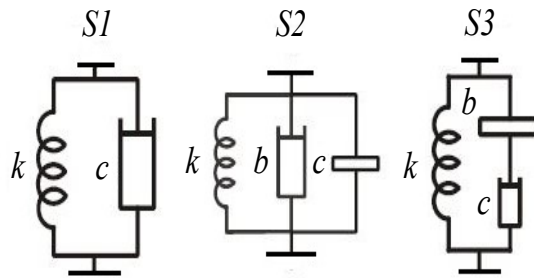


Figure 6.16 WEC power take-off devices: S1 basic ideal, S2 parallel idea with mass term, S3 serial idea with mass term

The force given by the above configurations can be given as follows:

$$S1 : F_u(s) = \left(\frac{k}{s} + c\right)V(s) \quad (6.37)$$

$$S2 : F_u(s) = \left(\frac{k}{s} + c + bs\right)V(s) \quad (6.38)$$

6.4 Mechanical network realisation for WEC

$$S3 : F_u(s) = \left(\frac{k}{s} + \frac{1}{\frac{1}{bs} + \frac{1}{c}} \right) V(s) \quad (6.39)$$

where $S2$ is a basic parallel connection with the mass term, and $S3$ is a basic serial connection.

There are several different connections that can be obtained using the above basic connection. They can produce different order Laplace transforms, and can be written as follows:

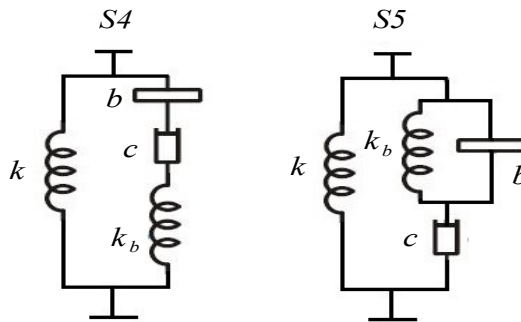


Figure 6.17 Configurations $S4$ and $S5$

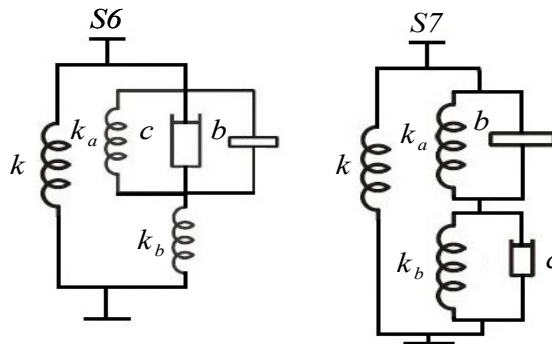


Figure 6.18 Configurations $S6$ and $S7$

The forces given by the above configurations can be shown as follows:

$$S4 : F_u(s) = \left(\frac{k}{s} + \frac{1}{\frac{s}{k_b} + \frac{1}{cs} + \frac{1}{b}} \right) V(s) \quad (6.40)$$

$$S5 : F_u(s) = \left(\frac{k}{s} + \frac{1}{\frac{1}{\frac{k_b}{s} + bs} + \frac{1}{c}} \right) V(s) \quad (6.41)$$

The forces given by the $S6$ and $S7$ configurations are given as follows:

$$S6 : F_u(s) = \left(\frac{k}{s} + \frac{1}{\frac{s}{k_b} + \frac{1}{\frac{k_a}{s} + c + bs}} \right) V(s) \quad (6.42)$$

$$S7 : F_u(s) = \left(\frac{k}{s} + \frac{1}{\frac{1}{\frac{k_a}{s} + bs} + \frac{1}{\frac{k_b}{s} + c}} \right) V(s) \quad (6.43)$$

These correspond to second-, third-, fourth- and fifth-order transfer functions.

Note that the $S1$ configuration, eq(6.37), can be used to express the spring-damping system. The $S2$ configuration can be used to express the mass-spring-damping system. It has been shown that non-causality can be overcome with a second-order model in section 5.3, which means that such a system can easily deal with a WEC system. It is worth pursuing high-order transfer functions with mass that may potentially improve the performance of the control.

6.4.2 Mechanical network realisation for WEC systems and simulation results

The wave energy conversion system has a similar structure to a suspension strut, the latter being one example of mechanical network realisation [86, 100]. Maximum power absorption from the WEC system requires the excitation force and velocity to be in phase. This is also the case for the optimal performance of a suspension strut with a mass term. However, in a suspension strut all elements are passive; the design of mechanical networks for PTO includes some active elements that are negative.

A typical oscillating system for the WEC was given in section 2.3.1. Hence, a basic model for the PTO device that includes a mass term is shown in fig6.19. The equation of motion in the Laplace-transformed domain is:

$$ms^2z = F_{ex}(s) - F_r(s) - F_s(s) - F_v(s) - sY(s)z \quad (6.44)$$

where m is the buoy's mass, k is the spring stiffness, c is the damper, and b is the mass.

The mechanical admittance, $Y(s)$, is the PTO impedance, $Z_{pto}(s)$. The optimal control is a fifth-order transfer function, which is given in eq(6.20). The simple spring-damper system with a mass does not meet the requirements for optimal control, and more complex configurations should be considered in the following discussion. Firstly, a general form of a

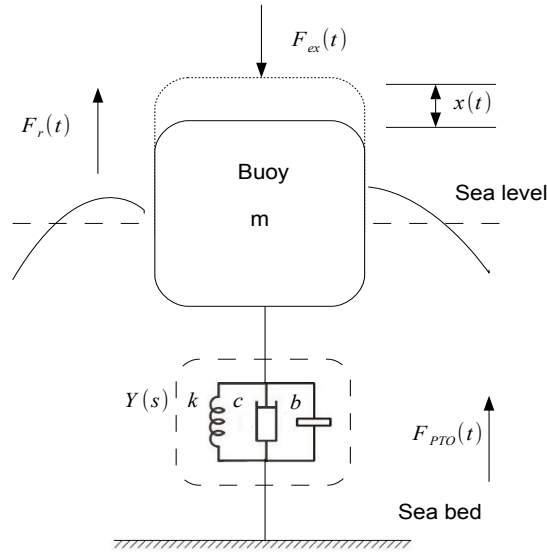


Figure 6.19 PTO device includes mass term

real rational function can be considered as follows:

$$Y(s) = k \frac{a_0 s^2 + a_1 s + 1}{s(d_0 s^2 + d_1 s + 1)} \quad (6.45)$$

Secondly, [86] the Brune Synthesis can be introduced to realise the admittance of eq(6.45). The first step of the Brune Synthesis is to remove the imaginary axis poles and zeroes of eq(6.45) [8, 86]. An increased complexity impedance with a mass term can be considered. Thus, eq(6.45) can be rewritten as:

$$Y(s) = k \frac{a_0 s^2 + a_1 s + 1}{s(d_0 s^2 + d_1 s + 1)} + ms = \frac{k}{s} + \frac{k(\beta_2 s + \beta_3)}{d_0 s^2 + d_1 s + 1} + ms \quad (6.46)$$

and the second term of eq(6.46) can be decomposed as follows:

$$\frac{d_0 s^2 + d_1 s + 1}{k(\beta_2 s + \beta_3)} = \frac{d_0}{\beta_2 k} s + \frac{\beta_1 s + \beta_2}{\beta_2 k(\beta_2 s + \beta_3)} \quad (6.47)$$

$$= \frac{d_0}{\beta_2 k} s + \frac{\beta_1}{\beta_2^2 k} s + \frac{\beta_4 / (\beta_2^2 k)}{\beta_2 s + \beta_3} \quad (6.48)$$

$$= \frac{d_0}{\beta_2 k} s + \left(k\beta_3 + \frac{\beta_4 k s}{\beta_1 s + \beta_2} \right)^{-1} \quad (6.49)$$

6.4 Mechanical network realisation for WEC

where β_1 equals to $a_0 d_1 - a_1 d_0$, β_2 is equal to $a_0 - d_0$, β_3 equals to $a_1 - d_1$, and β_4 equals to $\beta_2^2 - \beta_1 \beta_3$.

Eq(6.48) and eq(6.49) give the admittance, $Y(s)$, which is used to replace the mass-spring-damper of the PTO device in fig6.19. The system with admittance in eq(6.48) can be used to provide the following model: [86]:

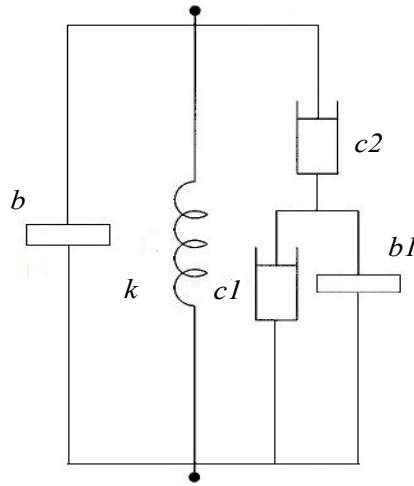


Figure 6.20 System with admittance 6.48

and the system with admittance in eq(6.49) provides the following model, as shown in figure 6.21:

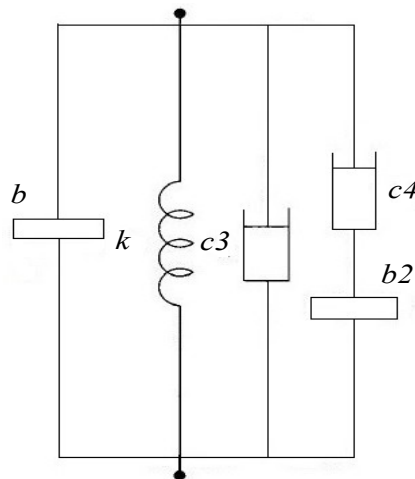


Figure 6.21 System with admittance 6.49

6.4 Mechanical network realisation for WEC

Each element of the model can be calculated as shown below [86]:

$$c1 = \frac{k\beta_2^2\beta_3}{\beta_4} \quad c2 = \frac{k\beta_2^2}{\beta_1} \quad b1 = \frac{k\beta_2^3}{\beta_4} \quad (6.50)$$

$$c3 = k\beta_3 \quad c4 = \frac{k\beta_4}{\beta_1} \quad b2 = \frac{k\beta_4}{\beta_2} \quad (6.51)$$

To consider the potential benefit of the mass term utility, simple spring-damper and mass-spring-damper systems can be compared; the maximisation of useful energy is the objective in this section. The energy absorbed is a combination of useful energy and reactive energy.

$$E_{abs} = E_{useful} + E_{reactive} \quad (6.52)$$

The approximated transfer functions calculated by the Nelder-Mead method are used in the following for convenience. The first-order transfer function of the PTO impedance of the simple spring damper is given by eq(6.26):

$$Z_{pto}(s)_{SD} = \frac{9.89e^4s - 7.436e^5}{s} \quad (6.53)$$

The spring damper system can be given as:

$$Z_{pto}(s)_{SD} = \frac{cs + k}{s} \quad (6.54)$$

Hence, the optimal values of spring stiffness, $k = -7.436e^5 \text{ kg/s}^2$, and the damper constant, $9.89e^4 \text{ KNsm}^{-1}$, can be obtained.

For the mass-spring-damper system with a positive real admittance of $Y(s)$, the transfer function of the PTO impedance of the system is given as follows:

$$Z_{pto}(s)_{MSD} = \frac{-4.076 \times 10^5 s^2 + 8.244 \times 10^4 s - 7.407 \times 10^5}{s} \quad (6.55)$$

The value of each element of the mass-spring-damper system can be calculated using eq(6.55) as follows:

$$b = -4.075e^5 \text{ kg} \quad k = -7.407e^5 \text{ kg/s}^2 \quad c = 8.244e^4 \text{ KNsm}^{-1}$$

6.4 Mechanical network realisation for WEC

Note that the parameters b and k are negative, and thus correspond to active elements, while the damper with the positive parameter c is the passive element absorbing energy.

The PTO realisation of impedance eq(6.55) is given as per fig6.22.

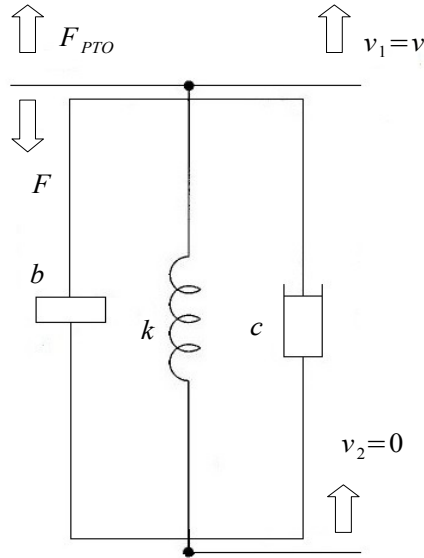


Figure 6.22 System with admittance 6.55

where v_1 and v_2 are used to denote the velocities at the terminals, and F denotes the force acting on the PTO. The control force, F_{PTO} , is equal to F though with the opposite sign.

The other optimised second-order approximated transfer function was given in eq(6.28) as follows:

$$Z_{pto}(s)_{MSD2} = \frac{-4.374e^4 s^3 - 4.776e^5 s^2 + 8272s - 7.416e^5}{0.1007s^2 + s} \quad (6.56)$$

The mass, b , and stiffness, k , can also be estimated using eq(6.56) and eq(6.45) as follows:

$$\begin{aligned} b &= -4.931e^5 kg & k &= -7.407e^5 kg/s^2 & a_0 &= 7.02e^{-2} \\ a_1 &= -5.04e^{-2} & d_0 &= 0 & d_1 &= 8.54e^{-1} \end{aligned} \quad (6.57)$$

The other elements of the systems using eq(6.48) and eq(6.49) are given as follows:

$$\begin{aligned} c1 &= -43.842kNsm^{-1} & c2 &= 103.488kNsm^{-1} \\ b1 &= 2.818e^5 kg & c3 &= -76.066kNsm^{-1} \\ c4 &= 17.956kNsm^{-1} & b2 &= 8.483e^5 kg \end{aligned}$$

The block diagram for the simple spring-damper system can be illustrated as follows:

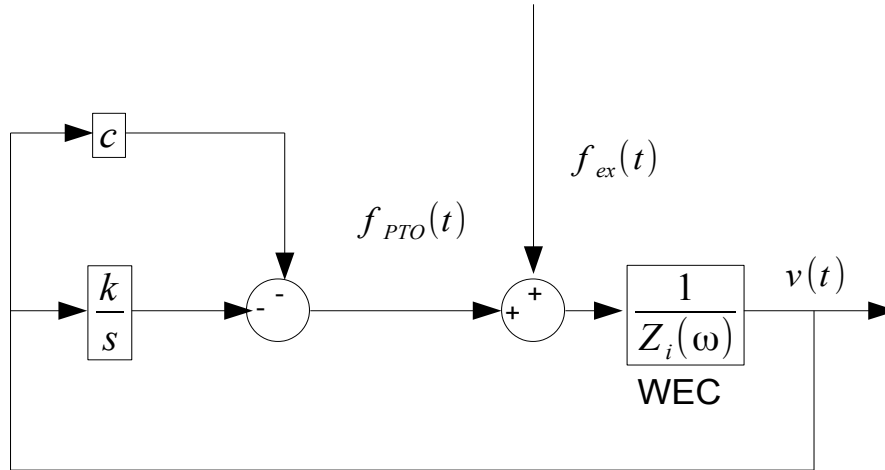


Figure 6.23 Block diagram of proposed spring-damper system

For comparison, the block diagram for the approximate complex conjugate control (spring-damper with mass) can also be given, as per figure 6.24:

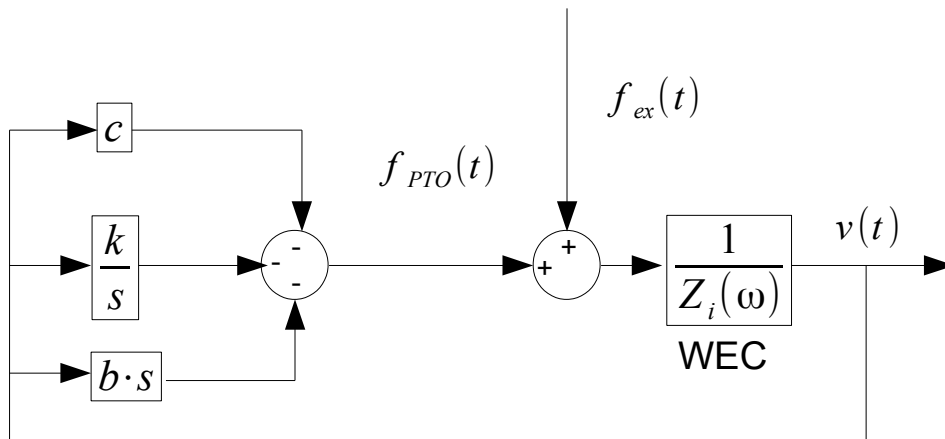


Figure 6.24 Block diagram of proposed complex conjugate control

This approach consists of the wave excitation force acting on the system. The velocity is generated by the combination of the wave excitation force and the PTO through a feedback complex conjugate control. The useful force, F_u , is generated by the positive damper resistance multiplied by the velocity of the buoy.

6.4 Mechanical network realisation for WEC

The real-time solutions with admittances eq(6.48) and eq(6.49) are presented below, whilst the block diagram of the control with admittance6.48 is also shown in fig6.25. The construction of the control with admittance6.48 is similar to the complex conjugate control. However, there is another force, F_i , acting on the system that is generated by damper $c1$ and inerter $b1$. Moreover, the force F_i moves in the opposite direction to the useful force, F_u .

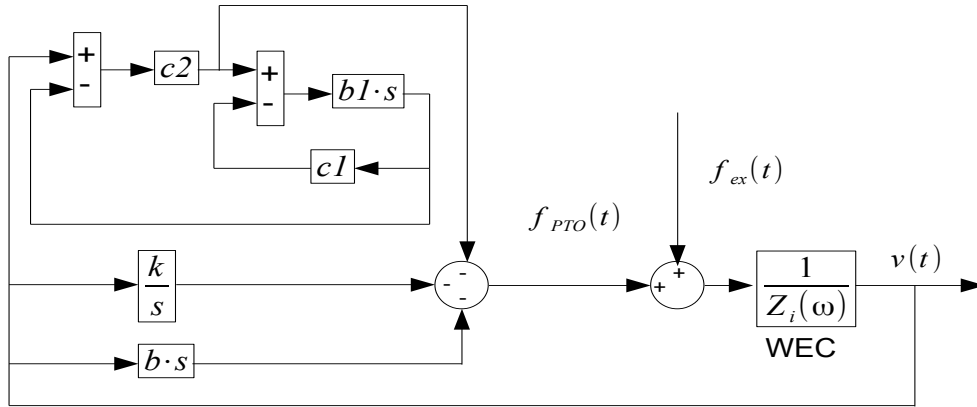


Figure 6.25 Block diagram of proposed control with admittance6.48

The block diagram for the proposed control with admittance6.49 is given as follows:

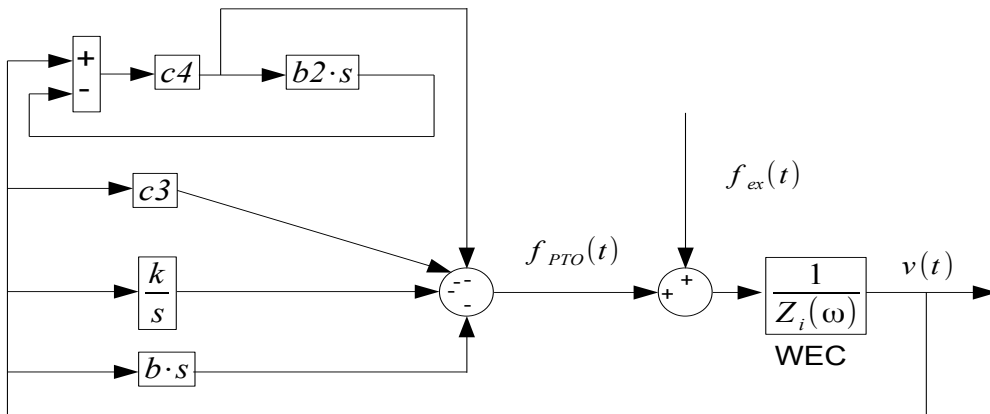


Figure 6.26 Block diagram of proposed control with admittance6.49

It has a similar construction to the admittance in eq(6.48). The force F_i acts on the system, which is generated by the damper $c3$ and inerter $b2$.

By recalling eq(6.52), the absorbed energy is the sum of the reactive and useful energies. The absorbed energy is used to denote the energy absorbed from the sea by the PTO. The useful energy is used to denote the energy absorbed by the energy-absorbing element in each

6.4 Mechanical network realisation for WEC

design. The reactive energy is the energy produced by all other elements of the PTO. The energy has a negative sign, which corresponds to negative work being done by the PTO. The useful energy produced is always negative, whilst the reactive and absorbed energy can be positive or negative.

The absorbed energy extracted by these control systems is given in fig6.27.

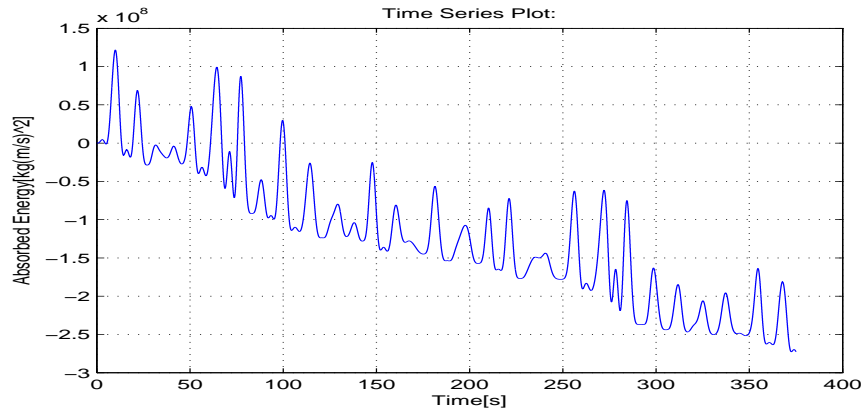


Figure 6.27 The absorbed energy extracted by the feedback control with the spring-damper system

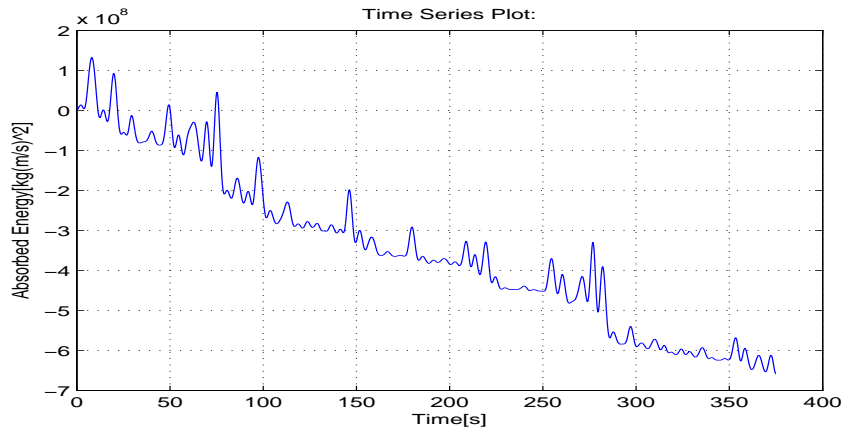


Figure 6.28 The absorbed energy extracted by the complex conjugate control with the mass-spring-damper system

The absorbed energy extracted by the mass-spring-damper system can achieve a maximum of $-6.58 \times 10^8 \text{ kg} \cdot (\text{m/s})^2$, while the absorbed energy extracted by the simple spring-damper system can only achieve $-2.72 \times 10^8 \text{ kg} \cdot (\text{m/s})^2$. The mass-spring-damper system using a mass (or inerter) can achieve 241.9% more absorbed energy than the SD system.

6.4 Mechanical network realisation for WEC

Systems with more complex configurations, such as admittance6.48 and admittance6.49 that are based on second-order approximated transfer functions with third-order numerators are expected to achieve better performances than the mass-spring-damper system. The absorbed energy extracted by these systems is given in fig6.29 and fig6.30.

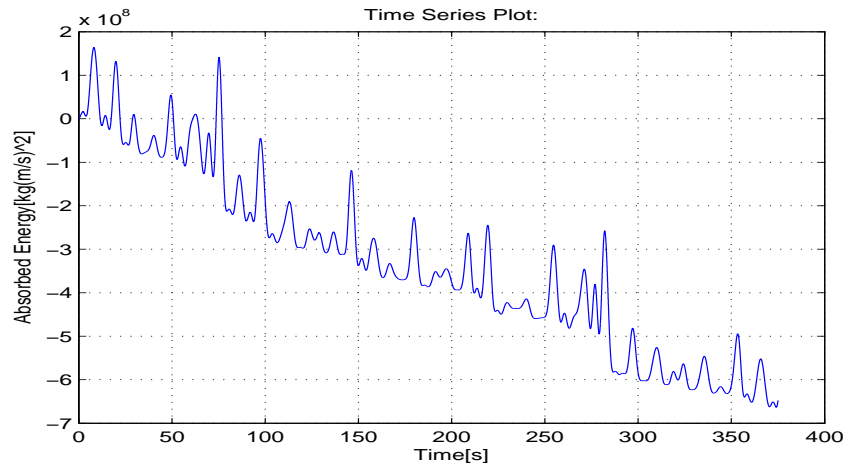


Figure 6.29 The absorbed energy extracted by the feedback control with admittance6.48

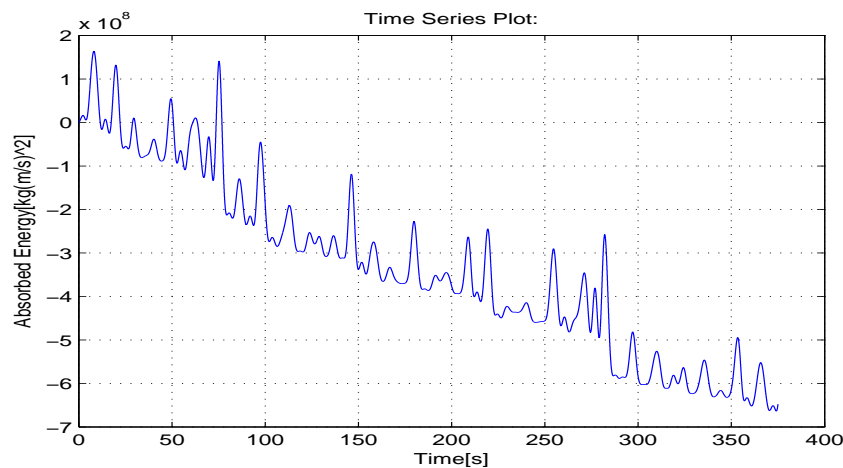


Figure 6.30 The absorbed energy extracted by the feedback control with admittance6.49

Both these systems are found to achieve an absorbed energy equal to $-6.64 \times 10^8 \text{ kg} \cdot (\text{m/s})^2$ due to the fact that they are both based on the same second-order approximated transfer function, eq(6.28). The absorbed energy is not dependent on its particular realisation, but rather on their PTO impedances. They achieve a slightly better performance than the mass-spring-damper system.

6.4 Mechanical network realisation for WEC

The other objective is to compare the maximum amount of useful energy that can be extracted by the different control systems. The useful energy comparison is as follows:

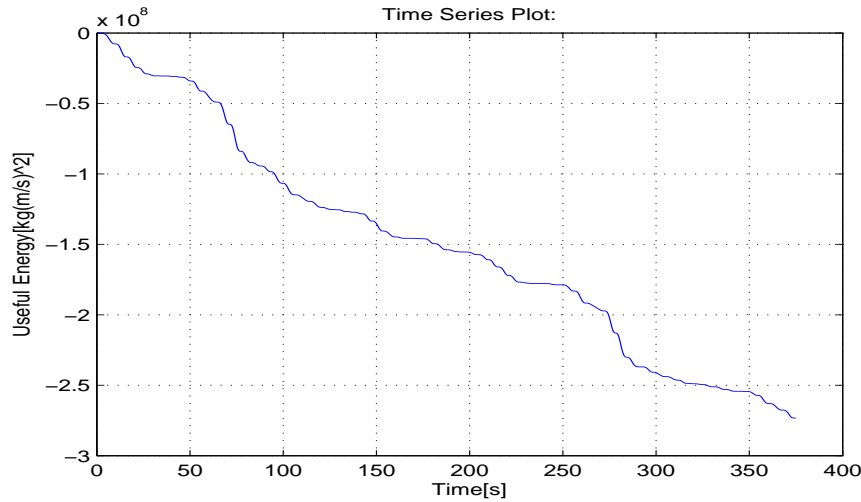


Figure 6.31 The useful energy extracted by the feedback control with the spring-damper system

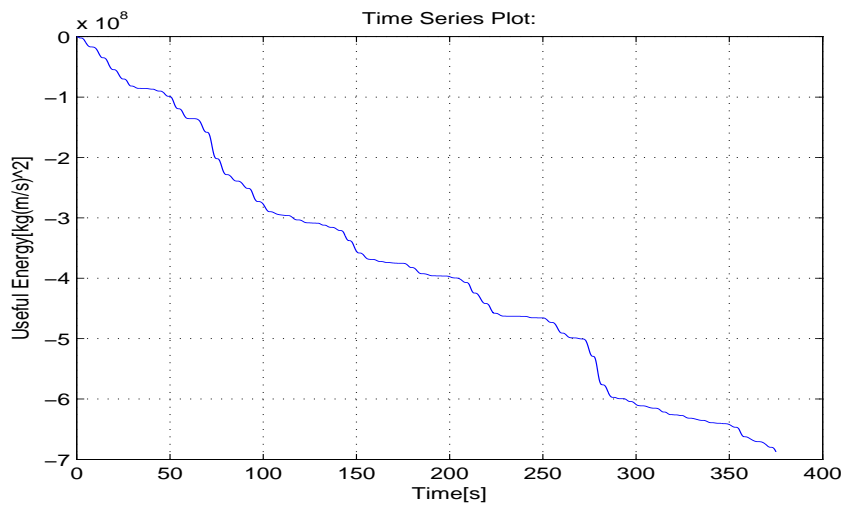


Figure 6.32 The useful energy extracted by the complex conjugate control with the mass-spring-damper system

The useful energy extracted by the SD system is $-2.74 \times 10^8 \text{ kg} \cdot (\text{m/s})^2$, whilst that extracted by the mass-spring-damper system is $-6.88 \times 10^8 \text{ kg} \cdot (\text{m/s})^2$. The absorbed energy extracted by admittance6.48 and admittance6.49 are identical; however, the amount of useful energy absorbed by each is different. The system with admittance6.48 absorbs a useful

6.4 Mechanical network realisation for WEC

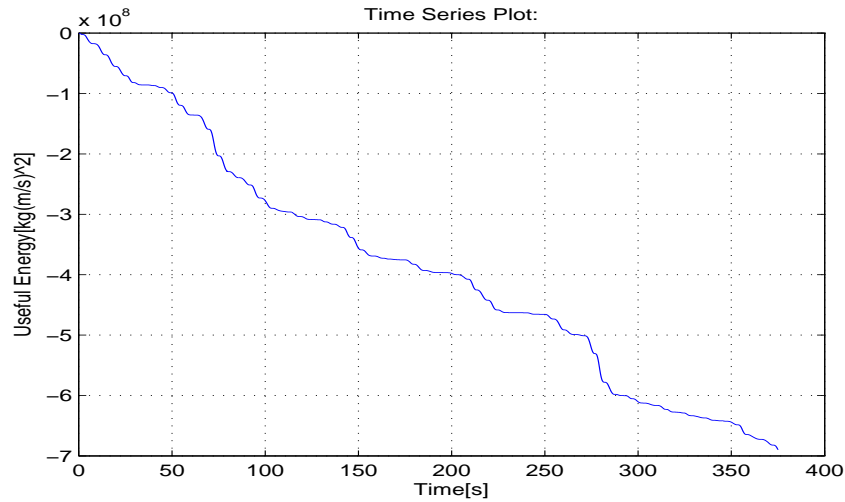


Figure 6.33 The useful energy extracted by the complex conjugate control with admittance6.48

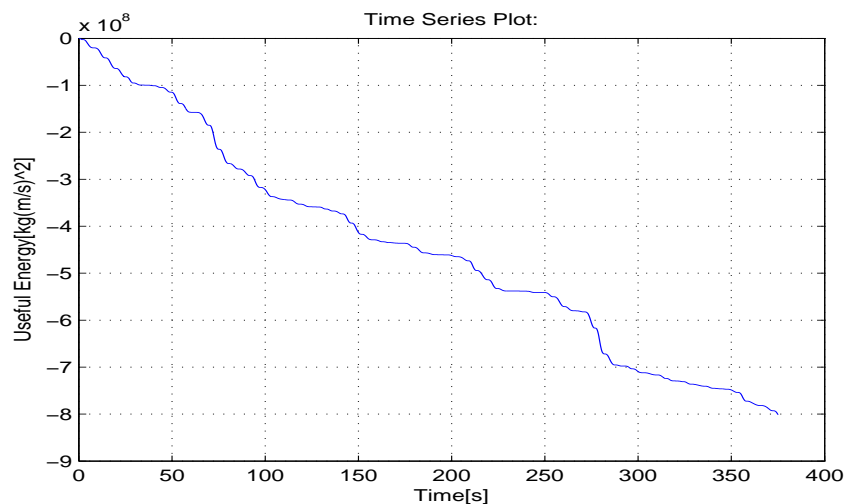


Figure 6.34 The useful energy extracted by the complex conjugate control with admittance6.49

energy of $-6.9 \times 10^6 \text{ kg} \cdot (\text{m/s})^2$, while the control system with admittance6.49 achieves a useful energy of $-8 \times 10^6 \text{ kg} \cdot (\text{m/s})^2$, that is, about 16% more than the admittance6.48.

The reactive energy for each system should be compared. The reactive energy from the SD system, which is generated by the spring term, is given in fig6.35. The reactive energy from the mass-spring-damper system is generated by the spring term and mass term. The reactive energy is given in fig6.36.

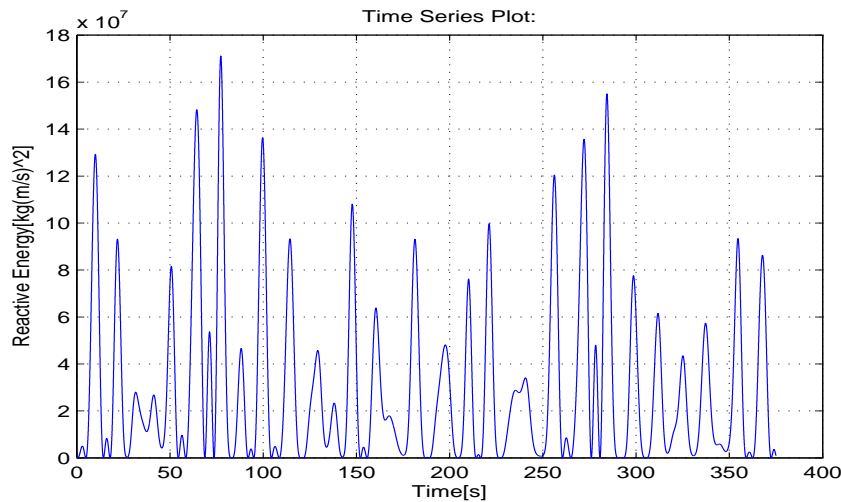


Figure 6.35 The reactive energy extracted by the feedback control with the SD system

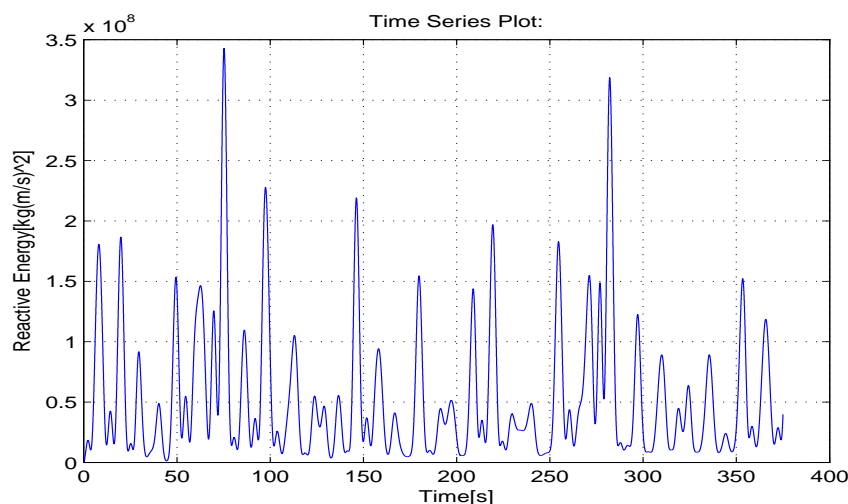


Figure 6.36 The reactive energy extracted by the feedback control with the mass-spring-damper system

The reactive energy from the system with admittance6.48 is more complex. It combines with the spring term, the mass term, and the force, F_i , that acts on damper c_1 and mass b_1 . The reactive energy is given in fig6.37.

The reactive energy from the system with admittance6.49 is similar to the system with admittance6.48. The force, F_i , acts on damper c_3 and mass b_1 such as to give the extra reactive energy. The total reactive energy can thus be given in figure6.38.

The system with admittance6.49 produces the most reactive energy of all the systems considered. Accordingly, it has the highest level of useful energy.

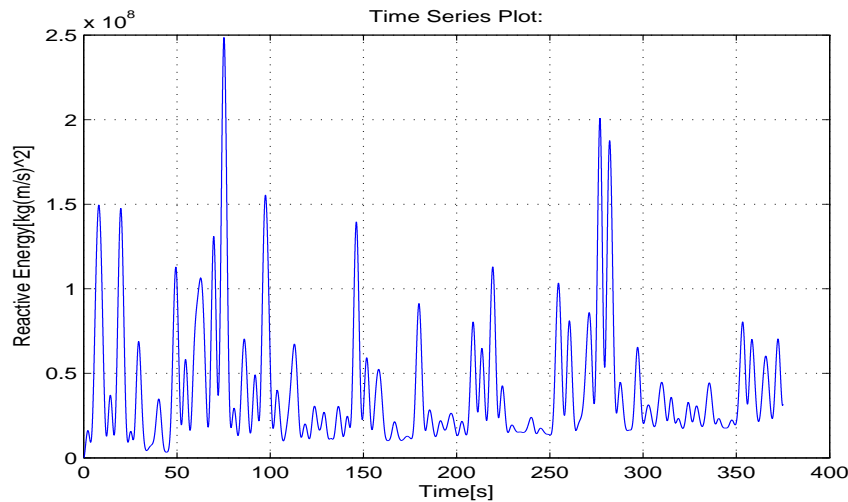


Figure 6.37 The reactive energy extracted by the feedback control with admittance6.48

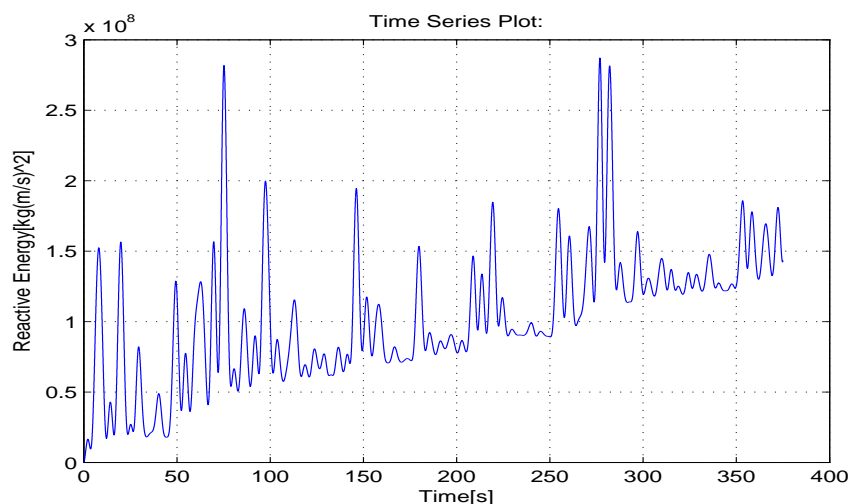


Figure 6.38 The reactive energy extracted by the feedback control with admittance6.49

The impedance eq6.53 produces the least useful energy, followed by the realisation of fig6.22, fig6.20, and the realisation of fig6.21. However, a large improvement in energy absorption can be obtained by increasing the complexity of the PTO design.

On the other hand, with respect to the basic impedance eq6.55, a small improvement in energy absorption can be obtained by increasing the complexity of the PTO design; this, however, spends more reactive energy. However, the realisation of fig6.20 is preferable to the realisation of fig6.21, since the former produces less reactive energy but with the same absorbed energy.

Table 6.1 Performance Table of Different Control Methods

	Absorbed Energy
The passive loading control	$-9.998 \times 10^{-7} \text{kg} \cdot (\text{m/s})^2$
The velocity-tracking control (PID)	$-6.33 \times 10^{-8} \text{kg} \cdot (\text{m/s})^2$
The velocity-tracking control (IMC)	$-6.386 \times 10^{-8} \text{kg} \cdot (\text{m/s})^2$
The approximate complex-conjugate control	$-6.58 \times 10^{-8} \text{kg} \cdot (\text{m/s})^2$

Table 6.2 Performance Table of Mechanical Network Realisation for WEC systems

	Absorbed Energy	Useful Energy
The spring-damper system	$-2.72 \times 10^{-8} \text{kg} \cdot (\text{m/s})^2$	$-2.74 \times 10^{-8} \text{kg} \cdot (\text{m/s})^2$
The mass-spring-damper system	$-6.58 \times 10^{-8} \text{kg} \cdot (\text{m/s})^2$	$-6.88 \times 10^{-8} \text{kg} \cdot (\text{m/s})^2$
Admittance eq6.48	$-6.64 \times 10^{-8} \text{kg} \cdot (\text{m/s})^2$	$-6.9 \times 10^{-8} \text{kg} \cdot (\text{m/s})^2$
Admittance eq6.49	$-6.64 \times 10^{-8} \text{kg} \cdot (\text{m/s})^2$	$-8 \times 10^{-8} \text{kg} \cdot (\text{m/s})^2$

6.5 Chapter summary

A comparison of the absorbed energy with different control methods was given in section 6.2. The performance table for different control methods was given in table 6.1. The non-optimal passive loading control was presented in section 6.2.1, and was subsequently used as a reference because it is convenient for modelling and simulation. The velocity-tracking control was introduced in section 6.2.2. It was used as a controller to track the error between the desired velocity and the real velocity. The PID and IMC (internal model control) controllers developed in reference [39] were used for comparative purposes. The complex conjugate control was given in section 6.3.3. This absorbed the most energy of all the control methods, and hence the design of the PTO followed the complex conjugate control.

The Nelder–Mead method **fminsearch** was introduced in section 6.2, which was used to find the approximated transfer functions for the control impedance. The cost function for the maximum absorbed energy was also presented in this section. The Nelder–Mead method was used to find a local minimum for the cost function $J(G(s))$ for the control impedance. The different order approximated transfer functions were then tested in order to draw a comparison in this regard. The bode diagram of approximated transfer functions was used to judge the performance. The higher order approximated transfer functions were shown to achieve better performance. The criterion $J(E)$ was then minimised with respect to different order approximated control impedances.

The mechanical network realisation for WEC was presented in section 6.4. The wave energy conversion system has a similar structure to a suspension strut [86, 100], though with the caveat that in a suspension strut, all elements are passive. The design of the

mechanical networks for PTO includes a number of active elements. There are several mechanical network realisations given in this section. An inerter could be one solution for mass realisation. They can be expressed with different order transfer functions. A simple second-order transfer function with a mass term can deal with complex conjugate control, and thus overcome the problems associated with non-causality. More complex configurations with masses are worth pursuing. Hence, an increased complexity impedance with two different mechanical network realisations was given for comparison.

The spring-damper system, mass-spring-damper system, and systems with complexity admittances were used for simulations in section 6.4.2. The performance table for these systems for WEC is given in table 6.2. A comparison of the absorbed energy extracted by these admittances was also given in this section. Note that the approximate complex-conjugate control is the same as the mass-spring-damper system. Hence, the absorbed energy for the approximate complex-conjugate control shown in table 6.1 and the absorbed energy of the mass-spring-damper system have the same value. The control systems with admittances 6.48 and 6.49 achieved the greatest absorbed energy of all the control systems, which can be seen in table 6.2. However, the control system with admittance 6.48 spends less reactive energy compared to that with admittance 6.49, so it can be said that the control system with admittance 6.48 has the best overall performance.

Chapter 7

Test with real ocean data

7.1 Chapter overview

First, real dataset will be described in section 7.2. Power spectra and wave elevations will also be presented. Secondly, real ocean data will be tested with the predictors introduced in chapter 4. The performance of the predictors in a real ocean will be discussed. Finally, the controllers proposed in chapter 6 will be tested with real ocean data in section 7.4. The energies absorbed and energies produced by the associated impedances will be discussed in terms of their use with real ocean data.

7.2 Description of real ocean data and wave spectrum

The Irish Marine Institute has provided real wave data sets from two different locations [52]. One of the datasets was collected from Berth, which is located on the west coast of Ireland; the longitude and latitude of this location is $54^{\circ}33'N$, $10^{\circ}08'W$. Datasets were collected in 2012. The sampling frequency used was $1.28Hz$, with data consisting of two 30-minute record sets collected each hour. This means that each dataset contains 2304 data. The second data were also collected in Galway Bay near Berth, at a longitude and latitude of $53^{\circ}13'N$, $9^{\circ}16'W$. This buoy also collected two 30 minute record sets each hour with a sampling frequency of $1.28Hz$, again for the year 2012. The last buoy was located at Pico Island, which is in the Atlantic Ocean. The longitude and latitude of Pico Island is $38^{\circ}33'N$, $28^{\circ}34'W$. Data also consists of two 30 minute record sets for each hour with a sampling frequency $1.28Hz$, though these were collected in 2008. Galway Bay has low energy sea states as a fact of its location; the other two locations contain very high energy waves [35].

7.2 Description of real ocean data and wave spectrum

A wave spectrum is the most important tool by which one can analyse the main characteristics of waves. Wave energy is distributed across different wave frequencies, and the reader is referred to the details of wave spectra that were introduced in chapter 2. A wave spectrum contains several important parameters. One is significant wave height, H_s , whilst a second is the peak period, T_p . The third is the zero-crossing period, T_z .

As mentioned above, real-world data for the first location at Berth was recorded for every half-hour period. Four dataset records will be given. Each wave spectrum for each half hour is given as per the following:

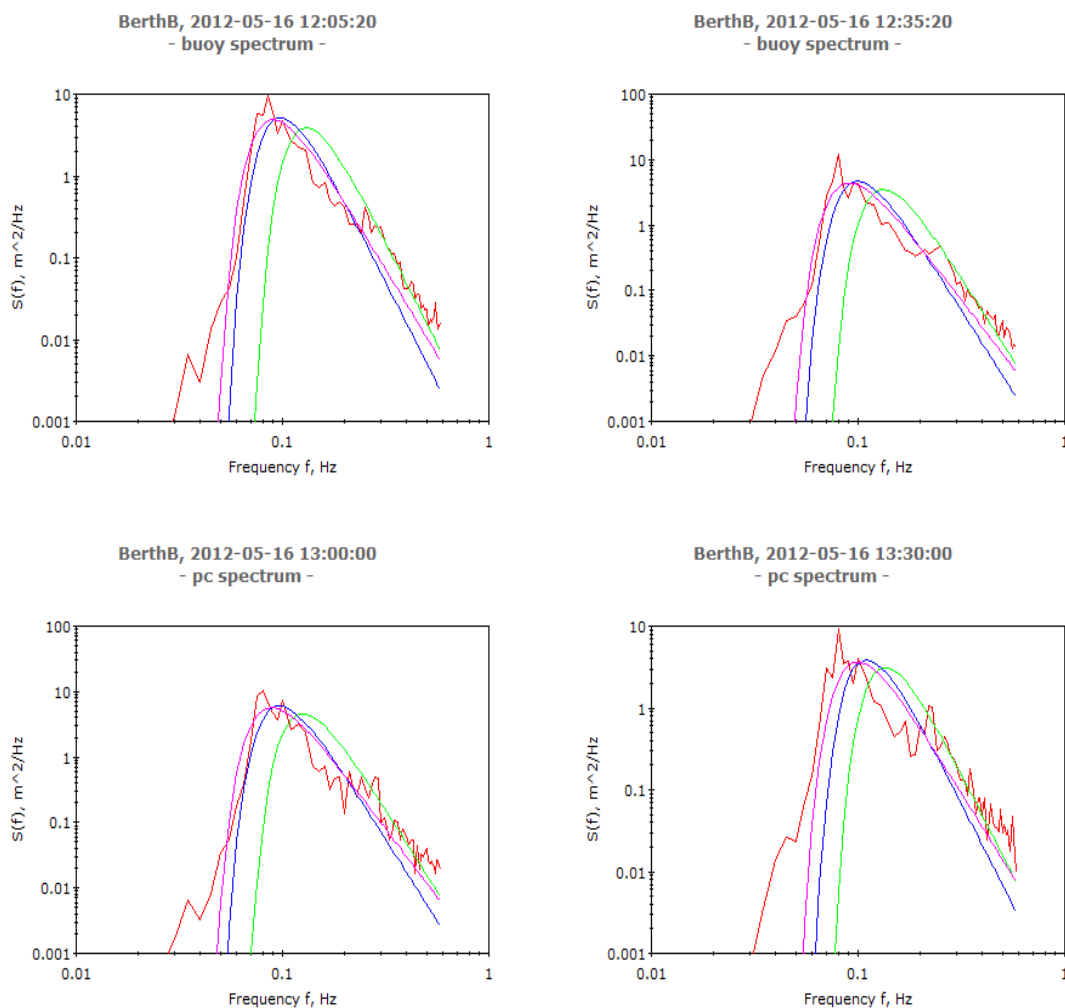


Figure 7.1 Wave spectra measured from 12 : 00 to 13 : 30

A wave spectrum is measured and estimated by the *W@ves21* software [11]. The spectrum has been estimated using three different spectrum methods. The measured spectrum

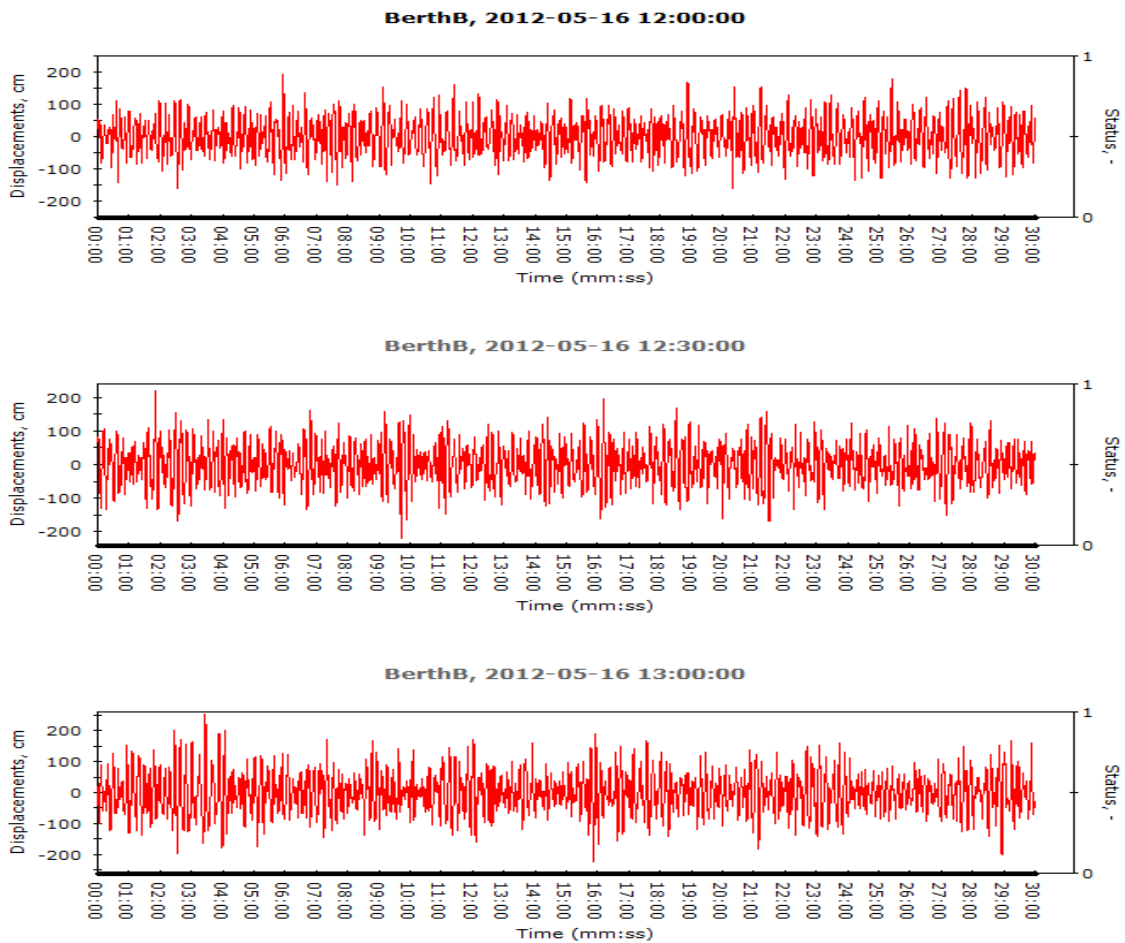
7.2 Description of real ocean data and wave spectrum

is shown with a solid red solid line, whilst the Pierson-Moskowitz spectrum is shown by a green line. The second method is the Bretschneider method, which is shown with a blue line, whilst the third method is the Ochi-Hubble spectrum ($3 - param$), which is shown with a purple line. More details about these wave spectra can be found in section 2.2.3.

Table 7.1 Main wave characteristics (Berth)

Time 12 : 00			12 : 30			13 : 00			13 : 30		
$H_s(m)$	$T_z(s)$	$T_p(s)$	$H_s(m)$	$T_z(s)$	$T_p(s)$	$H_s(m)$	$T_z(s)$	$T_p(s)$	$H_s(m)$	$T_z(s)$	$T_p(s)$
2.19	6.48	13.34	2.16	6.49	12.82	2.54	6.89	12.78	2.18	5.97	14.40

Significant wave characteristics for Berth are reported in the table 7.1. The dataset collected at 13 : 00 has the highest significant wave height, H_s , and zero crossing period, T_z . It can be seen from figure 7.1 that this dataset also has the biggest wave spectrum. Real wave datasets in the time domain are given as follows:



7.2 Description of real ocean data and wave spectrum

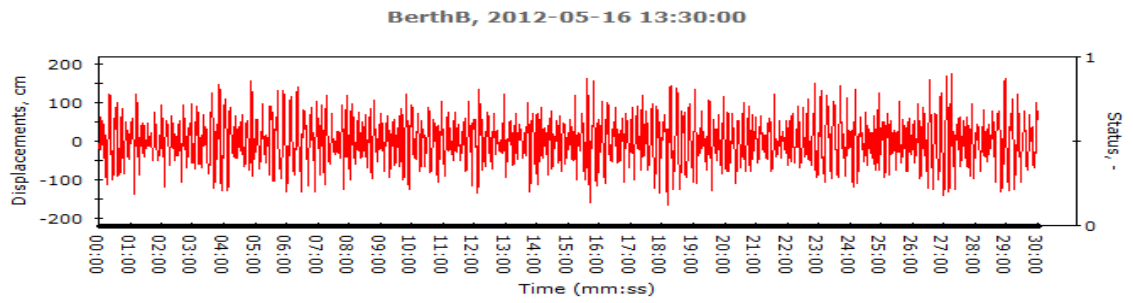


Figure 7.2 Wave elevations measured from 12 : 00 to 13 : 30

The second location is at Galway Bay. Each dataset contains 2304 data points due to the sampling frequency. The wave spectrum for each time interval is given below:

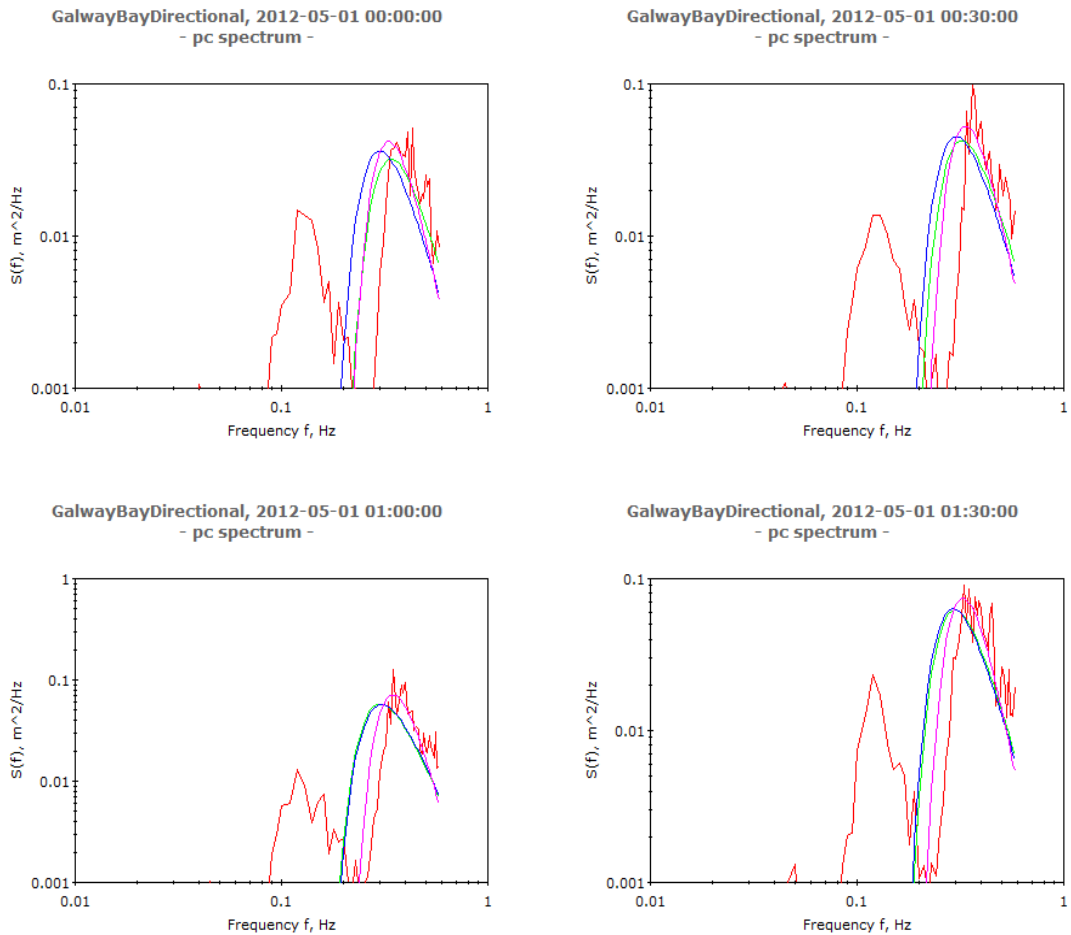


Figure 7.3 Wave spectra measured from 00 : 00 to 01 : 30

7.2 Description of real ocean data and wave spectrum

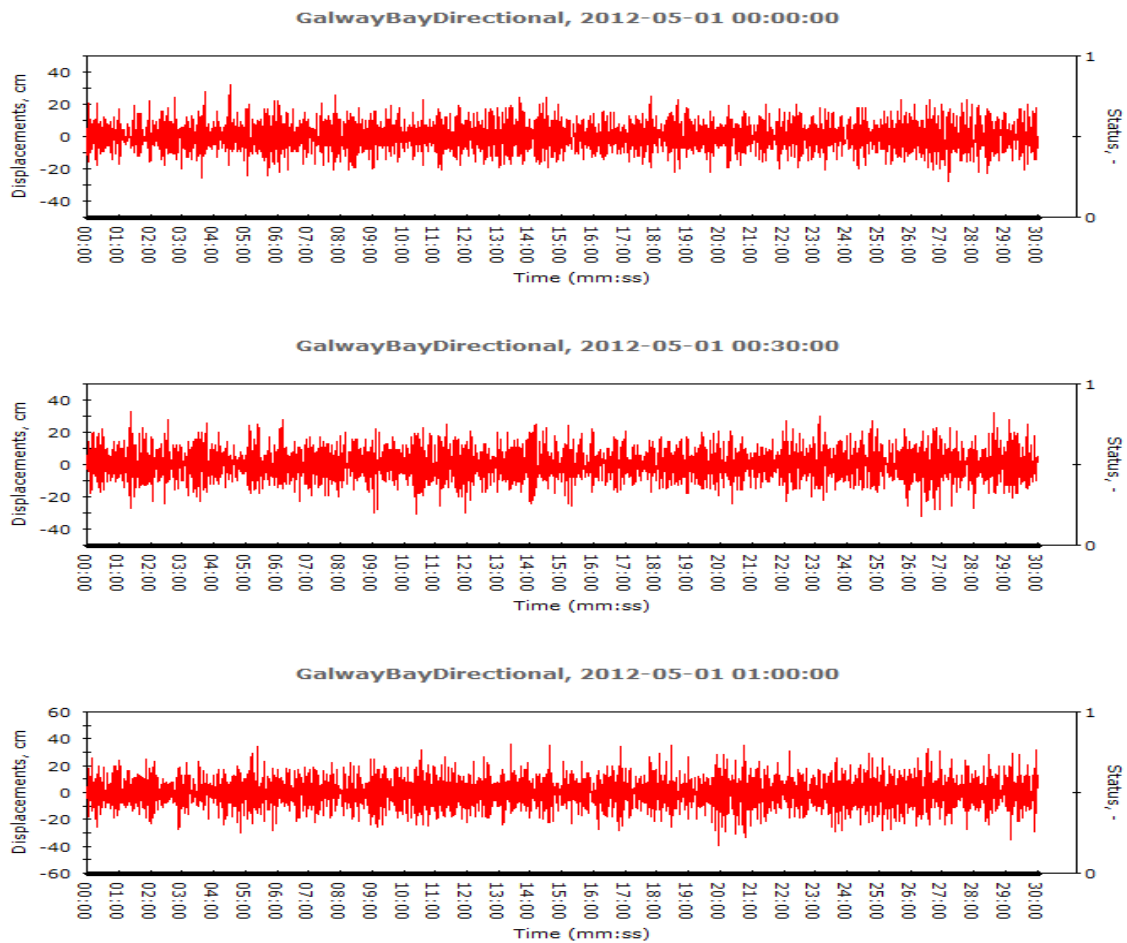
Table 7.2 Main wave characteristics (Galway Bay)

Time 00 : 00			00 : 30			01 : 00			01 : 30		
$H_s(m)$	$T_z(s)$	$T_p(s)$	$H_s(m)$	$T_z(s)$	$T_p(s)$	$H_s(m)$	$T_z(s)$	$T_p(s)$	$H_s(m)$	$T_z(s)$	$T_p(s)$
0.35	2.48	4.90	0.39	2.48	4.66	0.44	2.47	3.99	0.45	2.56	4.53

The main wave characteristics for each wave dataset, including H_s , T_z and T_p , are given in table 7.2.

A comparison of the datasets collected at 00 : 00 and 00 : 30 shows that each have the same zero crossing period though with different significant wave heights. The power spectrum measured at 00 : 00 is smaller than the one measured at 00 : 30, which can be shown using eq(2.11). The significant wave height collected at 01 : 30 is the highest; however, the zero crossing period collected at 01 : 30 is the highest. Hence, the spectrum for 01 : 30 is ultimately not the highest of the three.

Wave elevations measured in the Galway Bay area can be illustrated as follows:



7.2 Description of real ocean data and wave spectrum

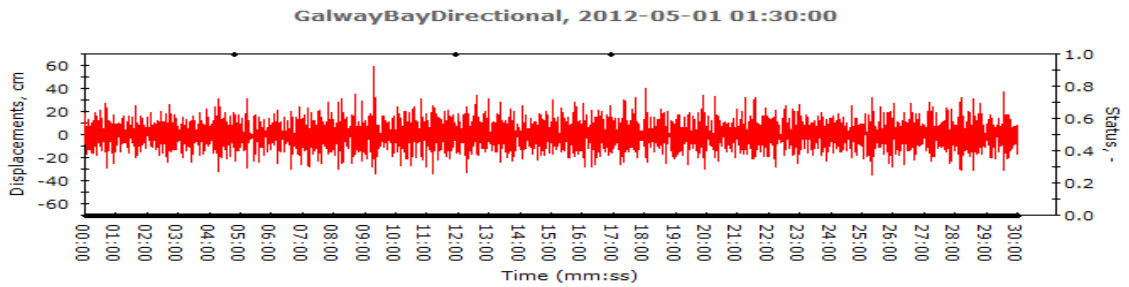


Figure 7.4 Wave elevations measured between 00 : 00 and 01 : 30

The significant wave height measured in Galway Bay is smaller than that of Berth. Real wave elevations collected in Galway Bay are also smaller than those at Berth. Comparisons of these data are given in fig7.2 and fig7.4.

The last real wave collection location was at Pico Island in the Atlantic. Each dataset contains 2304 data, again as a consequence of the sampling frequency of 1.28Hz . The wave spectrum for each measured time interval is similar to that of Berth:

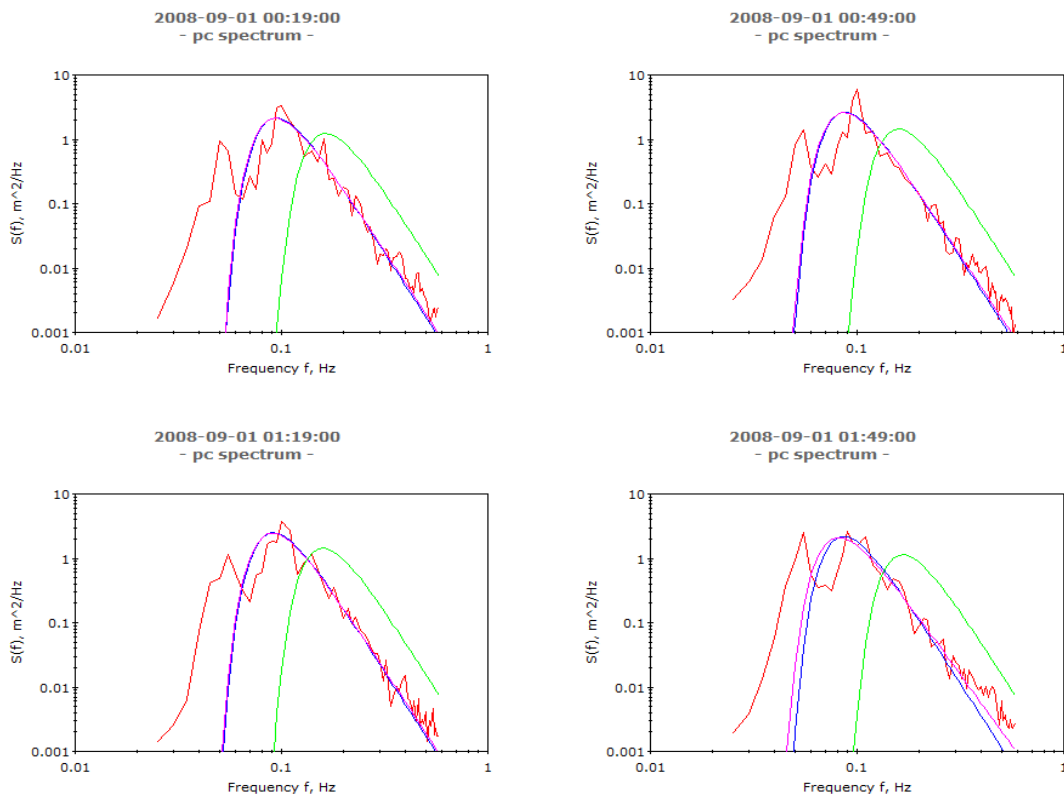


Figure 7.5 Wave spectrum measured between 00 : 19 and 01 : 49

7.2 Description of real ocean data and wave spectrum

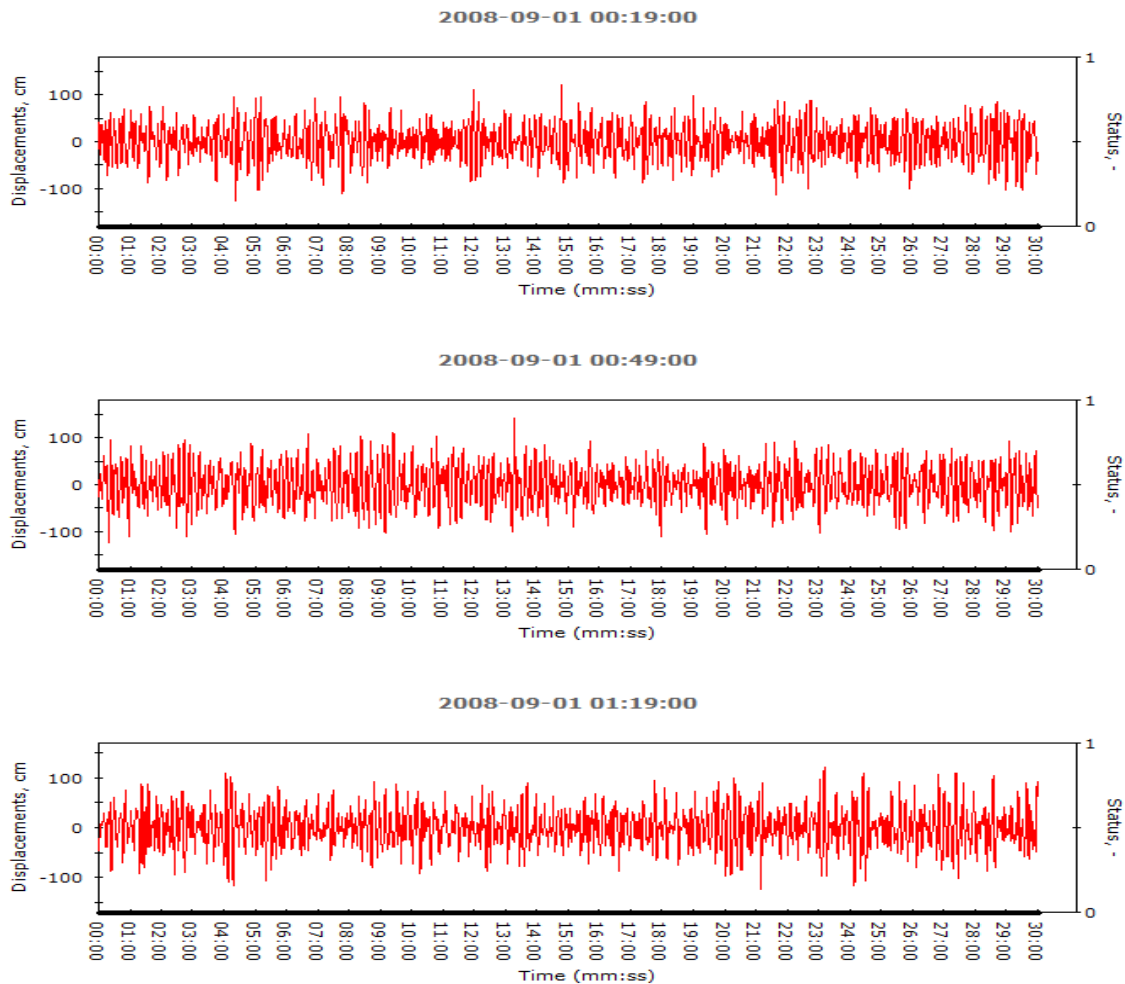
The main wave characteristics, including H_s , T_z and T_p , for Pico Island are as follows:

Table 7.3 Main wave characteristics (Pico)

Time 00 : 19			00 : 49			01 : 19			01 : 49		
$H_s(m)$	$T_z(s)$	$T_p(s)$	$H_s(m)$	$T_z(s)$	$T_p(s)$	$H_s(m)$	$T_z(s)$	$T_p(s)$	$H_s(m)$	$T_z(s)$	$T_p(s)$
1.50	7.52	12.49	1.59	7.76	12.87	1.59	8.09	12.84	1.45	7.97	15.08

The dataset measured at 00 : 49 has the same significant wave height as the one measured at 01 : 19; however, the zero crossing period collected for the former is slightly smaller, and hence the wave spectrum measured at 00 : 49 is considered to be the slightly larger of the two.

Wave elevations measured at Pico Island are shown as following:



7.3 Real waves tested with prediction methods

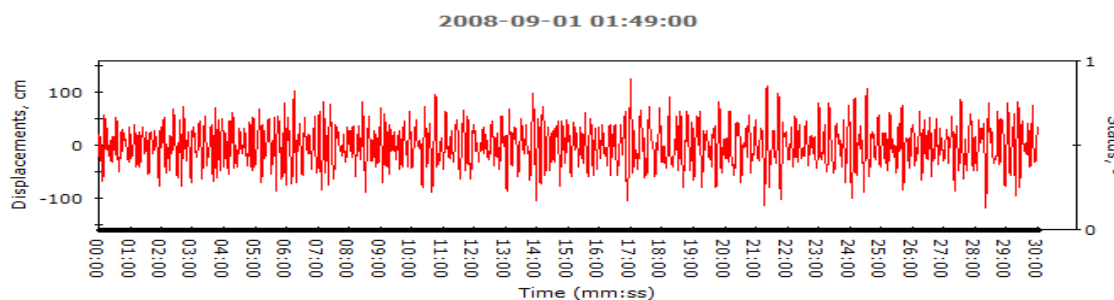


Figure 7.6 Wave elevation measured from 00 : 19 to 01 : 49

Comparing the wave elevations measured in the three different locations, the highest average significant wave height was found in Berth. Accordingly, overall wave elevations measured in Berth are the highest of the three locations; in contrast, the average significant wave height measured in Galway Bay is the lowest of the three locations. The lowest wave elevations are presented in fig7.4.

7.3 Real waves tested with prediction methods

As mentioned in chapter4, predictions of either the velocity of a wave energy conversion system or the excitation force can be used to overcome the non-causality problem. Simulation data has been tested with three different prediction methods in chapter4. Multi-step predictive identification has been shown to be a better prediction method than the least-squares system and long-range predictive identifications. However, real wave data collected in the above three locations is the main point that will be considered in this section.

7.3.1 Berth

Real wave elevations measured in Berth are presented in fig7.2. A comparison of prediction accuracies for the LS, the LRPI and the MSPI methods for the time periods from 12 : 00 to 12 : 30 and 12 : 30 to 13 : 00 are given in figure7.7.

Here, the prediction steps have been set to 10, the sample frequency to $1.28Hz$ and the model order is 12. Each time interval contains 2304 data points; however, only 500 points from each dataset have been used for both convenience and figure clarity. Note that these 500 data points can be divided into identification and validation data. The first 100 data are used for system identification, whilst the rest are used for validation. It can be seen from fig7.11 that wave elevations start from $100 \times 0.78 = 78s$, and end at $500 \times 0.78 = 390s$. As

7.3 Real waves tested with prediction methods

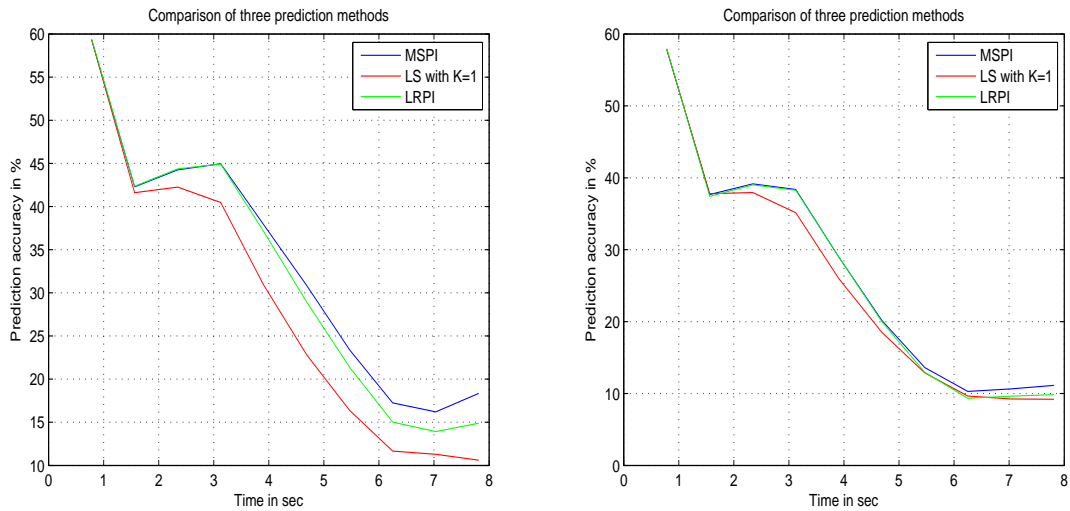


Figure 7.7 Comparison of prediction accuracies from 12 : 00 to 12 : 30

figure7.7 shows, the results of the two comparisons over different time intervals show similar performances. In the first few steps, the three prediction method results are almost identical, with their differences only starting to become apparent after 1.5 seconds. MSPI performs better than the other two methods. LRPI shows better performance than the LS method, the latter being based on the one step ahead estimation. Real wave elevations and estimated wave elevations generated by the three different methods in the time period 12 : 00 – 12 : 30 are shown below:

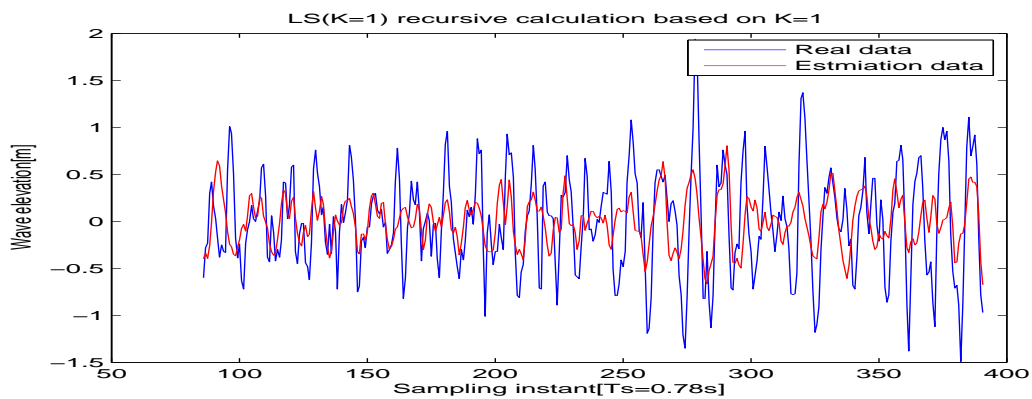


Figure 7.8 Real wave elevation and estimation using the LS method (12 : 00)

7.3 Real waves tested with prediction methods

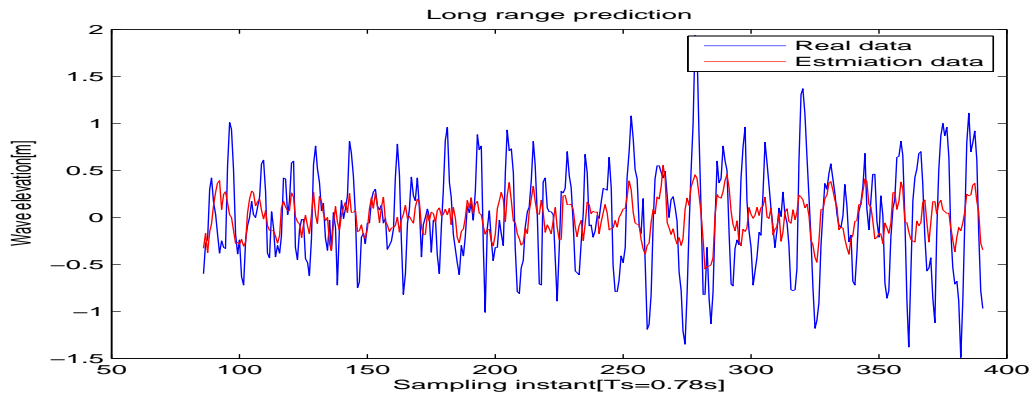


Figure 7.9 Real wave elevation and estimation using the LRPI method (12 : 00)

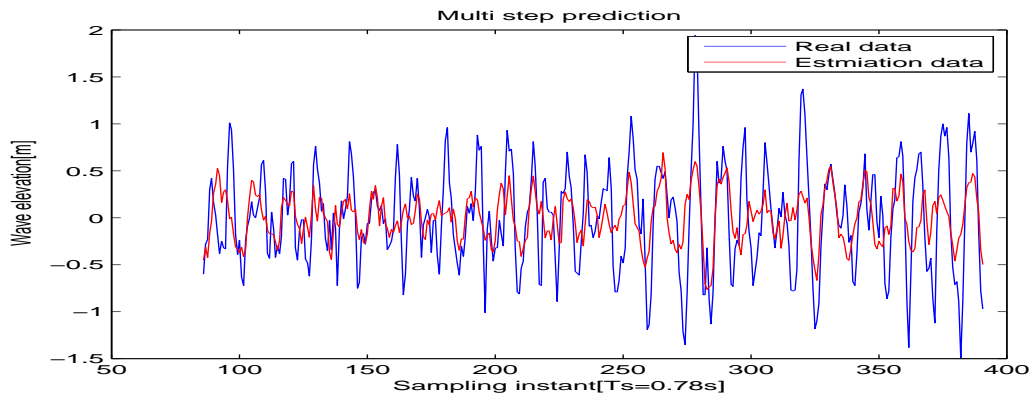


Figure 7.10 Real wave elevation and estimation using the MSPI method (12 : 00)

Real wave elevations measured in the 12 : 30 – 13 : 00 time period and the estimated wave elevations generated by the three different methods are shown below:

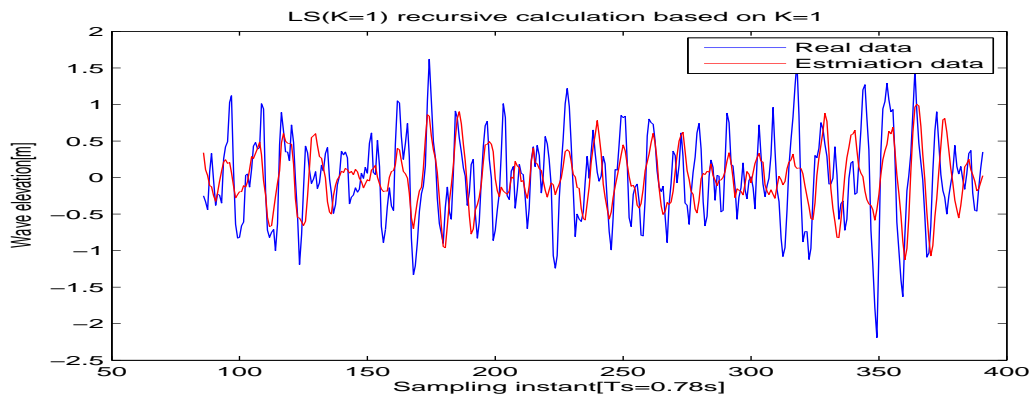


Figure 7.11 Real wave elevation and estimation using the LS method (12 : 30)

7.3 Real waves tested with prediction methods

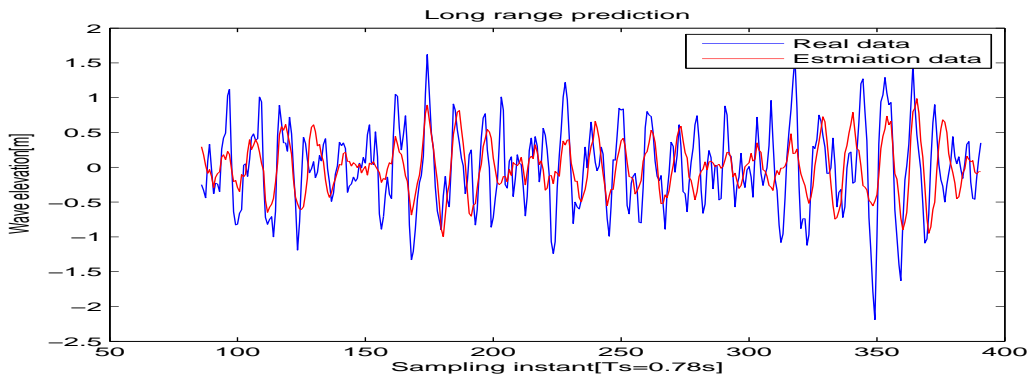


Figure 7.12 Real wave elevation and estimation using the LRPI method (12 : 30)

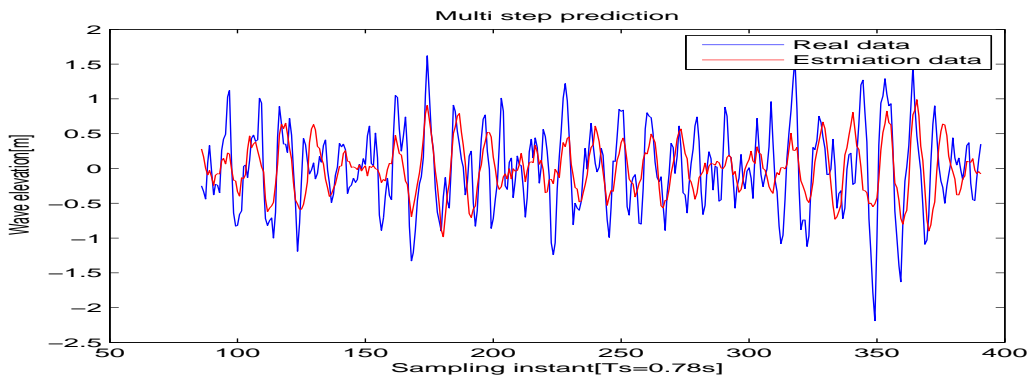


Figure 7.13 Real wave elevation and estimation using the MSPI method (12 : 30)

As mentioned in section 4.6, the model order in the autoregressive model can affect the accuracy of the prediction. By increasing the model order from 12 to 24 at the same time and location, a comparison of the subsequent prediction accuracies can be given as follows:

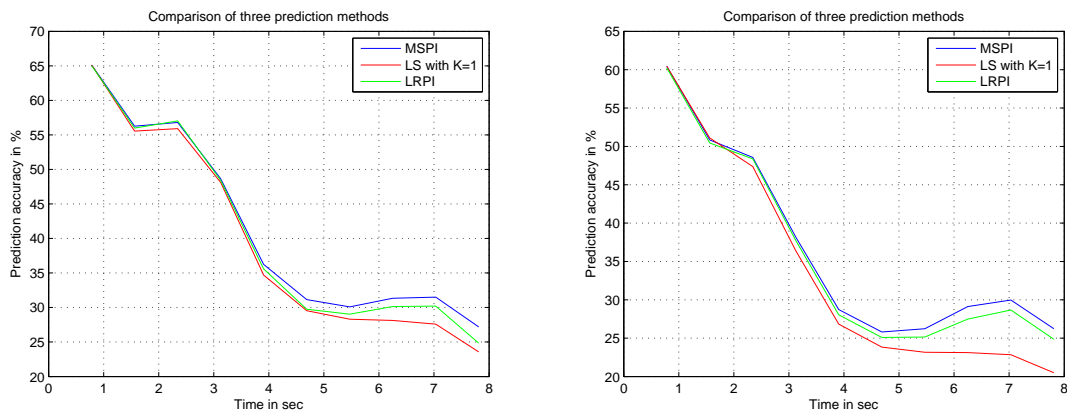


Figure 7.14 Comparison of prediction accuracies from 12 : 00 to 12 : 30 using a model order of 24

7.3 Real waves tested with prediction methods

As fig7.14 shows, prediction accuracy can reach greater than 25% after 7.8 s in the 12 : 00 – 12 : 30 period with a model order of 24. In fig7.7, all prediction methods gain only a 10% prediction accuracy after 7.8 s in the 12 : 00 – 12 : 30 period with a model order of 12. Similarly, a more than 20% prediction accuracy can be achieved after 7.8 s in the 12 : 30 – 13 : 00 period with a model order of 24. However, all the prediction methods only achieve around 10% prediction accuracy in the 12 : 30 – 13 : 00 period with a model order of 12. This shows that larger model orders can achieve higher prediction accuracies.

Real wave and estimated wave elevations generated by the three different methods for the time period between 12 : 00 and 12 : 30 with a model order of 24 are shown below:

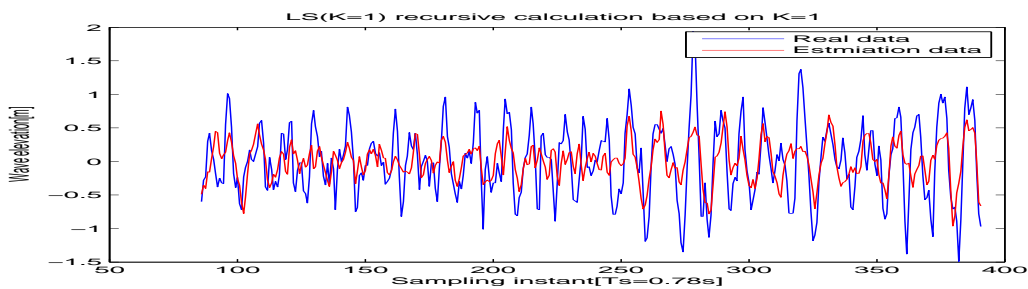


Figure 7.15 Real wave elevation and estimation using the LS method (12 : 00)

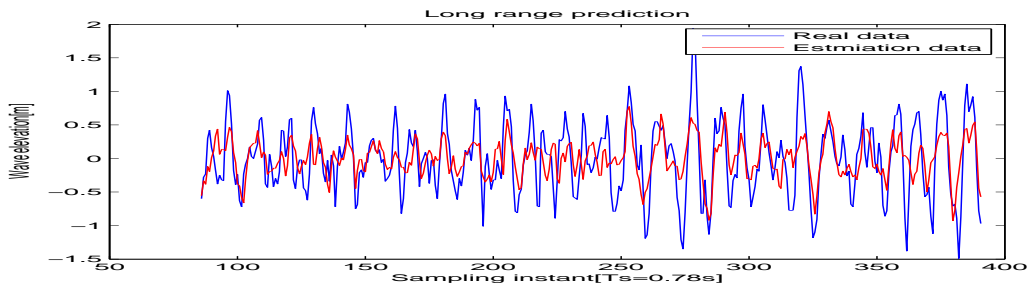


Figure 7.16 Real wave elevation and estimation using the LRPI method (12 : 00)

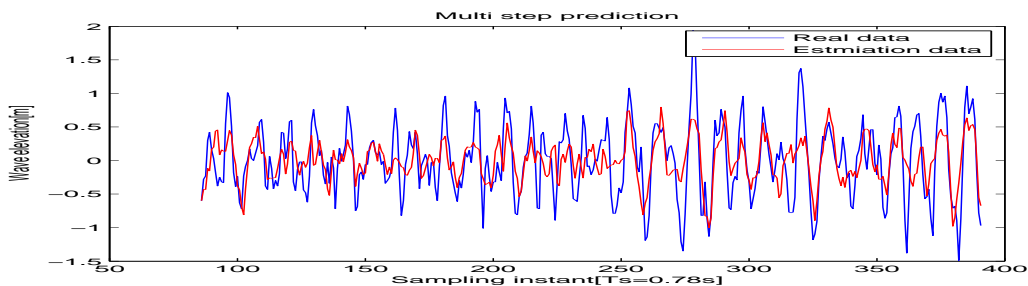


Figure 7.17 Real wave elevation and estimation using the MSPI method (12 : 00)

7.3 Real waves tested with prediction methods

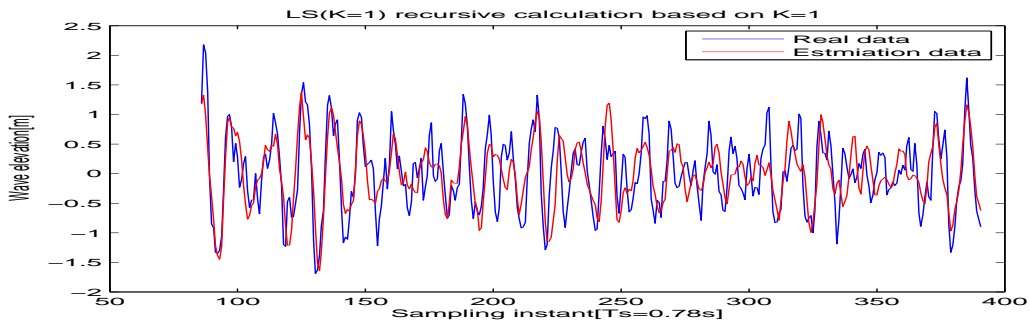


Figure 7.18 Real wave elevation and estimation using the LS method (12 : 30)

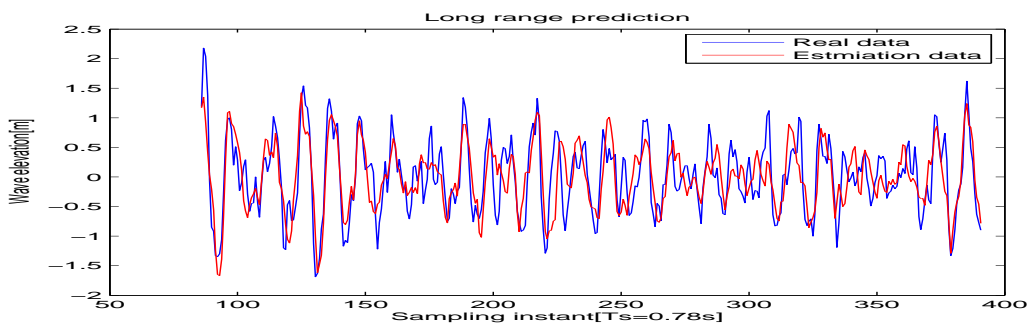


Figure 7.19 Real wave elevation and estimation using the LRPI method (12 : 30)

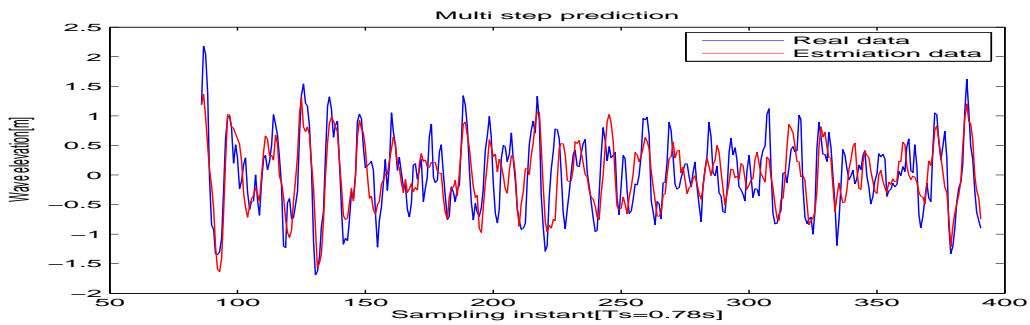


Figure 7.20 Real wave elevation and estimation using the MSPI method (12 : 30)

7.3.2 Galway Bay

Real wave elevations measured in Galway Bay have also been presented in fig7.4. The wave spectrum measured for Galway Bay is much smaller than that recorded for Berth, and so a comparison of prediction accuracies is particularly worth pursuing. The prediction accuracy of the wave elevations measured by the LS, the LRPI and the MSPI methods in the time period between 00 : 00 – 01 : 00 is given in fig7.21:

7.3 Real waves tested with prediction methods

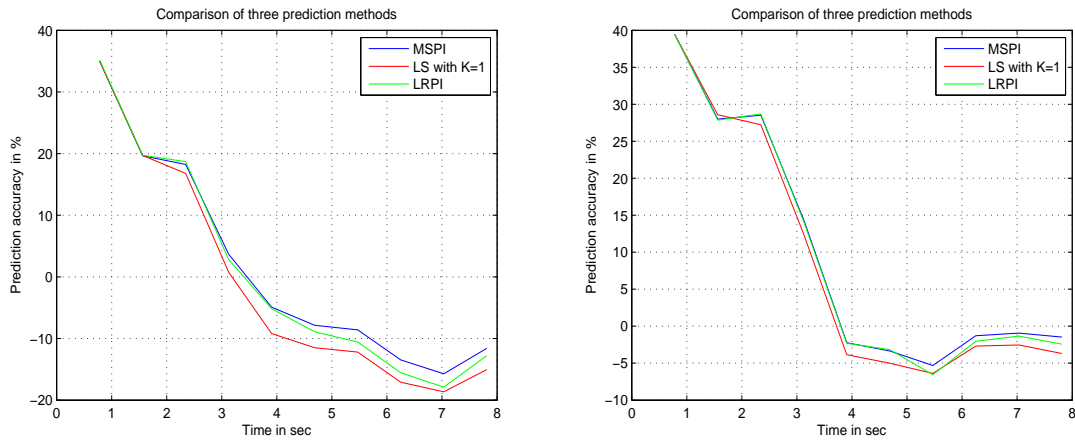


Figure 7.21 Comparison of prediction accuracies between 00 : 00 and 00 : 30

The predicted accuracy of wave elevations measured in Galway Bay is slightly lower than those measured in Berth, most likely as a consequence of the predictors showing better performance when fitting higher wave spectra. Note that the prediction step is 10 and the model order is 12.

Real wave and estimated wave elevations generated using the three different methods in the time period 00 : 00 – 01 : 00 and a model order of 12 are shown in the following figure:

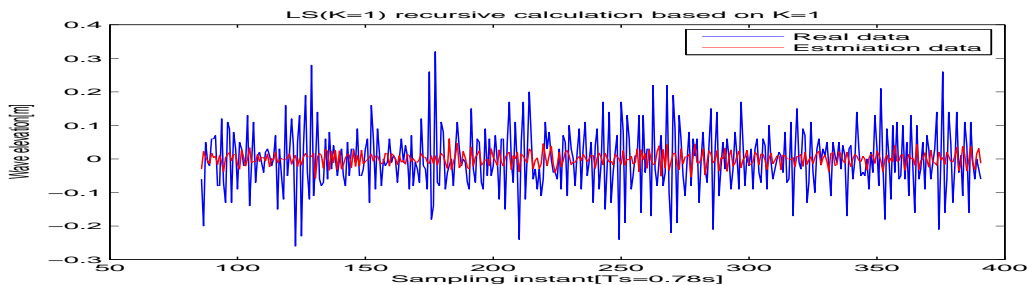


Figure 7.22 Real wave elevation and estimation using the LS method (00 : 00)

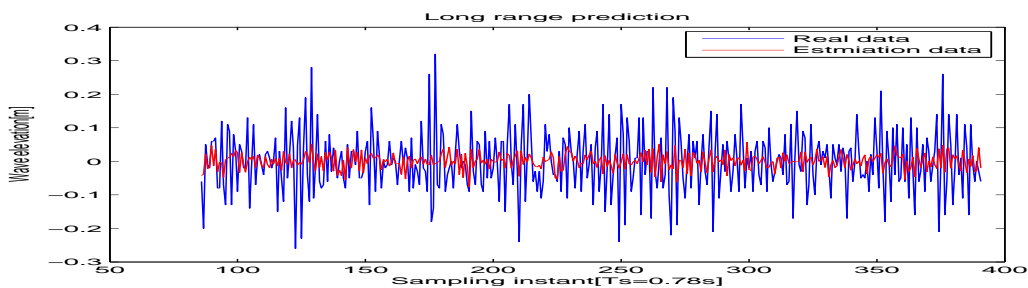


Figure 7.23 Real wave elevation and estimation using the LRPI method (00 : 00)

7.3 Real waves tested with prediction methods

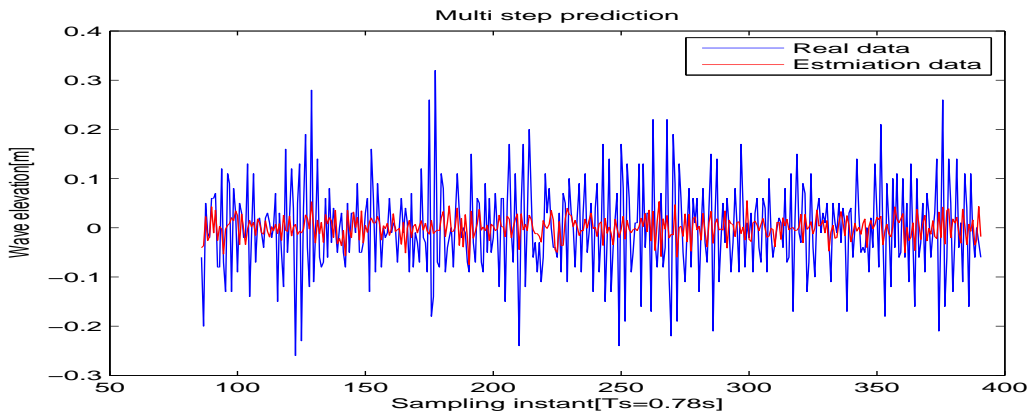


Figure 7.24 Real wave elevation and estimation using the MSPI method (00 : 00)

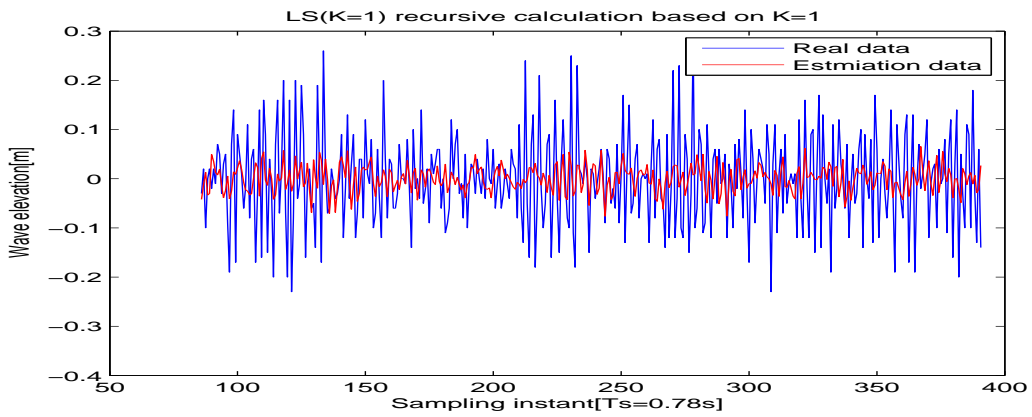


Figure 7.25 Real wave elevation and estimation using the LS method (00 : 30)

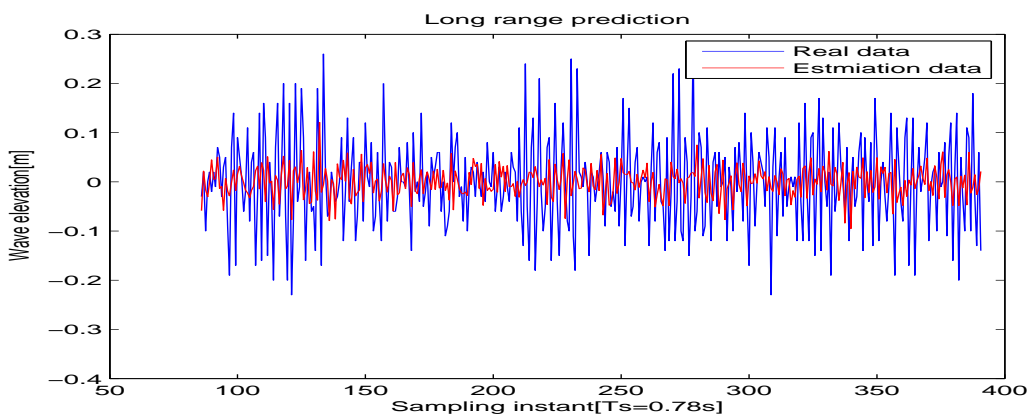


Figure 7.26 Real wave elevation and estimation using the LRPI method (00 : 30)

7.3 Real waves tested with prediction methods

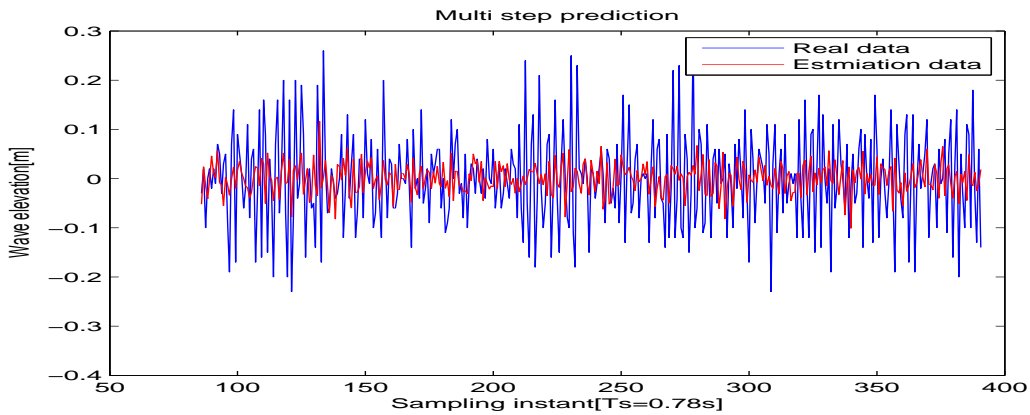


Figure 7.27 Real wave elevation and estimation using the MSPI method (00 : 30)

As the figures 7.22, 7.23, 7.24, 7.25, 7.26, and 7.27 show, wave elevations for this region are much smaller than those collected in Berth, which is because the significant wave heights of these waves are the smaller of the two. It can be seen from the previous figures that estimated wave elevations do not follow real wave elevations particularly well.

As mentioned before, increasing the model order can increase the associated prediction accuracy, so consequently the prediction accuracy of wave elevations measured in the Galway Bay with a model order of 24 are given in fig 7.28.

Prediction accuracies measured for the 00 : 00 time interval with this higher model order achieve approximately 10% greater prediction accuracy after 4s. However, the 00 : 30 time interval with a model order of 24 did not achieve any improvement compared with the same measurement using a model order of 12.

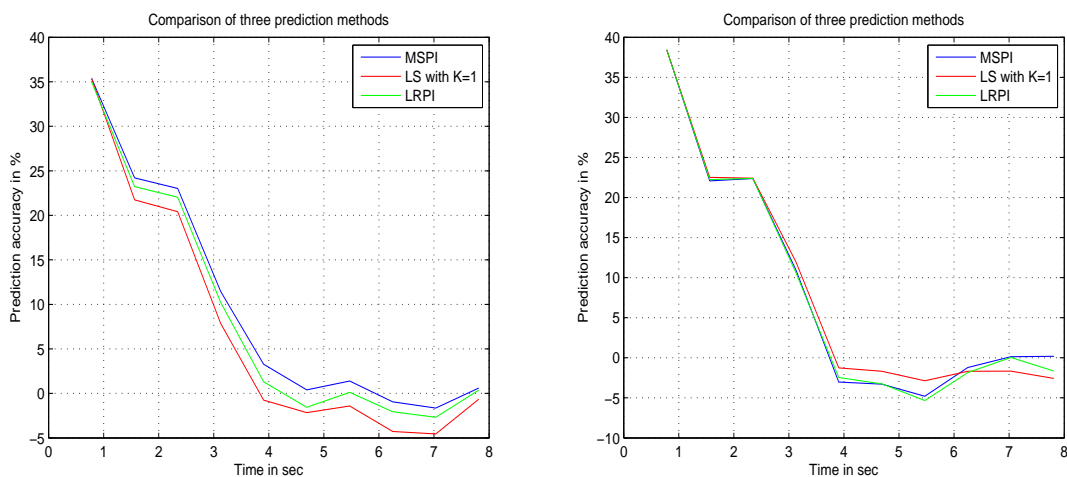


Figure 7.28 Comparison of prediction accuracies between 00 : 00 and 00 : 30

7.3 Real waves tested with prediction methods

Comparisons of real wave and estimated elevations computed with a model order of 24 can be illustrated as follows:

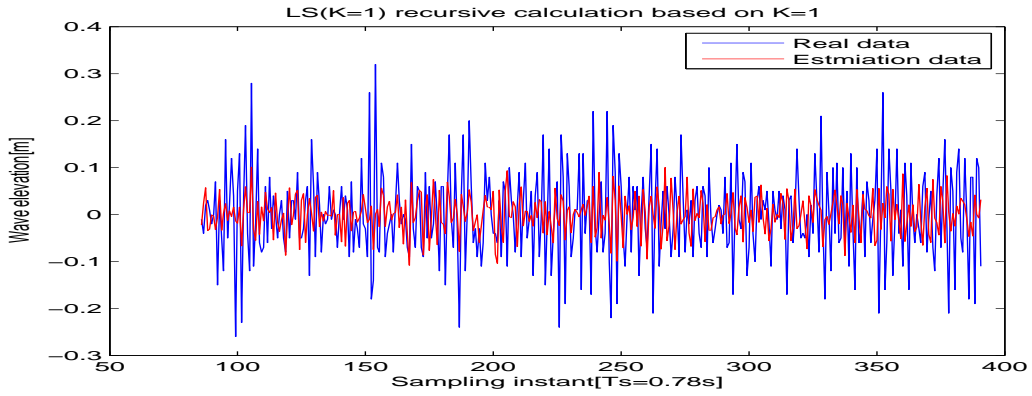


Figure 7.29 Real wave elevation and estimation using the LS method (00 : 00)

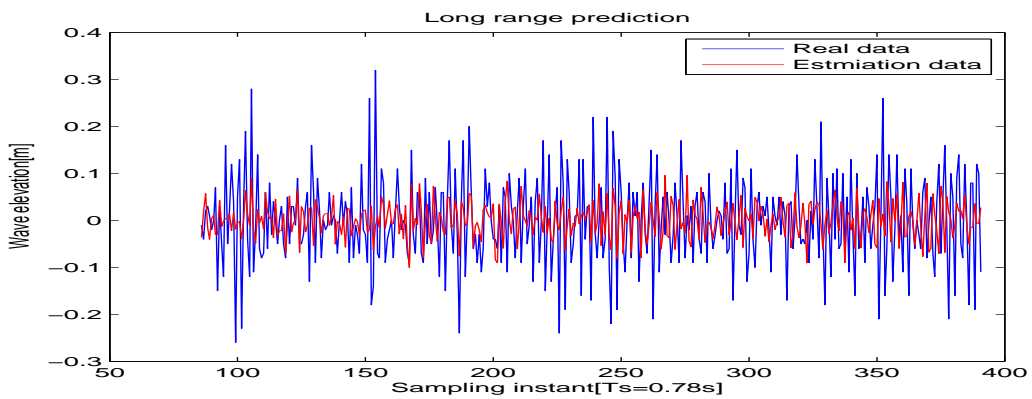


Figure 7.30 Real wave elevation and estimation using the LRPI method (00 : 00)

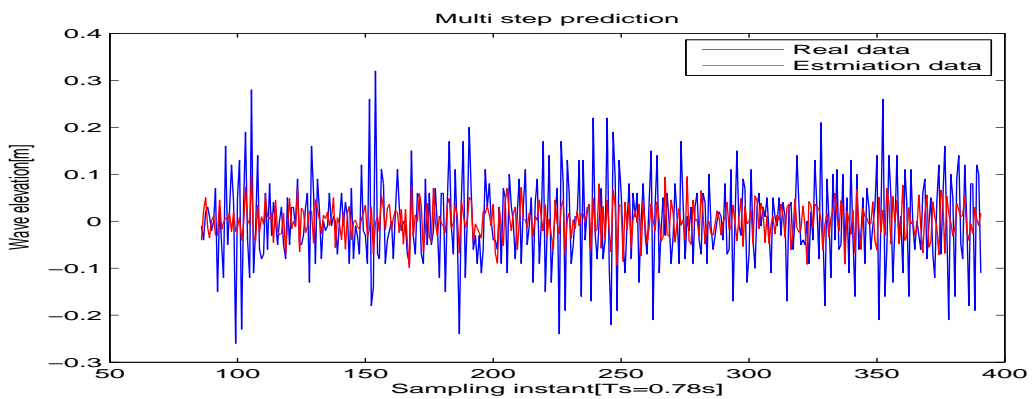


Figure 7.31 Real wave elevation and estimation using the MSPI method (00 : 00)

7.3 Real waves tested with prediction methods

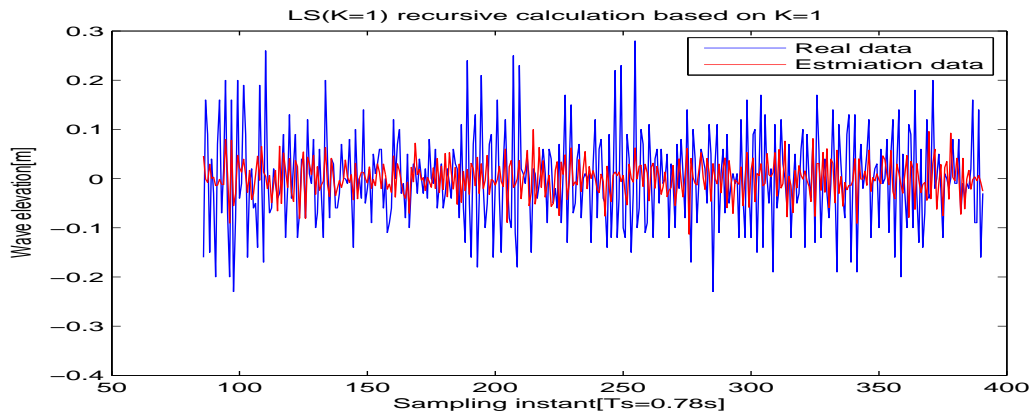


Figure 7.32 Real wave elevation and estimation using the LS method (00 : 30)

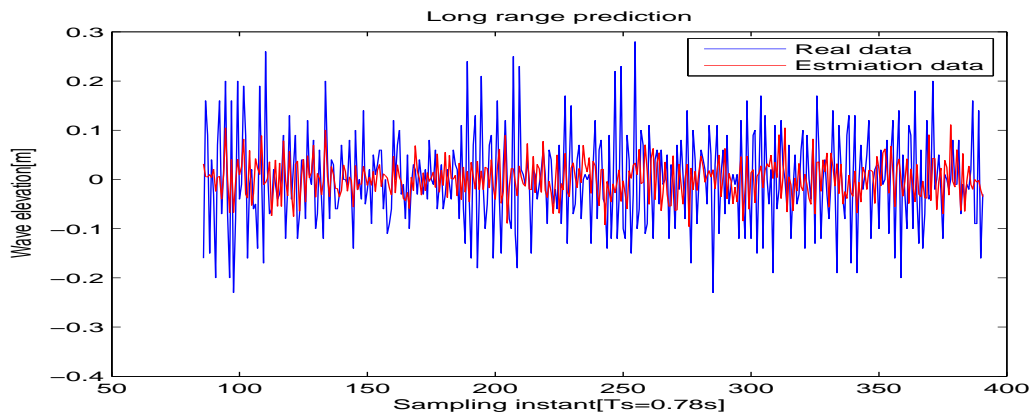


Figure 7.33 Real wave elevation and estimation using the LRPI method (00 : 30)

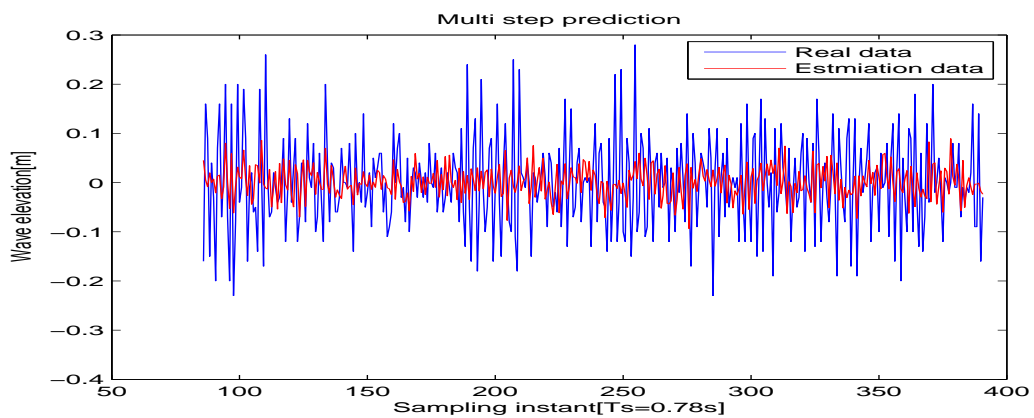


Figure 7.34 Real wave elevation and estimation using the MSPI method (00 : 30)

7.3.3 Pico

The significant wave height and zero crossing period measured at Pico Island are both slightly smaller than those measured at Berth. Hence, the prediction accuracies calculated using the three prediction methods for Pico island are expected to be fairly similar to those calculated for Berth; the prediction accuracy calculated for Pico Island between 00 : 19 and 01 : 19 with a model order of 12 is shown in fig7.35:

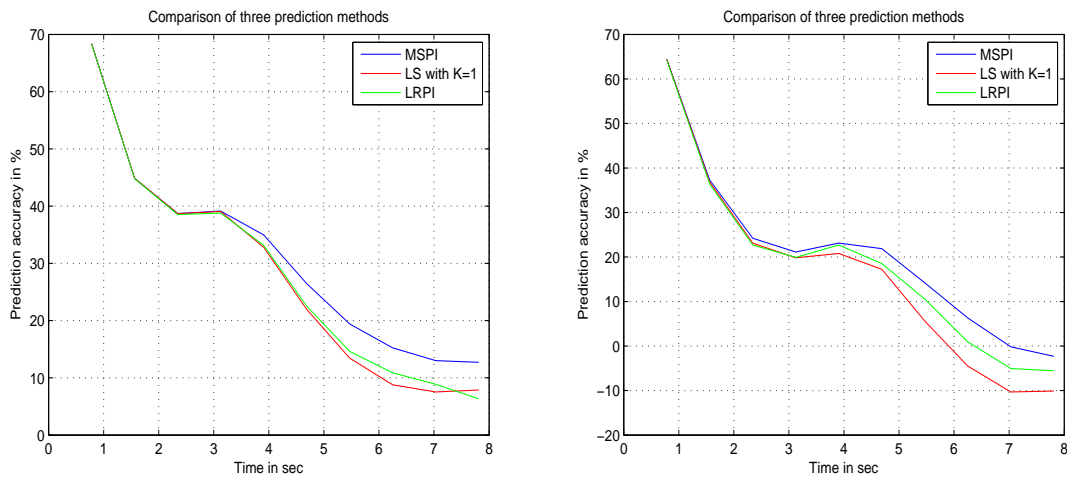


Figure 7.35 Comparison of prediction accuracies between 00 : 19 and 01 : 19

As shown in fig7.35, the prediction accuracy calculated for Pico Island is better than that determined for Galway Bay whilst being slightly worse than that calculated for Berth which, given the significant wave heights and zero crossing periods, is essentially as expected. Real wave elevations and estimated elevations related to the above sea states can be given as follows:

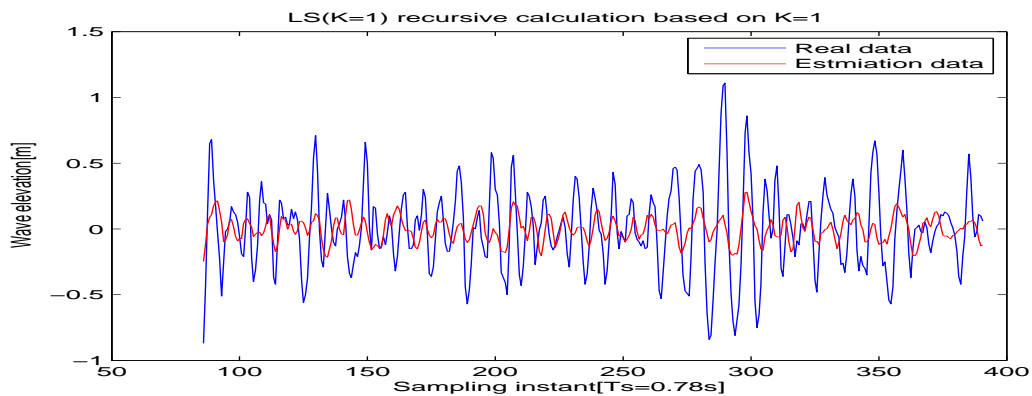


Figure 7.36 Real wave and estimated wave elevations using the LS method (00 : 19)

7.3 Real waves tested with prediction methods

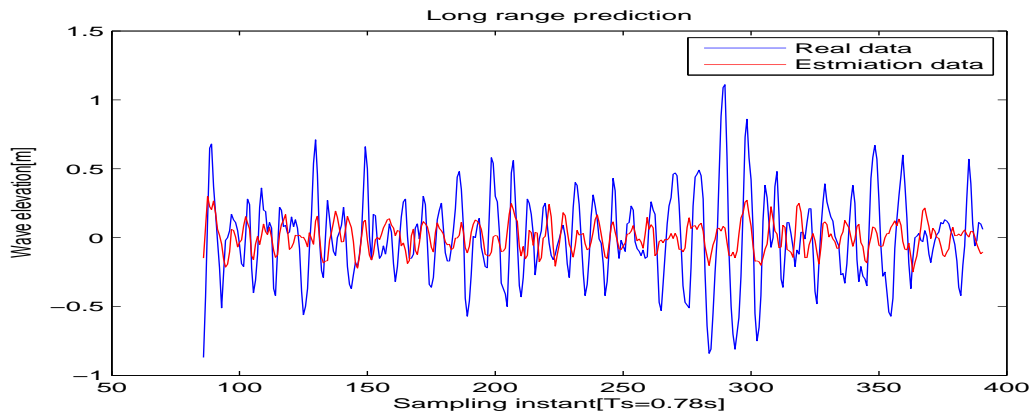


Figure 7.37 Real wave and estimated wave elevations using the LRPI method (00 : 19)

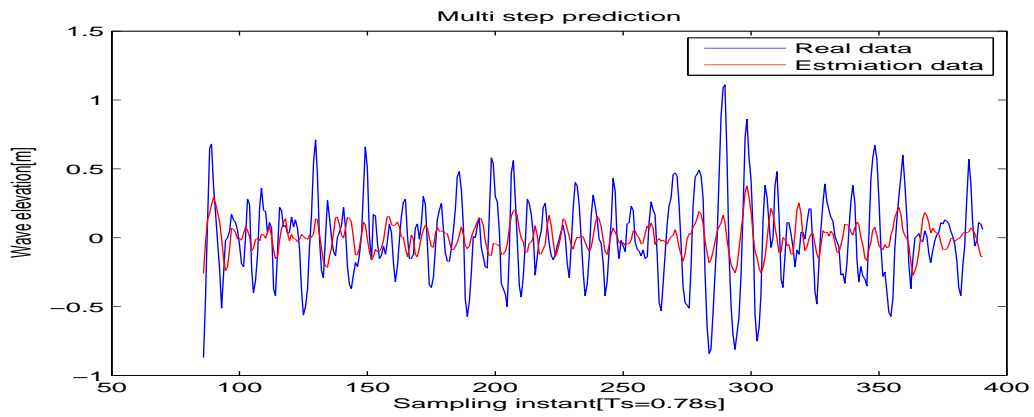


Figure 7.38 Real wave and estimated wave elevations using the MSPI method (00 : 19)

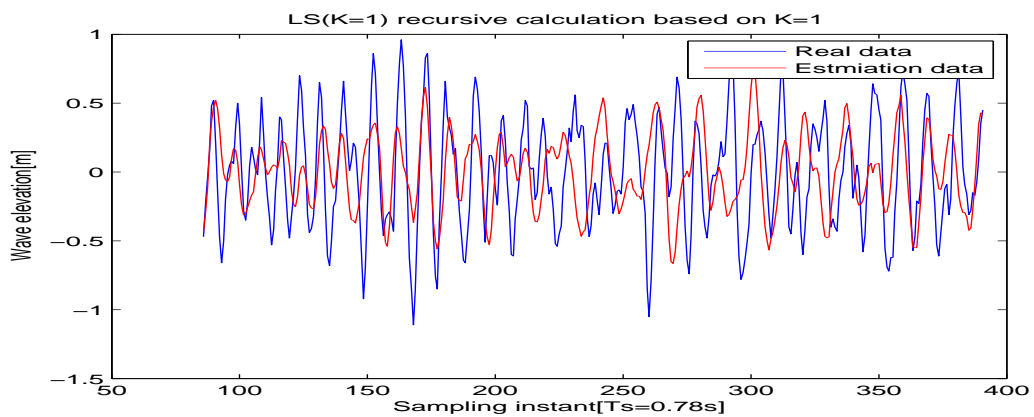


Figure 7.39 Real wave and estimated wave elevations using the LS method (00 : 49)

7.3 Real waves tested with prediction methods

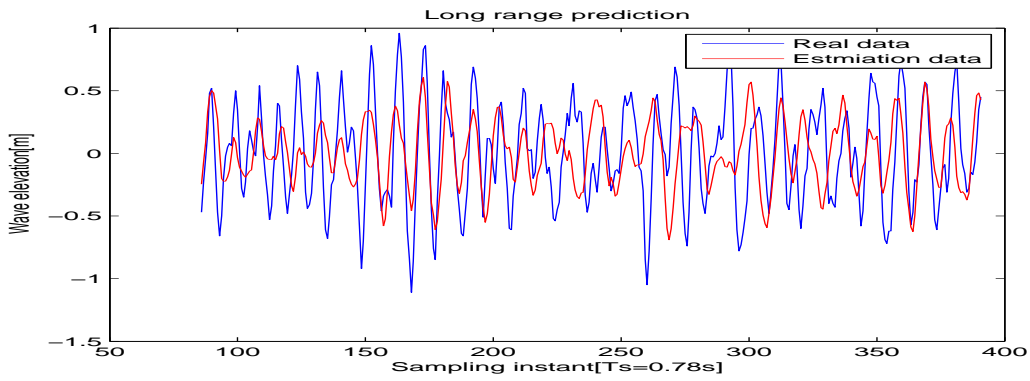


Figure 7.40 Real wave and estimated wave elevations using the LRPI method (00 : 49)

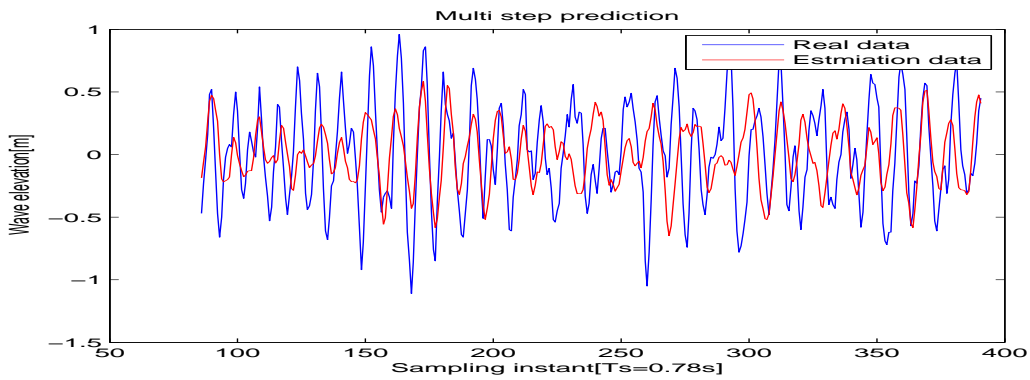


Figure 7.41 Real wave and estimated wave elevations using the MSPI method (00 : 49)

The model order used for the three prediction methods was increased to 24. The prediction accuracies that were calculated for the Pico Island data for this same time period as above but using the higher model order are given in fig.7.42.

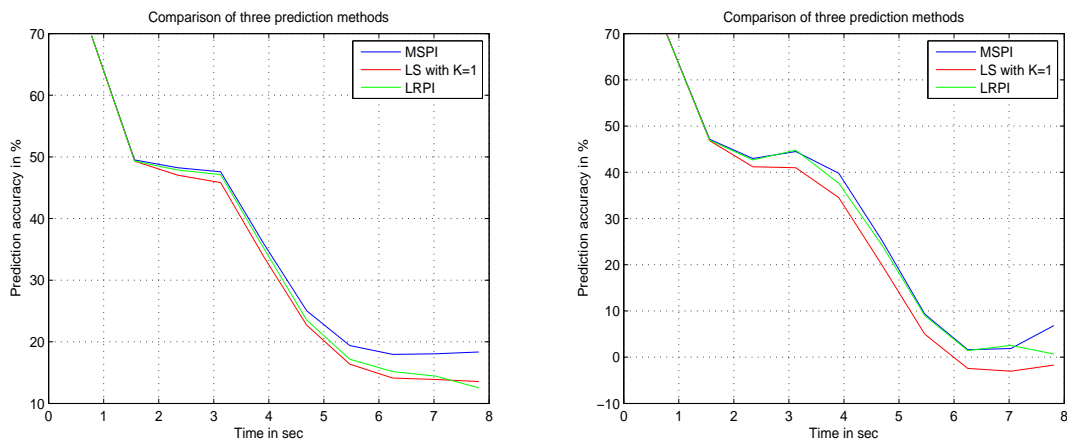


Figure 7.42 Comparison of prediction accuracies between 00 : 19 and 01 : 19

7.3 Real waves tested with prediction methods

The prediction accuracies calculated with a model order of 24 show slightly better performances compared with the model order of 12. The higher model order achieved a more than 10% increase in prediction accuracy for the 00 : 19 – 00 : 49 time period, and a more than 10% increase in prediction accuracy for the 00 : 49 – 01 : 19 time period.

Real wave elevations and estimated wave elevations computed with a model order of 24 were as follows:

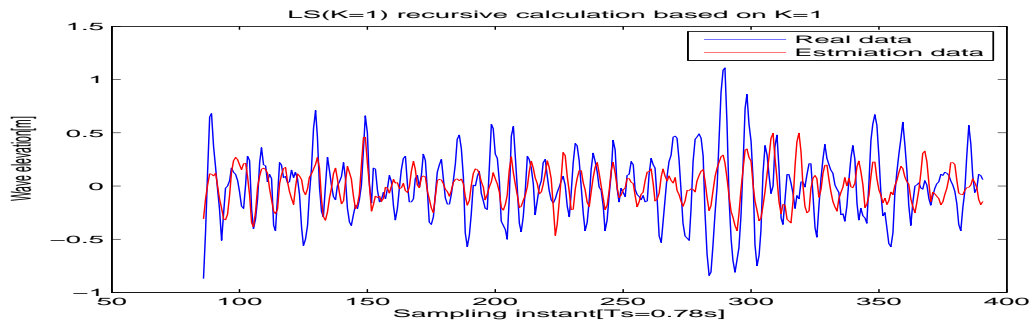


Figure 7.43 Real wave and estimated wave elevations using the LS method (00 : 19)

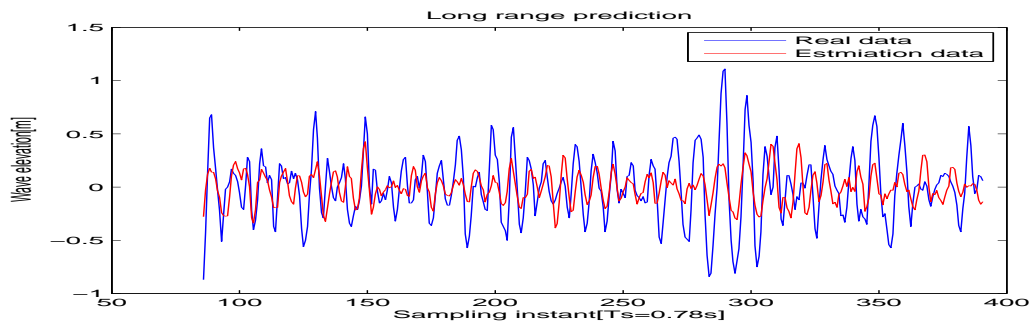


Figure 7.44 Real wave and estimated wave elevations using the LRPI method (00 : 19)

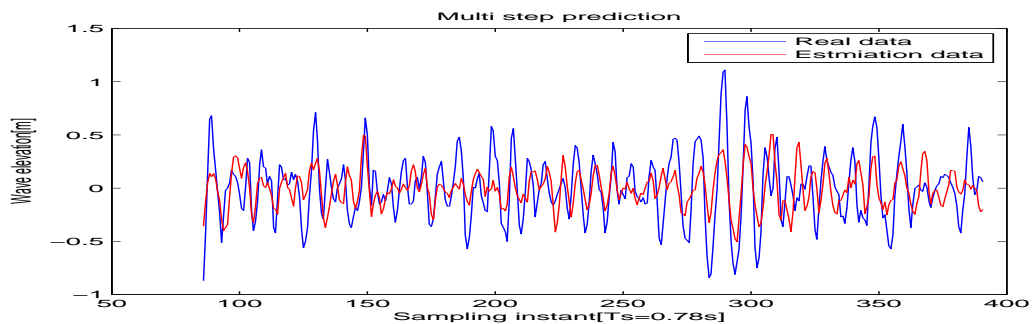


Figure 7.45 Real wave and estimated wave elevations using the MSPI method (00 : 19)

7.3 Real waves tested with prediction methods

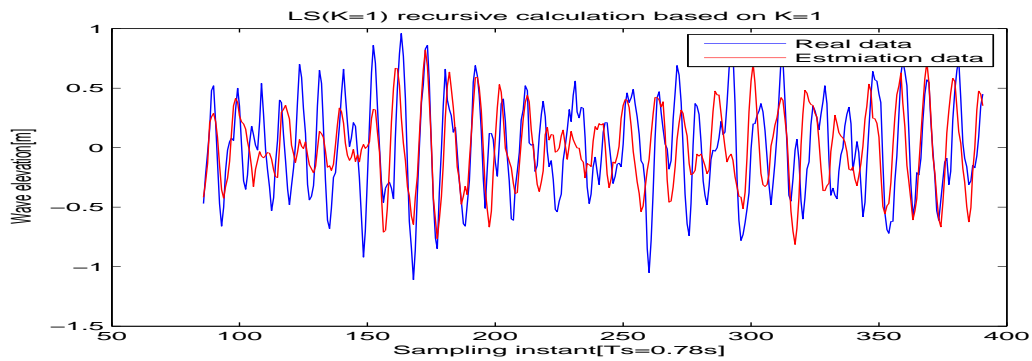


Figure 7.46 Real wave and estimated wave elevations using the LS method (00 : 49)

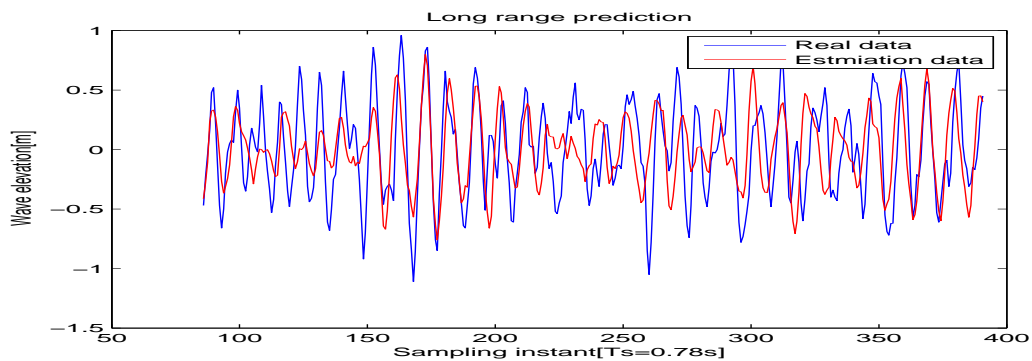


Figure 7.47 Real wave and estimated wave elevations using the LRPI method (00 : 49)

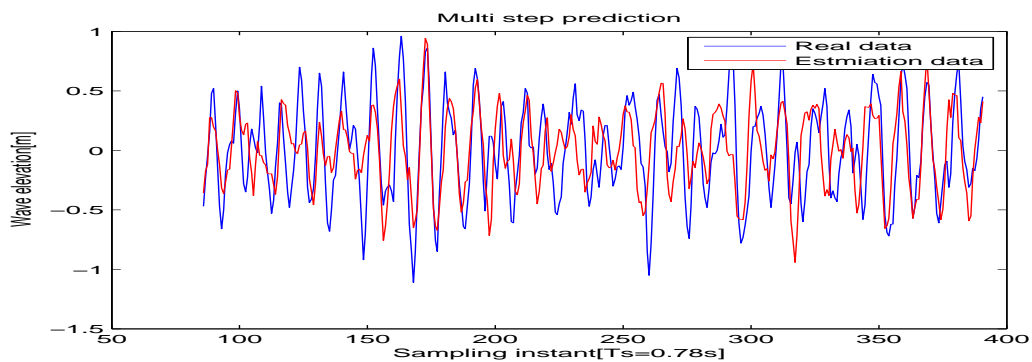


Figure 7.48 Real wave and estimated wave elevations using the MSPI method (00 : 49)

To summarise, prediction accuracy is clearly affected by the wave spectrum. The average wave spectrum measured in Berth was the largest of the three locations considered. Correspondingly, the prediction accuracy determined for this location showed the best performance. By comparison, the average wave spectrum measured in Galway Bay was the lowest of the three locations, and consequently it is hardly surprising that prediction accuracy for

7.4 Restricted complexity control tested with real wave data

this location was the worst of the three locations. Indeed, with the average wave spectrum measured for Pico Island being only slightly smaller than that of Berth, the fact that the prediction accuracy thus determined was worse than that for Berth but better than that for Galway Bay is entirely expected.

7.4 Restricted complexity control tested with real wave data

In section 6.5, restricted complexity controllers were introduced. The one normal (spring-damper-mass) impedance and two increased complexity impedances that were tested with simulated data have been compared. Parameters for the PTO impedance given by eq(6.55) and eq(6.56) have been optimised using the Nelder-Mead method. Two increased complexity impedances with the realisation of fig6.20 and the realisation of fig6.21 have been given. The results of these comparisons are given in section 6.4.2. The two increased complexity impedances obtain only a marginal improvement of about 3% compared to the normal complexity impedances. However, this apparent failure does not necessarily translate to the real world, and hence the real wave data collected from the three different locations will be tested instead of the simulation data generated by the PM spectrum in the following section.

7.4.1 Berth

For Berth, datasets containing 480 data points have been used for calculations. The significant wave height and zero-crossing period in the 12 : 00 – 12 : 30 period were 2.18831 m and 6.476 s, respectively. A comparison of the absorbed energies comparison extracted from the mass-spring-damper impedance and two increased complexity impedance models are illustrated in fig7.49.

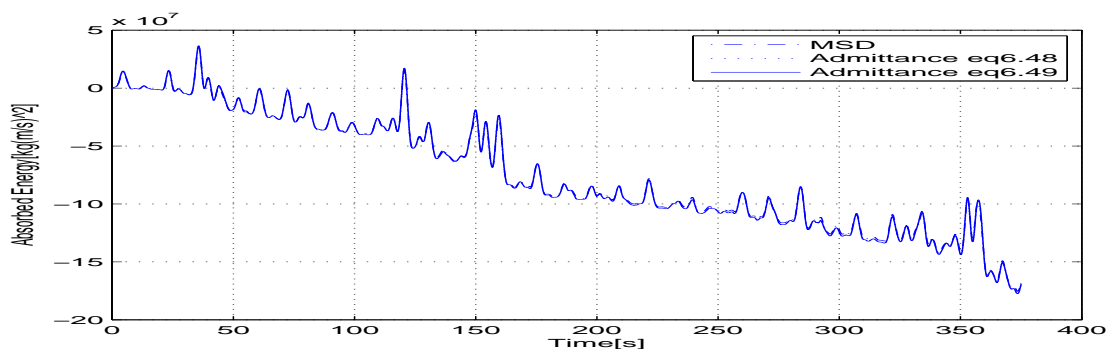


Figure 7.49 Absorbed energies extracted from the feedback control model using three admittances

7.4 Restricted complexity control tested with real wave data

As mentioned in section 6.4.2, the absolute value is the sum of the absolute values of the useful and reactive energies, which are also given in fig7.50 and fig7.51.

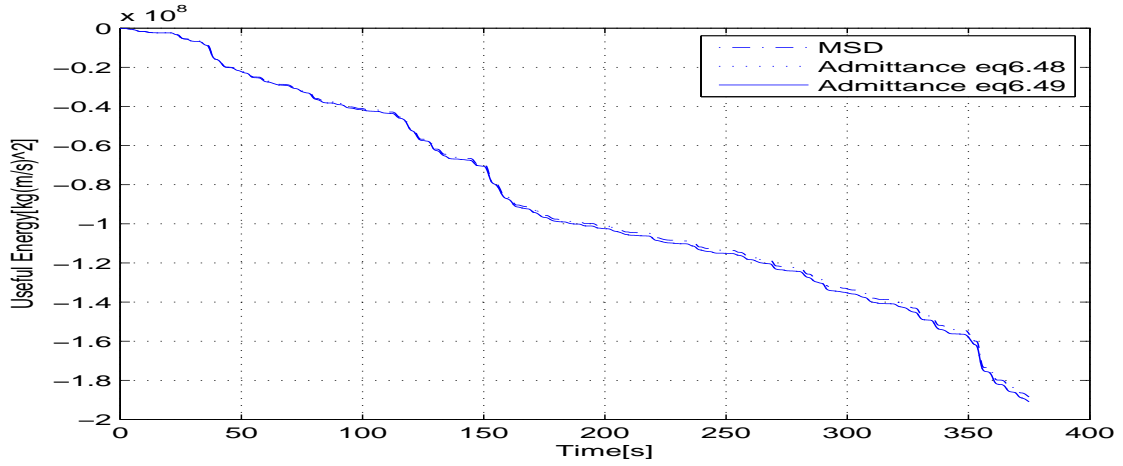


Figure 7.50 Useful energies extracted from the feedback control model using three admittances

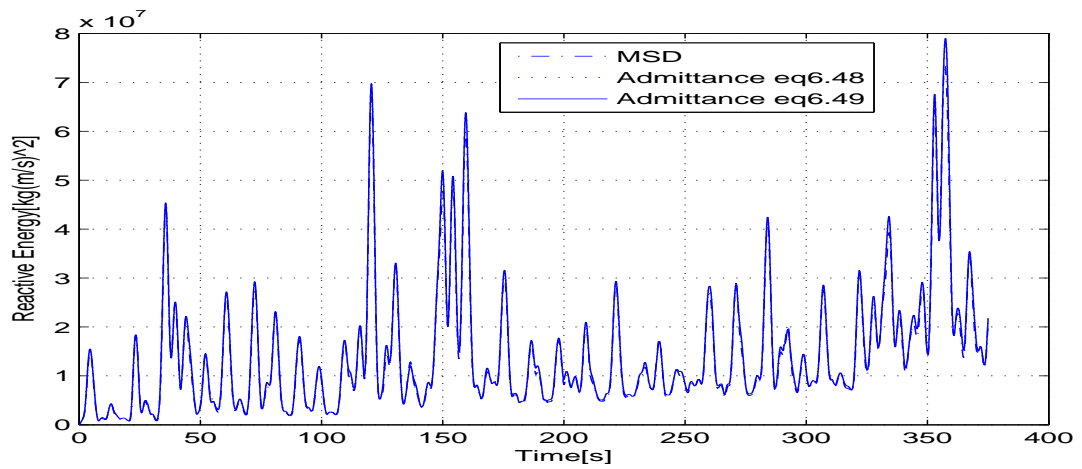


Figure 7.51 Reactive energies extracted by the feedback control model using three admittances

Finally, the useful energy that can be obtained can be determined as -1.885×10^8 J, whilst the absorbed energy can be obtained as -1.753×10^8 J when considering the mass-spring-damper impedance.

The two increased complexity impedances show identical performances when evaluated in terms of the real wave data. They each obtained -1.774×10^8 J absorbed energy and -1.898×10^8 J useful energy.

7.4 Restricted complexity control tested with real wave data

The other real wave dataset collected in Berth for the 12 : 30 – 13 : 00 time period has also been tested. A comparison of the results for the mass-spring-damper and two increased complexity impedance models is given as follows:

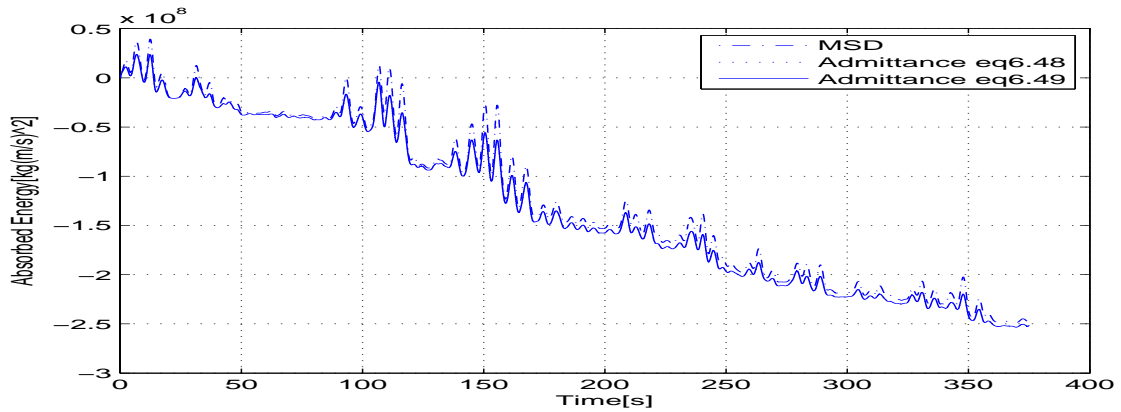


Figure 7.52 Absorbed energies extracted by the feedback control using three different kinds of admittance

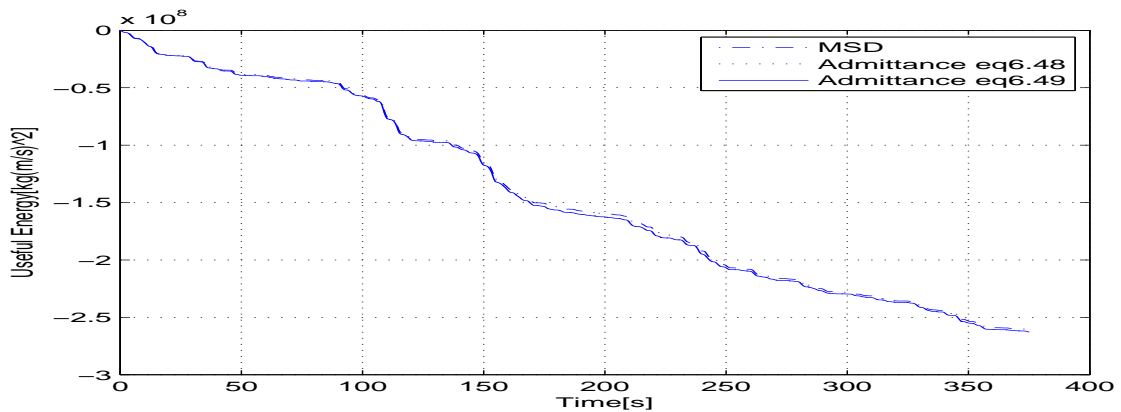


Figure 7.53 Useful energies extracted by the feedback control using three different kinds of admittance

The mass-spring-damper admittance is represented by the dash-dot line in the figureB1230abs, 7.53, and 7.54. The admittance 6.48 is represented by a dotted line, and the admittance 6.49 is represented by a solid line. The mass-spring-damper admittance can achieve -2.464×10^8 J of absorbed energy, as shown in fig7.52. Both admittances 6.48 and 6.49 achieved -2.518×10^8 J absorbed energy. The useful energy extracted by the mass-spring-damper admittance is -2.612×10^8 J, whilst the useful energy extracted by the admittances 6.48 and 6.49 are the same at -2.629×10^8 J. Also, as shown in fig7.54,

7.4 Restricted complexity control tested with real wave data

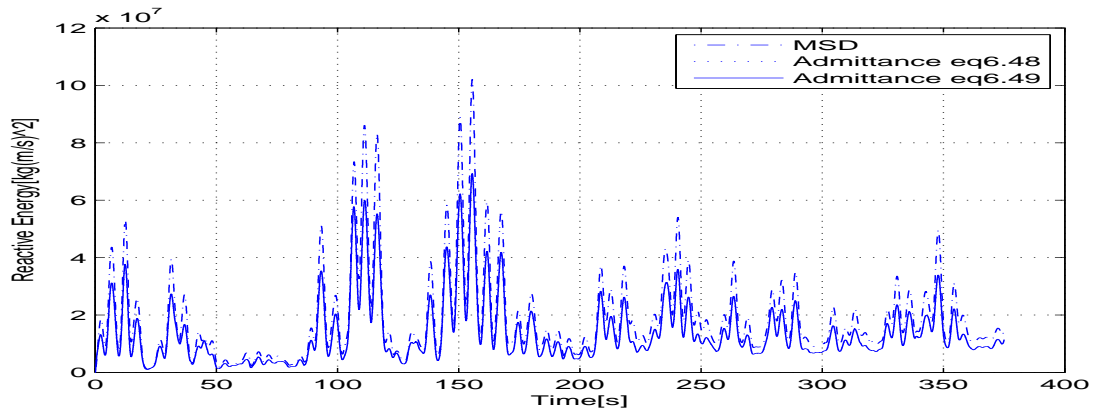


Figure 7.54 Reactive energies extracted by the feedback control using three different kinds of admittance

the reactive energy spent in the mass-spring-damper admittance is greater than that of the two increased complexity admittances. This was due to the fact that increased complexity impedances can absorb more of the absorbed energy and spend less reactive energy, and this is reflected in the Berth data for the 12 : 30 – 13 : 00 period.

7.4.2 Galway Bay

For Galway Bay, the wave spectrum is much smaller than for either of the other two locations. The working performances of the three admittances are worth investigating and comparing. In the 00 : 30 – 01 : 00 time period, the significant wave height and the zero-crossing period are 0.38873 m and 2.477 s, respectively. A comparison of the results for the normal and two increased complexity impedances are given in figure 7.55, 7.56, and 7.57:

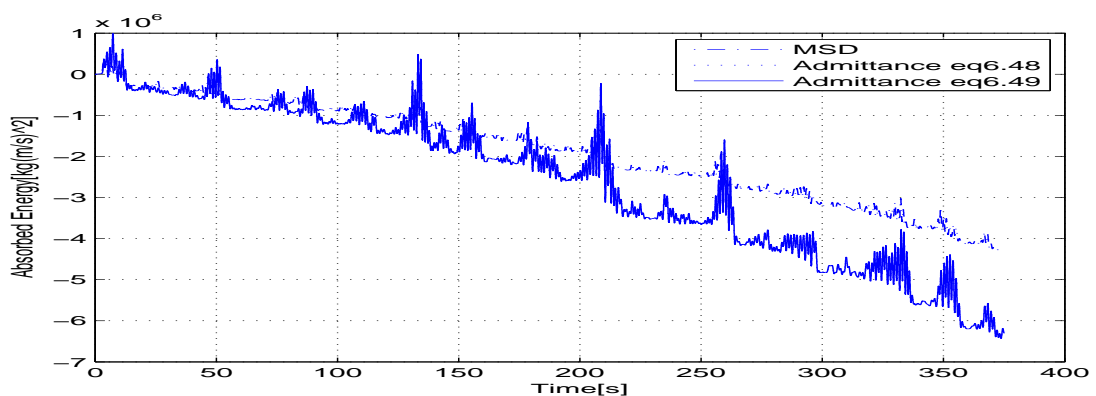


Figure 7.55 Absorbed energies extracted by the feedback control using three different admittances

7.4 Restricted complexity control tested with real wave data

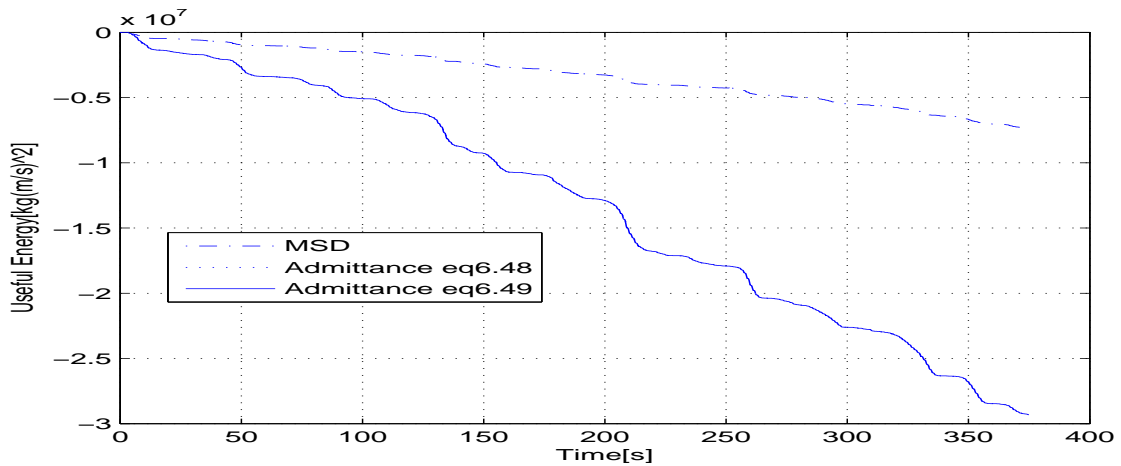


Figure 7.56 Useful energies extracted by the feedback control using three different admittances

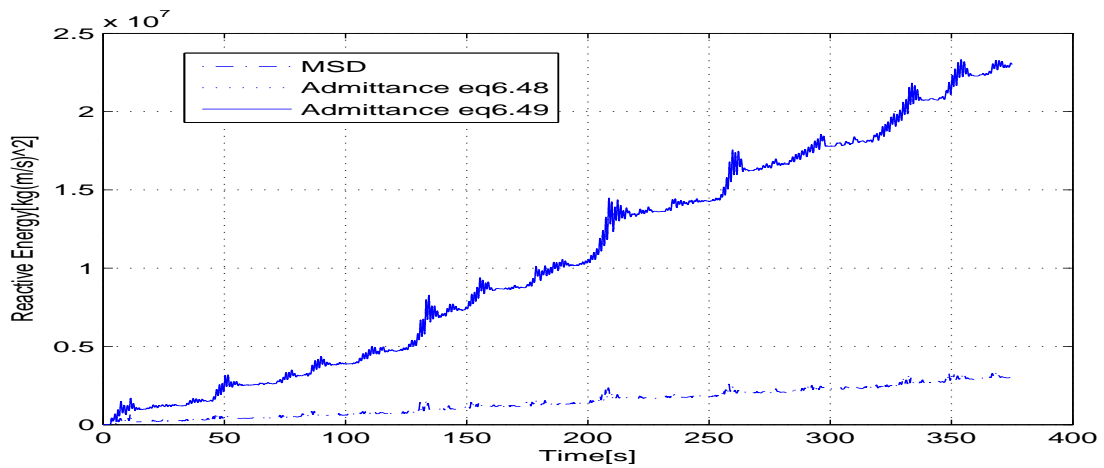


Figure 7.57 Reactive energies extracted by the feedback control using three different admittances

The two increased complexity impedances show much better performance than the normal impedance. In fig7.55, the two increased complexity impedances can obtain -6.432×10^6 J. By contrast, the normal impedance can only achieve -4.267×10^6 J. In other words, the increased complexity impedance can achieve about 66.34% more energy than the normal impedance. The useful energy obtained by the increased complexity impedances is also much greater than for the normal impedance, with the former achieving -2.932×10^7 J whilst the latter achieved only -7.299×10^6 J. However, the two increased complexity impedances expend much more reactive energy compared to the mass-spring-damper. A comparison of these results is presented in figure7.57.

7.4 Restricted complexity control tested with real wave data

The other set of real data measured in Galway Bay was recorded during the 00 : 00 – 00 : 30 time period. The significant wave height and the zero-crossing period are 0.34778 m and 2.482 s, respectively. The energies extracted with each of the three admittances are illustrated in the following figures:

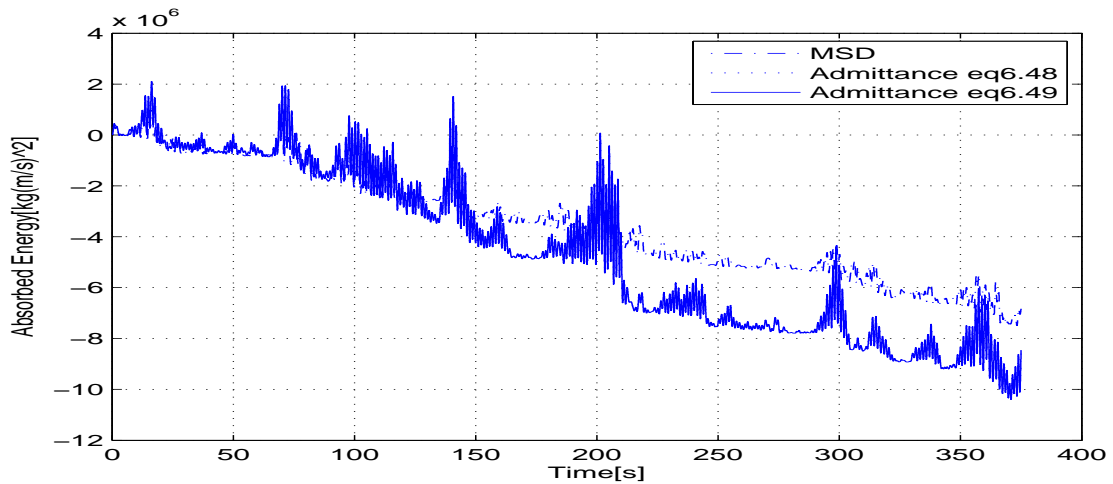


Figure 7.58 Absorbed energies extracted by the feedback control using three different admittances

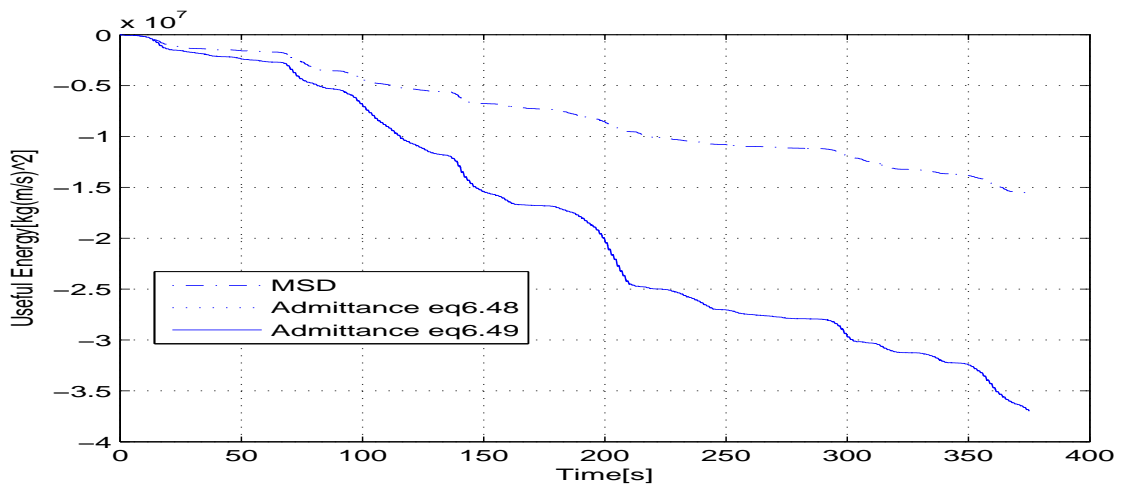


Figure 7.59 Useful energies extracted by the feedback control using three different admittances

The absorbed energy extracted by the increased complexity impedances was equal to -1.036×10^7 J, whilst that extracted by the normal impedance was -7.496×10^6 J. The useful energy extracted by the increased complexity impedances was almost three times

7.4 Restricted complexity control tested with real wave data

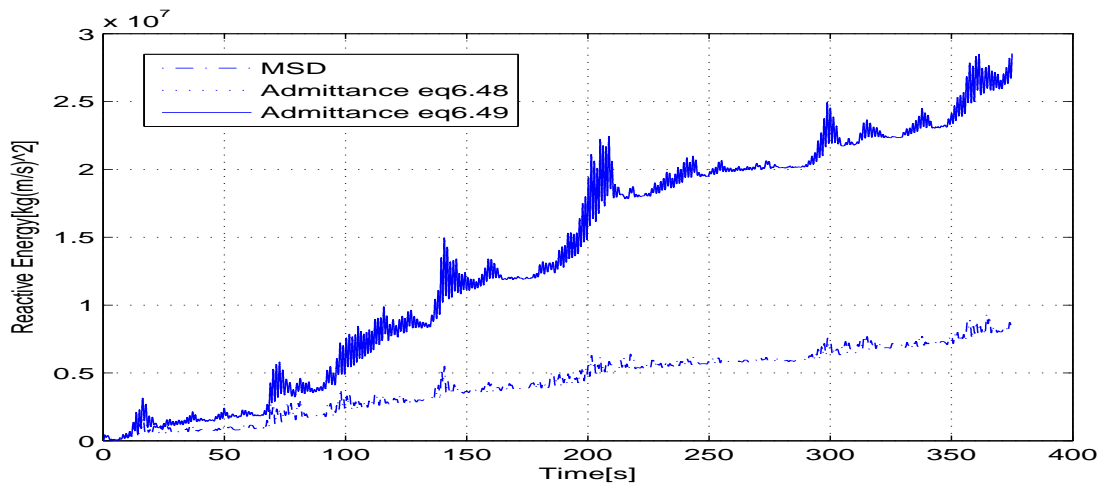


Figure 7.60 Reactive energies extracted by the feedback control using three different admittances

greater than the normal impedance, with the former achieving -3.719×10^7 J and the latter only -1.56×10^7 J. However, the increased complexity impedances expend more reactive energy than the mass-spring-damper impedance.

7.4.3 Pico

Pico Island has a similar wave spectrum to Berth. During the 00 : 19 – 00 : 49 time period, the significant wave height and zero crossing period were 1.49896 m and 7.519 s, respectively. A comparison of the results of the energy extractions are given as follows:

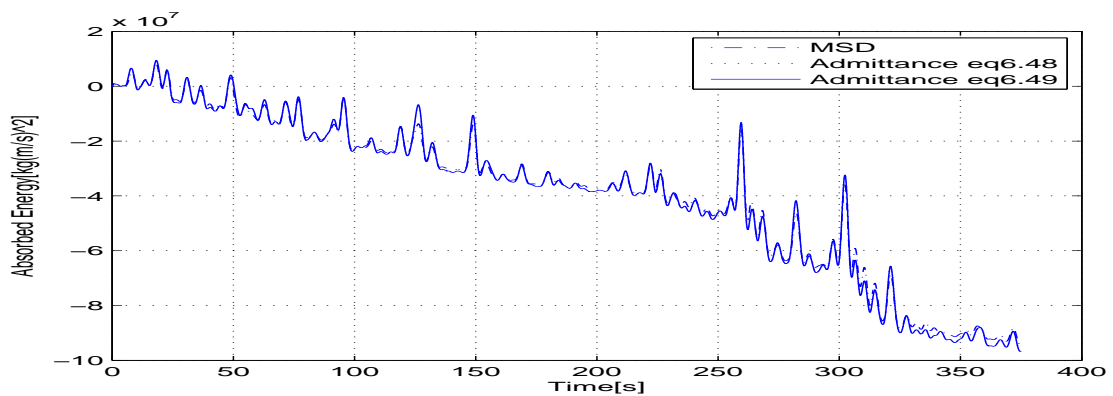


Figure 7.61 Absorbed energies extracted by the feedback control using three different admittances

7.4 Restricted complexity control tested with real wave data

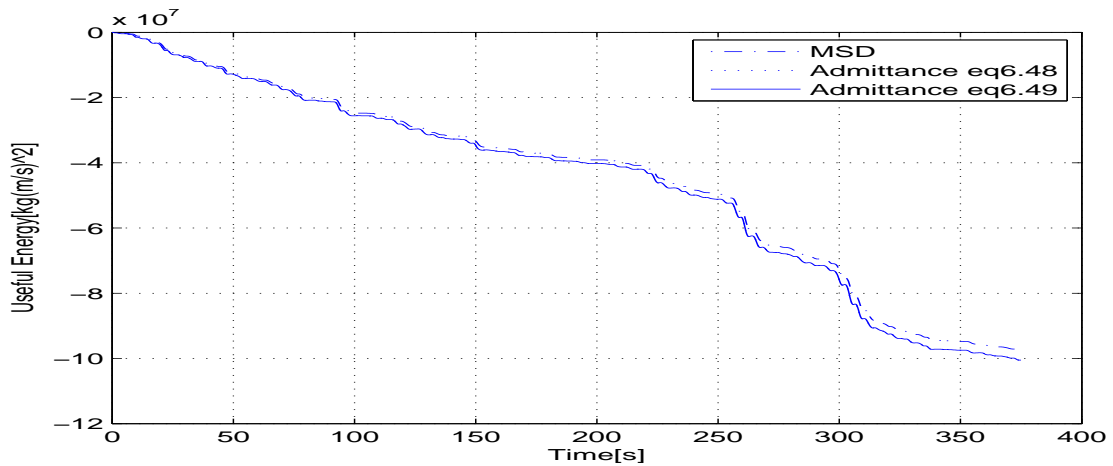


Figure 7.62 Useful energies extracted by the feedback control using three different admittances

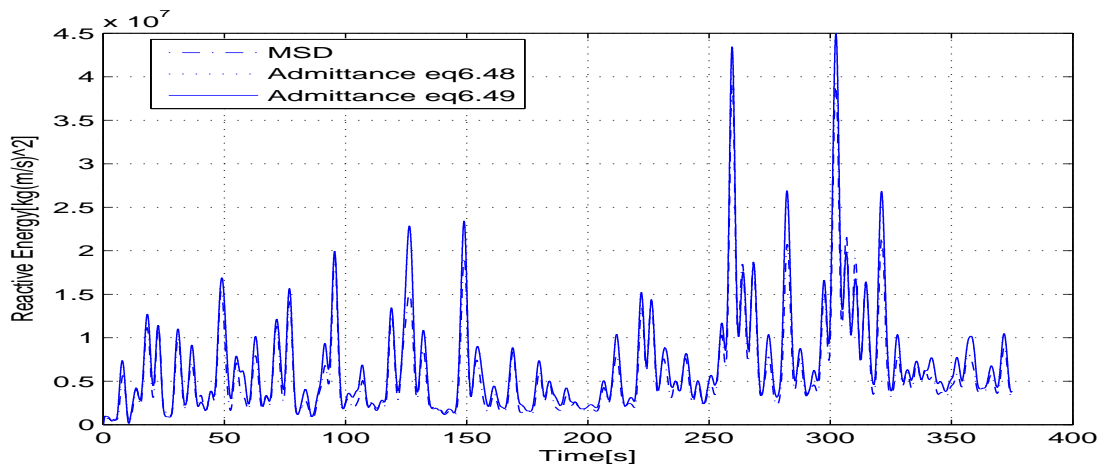


Figure 7.63 Reactive energies extracted by the feedback control using three different admittances

The absorbed energies extracted by the two increased complexity impedances were identical at -9.59×10^7 J, whilst the absorbed energy extracted by the mass-spring-damper impedance was found as -9.441×10^7 J. The useful energy captured by the two increased complexity impedances is -1.005×10^8 J, whilst that captured by the normal impedance was -9.762×10^7 J. However, the increased complexity impedances showed different performances for the Pico Island data. They expend a little more reactive energy than the mass-spring-damper impedance. As can be seen from fig7.63, the mass-spring-damper impedance expended more reactive energy than the increased complexity impedances in Berth.

7.4 Restricted complexity control tested with real wave data

Furthermore, the dataset recorded for the 00 : 49 – 01 : 19 time period was also tested with these three impedances. The significant wave height and the zero crossing period of the real wave dataset were found as 1.59321 m and 8.094 s, respectively. A comparison of the results of the energy extractions is given as follows:

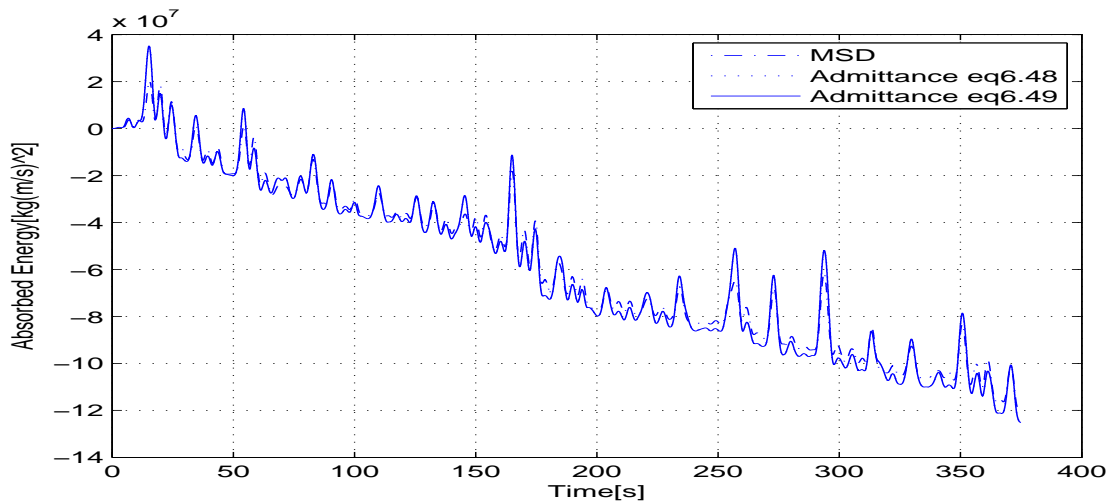


Figure 7.64 Absorbed energies extracted by the feedback control using three different admittances

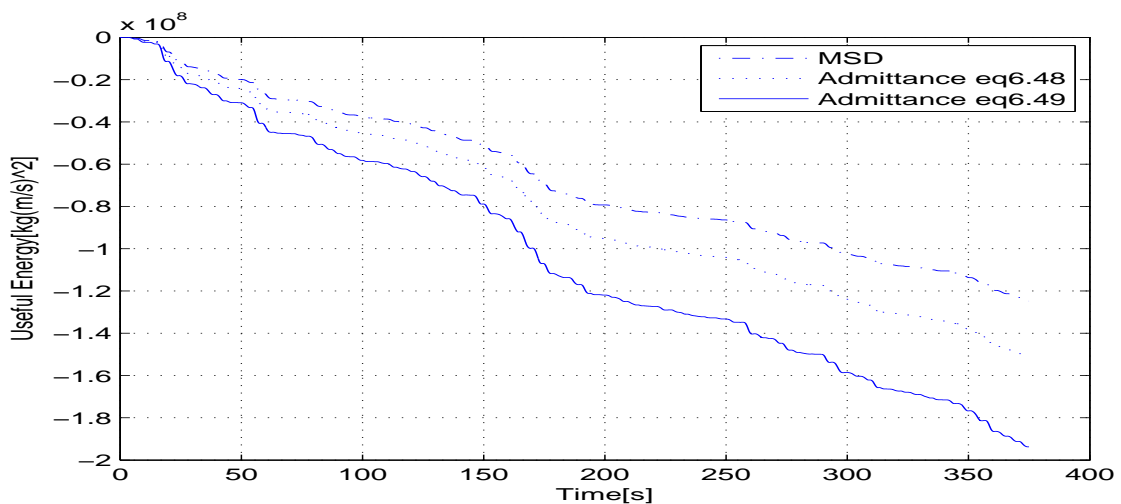


Figure 7.65 Useful energies extracted by the feedback control using three different admittances

The absorbed energy extracted by the increased complexity impedances is -1.251×10^8 J, whilst the normal impedance only achieved -1.19×10^8 J. The useful energies extracted

7.4 Restricted complexity control tested with real wave data

by each of the three admittances are shown in fig7.65. The mass-spring-damper impedance achieved -1.248×10^8 J useful energy, whilst the increased complexity impedances based on eq(6.48) only obtained -1.515×10^8 J useful energy, and -1.937×10^8 J, as based on eq(6.49). A comparison of the reactive energies is given as follows:

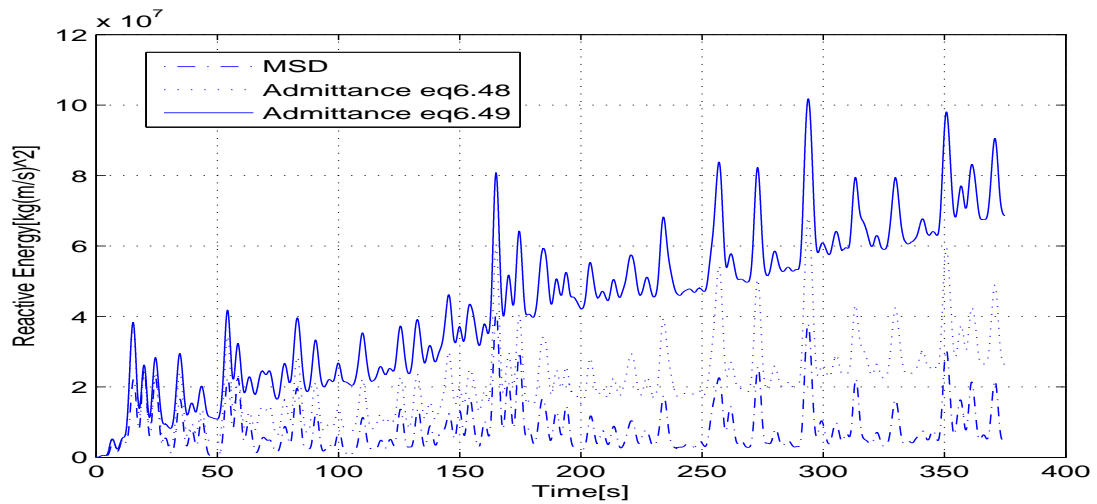


Figure 7.66 Reactive energies extracted by the feedback control using three different admittances

It can be seen that the reactive energy extracted by the increased complexity impedances is still slightly greater than that by the normal impedance. The increased complexity impedance based on eq(6.48) can thus be said to be preferable as it produced less reactive energy and absorbed the most absorbed energy.

The absorbed and useful energies captured by the three different impedances are reported in table7.4. It can be seen from table7.4 that all the absorbed energies reported for the increased complexity impedances are greater than the absorbed energies for the mass-spring-damper impedance. Furthermore, the useful energies produced by the two increased complexity impedances are greater than the useful energies produced by the mass-spring-damper impedance. In the majority of cases, the absorbed energies and useful energies produced by the two increased complexity impedances 6.48 and 6.49 are identical. These results are different than the results found using the simulated data, as reported in chapter 6. Only the result derived for the time period between 00 : 49 – 00 : 19 for Pico Island is similar to the result obtained from the simulation data. In this case, impedance 6.48 shows a better performance than impedance 6.49.

Table 7.4 Performance Table with real ocean data

	Normal impedance		Impedance6.48		Impedance6.49	
	Abs ($\times 10^8$ J)	Useful ($\times 10^8$ J)	Abs	Useful	Abs	Useful
Berth 12 : 00	-1.753	-1.885	-1.774	-1.898	-1.774	-1.898
Berth 12 : 30	-2.464	-2.612	-2.518	-2.692	-2.518	-2.692
Galway 00 : 00	-0.075	-0.156	-0.1036	-0.3719	-0.1036	-0.3719
Galway 00 : 30	-0.0427	-0.073	-0.0643	-0.2932	-0.0643	-0.2932
Pico 00 : 19	-0.9441	-0.9762	-0.959	-1.005	-0.959	-1.005
Pico 00 : 49	-1.19	-1.248	-1.251	-1.515	-1.251	-1.937

7.5 Chapter summary

Real wave data collected from three different locations has been investigated. In section 7.2, wave spectra measured using different methods in three locations have been compared. Real wave data also proves the relationship between significant wave height, zero crossing period, and the wave spectrum. Real wave datasets collected at Berth and Pico Island have similar wave characteristics, in particular their significant wave heights and zero-crossing periods. In the associated results, they show similar wave spectra. By contrast, the significant wave height and zero-crossing period measured for the Galway Bay dataset were much smaller than those found for the other two locations.

Wave predictors have been tested with the simulation data given in chapter 4; in this chapter, real wave data sets were tested using the same predictors. The MSPI method once again shows the best performance compared to the LRPI and LS methods when using real wave datasets. The other conclusion obtained from section 7.3 is that the larger the wave spectrum, the better the predictive performance that can be obtained. Wave spectra have the highest value in Berth. In the associated results, predictors that use the MSPI method can obtain the best prediction accuracy. By contrast, the Galway Bay data shows the smallest wave spectrum, and the predictors here achieve the worst prediction accuracy of all three datasets.

In section 7.4, the normal (mass-spring-damper) impedance and two increased complexity impedances have been tested with real wave datasets. They show considerably different results compared to the analogous results obtained from the simulation data. Admittances 6.48 and 6.49 have different useful energies and reactive energies using the simulation data. However, they show exactly the same results when tested with real wave datasets. In the Berth data, admittances 6.48 and 6.49 can extract a small additional amount of useful and absorbed energy compared to the normal admittance; they also expend less reactive energy. In the Galway Bay data, admittances 6.48 and 6.49 were capable of achieving considerably

greater absorbed and useful energies compared with the normal case. In addition, they expended much more reactive energy. In the Pico Island data, the useful and absorbed energies extracted by admittances 6.48 and 6.49 show similar performances and results to the Berth data. They extract a little more energy than the normal case, but expend more reactive energy. In the 00 : 19 time period, admittances 6.48 and 6.49 produce the same useful and reactive energies, in contrast to the 00 : 49 time period at Pico Island where admittance 6.48 produced less useful and reactive energy than admittance 6.49. However, admittance 6.48 still achieved the same absorbed energy as admittance 6.49. The sign and value of each element of admittances 6.48 and 6.49 can change with different values of significant wave height and zero-crossing period.

Chapter 8

Conclusion and further work

8.1 Conclusion

The objective of this thesis was to optimise the parameters of a PTO impedance to improve the energy absorbed by a WEC system. The WEC system was proposed in reference [38], which supplied the parameters describing a WEC system, whilst an internal model control (IMC) was used to maximise the absorbed energy.

In chapter 2, wave generation was introduced. Wave energy was also described in this chapter. Several wave spectra have been discussed: the Pierson-Moskowitz spectrum was simulated with wave records supplied by reference [67], and wave elevations were simulated with the Pierson-Moskowitz spectrum. Various important wave characteristics, such as significant wave height and zero crossing period, were described and compared with spectra described by different wave characteristics in this chapter. A WEC dynamic model was the key point addressed in section 2.3. The forces acting on an oscillating body were also analysed. The power transmission of the WEC system was based on the frequency domain of external forces.

In chapter 3, the most important objective was to discover the optimal conditions for maximising absorption energy. Two optimal conditions were introduced in this chapter. One was that of complex conjugate control, whilst the other was velocity-tracking control. Complex conjugate control was used to find the complex conjugate of the intrinsic impedance. The control impedance is equal to the complex conjugate of the intrinsic impedance, and allows the maximum absorption of energy with the WEC system. Velocity-tracking control was used to track the optimal relationship between the optimal velocity and the excitation force. A feedback control construction was used to minimise the error between the optimal velocity and the measured velocity. Problems arising due to causality and non-causality were

discussed, and several possible solutions were examined to address their associated problems; for instance, the prediction of wave elevation or excitation force could be one such solution. The other solution discussed was that of using a constant approximation to optimal conditions to instead address the problem via non-causal conditions. Several different control methods were presented in section 3.4, some of which were described by two optimal conditions. Additionally, although they are not considered either of the two optimal conditions, passive loading control and latching control have also been described.

The prediction of wave elevation and excitation force is one of the possible solutions to overcoming non-causality. The prediction of wave elevation was the main consideration of chapter 4, for which three different system identifications were described. The least-squares (LS) system identification is the simplest method as it predicts the future wave elevation based on only one past data, but unfortunately is too simplistic to meet the requirements of wave elevation prediction. The second method proposed to solve this problem was that of long-range predictive identification (LRPI), which predicts future wave elevation based on several past data. However, a new method called multi step predictive identification (MSPI) was also introduced at this point. It can achieve more accurate results than either of the above two methods because it identifies each future data with an individual model. A comparison of the predictive accuracy of these three methods supported the proposal that MSPI showed the best performance, and that LS had the worst performance, of the three models. It also proved that the majority of the energy in a wave is stored in a low frequency sea state. Prediction accuracy was also found to be related to model order. Higher order models were found to achieve more accurate predictions. The Akaike information criterion (AIC) and Bayesian information criterion (BIC) were used to choose a suitable order for a given model.

A further means of overcoming the non-causal problem was proposed in chapter 5. Firstly, the prediction error method was used to find the different order approximated transfer function of the intrinsic impedance. A highly accurate eighth-order approximated transfer function of complex conjugate of intrinsic impedance, and a fourth-order approximated optimal non-causal impedance was found. A second-order approximated model was introduced in section 5.3. A constant impedance was found to express the relationship between velocity and the excitation that could overcome the non-causal problem of the optimal non-causal impedance. Furthermore, this model showed the absorption of more energy compared to the normal model. "The Tracer" software was also introduced in this chapter to capture hydrodynamic coefficients from reference [38]. Hydrodynamic coefficients can be used for excitation force calculations, with the excitation force subsequently used as a disturbance to the control system. Control systems that used constant approximations were compared in

section 5.5, with the observation that constant approximations calculated by the prediction error method performed better than those calculated by partial fraction decomposition.

Chapter 6 represents the main contribution by this thesis. The different control methods introduced in chapter 3 were compared using simulation data. The complex conjugate control achieved the greatest absorbed energy and hence was chosen as the control system. The Nelder–Mead method (*'fminsearch'*) was used to maximise the absorbed wave energy based on the maximum absorbed energy cost function. Three different order control impedances were obtained. Different realisations of the control impedances were calculated using Brune Synthesis. Control impedances can be decomposed into their active parts and passive parts, with the useful energy being generated by the passive parts and the active part generating reactive energy. The WEC systems with increased complexity impedances were found to absorb a small amount of additional absorbed energy compared with the spring-damper and mass-spring-damper systems; however, much more useful energy was obtained by the increased complexity impedance models. In conclusion, PTO realised with impedance 6.48 is preferable to that realised with impedance 6.49. Realisation of impedance 6.48 expends less reactive energy but the same absorbed energy.

In chapter 7, 16 sets of real ocean data were collected from three locations. The main wave characteristics for each dataset, namely significant wave height and zero crossing period, were reported in this chapter. The wave spectrum was measured using the *Waves21* software. Three spectrum-estimation methods were used to estimate these spectra. The wave elevations of all real ocean datasets have been reported. The findings may be summarized by saying that Galway Bay has low energy states whilst Berth and Pico Island have high energy states. Furthermore, two datasets for each location were tested using three different prediction methods. Datasets collected in Galway Bay were found to have the worst prediction accuracy. By contrast, datasets collected in high energy states have better prediction accuracies. In addition, multi step predictive identification was still found to have the best prediction performance compared with least-squares system identification and long-range predictive identification. Least-squares system identification did not give better predictive performance than the other two methods. Real ocean datasets were tested with a mass-spring-damper impedance and increased complexity impedances. The results obtained using real wave datasets were considerably different to the simulation data results. Impedance 6.48 produces identical useful and reactive energies as impedance 6.49 with most of the real wave datasets. It was only in the 00 : 49 – 01 : 19 time period for the Pico Island data that impedance 6.48 produced less useful and reactive energy than impedance 6.49, though it did still show the same absorbed energy.

8.2 Further work

Several directions for further research can be explored based on the work carried out in this thesis. One possible future research direction could be based on different wave spectra. The Pierson-Moskowitz spectrum can only simulate a single peak spectrum. Other methods, such as the Bretschneider spectrum and Ochi-Hubble spectrum can be used to simulate double-peak spectra. Control with impedances 6.48 and 6.49 may show better performance when using a double-peak spectrum.

Control with impedances 6.48 and 6.49 in chapter 6 expends considerable reactive energy. The design of penalty functions for optimal control of the wave energy converter system could be a possible solution to reducing reactive energy expenditure. It would be interesting to examine the design of a penalty function for the wave energy converter system.

The third possible direction for future research might focus on the physical realisation of impedances 6.48 and 6.49. Optimised PTO mechanical networks include various active and passive parts that correspond to negative and positive values of the impedance parameters. The realisation of the active parts may represent a rich area for future research.

Bibliography

- [1] Akaike, H. (1974). A new look at the statistical model identification. *Automatic Control, IEEE Transactions on*, 19(6):716–723.
- [2] Babarit, A. and Clément, A. (2006). Optimal latching control of a wave energy device in regular and irregular waves. *Applied Ocean Research*, 28(2):77–91.
- [3] Babarit, A., Duclos, G., and Clément, A. (2004). Comparison of latching control strategies for a heaving wave energy device in random sea. *Applied Ocean Research*, 26(5):227–238.
- [4] Belmont, M., Horwood, J., Thurley, R., and Baker, J. (2006). Filters for linear sea-wave prediction. *Ocean Engineering*, 33(17):2332–2351.
- [5] Bretschneider, C. L. (1957). Revisions in wave forecasting: deep and shallow water. *Coastal Engineering Proceedings*, 1(6):3.
- [6] Bretschneider, C. L. (1959). Wave variability and wave spectra for wind-generated gravity waves. Technical report, CORPS OF ENGINEERS WASHINGTON DC BEACH EROSION BOARD.
- [7] Bretschneider, C. L. (1968). Significant waves and wave spectrum. *Ocean Industry*, 3(2):44–46.
- [8] Brune, O. (1931). *Synthesis of a finite two-terminal network whose driving-point impedance is a prescribed function of frequency*. PhD thesis, Massachusetts Institute of Technology.
- [9] Budal, K. and Falnes, J. (1977). Optimum operation of improved wave-power converter. *Mar. Sci. Commun.:(United States)*, 3(2).
- [10] Budar, K. and Falnes, J. (1975). A resonant point absorber of ocean-wave power. *Nature*, 256:478.
- [11] BV, D. (2010). *W@ves21*. Datawell BV, <http://www.datawell.nl/Products/Software.aspx>.
- [12] Cakmakyapan, S. and Goktas, A. (2013). A comparison of binary logit and probit models with a simulation study. *Journal of Social and Economic statistics*, 2(1):1–17.
- [13] Carter, D. (1982). Prediction of wave height and period for a constant wind velocity using the jonswap results. *Ocean Engineering*, 9(1):17–33.

- [14] Clarke, D., Mohtadi, C., and Tuffs, P. (1987a). Generalized predictive control—part ii extensions and interpretations. *Automatica*, 23(2):149–160.
- [15] Clarke, D. W., Mohtadi, C., and Tuffs, P. (1987b). Generalized predictive control—part i. the basic algorithm. *Automatica*, 23(2):137–148.
- [16] Cruz, J. (2007). *Ocean wave energy: current status and future perspectives*. Springer Science & Business Media.
- [17] Cruz, J., Gunnar, M., Barstow, S., Mollison, D., and Cruz, J. (2008). Green energy and technology, ocean wave energy.
- [18] Cruz, J., Saramento, A., and Gardner, F. (2005). Aws pilot plant tests. In *Proc. 6th Euro. Wave and Tidal Energy Conf., Glasgow*, pages 105–111.
- [19] De Hoon, M., Van der Hagen, T., Schoonewelle, H., and Van Dam, H. (1996). Why yule-walker should not be used for autoregressive modelling. *Annals of Nuclear Energy*, 23(15):1219–1228.
- [20] Department of Communications, M. and Natural Resources, G. o. I. D. (2003). MS Windows NT kernel description.
- [21] Evans, D. (1981). Maximum wave-power absorption under motion constraints. *Applied Ocean Research*, 3(4):200–203.
- [22] Falnes, J. (1995). On non-causal impulse response functions related to propagating water waves. *Applied Ocean Research*, 17(6):379–389.
- [23] Falnes, J. (2002). *Ocean waves and oscillating systems*. Cambridge University Press.
- [24] Falnes, J. (2007). A review of wave-energy extraction. *Marine Structures*, 20(4):185–201.
- [25] Falnes, J. and Lillebekken, P. M. (2003). Budal’s latching-controlled-buoy type wave-power plant. In *Proceedings of the 5th European Wave Energy Conference, Cork, Ireland*, volume 1720.
- [26] Falnes, J. and Løvseth, J. (1991). Ocean wave energy. *Energy Policy*, 19(8):768–775.
- [27] Faltinsen, O. (1993). *Sea loads on ships and offshore structures*, volume 1. Cambridge university press.
- [French] French, M. Conceptual design for engineers , 1985. *Design Council, London*.
- [29] French, M. (2006). On the difficulty of inventing an economical sea wave energy converter: a personal view. *Proceedings of the Institution of Mechanical Engineers, Part M: Journal of Engineering for the Maritime Environment*, 220(3):149–155.
- [30] Fu, X. and Lecchini-Visintini, A. (2016). Optimisation of restricted complexity control for wave energy conversion. In *Control (CONTROL), 2016 UKACC 11th International Conference on*, pages 1–5. IEEE.

- [31] Fusco, F. (2012). *Real-time Forecasting and Control for Oscillating Wave Energy Devices*. PhD thesis, National University of Ireland Maynooth.
- [32] Fusco, F., Ringwood, and John (2011). Quantification of the prediction requirements in reactive control of wave energy converters. In *Proceedings of 18th IFAC World Congress*, pages 11483–11488. International Federation of Automatic Control (IFAC).
- [33] Fusco, F. and Ringwood, J. (2009). A study on short-term sea profile prediction for wave energy applications.
- [34] Fusco, F. and Ringwood, J. (2011). Suboptimal causal reactive control of wave energy converters using a second order system model. In *Proceedings of the 21st (2011) International Offshore and Polar Engineering Conference*, pages 687–694. International Society of Offshore and Polar Engineers (ISOPE).
- [35] Fusco, F. and Ringwood, J. V. (2010a). Short-term wave forecasting for real-time control of wave energy converters. *Sustainable Energy, IEEE Transactions on*, 1(2):99–106.
- [36] Fusco, F. and Ringwood, J. V. (2010b). Short-term wave forecasting with ar models in real-time optimal control of wave energy converters. In *Industrial Electronics (ISIE), 2010 IEEE International Symposium on*, pages 2475–2480. IEEE.
- [37] Fusco, F. and Ringwood, J. V. (2012). A study of the prediction requirements in real-time control of wave energy converters. *Sustainable Energy, IEEE Transactions on*, 3(1):176–184.
- [38] Fusco, F. and Ringwood, J. V. (2013). A simple and effective real-time controller for wave energy converters. *Sustainable Energy, IEEE Transactions on*, 4(1):21–30.
- [39] Fusco, F. and Ringwood, J. V. (2014). Hierarchical robust control of oscillating wave energy converters with uncertain dynamics. *Sustainable Energy, IEEE Transactions on*, 5(3):958–966.
- [40] Gato, L. and Falcão, A. d. O. (1988). Aerodynamics of the wells turbine. *International Journal of Mechanical Sciences*, 30(6):383–395.
- [41] Haber, R., Bars, R., and Schmitz, U. (2012). *Predictive Control in Process Engineering-From the Basics to the Applications*. Wiley. com.
- [42] Hals, J. (2010). Modelling and phase control of wave-energy converters.
- [43] Hals, J., Bjarte-Larsson, T., and Falnes, J. (2002). Optimum reactive control and control by latching of a wave-absorbing semisubmerged heaving sphere. In *ASME 2002 21st International Conference on Offshore Mechanics and Arctic Engineering*, pages 415–423. American Society of Mechanical Engineers.
- [44] Hals, J., Falnes, J., and Moan, T. (2011a). A comparison of selected strategies for adaptive control of wave energy converters. *Journal of Offshore Mechanics and Arctic Engineering*, 133(3):031101.
- [45] Hals, J., Falnes, J., and Moan, T. (2011b). Constrained optimal control of a heaving buoy wave-energy converter. *Journal of Offshore Mechanics and Arctic Engineering*, 133(1):011401.

- [46] Hasselmann, K., Barnett, T., Bouws, E., Carlson, H., Cartwright, D., Enke, K., Ewing, J., Gienapp, H., Hasselmann, D., Kruseman, P., et al. (1973). Measurements of wind-wave growth and swell decay during the joint north sea wave project (jonswap). Technical report, Deutsches Hydrographisches Institut.
- [47] Hover., Franz, S., and Triantafyllou, M. S. (2010). System design for uncertainty @ONLINE.
- [48] Hughes, S. A. (1993). *Physical models and laboratory techniques in coastal engineering*, volume 7. World Scientific.
- [49] Iannario, M. (2009). Fitting measures for ordinal data models. *Quaderni di Statistica*, 11:39–72.
- [50] Inc., W. (20088). *WAMIT*. Wamit Inc., <http://www.wamit.com/version7.0.htm>.
- [51] Institute, G. G. E. N. (2016). Tracer 1.71 @ONLINE.
- [52] Institute, M. (2005). *Access Data*. Marine Institute, <https://www.marine.ie/Home/site-area/data-services/search-marine-data/access-data>.
- [53] Ireland, T. S. O. (2005). Generation adequacy report 2006-2012.
- [54] Kamenskỳ, M. and Guglielmi, M. (2007). Optimal control of power take-off from mass spring-damper system. *16th International on Process Control*.
- [55] Karolewski, M. (2012). *Tracer 2.01*. Kalypso, <https://sites.google.com/site/kalypsosimulation/Home/data-analysis-software-1>.
- [56] Khan, M., Bhuyan, G., Moshref, A., and Morison, K. (2008). An assessment of variable characteristics of the pacific northwest regions wave and tidal current power resources, and their interaction with electricity demand & implications for large scale development scenarios for the region. *BPA Technology Innovation project*, pages 17458–21.
- [57] Korde, U. (1999). Efficient primary energy conversion in irregular waves. *Ocean engineering*, 26(7):625–651.
- [58] Korde, U. A. (1998). On control approaches for efficient primary energy conversion in irregular waves. In *OCEANS'98 Conference Proceedings*, volume 3, pages 1427–1431. IEEE.
- [59] Lekka, A., Turner, M. C., and Ringwood, J. V. (2012). A class of globally stabilising controllers for the control of wave energy devices for potable water production. In *Control Applications (CCA), 2012 IEEE International Conference on*, pages 1369–1373. IEEE.
- [60] Ljung, L. (1999). *System identification Theory for the User Second Edition*. Prentice-Hall, Inc.
- [61] Ljung, L. (2002). Prediction error estimation methods. *Circuits, Systems and Signal Processing*, 21(1):11–21.
- [62] MacCamy, R. and Fuchs, R. (1954). Wave forces on piles: a diffraction theory. Technical report, DTIC Document.

- [63] Mathews, J. H. and Fink, K. D. (1999). *Numerical methods using MATLAB*, volume 31. Prentice hall Upper Saddle River, NJ.
- [64] Naito, S. and Nakamura, S. (1986). Wave energy absorption in irregular waves by feedforward control system. In *Hydrodynamics of ocean wave-energy utilization*, pages 269–280. Springer.
- [65] Newman, J. N. (1977). *Marine hydrodynamics*. MIT press.
- [66] Nolan, G. and Ringwood, J. (2006). Control of a heaving buoy wave energy converter for potable water production.
- [67] Nolan, G., Ringwood, J., and Holmes, B. (2007). Short term wave energy variability off the west coast of Ireland. In *Proceedings of the 7th European Wave and Tidal Energy Conference, Porto, Portugal (EWTEC)*.
- [68] Nolan, G., Ringwood, J., Leithead, W., and Butler, S. (2005). Optimal damping profiles for a heaving buoy wave-energy converter. In *Proceedings of the Fifteenth International Offshore and Polar Engineering Conference (ISOPE)*, volume 1, pages 477–485.
- [69] Nolan, G. A. (2006). *Modelling and Optimisation of a Heaving Buoy Wave Energy Converter for Potable Water Production*. PhD thesis, National University of Ireland Maynooth.
- [70] Ochi, M. K. (2005). *Ocean waves: the stochastic approach*, volume 6. Cambridge University Press.
- [71] Ochi, M. K. and Hubble, E. N. (1977). Six-parameter wave spectra. In *Coastal Engineering 1976*, pages 301–328.
- [72] Ochi, M. K. and Tsai, C.-H. (1983). Prediction of occurrence of breaking waves in deep water. *Journal of Physical Oceanography*, 13(11):2008–2019.
- [73] Parker, R. M., Harrison, G., and Chick, J. (2007). Energy and carbon audit of an offshore wave energy converter. *Proceedings of the Institution of Mechanical Engineers, Part A: Journal of Power and Energy*, 221(8):1119–1130.
- [74] Perdigão, J. and Sarmiento, A. (1989). A phase control strategy for owc devices in irregular seas. In *Proc. 4th Int. Workshop on Water Waves and Floating Bodies*, pages 205–209.
- [75] Pérez, T. and Fossen, T. I. (2008). Time-vs. frequency-domain identification of parametric radiation force models for marine structures at zero speed. *Modeling, Identification and Control*, 29(1):1–19.
- [76] Pierson Jr, W. J. and Moskowitz, L. (1963). A proposed spectral form for fully developed wind seas based on the similarity theory of sa kitaigorodskii. Technical report, DTIC Document.
- [77] Pierson Jr, W. J. and Moskowitz, L. (1964). A proposed spectral form for fully developed wind seas based on the similarity theory of sa kitaigorodskii. *Journal of geophysical research*, 69(24):5181–5190.

- [78] Press, W. H. (2007). *Numerical recipes 3rd edition: The art of scientific computing*. Cambridge university press.
- [79] Ringwood, J. (2010). Ahead of the wave. *Journal of Ocean Technology*, 5(2):73–91.
- [80] Rossiter, J. (1993). Notes on multi-step ahead prediction based on the principle of concatenation. *Proceedings of the Institution of Mechanical Engineers, Part I: Journal of Systems and Control Engineering*, 207(4):261–263.
- [81] Rossiter, J. and Kouvaritakis, B. (2001). Modelling and implicit modelling for predictive control. *International Journal of Control*, 74(11):1085–1095.
- [82] Schwarz, G. et al. (1978). Estimating the dimension of a model. *The annals of statistics*, 6(2):461–464.
- [83] Setoguchi, T., Santhakumar, S., Maeda, H., Takao, M., and Kaneko, K. (2001). A review of impulse turbines for wave energy conversion. *Renewable energy*, 23(2):261–292.
- [84] Shook, D., Mohtadi, C., and Shah, S. (1991). Identification for long-range predictive control. In *IEE Proceedings D (Control Theory and Applications)*, volume 138, pages 75–84. IET.
- [85] Singer, S. and Nelder, J. (2009). Nelder-mead algorithm. *Scholarpedia*, 4(7):2928.
- [86] Smith, M. C. (2002). Synthesis of mechanical networks: The inerter. *Automatic Control, IEEE Transactions on*, 47(10):1648–1662.
- [87] Smith, M. C. and Wang, F.-C. (2004). Performance benefits in passive vehicle suspensions employing inerters. *Vehicle System Dynamics*, 42(4):235–257.
- [88] Society, A. M. (2012). Fully developed sea.
- [89] Soerensen, H., Friis-Madsen, E., Panhauser, W., Duncce, D., Nedkvintne, J., Frigaard, P. B., Kofoed, J. P., Knapp, W., Riemann, S., Holmén, E., et al. (2003). Development of wave dragon from scale 1: 50 to prototype. In *The Fifth European Wave Energy Conference*.
- [90] Stewart, R. H. (2004). *Introduction to physical oceanography*, chapter Chapter 16 Ocean Waves. Texas A & M University.
- [91] Stokes, G. G. (1847). On the theory of oscillatory waves. *Trans Cambridge Philos Soc*, 8:441–473.
- [92] Techet, A. (2005). Design principles for ocean vehicles. *Massachusetts Institute of Technology, Department of Ocean Engineering*.
- [93] Tedd, J., Frigaard, P., et al. (2007). Short term wave forecasting, using digital filters, for improved control of wave energy converters. In *The Seventeenth International Offshore and Polar Engineering Conference*. International Society of Offshore and Polar Engineers.
- [94] Thorpe, T. (1999). An overview of wave energy technologies: status, performance and costs. *Wave power: moving towards commercial viability*, 26:50–120.

- [95] Tutorials, A. E. (2016). Devices that harness the energy of the waves @ONLINE.
- [96] Valério, D., Beirao, P., and da Costa, J. S. (2007a). Feedback linearisation control applied to the archimedes wave swing. In *Control & Automation, 2007. MED'07. Mediterranean Conference on*, pages 1–6. IEEE.
- [97] Valério, D., Beirão, P., and da Costa, J. S. (2007b). Optimisation of wave energy extraction with the archimedes wave swing. *Ocean Engineering*, 34(17):2330–2344.
- [98] Valério, D., Mendes, M. J., Beirão, P., and da Costa, J. S. (2008). Identification and control of the aws using neural network models. *Applied Ocean Research*, 30(3):178–188.
- [99] Vogel, F., Holm, S., and Lingjærde, O. C. (2001). Spectral moments and time domain representation of photoacoustic signals used for detection of crude oil in produced water. In *Proc. Nordic Symp. on Physical Acoustics, Ustaoset, Norway*.
- [100] Wang, F.-C. and Su, W.-J. (2008). Inerter nonlinearities and the impact on suspension control. In *American Control Conference, 2008*, pages 3245–3250. IEEE.
- [101] Whittaker, T. (2010). Perfomance of the limpet wave power plant-prediction, measurement & potential.
- [102] Yemm, R., Pizer, D., and Retzler, C. (2002). Floating apparatus and method for extracting power from sea waves. US Patent 6,476,511.

Appendix A

Test with real ocean data

```
1 %%=====Real data (spectrum)=====%%
2 fileID=fopen('BerthB2012-05-16T12h00Z-sprctrum.txt'); %
   Real wave spectrum data collected in BerthB at 12:00
   16/5/2012.
3 % fileID=fopen('BerthB2012-05-16T12h30Z-sprctrum.txt'); %
   Real wave spectrum data collected in BerthB at 12:30
   16/5/2012.
4 % fileID=fopen('Pico2008-09-01T00h19-spectrum.txt'); % Real
   wave spectrum data collected in Pico at 00:19 1/9/2008.
5 % fileID=fopen('Pico2008-09-01T00h49-spectrum.txt'); % Real
   wave spectrum data collected in Pico at 00:49 1/9/2008.
6 % fileID=fopen('GalwayBayDirectional2012-05-01T00h00Z-
   spectrum.txt'); % Real wave spectrum data collected in
   GalwayBay at 00:00 1/5/2012.
7 % fileID=fopen('GalwayBayDirectional2012-05-01T00h30Z-
   spectrum.txt'); % Real wave spectrum data collected in
   GalwayBay at 00:30 1/5/2012.
8
9 D = textscan(fileID,'%f %f %f %f %u8 %f',...
10 'Delimiter',' ',' ','EmptyValue',-Inf);
11 fclose(fileID);
12 column2 = D{2};
13 column1 = D{1};
14 y_data1=column2(1:end)'; % Wave spectrum data
```

```

15 x_data1=column1(1:end)'; % Frequency
16 Xq1=0.025: (0.58-0.025)/479:0.58; % Wave spectrum interval(
    relates to section 2.2.2)
17 Xq=2*pi.*Xq1; % Converting Hz to rad
18 Vq = interp1(2*pi.*x_data1,y_data2,Xq); % Returning
    interpolated values
19 plot(Xq,Vq) % Plotting freq against real wave spectrum
20 xlabel('Frequency[rad/s]'); ylabel('Wave spectrum[m^2 s/rad]
    ');
21
22 %%==Excitation force coefficient Hex phase estimatation==%%
23 u = Xq; % Giving freq omega w
24 p1 = -0.025396;
25 p2 = 0.20462;
26 p3 = 0.06207;
27 p4 = -0.0084896;
28 p5 = -0.0013623;
29 y_phase=p1*u.^4+p2*u.^3+p3*u.^2+p4*u.^1+p5;
30 %Computing phase of the excitation coefficient which follows
    eq5.41
31
32 %%Excitation force coefficient Hex magnitude estimatation%%
33 p11 = -5909.2;
34 p21 = 61936;
35 p31 = -2.3279e+05;
36 p41 = 2.9547e+05;
37 p51 = 2.7453e+05;
38 p61 = -8.8359e+05;
39 p71 = 47066;
40 p81 = 8.0081e+05;
41 y_mag = p11*u.^7+p21*u.^6+p31*u.^5+p41*u.^4+p51*u.^3+p61*u
    .^2+p71*u.^1+p81;
42 %Computing magnitude of the excitation coefficient which
    follows eq5.40

```

```

43 y_new = (y_mag) .* (cos(rad2deg(y_phase))+1i*sin(rad2deg(
    y_phase)));
44 %Creating excitation coefficient which follows eq5.39
45
46 %%=====Real wave elevation data=====%%
47 fileID=fopen('BerthB2012-05-16T12h00Z.txt');
48 % fileID=fopen('BerthB2012-05-16T12h30Z.txt');
49 % fileID=fopen('Pico2008-09-01T00h19.txt');
50 % fileID=fopen('Pico2008-09-01T00h49.txt');
51 % fileID=fopen('GalwayBayDirectional2012-05-01T00h00Z.txt');
52 % fileID=fopen('GalwayBayDirectional2012-05-01T00h30Z.txt');
53
54 C = textscan(fileID,'%f %f %f %f %u8 %f',...
55 'Delimiter',' ','EmptyValue',-Inf);
56 fclose(fileID);
57 column2 = C{2};
58 x_data=0.01*column2(1:480)'; % Converting wave elevation cm
    to meter
59 Y= fft(x_data(1:480)).*(y_new); % DFT of excitation force
    which follows eq5.38
60 F_ex = ifft(Y,'symmetric'); % Excitation force
61
62 %%=====Frequency response of intrinsic impedance Zi=====%%
63 Zi_hat = tf([1.8e-06 4.86e-06 7.128e-06 4.716e-06 1.296e
    -06 0], [1 2.7 5.44 6.748 6.408 3.784 0.96]); %
    Given in eq5.6
64 Zi=1/Zi_hat; % Intrinsic impedance (it is the inverse of
    Zi_hat)
65 Zi_jw = freqresp(Zi,Xq);
66
67     for j=1:size(Zi_jw,3)
68         Zi_jw1(j)=Zi_jw(:, :, j); % Frequency response of Zi
69     end
70
71 %%=Frequency response of optimal control impedance Zpto=%%

```

```

72
73 Zpto_opt=tf([1 -2.7 5.44 -6.748 6.408 -3.784 0.96],[-1.8e
      -06 4.86e-06 -7.128e-06 4.716e-06 -1.296e-06 0]); %
      Optimal control impedance from eq5.16
74 Zpto_jw = freqresp(Zpto_opt,Xq);
75
76     for j=1:size(Zpto_jw,3)
77         Zpto_jw1(j)=Zpto_jw(:, :, j);    % Frequency response
              of Zpto
78     end
79
80 sysg=frd(Zpto_opt,Xq);
81 %Computing frequency response data model for optimal control
      impedance Zu
82
83 %%=====Computing Phi_Fex=====%%
84 phi=Vq.*abs((y_new)).^2; % Computing phi_Fex from eq6.13
85 E_int= (Zpto_jw1./abs(Zpto_jw1+Zi_jw1).^2.*phi);
86 % Computing the total energy from eq6.13
87
88 %%=====Computing frequency response of omega=====%%
89 s1=tf([1 0],[0 1]);
90 S_1 = freqresp(s1,Xq);
91
92     for j=1:size(S_1,3)
93         S1(j)=S_1(:, :, j);    %Frequency response of omega
94     end
95
96 %%=Initial numbers of estimated control impedance Zpto=%%
97 a0=1e3*rand;
98 b0=1e3*rand;
99 c0=1e3*rand;
100 d0=1e3*rand;
101 e0=1e3*rand;
102

```

```

103 %%=====Computing eq6.22=====%%
104 err1=@(k1) trapz(Xq,abs(Zu_jw1-(fmineq(k1(1),k1(2),S1))).^2)
    ; % Returns the approximate integral of cost fun eq6.21
105 format short,[k1,fval1] = fminsearch(err1,[a0 b0]);
106 % Starts at the point a0 and b0 and attempts to find a local
    minimum k1 of the function described in err1
107 sys1=tf([k1(1,2) k1(1,1)],[1 0]); % Obtains eq6.22
108
109 %%=====Computing eq6.26=====%%
110 err11=@(k11) trapz(Xq,-1./2./pi.*(fmineq(k11(1),k11(2),phi,
    Zi_jw1,S1)))));
111 % Returns the approximate integral of cost fun eq6.25
112 nonlcon1 = @fq1; %Defining optimization constraints in @fq1
    : make sure the system to be stable.
113 format short,[k11,fval11] = fmincon(err11,[k1(1,1) k1(1,2)
    ],[],[],[],[],[],[],nonlcon1);
114 % Attempts to find a local minimum k11 of the function
    described in err11 with initial values k1(1,1) and k1
    (1,2)
115 sys11=tf([k11(1,3) k11(1,2) k11(1,1)],[1 0]); % Obtains eq6
    .26
116
117 %%=====Computing eq6.23=====%%
118 err2=@(k2) trapz(Xq,abs(Zpto_jw1-(fmineq(k2(1),k2(2),k2(3),
    S1))).^2);
119 % Returns the approximate integral of cost fun eq6.21
120 format short,[k2,fval2] = fminsearch(err2,[a0 b0 c0]);
121 % Starts at the point a0, b0 and c0 and attempts to find a
    local minimum k2 of the function described in err2
122 sys2=tf([k2(1,3) k2(1,2) k2(1,1)],[1 0]); % Obtains eq6.23
123
124 %%=====Computing eq6.27=====%%
125 err22=@(k22) 2.*real(trapz(omega1,-1./2./pi.*((fmineq(k22
    (1),k22(2),k22(3),phi,Zi_jw1,S1,0)))));
126 % Returns the approximate integral of cost fun eq6.25

```

```

127 nonlcon2 = @fq2; %Defining optimization constraints in @fq2
    : make sure the system to be stable.
128 format short,[k22,fval22] = fmincon(err22,[k2(1,1) k2(1,2)
    k2(1,3)],[],[],[],[],[],[],nonlcon2);
129 % Attempts to find a local minimum k22 of the function
    described in err22 with initial values k2(1,1), k2(1,2),
    and k2(1,3)
130 sys22=tf([k22(1,3) k22(1,2) k22(1,1)],[1 0]); % Obtains eq6
    .27
131
132 %%=====Computing eq6.24=====%%
133 err3=@(k3) trapz(Xq,abs(Zpto_jw1-(fmineq(k3(1),k3(2),k3(3),
    k3(4),k3(5),S1))).^2); % Returns the approximate integral
    of cost fun eq6.21
134 format long,[k3,fval3] = fminsearch(err3,[a0 b0 c0 d0 e0]);
    % Starts at the point a0, b0, c0, d0 and e0 and attempts
    to find a local minimum k3 of the function described in
    err3
135 sys3=tf([k3(1,4) k3(1,3) k3(1,2) k3(1,1)],[k3(1,5) 1 0]); %
    Obtains eq6.24
136
137 %%=====Computing eq6.28=====%%
138 err33=@(k33) 2.*real(trapz(omega1,-1./2./pi.*((fmineq(k33(1)
    ,k33(2),k33(3),k33(4),k33(5),phi,Zi_jw1,S1)))));
139 % Returns the approximate integral of cost fun eq6.25
140 nonlcon3 = @fq3; %Defining optimization constraints in @fq3
    : make sure the system to be stable.
141 format long,[k33,fval33] = fmincon(err33,[k3(1,1) k3(1,2) k3
    (1,3) k3(1,4) k0(1,5)],[],[],[],[],[],[],nonlcon3);
142 % Attempts to find a local minimum k33 of the function
    described in err22 with initial values k3(1,1), k3(1,2),
    k3(1,3), k3(1,4), and k3(1,5)
143 sys33=tf([k33(1,4) k33(1,3) k33(1,2) k33(1,1)],[k33(1,5) 1
    0]); % Obtains eq6.28
144

```

```

145 %%====Calculating elements of spring-damper system====%%
146 [num1,den1] = tfdata(sys11,'v'); % Returns the numerator and
      denominator of eq6.53
147 k1=num1(1,2); % Returns value k in figure 6.23
148 c=num1(1,1); % Returns value c in figure 6.23
149
150 %%====Calculating elements of spring-damper system====%%
151 [num2,den2] = tfdata(sys22,'v'); % Returns the numerator and
      denominator of eq6.55
152 k2=num2(1,3); % Returns value k in figure 6.24
153 c0=num2(1,2); % Returns value c in figure 6.24
154 b0=num2(1,2); % Returns value b in figure 6.24
155
156 %%=Calculating each elements of admittances eq6.48 and eq6
      .49=%%
157 [num3,den3] = tfdata(sys33,'v'); % Returns the numerator and
      denominator of eq6.56
158 K=num3(1,4); % Returns value k in eq6.57
159 d_1=den3(1,2); % Returns value d1 in eq6.57
160 b=num3(1,1)/d_1; % Returns value b in eq6.57
161 a_0=(num3(1,2)-b)/K; % Returns value a0 in eq6.57
162 a_1=num3(1,3)/K; % Returns value a1 of eq6.57
163 beta1=a_0*d_1; % Returns value beta1 in eq6.47
164 beta2=a_0; % Returns value beta2 in eq6.47
165 beta3=a_1-d_1; % Obtains value beta3 in eq6.47
166 beta4=beta2^2-beta1*beta3; % Returns value beta4 in eq6.47
167 c_1=K*beta2^2*beta3/beta4; % Returns value c1 in figure 6.25
168 c_2=K*beta2^2/beta1; % Returns value c2 in figure 6.25
169 b_1=K*beta2^3/beta4; % Returns value b1 in figure 6.25
170 c_3=K*beta3; % Returns value c3 in figure 6.26
171 c_4=K*beta4/beta1; % Returns value c4 in figure 6.26
172 b_2=K*beta4/beta2; % Returns value b2 in figure 6.26

```

Appendix B

BerthB2012-05-16T12h00Z-spectrum

0.025,4.2756E-5,357.2,70.2,-2.00,1.90
0.030,1.1798E-4,66.1,69.6,0.86,1.67
0.035,6.8575E-4,75.9,78.6,1.10,1.65
0.040,3.1122E-4,324.8,71.2,-0.49,1.47
0.045,1.3878E-3,268.6,57.4,1.73,2.83
0.050,2.9089E-3,260.2,67.3,0.98,1.85
0.055,4.3178E-3,296.7,76.2,0.80,1.44
0.060,1.0514E-2,350.2,68.5,-1.04,1.76
0.065,5.0540E-2,355.8,45.4,-1.26,4.03
0.070,2.1763E-1,0.0,25.4,-2.22,11.76
0.075,5.9156E-1,358.6,27.9,-1.08,11.71
0.080,5.7408E-1,0.0,32.2,-2.46,9.26
0.085,1.0000E+0,358.6,20.5,2.53,20.02
0.090,6.1879E-1,353.0,31.1,-1.84,5.07
0.095,3.4130E-1,351.6,29.2,6.38,10.95
0.100,4.8920E-1,358.6,28.8,-3.98,9.66
0.110,2.8508E-1,344.5,36.9,-0.83,3.81
0.120,2.3340E-1,327.7,36.9,0.77,3.85
0.130,2.1653E-1,324.8,34.1,-0.03,5.78
0.140,8.8921E-2,320.6,38.7,-0.34,2.94
0.150,7.5396E-2,316.4,41.3,-0.31,3.14
0.160,8.5863E-2,312.2,38.6,-0.48,3.80
0.170,5.1303E-2,317.8,41.6,-1.21,3.78
0.180,4.3937E-2,308.0,47.6,-0.10,2.71

0.190,5.0037E-2,312.2,45.1,0.01,2.15
0.200,4.2214E-2,312.2,39.8,-0.46,3.94
0.210,2.6649E-2,310.8,52.7,-0.41,2.63
0.220,2.7052E-2,293.9,42.0,-0.51,4.02
0.230,2.6782E-2,274.2,43.1,0.10,3.13
0.240,2.1279E-2,261.6,48.0,0.39,2.71
0.250,4.3067E-2,258.8,43.6,-0.11,2.67
0.260,3.2064E-2,254.5,39.6,0.88,3.96
0.270,2.1494E-2,251.7,41.5,0.52,3.37
0.280,2.5477E-2,260.2,35.7,1.11,5.57
0.290,2.3993E-2,244.7,44.5,0.70,3.06
0.300,2.4848E-2,240.5,38.9,1.29,3.49
0.310,1.7249E-2,240.5,45.3,0.78,2.89
0.320,1.4407E-2,240.5,46.8,0.79,3.05
0.330,1.3300E-2,255.9,45.1,0.66,3.22
0.340,1.1563E-2,244.7,42.4,0.17,4.35
0.350,1.1620E-2,244.7,52.0,0.71,2.31
0.360,8.6517E-3,236.3,51.1,0.95,2.39
0.370,9.1409E-3,253.1,45.4,-0.27,3.21
0.380,5.0166E-3,265.8,49.6,-0.49,3.14
0.390,4.4493E-3,227.8,58.4,0.35,2.09
0.400,4.4272E-3,216.6,48.8,1.39,3.32
0.410,4.3613E-3,226.4,50.8,0.96,2.45
0.420,5.3002E-3,227.8,43.3,1.43,3.84
0.430,4.8928E-3,226.4,40.1,0.17,3.83
0.440,3.3460E-3,230.6,44.3,-0.07,2.89
0.450,3.7351E-3,244.7,48.3,-0.04,2.60
0.460,3.6610E-3,251.7,47.0,-0.03,2.26
0.470,2.5288E-3,237.7,50.2,0.34,2.16
0.480,2.6986E-3,213.8,45.0,0.71,3.78
0.490,2.4055E-3,234.8,51.5,0.71,2.40
0.500,2.4664E-3,237.7,52.8,0.26,2.13
0.510,1.5110E-3,236.3,55.2,0.49,1.70
0.520,1.8363E-3,240.5,45.5,0.51,2.47
0.530,1.7207E-3,239.1,49.7,-0.22,2.25

0.540,2.1017E-3,218.0,52.7,0.77,2.53
0.550,2.9528E-3,225.0,49.2,1.21,2.67
0.560,1.8090E-3,222.2,52.8,0.61,2.07
0.570,1.4089E-3,219.4,51.7,0.74,2.24
0.580,1.6867E-3,220.8,47.7,0.21,2.74

Appendix C

BerthB2012-05-16T12h00Z

0, 55, 14, 3
0, 52, 1, -28
0, -2, -17, -13
0, 16, -45, 7
0, 50, -49, 0
0, 8, -29, 0
0, -1, -41, 4
0, 36, -53, -25
0, -12, -23, -59
0, -82, 11, -26
0, -60, 19, -11
0, -26, 23, -21
0, -5, 30, -10
0, -2, 26, -1
0, 8, -4, 10
0, 26, -37, 26
0, 37, -31, 31
0, 10, -18, 19
0, 4, -10, -4
0, -4, 22, -5
0, -10, 29, -1
0, -21, -1, 5
0, 21, -24, 10
0, 20, 29, -18

0, -20, 49, 7
0, 10, -8, 15
0, 0, -13, 12
0, 7, 5, 10
0, 19, 16, -2
0, 28, -3, 17
0, 16, -41, 23
0, 21, -32, -8
0, -47, 13, -45
0, -98, 54, -14
0, -68, 79, -2
0, -39, 59, 5
0, 28, 6, 35
0, 67, -2, 9
0, 20, -17, -10
0, 5, -56, 11
0, 29, -35, 3
0, 4, -25, -3
0, -7, -24, 14
0, 17, -37, 40
0, 109, -57, 24
0, 79, -32, -28
0, 6, -44, -47
0, -41, -62, -73
0, -92, -9, -74
0, -133, 65, -42
0, -144, 62, 8
0, -50, 65, 39
0, 44, 89, 34
0, 86, 72, 10
0, 78, 33, -8
0, 74, -18, -5
0, 48, -35, -8
0, 23, -12, 17
0, 4, 12, 24

0, -32, 0, 10
0, -38, -33, 21
0, -14, -50, 0
0, -23, -14, 0
0, -27, 12, 33
0, 10, 14, 25
0, 26, 25, 30
0, 60, -1, 22
0, 37, -31, -41
0, -57, -54, -54
0, -82, -51, -4
0, -64, -10, 21
0, -31, 25, 17
0, -23, 34, 5
0, 43, 37, -13
0, 79, 47, -24
0, 42, 23, -3
0, 31, -19, 21
0, 36, -44, 27
0, 80, -43, -16
0, 9, -19, -62
0, -65, 2, -23
0, -64, -19, 7
0, -43, -29, 28
0, -27, -2, 24
0, -48, 28, -7
0, -34, 47, -23
0, -2, 54, -29
0, 10, 80, -25
0, 21, 75, -43
0, 43, 52, -10
0, 52, 11, 36
⋮